Design and Modeling of High Performance Permanent Magnet Synchronous Machines

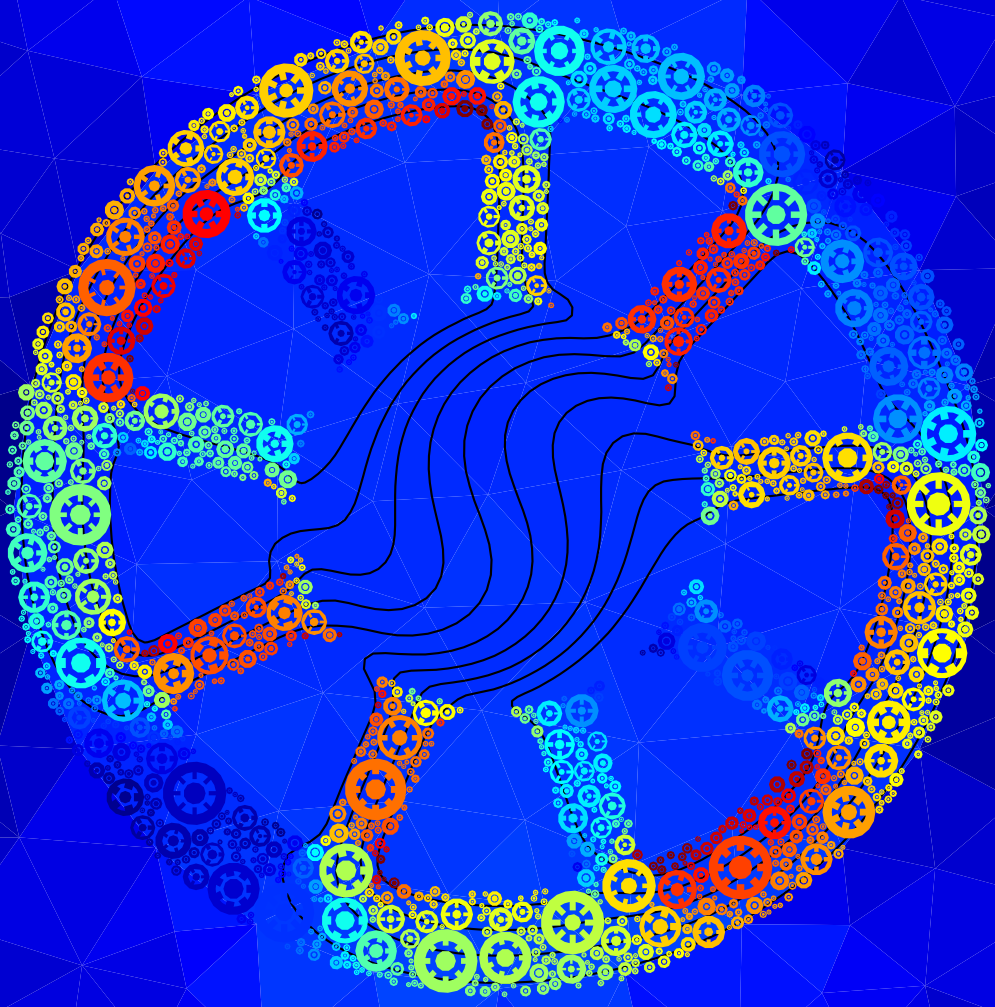

Martin van der Geest

Design and Modeling of High Performance Permanent Magnet Synchronous Machines

Proefschrift

ter verkrijging van de graad van doctor
aan de Technische Universiteit Delft,
op gezag van de Rector Magnificus prof. ir. K.C.A.M. Luyben;
voorzitter van het College voor Promoties,
in het openbaar te verdedigen op
vrijdag 27 november 2015 om 10:00 uur

door

Martin VAN DER GEEST

elektrotechnisch ingenieur,
Technische Universiteit Delft, Nederland,
geboren te Rijpwetering, Nederland

Dit proefschrift is goedgekeurd door de

promotor:	Prof. dr. eng. J.A. Ferreira en
copromotor:	Dr. ir. H. Polinder

Samenstelling promotiecommissie bestaat uit:

Rector magnificus,	voorzitter
promotor:	Prof. dr. eng. J.A. Ferreira
copromotor:	Dr. ir. H. Polinder

onafhankelijke leden:

Prof. dr. B.C. Mecrow	Newcastle University, United Kingdom
Prof. dr. C. Gerada	University of Nottingham, United Kingdom
Prof. dr. ir. J. Hellendoorn	Technische Universiteit Delft
Prof. dr. ir. M. Zeman	Technische Universiteit Delft

Overig lid:

Dr. M. Gerber	Aeronamic B.V.

The research leading to these results has received funding from the European Union's Seventh Framework Programme (FP7/2007-2013) for the Clean Sky Joint Technology Initiative under grant agreement № CSJU-GAM-SGO-2008-001.

Printed by: Gildeprint

ISBN: 978-94-6233-158-7

Contents

Summary

The electrification of aerospace transportation calls for a wide range of challenging electrical machines. Those machines often have very high rotational speeds, wide operating ranges in terms of torque and speed, high safety requirements, and they should interface well with both the inverter and mechanical surroundings. At the same time, both the mass and the development and production cost should be kept at a minimum. To meet those expectations, analysis and design tools are required that are flexible, accurate and fast, and can be used at both an abstract system level and a very specific detail level. Typical tools include analytical or finite element analysis (FEA), combined with various optimization strategies.

The goal of this thesis is to propose and demonstrate new design and analysis methods for high performance electrical machines. Throughout this thesis, the design process of a brushless permanent magnet (PM) starter/generator (S/G) for aerospace applications serves as a central theme. The basic behavior and modeling methods of the selected machine topology, a surface mounted PM (SPM) machine with retaining sleeve, are well known, but to successfully meet the conflicting S/G requirements, a range of advanced topics needs to be investigated. In particular:

- An optimization method is needed to examine and compare machine layouts and ultimately obtain a satisfactory candidate machine.
- A computationally efficient rotor eddy current loss calculation method is needed for use with the optimization method.
- To obtain a safe system, all aspects of turn-to-turn short circuit faults, which includes detection, propagation and mitigation, need to be researched.
- To achieve a high power densities, a high electrical frequencies is needed. This requires a study into AC losses in the windings.
- The machine will be driven by an inverter and the interaction between them needs to be accounted for. This includes sizing considerations as well as parasitic loss effects.

Although this thesis exclusively considers PM machines, the proposed methods and approaches can be applied to a much broader range of machine types. Finally, the earlier chapters focus more on the modeling and optimization methods, with a shift in the later chapters to the insights that are obtained by using the models.

Optimization
A first step is to develop a suitable optimization strategy. A variety of multi-objective particle swarm optimization (PSO) is used together with FEA to analyze the performance of the electrical machines. When using FEA in this way, one should carefully select the necessary simulation steps to bring the calculation time down to manageable levels. If this is done properly, the use of FEA offers many benefits, because many electromagnetic effects that affect machine performance can be included with great ease for a wide variety of machines, thereby shifting the designer

effort from developing and validating the models, to actual machine design problems. In turn, multi-objective optimization algorithms are an effective means to gain insight into complex design problems, because they can reveal trends that are not always evident at the start, especially with multiple highly conflicting targets. The first chapter discusses all of those aspects.

Rotor eddy current losses
Next, the calculation of rotor eddy current losses is discussed. Computing those losses becomes complex when the induced currents are (partially) inductance limited. A custom FEA approach is employed to reduce the time needed for those calculations, best suited for SPM machines. In this approach, a conventional 2D or 3D FE model of a full machine is first solved in a number of static steps. The results from this step are used to compute torque and torque ripple, iron losses and winding proximity losses. The tangential airgap H-field is then extracted and applied to a FE model containing only the rotor geometry, which is solved with a time-dependent simulation. This second model has fewer degrees of freedom and may be solved with linear material properties, providing time gains up to one order of magnitude, particularly in heavily saturated machines. This approach is used in 2D during optimization and in 3D during post-processing steps.

Winding AC losses
In high-speed high-performance machines, the winding design requires special attention, because the high electrical frequency can lead to significant AC losses. Moreover, fewer but thicker turns are needed to obtain a given back emf, leading to even higher induced losses. Litz wire can reduce those losses, but has a somewhat poorer fill factor and thermal ratings. As an alternative, parallel strands of conventional solid magnet wire may be used. The use of parallel strands potentially creates an unbalanced current distribution across the strands. FE models with individual strands are needed to analyze this effect, but these are numerically cumbersome (2D) or simply infeasible (3D). This thesis shows that with the inductance matrix, obtained from multiple FE models with single strands, the current imbalance can be predicted correctly over a wide frequency range, as demonstrated by experiments. Using those models, the effectiveness of a single twist is demonstrated and design rules for using parallel strands are established.

Short circuit faults
Fault behavior is an important aspect in aerospace machines. Internal turn-to-turn short circuits are particularly dangerous due to the extremely high local loss densities. If the machine cannot be de-excited or stopped, as with the S/G, this failure can become catastrophic. A commonly used approach to avoid such a catastrophic failure is to design the machine with a 1-pu inductance. This allows a machine to be safely short-circuited at its terminals after detection of a fault, which should reduce internal short circuit currents to nominal values. This thesis considers the effectiveness of this approach, as well as methods to detect the fault in the first place. The advantages and disadvantages of using parallel strands with regards to safety are highlighted. Additionally, experiments are performed with the proposed fault detector, showing the ability to detect short circuits across 0.4% of the winding. Practical limits of the proposed detector are also discussed.

PWM induced losses
High performance machines are often driven by a non-filtered switching inverter. This leads to a high frequency ripple in the phase currents, which in turn induces additional losses in the entire machine. In this short-chapter, the dependency of the iron, rotor and winding losses on the switching frequency and dc-link voltage is explored.

Starter/generator design
Using the knowledge and models from the previous chapters, the actual S/G is designed. The specific machine has to deliver a starting torque of approximately five times the generator torque. This rules out the possibility of using a 1 pu inductance, from both the machine and inverter sizing perspective, and a 0.25 pu inductance is used instead. The designed machine is constructed and tested, showing expected performance in all areas and demonstrating that a brushless PM S/G can be realized.

Power density limits
Finally, after demonstrating the correctness of the FE models, the optimization method is used to determine quantitative specific power density limits and trends of surface mounted PM machines, as function of rotor surface speed, power level and cooling scenario. The strong dependency on cooling effort, even stronger than rotor surface speed, is highlighted. Underlying trends in design variables and machine parameters are also shown and discussed. This allows the results to also be used as starting or reference point for new designs.

Samenvatting

De elektrificatie van de luchtvaart vraagt om een breed scala aan uiteenlopende elektrische machines. Deze machines hebben vaak een hoog nominaal toerental, een groot werkgebied qua koppel en snelheid, moeten voldoen aan strenge veiligheidseisen, in een beperkte ruimte passen en aangestuurd kunnen worden door een zo klein mogelijke omvormer. Tegelijkertijd moeten de massa en de ontwikkel- en productiekosten zo laag mogelijk zijn. Om aan deze verwachtingen te kunnen voldoen, zijn ontwerptools nodig die flexibel, precies en snel zijn; en in eenvoudig ingezet kunnen worden op zowel een abstract systeemniveau als een zeer laag detailniveau. Gangbare tools zijn analytische of eindige-elementen-analyse (FEA), in combinatie met allerlei optimalisatiemethodes.

Het doel van dit proefschrift is het voorstellen en demonstreren van nieuwe ontwerp- en analysemethodes voor hoog presterende elektrische machines. Het ontwerpproces van een borstelloze permanent-magneet (PM) starter/generator (S/G) voor luchtvaartoepassingen vormt hierbij een rode draad. De basale eigenschappen en modelleringsmethodes van het gekozen machinetype, een PM machine met oppervlaktemagneten en bandage (SPM), zijn algemene kennis, maar om succesvol aan alle conflicterende S/G-eisen te voldoen, moet een aantal specifieke onderwerpen nader onderzocht worden. Dit omvat onder andere:

- Een optimalisatiemethode om machinetypes te onderzoeken en vergelijken, en uiteindelijke een kandidaat-machine te selecteren.
- Een efficiënte methode voor het berekenen van rotorwerverstroomverliezen voor gebruik binnen de optimalisatiemethode.
- Om een veilig systeem te verkrijgen moeten alle aspecten van windingsluitingen onderzocht worden. Dit bestaat uit detectie, propagatie en tegenmaatregelen.
- Een hoge elektrische frequentie is nodig om een hoge vermogensdichtheid te verkrijgen. Hierdoor is een onderzoek naar wervelstroomverliezen in de wikkeling nodig.
- De interactie tussen de omvormer en de machine, zowel qua dimensionering als parasitaire verliezen.

Alhoewel in dit proefschrift uitsluitend PM-machines aan bod komen, zijn veel van de voorgestelde methodes en aanpakken toepasbaar op een veel groter aantal machinetypes. Tenslotte zullen de eerdere hoofdstukken zich met name richten op modelvorming, terwijl in de latere hoofdstukken de aandacht verschuift naar de inzichten die verkregen worden door het gebruik van de modellen.

Optimalisatie
Een eerste stap is het ontwikkelen van een geschikte optimalisatie-aanpak. Een versie van multi-objective particle swarm optimalisatie (PSO) wordt gebruikt, in combinatie met 2D FEA voor het bepalen van de machineprestaties. Wanneer FEA op deze manier wordt gebruikt moeten de

benodigde simulatiestappen zorgvuldig gekozen worden om de rekentijd laag te houden. Indien dit correct is gedaan, biedt het gebruik van FEA veel voordelen, omdat veel elektromagnetische effecten die invloed hebben op de machineprestaties eenvoudig meegenomen kunnen worden voor een grote verscheidenheid aan machines. Hierdoor kan de ontwerper meer tijd besteden aan het daadwerkelijke ontwerpprobleem, in plaats van het opstellen en valideren van modellen. Multi-objective optimalisatie is op zijn beurt een manier om inzicht te krijgen in complexe ontwerpproblemen, omdat hiermee trends gevonden kunnen worden die niet eenvoudig vallen te voorspellen, zeker wanneer meerdere sterk conflicterende doelen worden gebruikt. Dit hoofdstuk bepreekt al deze zaken.

Rotorwervelstroomverliezen
Vervolgens wordt de berekening van rotorwervelstroomverliezen besproken. Het berekenen van deze verliezen wordt complex wanneer de geïnduceerde stromen (deels) inductief begrensd zijn. Een aangepaste FEA-aanpak, met name geschikt voor SPM-machines, wordt gebruikt om deze berekening te versnellen. In de voorgestelde aanpak wordt eerst een conventioneel FE-model van een volledige machine opgelost met een aantal rotor-posities. Deze resultaten worden eerst gebruikt voor de berekening van het koppel, de ijzerverliezen en de wisselstroomverliezen in het koper. Voor de rotorverliezen wordt de tangentiële component van het magnetisch veld in de luchtspleet als randvoorwaarde toegepast op een tweede FE-model van alleen de rotor, waarmee een tijdsafhankelijke berekening wordt uitgevoerd. Dit tweede model heeft minder onbekenden en kan opgelost worden met lineaire materiaaleigenschappen, waardoor een tijdsbesparing tot één ordegrote verkregen kan worden, in het bijzonder in zwaar verzadigde machines. Deze aanpak wordt in 2D toegepast tijdens de optimalisaties en in 3D tijdens nabewerkingsstappen.

Wisselstroomverliezen in de wikkeling
In elektrische machines met een hoge draaisnelheid heeft het ontwerp van de wikkeling extra aandacht nodig, doordat de hoge elektrische frequentie tot significante geïnduceerde verliezen kan leiden in het koper. Daarbij zijn minder maar dikkere windingen nodig om een gegeven emk te verkrijgen, wat de situatie verergert. Met behulp van Litze-draad kunnen deze verliezen verlaagd worden, maar Litze-draad heeft een wat lagere vulgraad en slechtere thermische prestaties dan massief draad. Een alternatief is het gebruik van meerdere massieve draden in parallel. Dit kan echter leiden tot een ongelijke verdeling van de opgedrukte stroom over de draden. FE-modellen met afzonderlijk gemodelleerde draden kunnen dit effect simuleren, maar zijn numeriek zwaar (2D) of zelf onhaalbaar (3D). Dit proefschrift laat met simulaties en experimenten zien dat met de inductantiematrix op draad-niveau, verkregen uit meerdere FE-modellen met steeds één draad, de stroomverdeling correct voorspeld kan worden over een breed frequentiebereik. Met deze methode worden de effectiviteit van één draaiing van een bundel draden per machine-lengte gedemonstreerd en ontwerpregels voor het gebruik van parallelle draden opgesteld.

Windingsluitingen
Het gedrag bij fouten is een belangrijke eigenschap voor machines in luchtvaarttoepassingen. Windingsluitingen zijn bijzonder gevaarlijk door de potentieel zeer hoge lokale verliezen. Als de machine niet mechanisch kan worden gestopt of elektrisch uitgeschakeld, zoals bij de beoogde S/G, kan deze fout catastrofale gevolgen hebben. Een veel gebruikte aanpak om dit te voorkomen

is de machine te ontwerpen met een inductantie van 1 pu. Hierdoor kan een machine veilig worden kortgesloten aan de klemmen na de detectie van een windingsluiting, en wordt de kortsluitstroom idealiter gelijk aan de nominale stroom. Dit proefschrift analyseert de effectiviteit van deze methode en presenteert een manier om sluitingen te kunnen detecteren. Ook komen de gevolgen van het gebruik van parallelle draden voor de veiligheid komen aan bod. Verder worden experimenten uitgevoerd met de voorgestelde foutdetector, waarbij wordt aangetoond dat sluitingen over 0.4% van een spoel gedetecteerd kunnen worden. Tenslotte worden praktische limieten van de detector besproken.

PWM-geïnduceerde verliezen
Elektrische machines in veeleisende toepassingen worden vaak aangestuurd met een omvormer, meestal zonder filter. Dit leidt tot een hoogfrequente rimpelstroom in de fasestromen, die tot parasitaire verliezen in de gehele machine kan leiden. In dit korte hoofdstuk wordt de afhankelijkheid van de ijzer-, rotor- en koperverliezen van de schakelfrequentie en tussenkringspanning verkend.

Starter/generator-ontwerp
Met de modellen en opgedane kennis uit de vorige hoofdstukken, kan nu de daadwerkelijke S/G ontworpen worden. De toepassing vraag om een startkoppel ongeveer vijf maal groter dan het generatorkoppel. Dit sluit het gebruik van een 1 pu inductantie uit, zowel qua machine- als omvormerontwerp, en een inductantie van 0.25 pu wordt in plaats daarvan gebruikt. De ontworpen machine wordt gebouwd en getest, waarbij de gemeten eigenschappen overeenkomen met de voorspelde eigenschappen. Dit laat zien dat een borstelloze PM S/G haalbaar is.

Vermogensdichtheidslimieten
Nadat de juistheid van de modellen is aangetoond wordt de optimalisatiemethode gebruikt om de vermogensdichtheidslimieten en achterliggende trends van SPM machines te kwantificeren als functie van rotor-omtreksnelheid, vermogensniveau en koelmethode. De vermogensdichtheid blijk nog sterker afhankelijk van de koelmethode dan de omtreksnelheid. De bijbehorende trends in de ontwerpparameters en machine-eigenschappen worden ook getoond en besproken. Hierdoor kunnen de resultaten ook gebruikt worden als start- of referentiepunt voor nieuwe ontwerpen.

Glossary

CF	carbon fiber
CW	concentrated winding
d	direct axis
DW	distributed winding
FE(M)	finite element (method/model)
FSM	flux switching machine
GA	genetic algorithm
i	current (A)
IPM	interior permanent magnet (machine)
LEM/N	lumped element model/network
MVP	magnetic vector potential
PI	proportional-integral
PLL	phase locked loop
PM	permanent magnet
PMSM	PM synchronous machine
POF	Pareto optimal front
PSO	particle swarm optimization
pu	per-unit
PWM	pulse width modulation
q	quadrature axis
	slots per pole per phase
RMS	root mean square
S/G	starter/generator
SPM	surface mounted permanent magnet (machine)
TE	totally enclosed
u	voltage
x	scalar number
$\mathbf{x}$	vector
$\mathbf{X}$	matrix
θ	tangential component in cylindrical systems
λ	linked flux (Wb)
	thermal conductivity (W/(m·K))
μ_r	relative permeability

ρ	resistivity (Ωm)
σ	conductivity (S/m)
ω	angular frequency (rad/s)

CHAPTER 1

Introduction

Electrical machines have been in commercial use for over 150 years. Obviously, machine designs have changed over this period, but the changes in the way machines were analyzed and designed are perhaps even larger. Initially using empirical approaches, then slowing shifting into more mathematics based methods, and with the onset of cheap computing power, a rise in use of numerical methods. At the same time, the economical situation changed, with varying relative prices of raw materials, energy and labor. These two trends together changed the goals and intentions of a machine design. Historically, the limited understanding or modeling capabilities together with cheap materials led to low risk designs, but as the accuracy of the models increases, designs can be increasingly optimized.

This leads to the current design situation for high performance application-specific machines, such as those found in transportation applications, but also in e.g. high-speed turbine-based generation systems. In those applications, the market imposes requirements on the machine design that are non-existent in classic machine applications:

- Close integration in a larger system. While machines have always intrinsically been part of larger systems, the interface with those systems could be neglected or strongly simplified. In high-performance systems, the system integration imposes strict requirements on e.g. weight, dimensions, operational speed ranges, inductance and efficiency.
- A trend towards higher frequencies. Historically the grid imposed a working frequency of 50 or 60 Hz (and an associated maximum rotational speed), allowing many ac loss sources, such as winding or rotor eddy current losses, to be neglected or analyzed in a simplified fashion. In high-speed applications frequencies above 1 kHz are not uncommon, necessitating a careful analysis of those effects as well.
- Shorter and more flexible development process. For standard industrial applications one may use off-the-shelf machines, selected from a wide range of standardized machine types and having predictable lead times. Unfortunately, such machines are often unsuitable for high performance applications and a custom machine needs to be designed. However, the

development cost and time are often limited, with little room for later revisions. Moreover, the specifications may not be fully fixed –or understood– at the start of a project and may change as insights are gained, necessitating additional development cycles. Ultimately, this development climate calls for a fast and flexible design and analysis strategy, while still having sufficient accuracy to avoid the need for a redesign.

- Fault-tolerance and reliability. In certain applications, including aerospace, automotive and off-shore wind energy, a high reliability is necessary. If this is to be obtained through component level redundancy, additional constraints are placed on the machine design.

- Cost. The emphasis on low cost, whether that are acquisition or operation costs, seems stronger than ever. This limits for instance the selection of materials or constrains the geometric design to enable a simple manufacturing process ('design for manufacturability'). This too places additional constraints on the machine design.

To successfully design a machine with full consideration of those requirements, an integral design approach is needed where both the system level machine design and more detailed loss mechanisms receive attention. This thesis proposes such an approach. As a result, there is no extreme emphasis on one specific topic. Instead, the various aspects needed to design a feasible prototype machine are discussed separately in the chapters.

The contributions of this thesis cover a comparatively wide range of topics. In particular, there are contributions on the efficient usage of 2D and 3D FEA to calculate rotor eddy current losses and current sharing between parallel strands; on the consequences and detection of turn-level short circuit faults; on the determination of machine design trends; and on the design trade-offs and considerations for a high-speed permanent magnet starter/generator machine. An implicit contribution is the demonstration that through effective modeling, a wide range of topics can be addressed in a short time frame, yet with a high level of detail.

1.1 Motivation

The work in this thesis is ultimately driven by the desire to replace brushed dc starter/generator (S/G) machines in helicopter applications with a brushless counterpart. Brushed dc machines, although simple to control, require periodic brush inspection and maintenance, as well as mechanical torque dampers to handle the starting torque impulse. Brushless machines are typically lighter than dc machines, but at the cost of a most likely heavier inverter unit and increased control complexity. Nonetheless, the promise of reduced maintenance requirements warranted a research project on the feasibility of brushless starter/generators.

1.2 Objectives

1.2.1 Project objective

The primary objective of the research project is defined as follows:

Design a surface mounted PM machine starter/generator meeting the specifications summarized in Table 1.1.

To fully appreciate the trade-offs that follow from the specifications, a few calculations need to be made. The maximum generator mode torque is about 4 Nm; five times less than the minimum starting torque. To obtain good starting performance, one may be tempted to design a large machine with high flux densities, but this reduces the high-speed generator performance. In addition, the machine needs to be fail-safe. This will be achieved by designing the machine to be able to withstand a three phase short circuit, which in turn is achieved by using an adequate cooling system and per-unit phase inductance (a common approach often described in literature). However, minimizing the short circuit losses implies using a large inductance together with low excitation flux densities, which directly opposes the starting requirement. Hence, all major operating modes are expected to oppose each other, necessitating a careful machine design.

The original requirements included a dc-link voltage of 28 V. At peak starting power, the resulting dc supply current would be in the order of 1000 A. For the machine, currents of similar magnitude were to be expected. However, early design studies indicated that this approach was infeasible for the entire drive system, and the dc-link voltage was increased to 270 V.

Although the specifications do not specifically prescribe a surface mounted PMSM, this machine topology was chosen as it is suitable for high speed operation and it is believed that it offers the highest power density. Whether or not the latter is fully correct is irrelevant to this thesis, since the application and machine type only serve as an example problem in many of the following

Table 1.1 Summarized Starter/Generator requirements

Property	Requirement
Generator power	5 kW
Nominal speed	24,000 RPM
Generator speed	50–100 %
Generator efficiency	> 93%
Starting torque	>20 Nm, for 60 s
Safety level	fail-safe
DC-link voltage	Original: 28 V Modified: 270 V

analyses. In fact, many of the models and approaches to be proposed could equally well have been applied to e.g. an induction machine.

1.2.2 Thesis objectives

The specifications, together with the choice for a PM machine, present a number of additional problems. The initially very low dc link voltage implied that very few turns per coil will be necessary. Together with an electrical frequency of at least 400 Hz (in the case of one pole pair), high skin and proximity losses in the windings were to be expected. Using litz wire, a well known solution to those effects, was not desirable due to the somewhat poorer fill factor and thermal performance, amongst other reasons. Therefore, the aim was to still use conventional solid round enameled copper wire, leading to the objective

Determine the suitability of solid enameled wires in low voltage high-speed machines.

Next, the specifications call for a fail-safe design. As described above, this is achieved by applying a terminal level short circuit to the machine after the detection of internal faults. This leads to two research objectives:

Can a terminal level short circuit sufficiently reduce inter-turn short circuit currents?

and

Propose a fault detection concept suitable for stand-alone operation.

1.3 Outline and approach

The steps needed to fulfill the objectives are partially independent and are covered in individual chapters. Each of those chapters is mostly self-contained, having separate introduction, modeling & results, and conclusion sections; and can be read largely independent of the other chapters.

The S/G serves as a central theme in most chapters, but the specifications are often modified. This was necessary due to the confidentiality of the original specifications, but also to emphasize specific loss mechanisms. Nevertheless, most chapters are sufficiently broad to be useful beyond the specific S/G application.

Figure 1.1 schematically shows the steps (chapters) that are taken to address the objectives. In more detail, they are:

2. Machine selection and design with automated optimization To design a machine that satisfactorily meets the set of conflicting starting, generating and safety requirements, a multi-objective optimization method is deemed necessary. Hence, this chapter presents and describes such a method. Additionally, it takes a preliminary look at the S/G design problem.

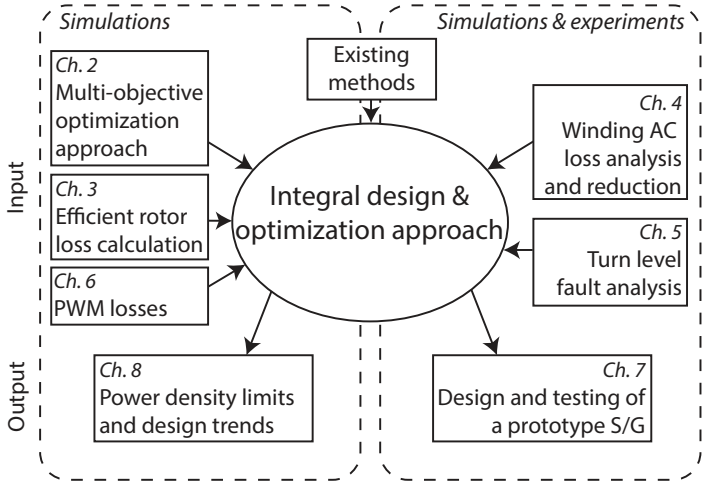

Figure 1.1 Outline of this thesis.

3. Efficient finite element based rotor eddy current loss calculation At high rotational speeds, rotor eddy current losses in PMSMs can become significant and need to be accounted for. Unfortunately, rotor loss calculations are expensive, both from human effort and numerical perspectives. Therefore, alternative 2D and 3D FEM methods are studied, particularly suited to a purely FEM-based optimization approach as proposed in the previous chapter.

4. AC winding losses in high-speed PM machines Another potential problem in high-speed machines are the AC winding losses, an effect that is exaggerated by the extremely low supply voltage of the initial S/G specifications. Under those conditions, conventional solid enameled strands can suffer from excessive AC losses, while litz wire may have a lower fill factor. In this chapter alternatives are therefore studied and a method to efficiently determine current sharing effects among parallel strands using 3D FEM is presented and experimentally validated.

5. Inter-turn faults – modeling, detection and consequences The S/G cannot be mechanically disconnected during internal faults, but will be short circuited across all phases instead. This requires estimates of the expected turn-level short circuit losses before and after the all-phase short circuit, which are calculated in this chapter using the models presented in the previous chapter. Furthermore, a fault detection circuit is proposed and the performance is simulated and experimentally validated in great detail.

6. Analysis of additional losses due to PWM induced current ripple The previous chapters consider the rotor and winding losses in detail, but do not account for the effects of time-harmonic currents on those losses. This brief chapter considers the additional losses in the windings, stator iron and rotor versus dc-link voltage and switching frequency. A large non-S/G machine is used to better demonstrate the potentially high losses.

7. Design and testing of a prototype permanent magnet starter/generator This chapter starts with an overview of existing S/G research. Then, using the optimization approach, models and knowledge gained in the previous chapters, the tradeoffs following from the specifications are analyzed and discussed. The relation between the machine design and the basic inverter rating are also considered. A final candidate machine suitable for manufacturing is designed. After manufacturing, the electromagnetic performance of the machine is tested to confirm the models used in this thesis.

8. Power density limits and design trends of high-speed PMSMs The final chapter looks beyond the S/G application and determines power density limits and trends of PMSMs, by using the optimization method at a large scale. This chapter can be used both as a reference when performing such a study, or as a reference on the limits of PMSMs and associated design trends.

Finally, one appendix provides background information:

A. Thermal model This appendix presents the thermal model used in several of the main chapters.

CHAPTER 2

Machine selection and design with automated optimization

The rising demand for machines with high a technological and economical performance calls for an automated design and optimization strategy. Due to the continuous reduction of computing costs, the possibilities in this area are continuously increasing. This chapter proposes such a method, based on particle swarm optimization combined with finite-element based machine analysis. After discussing the basic modeling and optimization approach, two examples are provided, demonstrating the basic steps applicable to any optimization problem as well as a number of involved post-processing steps.

Based on

- M. van der Geest, H. Polinder, J. A. Ferreira, and D. Zeilstra, "Optimization and comparison of electrical machines using particle swarm optimization," in *20th Int. Conf. Elec. Machines (ICEM)*, 2012, pp. 1380–1386; and
- M. van der Geest, H. Polinder, J. A. Ferreira, and D. Zeilstra, "Machine selection and initial design of an aerospace starter/generator," in *IEEE Int. Electric Machines Drives Conf. (IEMDC)*, 2013, pp. 196–203.

2.1 Introduction

Selecting an electrical machine for a given application usually starts with choosing a certain machine type, such as a switched reluctance machine or a PM machine, based on qualitative arguments. Due to the distinct differences between various machine types, this approach usually suffices. Once the machine type has been fixed, the specific machine configuration has to be chosen. Especially with PM machines many variations exist in terms of flux direction, winding layout or magnet placement. Qualitative arguments may then no longer suffice to make a proper selection and the differences need to be quantified. Furthermore, to ensure a fair comparison between the various machines, each design should be optimized for the specific application at hand.

Quantifying the performance of each machine variation requires models to estimate the performance. Analytical models are often used for this purpose and although these can be evaluated very fast, they cannot accurately or easily take into account complex geometric shapes or non-linear effects. Also, separate models may be required for different machine variations, requiring the designer to spend precious time on creating those. Of course those disadvantages can be overcome by using FEA, shifting the required time from human to computer, but this creates other problems, such as a potential loss of insight and possibly very long calculation times. Nonetheless, hardware and software technologies have evolved to a point where the latter approach can be used.

The early attempts to use FEA in an electrical machine optimization process usually combine multiple goals in a single target with a weighted sum and use a limited number of variables. In [1, 2] induction machines are optimized for a single target with a genetic algorithm (GA), while deterministic algorithms were used for this purpose in [3]. However, the long calculation times limited the use to individual machines, optimized for a single task.

With the increase of computer speeds it became feasible to optimize entire machines, sometimes for multiple targets. Other physical domains can also be included, such as the thermal [4] or mechanical [5] domains. The latter is especially relevant at higher rotational speeds, where the stresses in the rotor can reach the material limits or dynamic behavior prevents operation at certain speeds. Optimizing for multiple targets is sometimes (still) achieved with a weighted sum, but this requires an a priori decision on the relative importance of all targets and thereby hides the trade-off between the optimization targets from the user. Several optimization trails with differing weights are then necessary to gain insight in the design problem. Referring to such an approach as 'multi-objective' may even be considered as misleading. If instead the concept of Pareto optimality is used, the trade-off between all targets can be visualized after the optimization and the user can make a more informed decision on the final design space for a new machine [6]. Figure 2.1 shows an abstracted Pareto optimal front, which demonstrates that in the presence of conflicting targets, no single optimal design exists. Instead, an infinite number of optimal designs exist, each with a different trade-off between the targets. For electrical machines, x and y could for instance be losses and mass, among many other parameters. Lastly, Pareto optimal fronts also

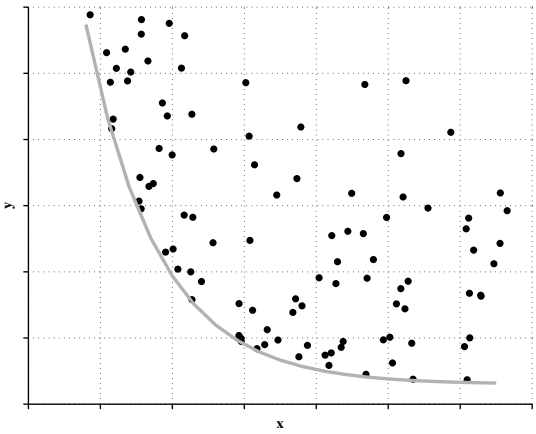

Figure 2.1 Abstract Pareto optimal front. Both x and y are ideally minimized, but no designs below the grey line can be found.

are an effective means to communicate machine design limits to a wider audience, as the targets often involve broadly understood figures such as weight, cost or efficiency.

To perform the actual machine optimization, a wide range of optimization algorithms can be used, but as the cost function becomes expensive to evaluate, the selection of a suitable algorithm becomes more important. Since the computation time is very significant with FE modeling, the algorithm should require as little function calls as possible to achieve convergence. In addition, the results from FEA can be noisy due to e.g. meshing differences, which impedes convergence in algorithms using the gradient of the results. These considerations usually lead to the selection of an evolutionary algorithm.

In machine optimization two major evolutionary algorithms are often applied: particle swarm optimization (PSO) and genetic algorithms (GA). There have been attempts to compare the two methods [7, 8], suggesting that, in general, PSO performs slightly better in terms of optima found, time required to find these optima and ease of tuning. These methods are mostly used in combination with analytical models [9–12] or magnetic equivalent circuits [13], but the combination with FEA is gaining popularity [6, 14–16].

This chapter demonstrates a method to combine machine optimization and comparison. To this end, multi-objective PSO is used to optimize complete machines, resulting in Pareto optimal fronts. These fronts then provide a simple means for comparison of various machines. 2D finite element analysis is used to analyze the machines, allowing all relevant effects to be considered and simplifying the comparison of completely different machine architectures.

In the next section the modeling approach and the PSO algorithm used in this thesis are explained. In the following section they are applied to a simple two-objective problem to compare three

PM machines and introduce the concept to the reader, while the fourth section presents a more involved example with four objectives.

2.2 Optimization and modeling strategy

Any engineering related optimization approach consists of two parts: models to describe the problem and an algorithm to perform the actual optimization. The models used here are all based on 2D FE computations, which allows a simple comparison of completely different machines without the need for separate analytical models. Nonlinearity can also be taken into account, which is essential to obtain realistic results. The optimization algorithm used here is PSO. This algorithm was selected because it is gradient free, simple to implement and tune, and potentially requires very few function calls [7, 8].

2.2.1 Machine analysis

The numerical machine analysis is performed by a combination of MATLAB to create and postprocess the FE models and COMSOL Multiphysics to solve the FE models. To save time a minimum number of preferably static simulations is executed and the machine characteristics are obtained by postprocessing the results. The analysis of a single machine consists of the following baseline steps:

- Compute the linked flux shape, magnitude and offset position. Four static simulations provide the linked flux at 24 points in time due to symmetry between the phases [17], allowing the back-emf to be computed up to the 12^{th} harmonic. The phase order is also determined in this step. To obtain the linked flux from the 2D FE model, the average magnetic vector potential tangential to the winding path is used:

$$\lambda_{\text{dom}} = \frac{1}{A_{\text{dom}}} \iint A_z \, dA \tag{2.1}$$

  where λ_{dom} is the flux linked with a given domain, A_{dom} the area of that domain and A_z the z-component of the magnetic vector potential.
- Compute the inductances. The computation is based on a change in linked flux due to an applied current:

$$L = \frac{\lambda_I - \lambda_0}{I} \tag{2.2}$$

  where λ_I and λ_0 are the linked flux with and without current I, respectively. This allows saturation due to the magnets to be taken into account. If necessary, more involved inductance definitions could be used, such as a current dependent inductance or dq inductances (versus current if necessary).

- Iteratively determine the phase current needed to obtain the desired torque and then compute that torque including the torque ripple, using a filtered Maxwell stress tensor method [18]. This method offers a better accuracy for a given mesh size than a direct application of the Maxwell stress tensor in COMSOL, saving computational time.
- Compute the mass (of the stack and end-windings), copper losses (in the stack and end-windigs) and iron losses. The iron losses are computed by using manufacturer data to obtain an equation for the specific loss density of the form

$$P = k_h f^{\alpha} B^{\beta} + k_e f^2 B^2 \tag{2.3}$$

  where P is the specific power density, f the frequency and B the peak flux density; and k_h, α, β and k_e are material dependent constants. With this equation, the loss density distribution is computed from the AC flux density distribution throughout the entire stator, thereby correctly taking local high flux densities into account. An example of such a distribution is shown in Figure 2.2.
- Compute the rotor eddy current losses. The induced currents are computed with

$$J_{z,ind} = \sigma \frac{dA_z}{dt}. \tag{2.4}$$

  It is assumed that the magnet pieces are electrically insulated from each other. In 2D models, this implies that within each magnet piece, the total z-current must be zero (otherwise, an axial electric field would build up inside the magnet). This is specifically enforced in the models by subtracting the average induced current density from the locally induced current density for each individual magnet piece:

$$J_z = \sigma \frac{dA_z}{dt} - \iint_{\text{magnet}} \sigma \frac{dA_z}{dt} dA. \tag{2.5}$$

  To compute dA_z/dt a transient ('time-stepping') simulation is necessarily used if interaction between the eddy currents and the inducing stator field (i.e. shielding) can occur. Such simulations are expensive, particularly with heavily saturated iron parts, and a modified FEA-based method is used; see Chapter 3 for more details. If the eddy currents are known to be purely resistance limited over the entire design space, dA_z/dt may simply be obtained from the static solutions used to compute the torque. Lastly, if laminations are present in the rotor, the lamination losses are computed as for the stator.

Additional problem dependent steps may also be taken, including:

- Compute the static or transient machine temperatures. See appendix A for details.
- Determine the worst case magnet operating point to estimate the risk of demagnetization.
- Compute the steady state short circuit performance (particularly the rotor losses) using a transient simulation with linear material properties. The short circuit repels the flux from the stator, warranting the use of linear material properties.

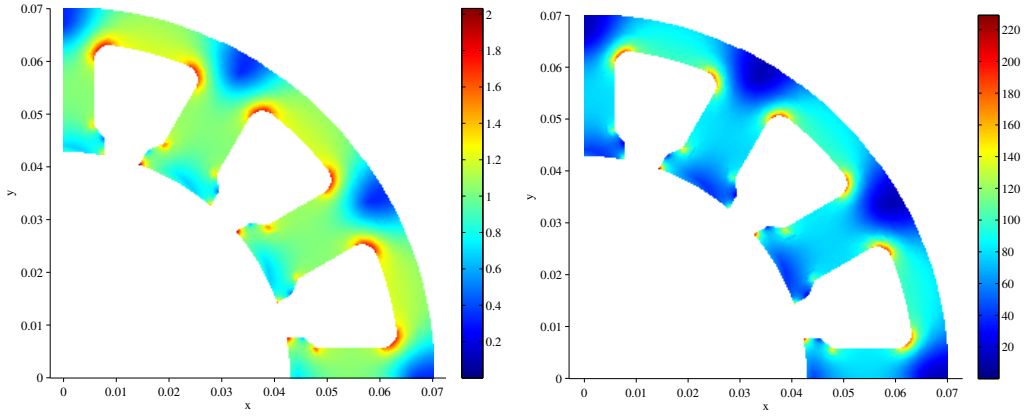

(a) Peak AC magnetic flux density distribution (T)

(b) Loss distribution (W/kg)

Figure 2.2 Example of stator lamination magnetic flux density and corresponding loss density distributions.

- Determine the maximum number of turns for a given DC-link voltage without and with the use of flux weakening and estimate the bare minimum inverter VA-rating, both using the PM-flux, synchronous inductance and a predefined torque-speed profile.
- Analyze starting (boost torque) capability, for example by analyzing the losses or temperature rise rate that would occur when operating at a given torque level, which has been determined iteratively.

Not all of these steps are required for all optimization problems. The time required to evaluate a complete model varies between 30 and 90 seconds, depending on the saturation level and the desired torque ripple resolution. This may not seem extremely fast, but combined with the PSO algorithm it can yield acceptable results in one or two days.

2.2.2 Particle Swarm Optimization

The optimization algorithm that will be used is particle swarm optimization [19], an evolutionary population based gradient free method based on the movement of birds or insects in a swarm. The original algorithm can only optimize for a single objective and multiple targets would need to be combined in a weighted sum. This is undesirable for machine design and optimization problems, and a multi-objective variant is used instead.

Single-objective PSO

The following equations define the basic algorithm:

$$\mathbf{v}_n = m\mathbf{v}_{n-1} + c_1\mathbf{r}_1(\mathbf{x}_{pbest} - \mathbf{x}_{n-1}) + c_2\mathbf{r}_2(\mathbf{x}_{gbest} - \mathbf{x}_{n-1}) \tag{2.6}$$

$$\mathbf{x}_n = \mathbf{x}_{n-1} + \mathbf{v}_n, \tag{2.7}$$

where $\mathbf{v}$ and $\mathbf{x}$ are vectors holding the velocity and position for a given particle, n is the iteration step, m, c_1 and c_2 are weights and $\mathbf{r}_1$ and $\mathbf{r}_2$ are vectors with random numbers on $[0,1]$. The length of all vectors equals the number of variables. The vectors $\mathbf{x}_{pbest}$ and $\mathbf{x}_{gbest}$ hold the vectors of the personal and global best positions in the search space known so far, for respectively each particle and the entire swarm, and should be updated after every iteration if better results are obtained. All values are initialized randomly.

In words, the equations resemble the movement of particles (originally fish, bees, birds, etc. searching for food) through a higher dimensional problem space. The direction each member moves in depends on three factors, each with its own scaling parameter:

- their current velocity combined with a mass; $m\mathbf{v}_{n-1}$,
- a tendency to move to their own known best position; $c_1\mathbf{r}_1(\mathbf{x}_{pbest} - \mathbf{x}_{n-1})$,
- a tendency to move to the best position known to the group; $c_2\mathbf{r}_2(\mathbf{x}_{gbest} - \mathbf{x}_{n-1})$.

Particles with a high m(-ass) and low $c_{1,2}$ show highly explorative behavior, while the opposite properties may lead to an early convergence. These three parameters are the main tuning parameters of the algorithm. Lastly, the number of particles has to be chosen. Fortunately, the performance does not depend strongly on this [8] and in most optimizations in this thesis, 20–30 particles are used.

Multi-objective PSO

The specific algorithm used here is modified to work with multiple targets simultaneously [7], which allows the Pareto optimal fronts to be computed. This is accomplished by storing all Pareto optimal solutions in a repository and picking the global best target randomly from this repository. The personal best of each particle is updated if a Pareto optimal design is found. If both the current and new designs are Pareto-optimal, the new design gets accepted with 50% possibility. After performing different optimization runs, the results can be compared by simply comparing the repositories. The major downside of this approach compared to single-objective optimization is that a larger part of the optimization space is considered so that more time is required to obtain the optimal designs. However, the ability to obtain a Pareto optimal front is deemed to outweigh the increased optimization time.

Certain parts of the solution space, such as extremely inefficient or heavy designs, will not be of interest. To prevent unnecessary exploration of these regions, the global target is confined to interesting parts of the solution space. Note that all results from particles that were successfully

evaluated and are Pareto optimal are kept in the repository, since they possibly yield insight into the design problem. Further note that selecting a too narrow solution space for the global best target will reduce the true multi-objective nature of the optimization. For such local searches, alternative algorithms may offer better performance.

Handling boundary conditions

The original PSO formulation does not constrain the optimization variables. However, in most engineering applications there are restrictions on practically all parameters, and it becomes necessary to limit the search space. In addition, certain combinations of parameters, where each parameter individually is within the outer search boundaries, can still lead to geometrically infeasible designs (e.g. negative lengths, disappearing slots) that cannot be evaluated, further reducing the search space. Hence, an approach to keep particles inside the allowed and feasible parts of the search space is therefore required.

In many optimization strategies, constraints are implemented through a penalty on the function output if the function input is outside the feasible search space. Since this still requires the cost function to be evaluated, it cannot be used with FE based machine optimization. Another approach is to place particles that would fall outside the search space, back on the border of the search space. Several variations of this approach have been proposed, such as speed reduction, variable clipping or reflecting [15, 20].

For inner infeasible regions those boundary handling methods become more complex, because often multiple approaches exist to move a particle back in the feasible region. For example, if the outer radius is fixed and all radial thicknesses are variable, the shaft inner diameter could become negative. This can be resolved by modifying any of the parameters, or a combination of them, which requires a complex decision strategy. To avoid this, an approach is used where the velocity of particles that would drift into an inner infeasible part of the search space is reduced until they become feasible again. Practise shows that this allows particles to get sufficiently close to the boundaries of the search space.

It should be noted though that the number and size of inner infeasible regions should and can be avoided by a proper specification of the geometry, because this generally allows a faster convergence [16]. For example, it is better to specify the relative than the absolute magnet span, because the latter, combined with the rotor radius, excludes a part of the search space.

2.2.3 Additional remarks

This section discusses a few additional practical aspects related to performing multi-objective machine optimization.

When creating a model to be used within an optimization approach, a balance needs to be found between accuracy, execution speed, ease of creation, and level of detail. Doing so requires

a clear picture of the total problem, so that one can determine the amount of modeling and calculation time spent on a given aspect. Unfortunately, the required insights are often not available at the start of a new research project, and can only be obtained through several iterations of optimization and postprocessing. Hence, it is important to not consider the optimization and modeling approach as a static object.

Next, it is recommended to always include 'sensibility checks' in machine analysis code where easily possible and stop when such an error is encountered. This includes for instance checking the input to a model against the assumptions used in that model; checking the convergence of any iterative solver; or checking for nonsensical values such as negative losses or unbalanced currents. To further find setup or user errors in an early stage of e.g. an optimization, it is important to display intermediate results, such as average torque, various losses, current density or inductance, during the analysis of a model. This allows an analysis or optimization run to be stopped and corrected to prevent a waste of time. In other words, an optimization process that only shows 'running…' for three days, is poor practice.

The results of numerically expensive calculations and any derived values should be stored, even if they are not directly used in the optimization targets. After an optimization, those results can reveal related design trends (see also Chapter 8); they may be used to correct for errors found after the optimization is executed; or they can help in the selection of final candidate machines, where differences in secondary variables can be a deciding factor when all primary performance targets are met.

2.3 Optimization example 1

To demonstrate the optimization method and familiarize the reader with Pareto based multi-objective optimization, a simple problem with two targets is presented in this section. Readers familiar with this topic could skip to Section 2.4. Three electrical machines in some varieties will be optimized for a theoretical motor application, see Table 2.1 for the specifications. The chosen rotational speed is fairly high, as this requires the rotor eddy current losses to be considered as well, which introduces additional complexity. Temperatures, inverter ratings or fault behavior are not yet considered for this example.

Table 2.1 Theoretical machine requirements

Parameter	Requirement
Generator power	10 kW
Rotational speed	10,000 RPM
Stator outer radius	70 mm

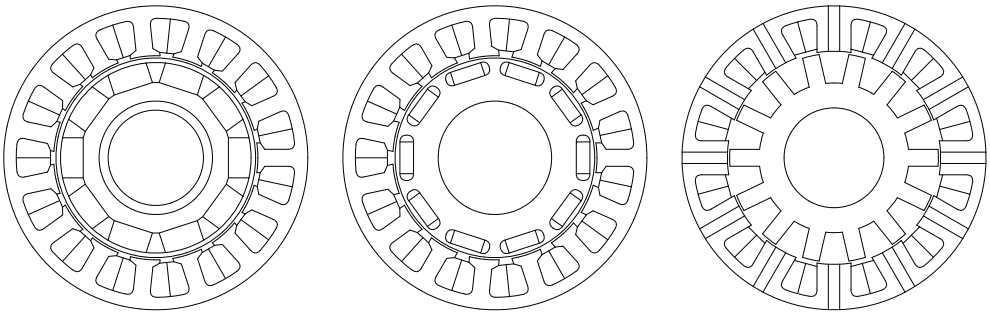

Figure 2.3 Three machine types: (a) Surface mounted magnets with retaining sleeve; (b) Buried (interior) magnets; (c) Flux switching machine.

2.3.1 The PM machines considered

Three interior rotor PM machines will be considered, some in slightly different combinations. These are:

- Surface mounted magnet machine (SPM, Figure 2.3(a)) with an Inconel retaining sleeve,
- Buried magnet machine (IPM, Figure 2.3(b)),
- Flux switching machine (FSM, Figure 2.3(c)) with:
  - ▷ 12 slots, 10 rotor teeth and
  - ▷ 12 slots, 14 rotor teeth.

Exploratory studies have been performed for the SPM machine on appropriate slot/pole combinations, leading to the selection of a 15 slot, 10 pole concentrated non-overlapping winding layout (one coil per tooth). This specific combination has the benefits of tooth-coil windings (short end-windings, easy manufacturing, potentially high fill factor), but, compared to other non-overlapping winding layouts, a fairly clean space harmonic spectrum and therefore low rotor losses, an important design aspect in higher speed machines. For this reason a machine with an Inconel retaining sleeve was considered. Note that, compared to the often used 12/10 combination, the 15/10 combination has a slightly lower winding factor and a potentially higher torque ripple [21].

The IPM machine is often quoted for its robustness, because the magnets are both mechanically and magnetically protected by the laminations containing them. Compared to SPM machines, IPM machines are better suited for flux-weakening operation due to the reluctance torque they exhibit [22] and the tendency for higher per-unit inductances. For the IPM a 15/10 slot/pole combination will be optimized too. Note that to fully exploit the reluctance torque, a distributed winding should be used, but for the sake of comparison, only tooth-coil winding layouts are used.

Flux switching machines received a lot of attention in the past ten years and they are being considered for many applications [23]. They have a robust rotor suitable for high-speed operation, and compared with regular rotor-mounted PM machines they possess a potentially higher power density [24, 25]. A very common stator/rotor teeth combination is 12/10, which for three phase winding schemes is the layout with the minimum number of teeth that still provides a balanced force and back-emf [26]. Note that in FSMs every rotor tooth resembles a pole pair to the stator, so that the electrical frequency in the stator of a 1210 FSM is twice that of a 1210 SPM, potentially leading to increased iron losses.

2.3.2 Optimization targets, assumptions and search space

The machines will be compared in terms of efficiency and weight. These objectives apply to many applications and by using only two Pareto targets the fronts can be presented as 2D plots, which aids comprehensibility when printed.

Table 2.2 summarizes the material properties used. Non-linear iron is assumed in all cases. Saturation could be neglected at low field strengths, reducing the computation time, but neglecting saturation will generally lead to over-predicted machine performance. The non-linear iron in the stator is of the 10JNEX900 type, for which extensive saturation curves are available [27]. For the rotor of the IPM, iron with a lower saturation level was chosen, leading to better performance due to less leakage flux in the bridges.

Table 2.3 shows the limits used for all parameters. A properly selected range avoids useless computations on models that will not offer a realistic performance. Common to all designs is a fixed outer stator radius, a typical requirement when a machine has to fit inside a given space. For the IPM two optimization runs were executed, one with a fixed current angle of 0°(i.e. not using reluctance torque) and one where it was variable.

There are no limits placed on the current or flux density, which may lead to unrealistic designs from e.g. a thermal or electrical perspective to be considered. To avoid wasting computational cycles on those designs, the global target in the PSO algorithm was selected from particles with at least 93 % efficiency.

Table 2.2 Assumed material properties

Part	Property
Magnets	B_r= 1.2 T μ_r = 1.05 ϱ = 1 μΩm
Sleeve	Inconel: ϱ = 1.2 μΩm μ_r = 1
Stator Iron	10JNEX900
Rotor Iron	FSM: 10JNEX900 IPM,SPM: M250-35
Fill factor	40 %

Table 2.3 Optimization variable range

Variable	SPM	IPM	FSM
Stator outer radius (mm)	70		
Yoke thickness (mm)	3–10		
Slot height (mm)	11–23		11–24
Tooth width (mm)	4–13		4–18
Tooth tip width (%)	40–85		NA
Airgap length (mm)	1–3.5	0.5–2	0.75–2
Rotor teeth length (mm)	NA		5–21
Rotor back iron (mm)	8	10	5–30
Bridge/sleeve thickness (mm)	2	1.5	NA
Magnet thickness (mm)	5–16	3–10	NA
Magnet span (%)	50–99		20–50
Stack length (mm)	20–100		
Current angle δ (°)	0	-45–0	0

2.3.3 Optimization results

The resulting Pareto fronts are shown in Figure 2.4, while Figures 2.5 and 2.6 show a selection of the resulting parameters. The actual front is represented by a line, since all particles by definition lie on this line. This does not necessarily apply to the derived variables, so these are presented as scatter plots.

When reviewing optimization results the first step should always be to check that no variable ran into the boundaries of the search space. This indicates that the boundaries where chosen too small and limit the performance. On the other hand, if this shows that there are no results in a certain part of the search space, this part can be omitted in future optimization runs to save time. Figure 2.6(a) shows that for light designs the IPM with variable angle and the FSM1210 reached the minimum airgap length, but this specific parameter is usually bound to a minimum from a mechanical viewpoint.

The next step is to consider the actual results. Since an optimization strategy like this produces a large amount of data, some time should be spend to examine the credibility of the results and investigate seemingly wrong behavior. Results in line with expectations are not necessarily correct. The computed Pareto fronts in Figure 2.4 all show the same trend: an increasing efficiency with increasing weight. This was to be expected, since heavier machines can operate with reduced flux and current densities, and since most loss mechanisms scale with the square of the driving force, the total losses are reduced. A simple plot like Figure 2.4 also immediately shows the power of Pareto fronts, since it reveals considerably more information than optimizations where the targets are combined in a weighed sum. (A weighted sum optimization would focus entirely on a single part of the Pareto optimal front, and the user has to make sure that this is indeed the desired

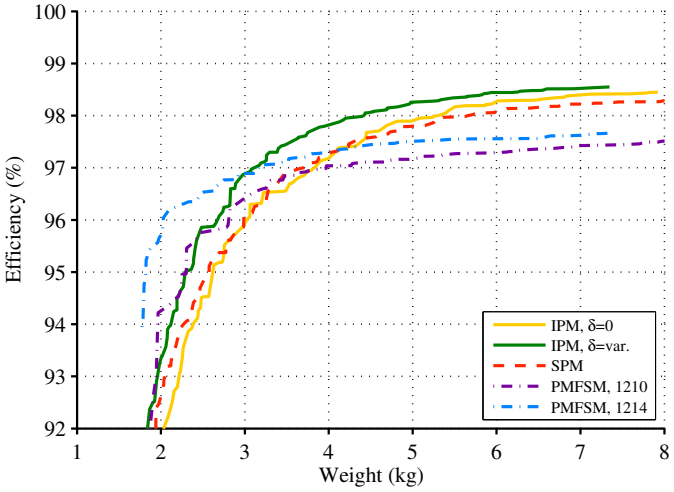

Figure 2.4 Maximum efficiency versus weight.

part of the design space.) Figure 2.5 is also a demonstration of the need to store all intermediate results: while the efficiency at a given weight may be very similar between the machine types (as can be seen from the true Pareto front), the loss distribution across the various machine parts may not be as similar.

Studying all results, the following individual observations are made:

- With respect to the maximum achievable efficiency, a FSM is the least attractive option. Reviewing the individual loss components shows that this is mainly caused by somewhat higher rotor, magnet and stator iron losses. The efficiency of light FSMs is however equal to or better than that of the considered SPM and IPM machines.
- The efficiency versus weight curves of the IPM and SPM machines follow the same trend, with the IPM with variable current angle offering the best performance. The only conclusion that can be drawn is that IPM and SPM machines perform rather similar in terms of weight and efficiency, endorsing the conclusions in [28].
- The copper losses in all machines follow the same trend, the 1214 FSM having the lowest copper losses at low weights.
- The 1214 FSM performs better on all aspects than the 1210 FSM, which corresponds with findings in [26]. Only the rotor losses have a similar magnitude, probably due to the higher electrical frequency.
- The split ratio (the stator inner radius divided by the outer radius) of the SPM machines is slightly lower than that of the IPM machines. This corresponds with results reported by others [29].

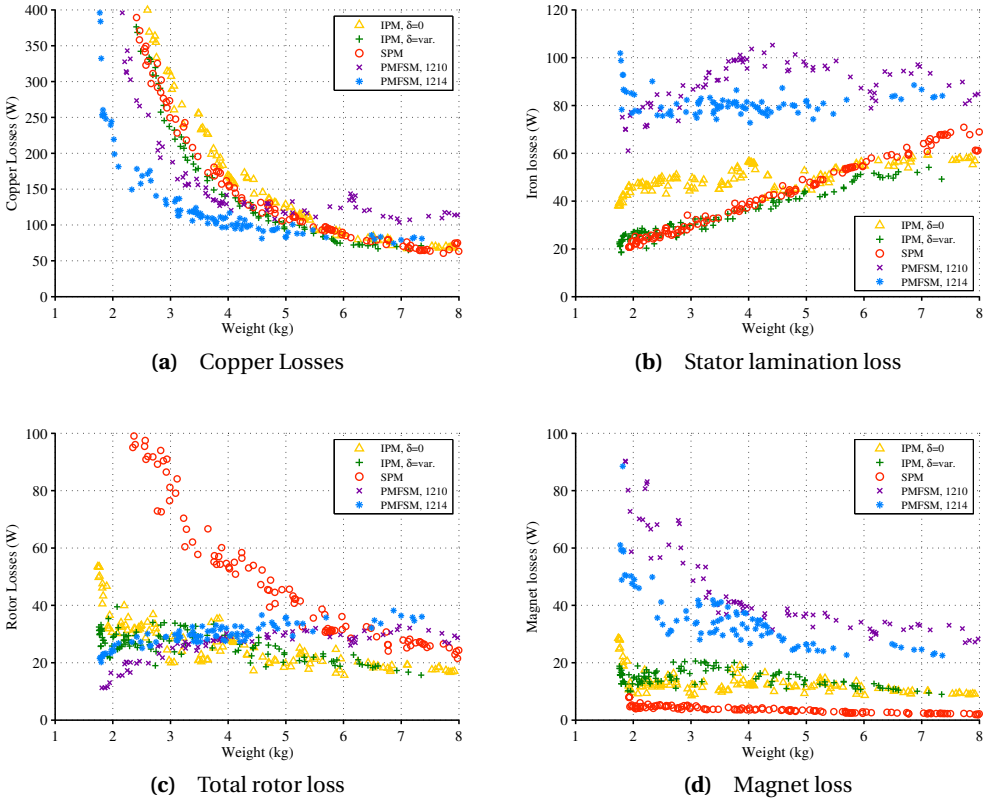

(a) Copper Losses

(b) Stator lamination loss

(c) Total rotor loss

(d) Magnet loss

Figure 2.5 Individual loss sources.

- The results for the two IPM machines are in accordance with expectations. With the optimization with a variable current angle the optimum angle deviates from 0 (Figure 2.6(c)), indicating that reluctance torque is used.
- The airgap in the Inconel sleeve SPM machine is significantly larger than the others to minimize the eddy current losses in the sleeve.
- The magnet losses in the FSMs are relatively high, even though two radial segments were assumed. This partly reduces the benefit of having the magnets in the stator.

All in all these findings suggest that the algorithm can correctly detect trends in the solution space and that the results obtained can actually be used to compare different machines, both in terms of input and output quantities.

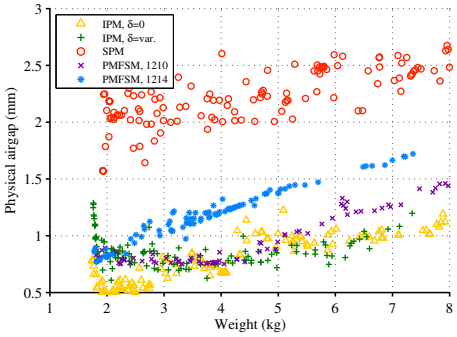

(a) Mechanical airgap

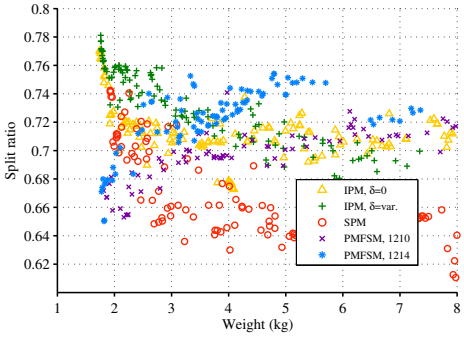

(b) Split ratio

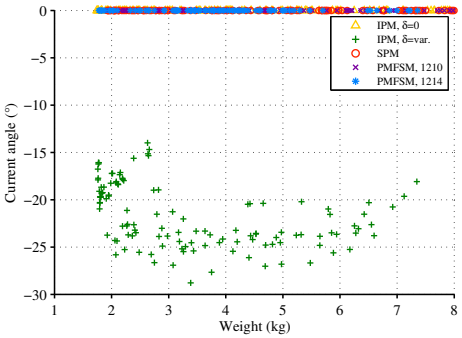

(c) Current angle relative to the q-axis

Figure 2.6 Resulting model parameters.

2.4 Optimization example 2: A first look at the S/G problem

This second example is more involved, having four objectives. It also serves as a first look at the starter/generator (S/G) design problem. Lastly, more emphasis is placed on a detailed investigation and presentation of the final results.

2.4.1 Target specifications

The basic S/G specifications used in this section are given in Table 2.4. The S/G is connected to the turbine via a gearbox, which is a common approach and results in a relatively low machine speed of 12,000 RPM. The minimum starting torque is about three times the maximum generator torque. When assuming an active length of 100 mm and split ratio of 0.6, the airgap shear stress during

Table 2.4 Starter/Generator requirements

Parameter	Requirement
Generator power	6 kW
Nominal speed	12,000 RPM
Generator speed range	50–100%
Generator efficiency	>93%
Starting torque (0-40% speed)	30 Nm
Starting duration	15–25 s
Starting copper losses	<2 kW
Maximum fault losses	< 600 W
Dimensions	max. 130×110 mm (l×dia)
Cooling	Forced air

starting is in the order of 50 kN/m²; which is an appreciable value for high-speed machines and cannot easily be maintained indefinitely with air cooling (See also Chapter 8). This high torque transient can take up to 25 s, thereby potentially overheating the windings. The starting copper losses are therefore limited to 2 kW. A trade-off thus needs to be made between over-dimensioning the machine for generator mode and overloading the machine in starting mode.

In addition, the machine should be fail-safe, meaning that it may fail, but not catastrophically. This is achieved by limiting the total short circuit losses to 600 W, which is believed to be a realistic upper limit. Ideally, a thermal model would be used to estimate the winding and rotor hot-spot temperatures. However, the outcome of a thermal model depends strongly on the boundary conditions. Establishing a realistic set of thermal boundary conditions requires involved heat and mass flow studies, combined with past experiences, and was therefore not yet undertaken at this point.

2.4.2 Machine optimization

For this problem, SPM machines with four to ten poles in a mixture of tooth-coil and non-tooth-coil windings will be considered, as well as 12/10 and 12/14 FSMs. Those machines were selected based on the expectation that they may be suitable as S/G, although this example does not involve all S/G related aspects, such as inverter dimensioning and control strategy. A more detailed analysis of the S/G design problem will be presented in Chapter 7. IPM machines are no longer considered because of their poorer mechanical performance at higher speeds, as well as preferences from project partners.

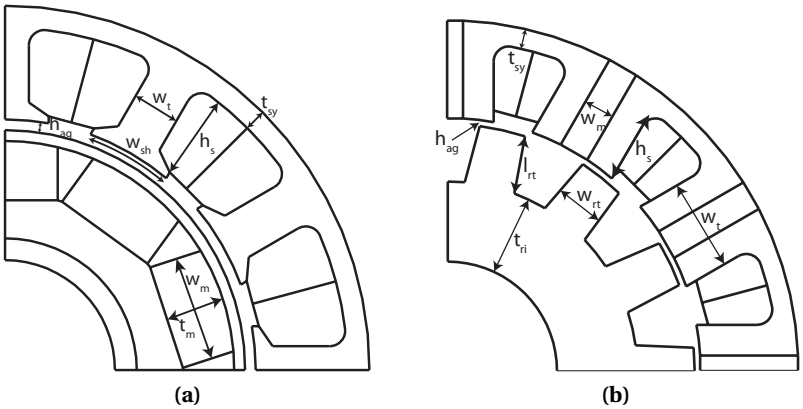

Figure 2.7 Optimization variables for the SPM (a) and FSM.

Description of the optimization approach

The analysis of each machine follows the same approach as the first example, but with the addition of calculating the rotor, copper and iron losses during a three phase short circuit, as well as the copper losses during starting. The iron and rotor losses are neglected during starting, both because they are expected to be low compared to the copper losses and their calculation is numerically expensive.

Optimization settings

Figure 2.7 shows the machine geometries to be optimized, with all variables indicated. The range of the variables was wide enough to allow the PSO algorithm to consider any design that would not lead to a degenerated (infeasible) geometry.

Four optimization objectives are used:

- *Maximize generator mode efficiency*
- *Minimize mass*
- *Minimize 3 phase short circuit losses*
  This objective ensures that the optimization progresses towards designs with acceptable fault losses. In case of a single phase short circuit, a three phase short circuit is applied by the inverter to reduce the losses in the faulted phase due to the mutual coupling.
- *Minimize copper losses during starting*
  During starting, the frequency is still low and the copper losses are the main cause of losses. Minimizing these will prevent heat-up of the machine as well as limit the additional power to be supplied by the inverter and source.

The fixed properties for all machine types are given in Table 2.5. SmCo magnets are considered because of their higher maximum operating temperatures compared to NdFeB magnets. The rotor retaining sleeve for the SPMs is made of carbon fiber (CF). Compared to metallic sleeves, a CF sleeve strongly reduces the eddy current losses and allows operation at higher speeds [30].

Table 2.5 Optimization settings and assumptions

Parameter	Value
Magnets	B_r=1 T μ_r=1.05 ϱ=1 μΩm
Magnet segmentation	SPM: 3 axial FMS: 3 radial
Lamination type	Iron–Cobalt
Slot fill factor	42%
Sleeve	Resistivity: ϱ=200 μΩm

For the PSO algorithm, 20 particles were used. The inertia-factor is decreased from 1 to 0.6 over 120 steps. The swarm and personal best weighing factors are drawn from a uniform distribution in the range of 1–1.4. The same global best target was used for at most four steps. With more than 1000 particles inside the repository, excess particles were removed from the repository with a hypercube algorithm using 10 segments per dimension. The optimizations were stopped after 250 steps. These values were selected based on literature (e.g. [14,20,31]) and prior experiments.

2.4.3 Optimization results

The optimization returns a 4D Pareto optimal front, which cannot be visualized easily. The results are therefore analyzed in three steps. At a high level, sub-fronts of two targets will be analyzed. At a second level, the complete fronts for one pole/slot combination are shown, separated based on one of the goals. This more clearly shows underlying trends, but can only be done for one Pareto optimal front at a time. As a third step, the fronts will be filtered to consider all targets for all slot/pole combinations simultaneously.

High-level results

Side-views to the 4D Pareto optimal front are shown in Figure 2.8. Only sub-fronts are shown for clarity, which means that designs located on e.g. the maximum efficiency versus weight sub-front do not necessarily lie on the minimum starting losses versus weight front as well. This representation can however reveal particularly strong or weak pole-slot combinations, as well as provide insight into the limits of each goal individually.

Figure 2.8(a) shows the efficiency versus weight. For the SPM machines, any slot/pole combination can yield a high generator efficiency (97.5–98%) if a large mass is allowed, but the highest efficiencies are obtained with a low pole count, because the lower frequencies allow a further reduction of the iron loss density. For lightweight machines of around 3 kg this trend is reversed and higher pole counts offer better performance, although the differences are small. The four

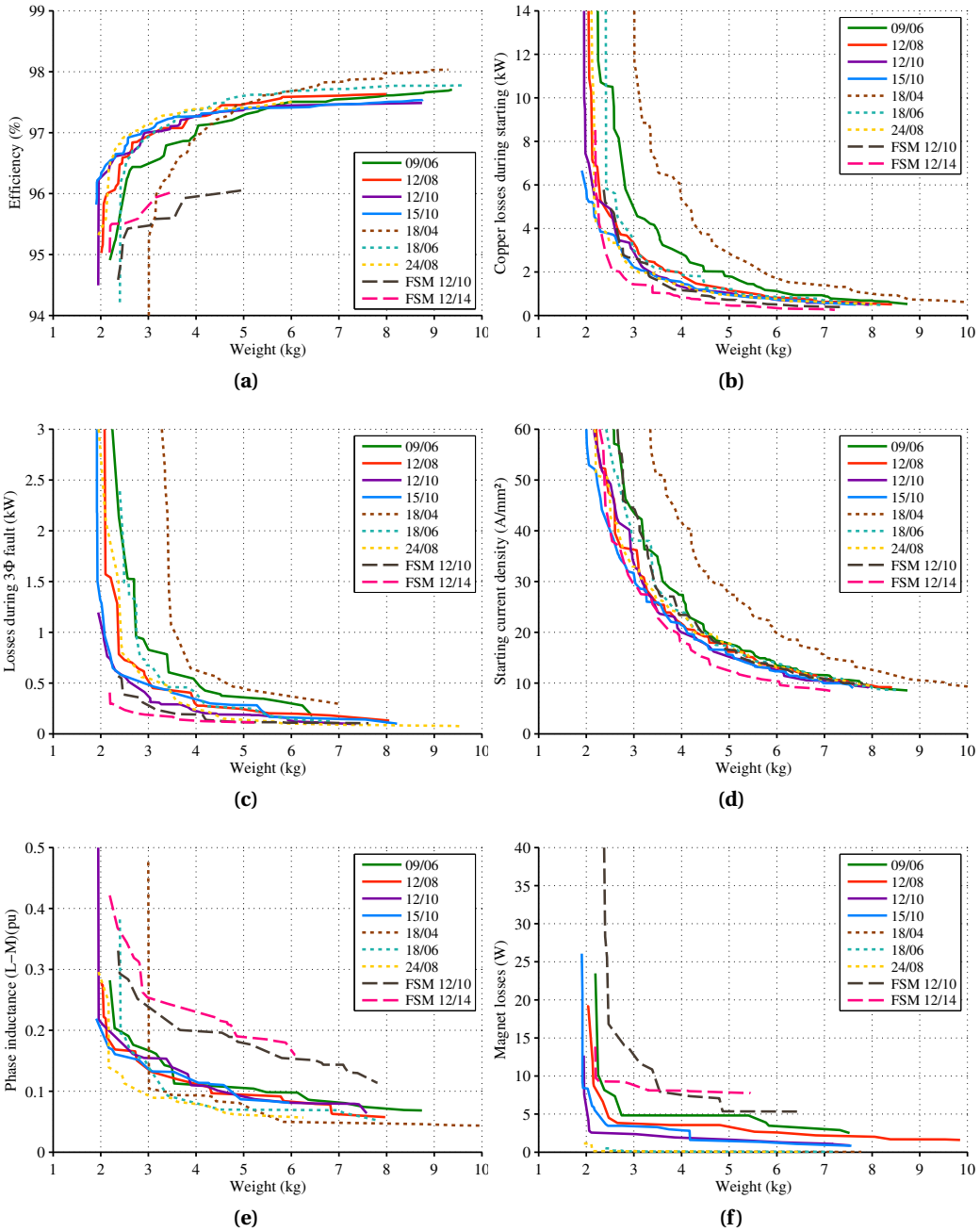

Figure 2.8 Sub-fronts of the Pareto optimal front. All plots show the maximum performance obtained for each goal, without consideration of the other goals.

pole distributed winding machine suffers from the heavy end-windings and is a poor choice for lightweight machines. The same efficiency/weight arguments hold for the FSMs, only the highest efficiency achievable is now about 96% due to the higher iron losses as result of the higher frequency.

A high number of poles is beneficial for the starting performance of the machines, as shown in Figure 2.8(b). There is no apparent difference between distributed or concentrated winding machines, apart from the 18/04 machine, which is again a poor choice. The FSM1214 is the lightest starter-only machine, but from 5 kg onward the other machines offer similar performance. When also considering the current density during starting (Figure 2.8(d)), an interesting observation can be made: the FSM1214 has the lowest starting losses at low weight, but not the lowest current density. This implies that the FSMs have less copper mass and that the winding will heat up more during starting. The current density at 3 kg is at least 30 A/mm², which will render air cooling ineffective and increases the importance of thermal capacity. For machines above 5 kg the severity of this issue decreases.

Figure 2.8(e) shows the per-unit (pu) phase inductance, referred to nominal generator mode. The FSM machines have a minimum inductance nearly twice that of the SPM machines. Moreover, the machines with $q > 0.5$ have somewhat lower inductances than the tooth-coil machines. This tendency of non-tooth-coil winding machines towards lower inductances negatively affects the possibility to limit the short circuit losses. The pu inductance links the machine design to the inverter design, since higher pu inductances require either a higher voltage rating (when using $i_d = 0$) or current rating (when allowing flux weakening). In the latter case, the machine current rating must also be increased.

It should be emphasized that these plots show the maximum achievable performance in one parameter only, disregarding the performance on the other parameters. Machines that perform favorably in these plots may perform not so well when considering all parameters. This is especially true for the fault losses, shown in Figure 2.8(c). Very low values, in the order of 100 W, can be obtained. These values are misleading however, as the next section will show that these designs have a very poor starting performance.

The magnet losses are shown in Figure 2.8(f). A clear separation between the concentrated and distributed winding designs can be observed. With distributed windings, designs with almost zero magnet losses can be found, while machines with tooth-coil windings will always have some magnet losses. This is simply the result of a richer space-harmonic content in the airgap of CW machines. Finally, in line with the previous example, the FSM machines have higher magnet losses than the SPM machines.

One particular front in detail

The fronts shown in Figure 2.8 are the 2D edges of the 4D front, which hides trends inside the front. A more detailed view is obtained by plotting all particles of one front, with the particles divided in groups based on some parameter. This is done in Figure 2.9 for the 12/10 FSM, with

the individual particles marked based on starting losses. Figure 2.9(a) shows this division; the horizontal bands are clearly visible. This same division is applied in Figures 2.9(b)–(f) as well, which immediately reveals design trends.

For example, designs with good starting performance, having starting copper losses less than 500 W (green crosses), also have the highest fault losses and the lowest generator efficiency. That is, a good starter is a bad fail-safe generator. Also, good starter machines have the highest rotor losses and the lowest per-unit inductance. The reasons behind this are simple: good starting performance requires a high torque-per-current-density rating, which in turn requires high excitation flux-densities in the machine. These are obtained with large magnet volumes and a short airgap. This leads to high iron and rotor losses at high speed and thus a poor generator performance. At the same time, the high excitation flux yields a low per-unit inductance, which in turn gives large short circuit losses. This contradiction applies to all of the machines considered here.

Figure 2.9 further shows that there is no contradiction between efficient generator operation and fault losses. In fact, the most efficient designs generally have the lowest fault losses. The explanation is exactly opposite to the one given above: low fault losses require little PM flux, which implies small magnets and a long airgap. The low flux density then allows efficient generator operation, because the generator torque is small compared to the starting torque.

A low per-unit inductance improves the power factor during starting, allowing an inverter with a lower current rating to be used. This means that the trade-off between starting and short circuit performance for the machine is coupled to the inverter design. To arrive at the optimal complete S/G system, it will then be necessary to consider this interaction at an early design stage. This aspect will be discussed in more detail in Chapter 7.

Another observation from Figure 2.9 is that in the corners of the Pareto space, e.g. at very low weights or with very low starting losses, the variation in secondary parameters is small. In other words, if obtaining the lowest possible starting losses is essential, the other parameters will be fixed. This makes sense, because the extreme corners of the Pareto optimal fronts resemble regions where a single objective optimization would converge to. From an optimization algorithm perspective, finding those extremes can be challenging and it is sometimes used as a performance measure when comparing algorithms. However, for engineering applications those extremes are rarely relevant and it is not necessary to use an optimization algorithm that excels at finding the extremes.

In summary, adding fail-safety to a generator has little impact on the performance, while adding fail-safety to a starter machine does strongly impact the performance, because starting is considered to be a transient overload condition.

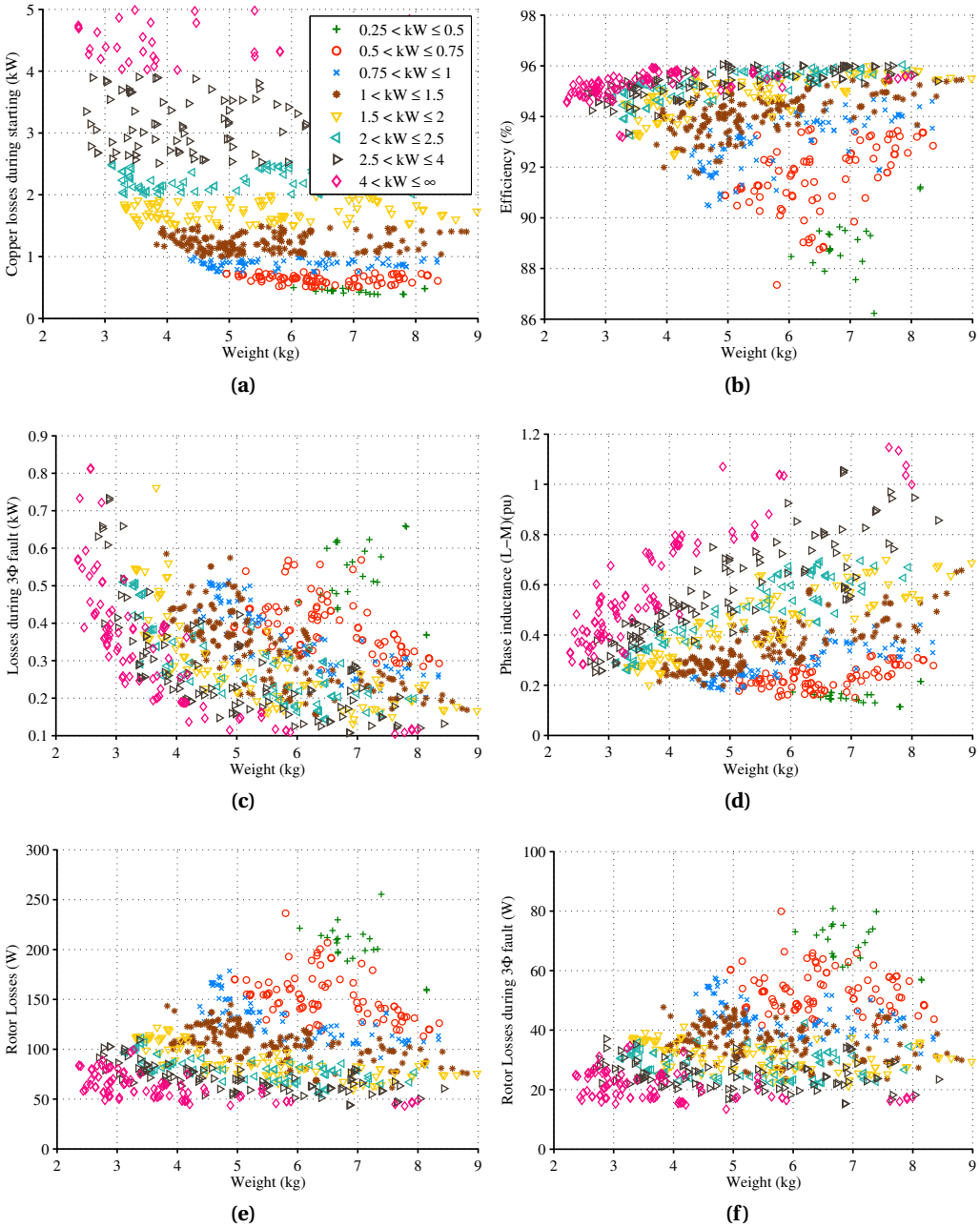

Figure 2.9 Multiple side-views of the Pareto optimal front of the FSM 12/10 machine, with the designs grouped based on the copper losses during starting.

Table 2.6 Initial number of particles on the front, fraction of particles meeting individual criteria and the fraction of particles meeting all criteria

Type	Initial particles	mass <9 kg	P_{start} <2 kW	93%< η	P_{SC} <600 W	Intersect
09/06	1196	98	43	96	25	2
12/08	972	98	46	99	23	5
12/10	1255	98	53	99	35	8
15/10	1366	99	51	100	18	3
18/04	1513	91	17	96	4	0
18/06	1343	96	30	99	22	0
24/08	1375	94	40	100	31	1
FSM 12/10	892	100	65	79	98	44
FSM 12/14	674	100	83	70	100	53

Considering all results

The previous section showed that a good starter machine has high fault losses and a poor generator efficiency. In order to assess the feasibility of each slot/pole combination, all performance criteria have to be considered simultaneously. To this end, constraints are set on the targets. The relative number of particles that meet all constraints is an indication of the feasibility of that specific design.

Table 2.6 shows the criteria that were used, the fraction of particles meeting each criterion individually and the fraction of particles meeting all criteria simultaneously. This way of representing the results is far from perfect too, in the sense that much information is lost, but it does allow a fast comparison of the individual machine types. For the FSM 12/10 machine the numbers in the table can be directly related to Figure 2.9. For example, Figure 2.9(b) shows that there are designs with $\eta < 93\%$ and Table 2.6 indicates that 21% of the FSM 12/10 designs have an efficiency below that limit.

A few observations can be made from Table 2.6. First, both FSMs show considerably more potential than the SPM machines, with about 50% of the front meeting all criteria. Of the SPM machines, those with tooth-coil windings show some feasibility, while machines with distributed windings lead to almost no feasible designs. The main reason lies in the ability to modify the per-unit inductance. With tooth-coil windings, the tooth-tips can be used to adjust the inductance independently from the back-emf (to some extent). Distributed windings do not offer this benefit. Since good starting performance requires a low per-unit inductance and low fault losses require a

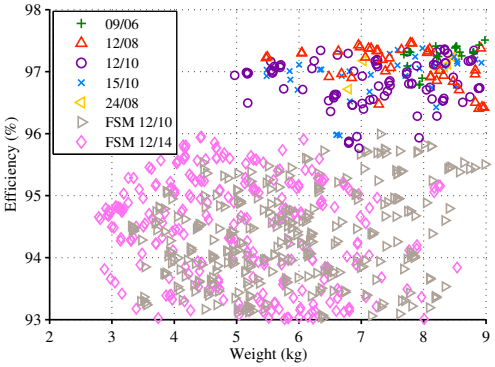

Figure 2.10 Efficiency of the Pareto optimal particles meeting all constraints.

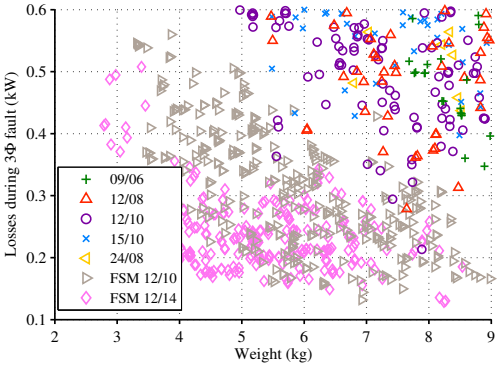

Figure 2.11 Fault losses of the Pareto optimal particles meeting all constraints.

per-unit inductance, the ability to fine-tune the inductance allows a better compromise between the two requirements to be found.

The performance of the feasible particles after filtering the Pareto optimal fronts is plotted in Figures 2.10–2.12. These figures show how the feasible designs relate to each other. Because the FSMs have far more feasible designs, they are presented with a lighter shade to avoid hiding the SPMs. Among the SPMs, the 12/10 is the lightest design, weighing about 5 kg. The 12/08 and 15/10 both need at least 5.5 kg, and the 9/6 machine even 7.5 kg. The only feasible DW machine, the 24/08, needs about 6.75 kg.

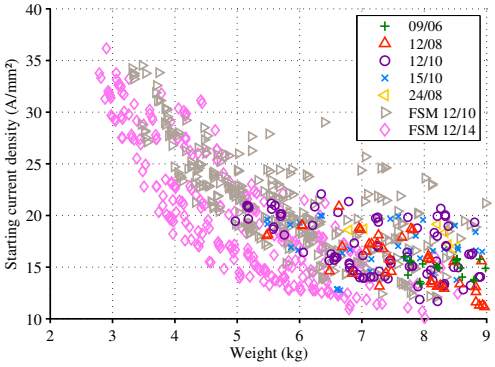

Figure 2.12 Starting current density of the Pareto optimal particles meeting all constraints.

2.5 Conclusion

This chapter presented a method to optimize electrical machines using multi-objective particle swarm optimization combined with finite element based machine models. Using this method, greatly different machines can be optimized in an identical (and thus fair) way, with little user effort, and a high accuracy. The outcome of each optimization run, a Pareto optimal front, reveals important design trends and limits and allows different machine topologies and layouts to be quantitatively compared. A major benefit of a multi-objective optimization strategy is the insight gained in the designed problem, both at high and low levels, which makes the execution time –one to two days on standard computers– worthwhile.

Analyzing optimization results is an essential part of any optimization strategy; without it, an optimization is not finished. This chapter described a number of possibilities to compare and present optimization results. The first step often consists of checking the results for obvious errors and whether or not any variable consistently ran into any boundary. Next, to compare results at a global level, Pareto optimal fronts may be directly compared. Side-views to the front may become cluttered with more than two objectives, which can be overcome by using Pareto optimal sub-fronts, although this removes the ability to correlate different side-views. That is, it shows only the most extreme designs possible. To study trends within a single Pareto optimal front, the front can be divided based on a parameter of interest. Finally, as a trade-off between high level comparisons and a detailed per-front investigation, fronts can be filtered based designs having desirable properties. The fraction of designs meeting a set of criteria is a first indication of the suitability of a given topology for the intended task.

The optimization method was demonstrated with two examples. In the first example five basic SPM, IPM and FSM machines were optimized for weight and efficiency, assuming a single operating point. This demonstrated the basic correctness of the optimization method. The second example served as a first look at the starter/generator design problem, having two additional targets: starting copper losses and three phase short circuit losses. Nine FSM and SPM machine variations were considered. Important observations are that mostly the requirements on both low starting and short circuit losses directly conflict; a fail-safe generator-only machine could be constructed with little penalty. Furthermore, concentrated non-overlapping winding machines ($q \leq 0.5$) allow a better fine-tuning of the phase inductance with respect to the linked magnet flux than distributed winding machines, which is essential to meet all design targets with a low machine weight. Lastly, FSMs offer lower copper losses than SPMs and in this respect lead to the lightest S/G. However, they operate with higher current densities and the transient thermal behavior may be worse. Also, they have large pu inductance values, which increases the minimum inverter VA-rating.

CHAPTER 3

Efficient finite element based rotor eddy current loss calculation

The rotor losses in tooth-coil winding machines cannot be neglected, particulary in high-speed machines. At high frequencies the rotor losses may not be fully resistance limited, leading to a coupled eddy current problem. Although analytical models can solve those problems quickly, they are inflexible and problem dependent. This contradicts with the FE-based optimization approach, where flexibility with respect to machine types and geometries is highly desired. The losses can obviously be computed using the existing FE model of the machine, but this is time consuming, especially with saturated machine parts. Therefore, this chapter proposes an alternate FE-based approach, using a transient simulation of only the rotor geometry with linear material properties. The method is demonstrated in 2D and 3D, showing that both winding distribution and slotting harmonic losses can be correctly computed, even in the presence of stator saturation or shielding effects in the rotor.

Based on

- M. van der Geest, H. Polinder, and J. A. Ferreira, "Efficient finite element based rotor loss calculation for permanent magnet synchronous machines," in *Int. Conf. Electrical Machines (ICEM)*, 2014, pp. 1133–1138; and
- M. van der Geest, H. Polinder, and J. A. Ferreira, "Computationally efficient 3D FEM rotor eddy current loss calculation for permanent magnet synchronous machines," in *IEEE Int. Electric Machines Drives Conf. (IEMDC)*, 2015.

3.1 Introduction

Rotor eddy current losses in permanent magnet machines can be one of the main electrical loss sources, especially at high rotational speeds in combination with fractional pitch concentrated non-overlapping windings. In addition, the cooling capacity at the rotor is limited compared to the stator. Therefore, obtaining an accurate estimation of the rotor losses and the effectiveness of any loss reduction method during the design stage of a machine is of great importance to prevent overheating of the constructed machine. Many rotor loss calculation methods have been proposed [32], but most can be divided in three categories.

One extreme in rotor eddy current loss calculation are fully analytical methods [33–38]. Typically, the rotor geometry is simplified to a number of concentric shells or a rectilinear geometry, boundary conditions to account for the stator are imposed, and Maxwell's equations are solved. This method is very fast, and can account for shielding effects due to the eddy current reaction field, but fine geometric details or magnet segmentation cannot be included easily.

The other extreme in rotor loss calculation is transient finite element modeling. Any details of interest can be accounted for, although some, like axial magnet segmentation, require 3D models [39]. Obviously, the major penalty is the time required for these calculations.

In between those extremes are methods that combine FE and analytical aspects. The rotor losses could for instance be computed with field distributions obtained from magnetic equivalent circuits [40]. For increased accuracy, the rotor field distribution obtained from static FE solutions may be used to compute the magnet losses, under the assumption that the eddy currents do not interact with the inducing field [41]. Magnet segmentation in all dimensions can also be included in this way [42].

Another approach is to simplify FE simulations. If the effect of rotor eddy currents on the stator field is not significant or of interest, static simulations of the complete machine may be used to obtain boundary conditions for models containing only the rotor geometry. The rotor-only model may be solved in the frequency domain for significant space-harmonics only, further saving time [43]. This concept can easily be extended to 3D [39, 44, 45].

In addition, a recent trend is to design electrical machines with a combination of automated optimization techniques and FEA, allowing one to arrive at very high performance machines, even for complex, multi-objective design tasks ([15, 46], Chapter 2). One optimization typically requires the evaluation of thousands of design candidates. Therefore, a fast analysis of individual designs while maintaining a high degree of accuracy is essential. To minimize the computational requirements, transient simulations are preferably avoided [17]. Besides offering a low evaluation time, the models should also be robust [46]. That is, they should compute correct values, even for unrealistic machine designs, as these may be considered during the optimization process.

Considering the above discussion, the ideal rotor loss calculation method should possess the following properties:

- Flexibility: can account for arbitrary rotor shapes and machine types, without manual customizations for each new machine.
- Generality: can account for slotting and space-harmonic induced losses, and remain accurate under stator saturation.
- Speed: requires few computational resources.
- Accuracy: Is as accurate as a full transient FE simulation.
- Shielding: accounts for shielding due to highly conductive rotor parts.

This chapter proposes and demonstrates a FE based rotor loss calculation method, using a rotor-only simulation with boundary conditions obtained from static solutions of the full machine model. Two-dimensional transient and three-dimensional transient and time-harmonic models are considered. Others have reported similar methods [43, 44], but did not demonstrate the limits and capabilities of the method, or used a boundary condition that cannot account for strong shielding effects inside the rotor. This modeling approach is ideally suited to an automated optimization technique, where the full machine model (containing both the rotor and stator) is also used to compute e.g. iron losses, torque and torque ripple.

The next section introduces the method and elaborates on some of the steps. The third and fourth sections compare, in respectively 2D and 3D, the accuracy and performance of the models to a direct solution of the full machine geometry, which serves in all cases as reference model. The last section draws the conclusions.

3.2 Proposed modeling method

The proposed modeling method consists of the following basic steps:

1. Solve a model of the full machine geometry, under the desired operating conditions over one electrical period in n static steps.
2. Extract the components of the H-field in the airgap tangential to the rotor surface as function of time and position. In the 2D case only H_θ is non-zero, in 3D H_z also needs to be extracted.
3. Analytically rotate the field(s) to the rotor reference frame.
4. With a model containing only the rotor geometry and airgap and having linear material properties, either
   (a) perform a transient (or 'time dependent', or 'time stepping') simulation, with the H-field(s) directly applied as time-dependent surface current boundary condition. The losses can be directly obtained from the solution.
   (b) decompose the airgap H-field into a set of spatial harmonics with associated frequencies, using a 1D and 2D Fourier transform for respectively the 2D and 3D models. Select the strongest harmonics based on a threshold with respect to the strongest

harmonic, and for each harmonic solve a time-harmonic (complex frequency domain) model. The eddy currents and subsequent losses can be obtained using the superposition principle.

The main advantage of the proposed method is that a simpler model is solved, having fewer degrees of freedom and no need to account for a moving rotor. Additionally, the proposed method also allows optimization of the meshes used. If the eddy currents in the rotor have small skin-depths compared to the rotor dimensions, a fine mesh is needed to accurately represent the eddy currents. In the proposed method, this fine mesh is only required in the rotor-only model. The full machine model can use a coarser rotor mesh, reducing the time required to solve the model.

The number of static steps n in step 1) that is used as input data poses an accuracy-speed trade-off that is addressed in the next section. Furthermore, it is important that the lookup function used as boundary condition has smooth spatial and temporal derivatives to speed up the transient solver, but not so smooth that the loss calculation is affected. A mild low pass filter in space could be used to this end. Lastly, the location of the boundary condition in the airgap is not critical, in this work it is placed at 70% of the mechanical airgap length, as seen from the rotor.

For the 2D models, both the full machine and rotor-only models use the quasi-static magnetic vector potential formulation of Maxwell's equations:

$$\sigma \frac{dA}{dt} + \nabla \times (\frac{1}{\mu} \nabla \times A) = J_{\text{ext}} \tag{3.1}$$

where A is the magnetic vector potential and J_{ext} an imposed current density, such as the phase currents. In 2D models only A_z is non-zero and a poisson equation results. It would seem attractive to then directly use A_z as a boundary condition instead of the magnetic field (which is the derivative of A_z), but a later section will show that leads to an overestimation of the losses in the presence of inductance limited eddy currents.

The transient rotor-only 3D models are also formulated using the quasi-static magnetic vector potential A. The time-harmonic models also include the scalar electric potential V_e, which is necessary to account for magnet segmentation:

$$j\omega\sigma A + \nabla \times (\frac{1}{\mu} \nabla \times A) + \sigma \nabla V_e = J_{\text{ext}} \tag{3.2}$$

$$-\nabla \cdot (j\omega\sigma A + \sigma \nabla V_e - J_{\text{ext}}) = 0. \tag{3.3}$$

Due to a limitation of the software used here (COMSOL Multiphysics) only time-harmonic models can use this mixed magnetic-electric formulation. Hence, the time-harmonic model can be seen as a means to avoid software limitations. Gauge fixing is enabled in all cases, which ensures a unique solution for the magnetic vector potential and helps to maintain a numerically correct conservation of current [47].

The time-harmonic approach, whether in 2D or 3D, brings an additional benefit: each of the harmonics is independent and can be solved without knowledge of the other harmonics, allowing

all harmonics to be solved in parallel in distributed computing environments, greatly accelerating the solution time (but not necessarily the total computational effort). In contrast, a transient model is sequential; solution of step n can only be started once step $n-1$ has completed.

With any FE analysis, mesh size is important. While modern computers have sufficient memory to handle a fine mesh for 2D FE models without major problems or concerns, this is not yet always the case for larger 3D problems. Still, the mesh should be fine enough to correctly capture all modeled phenomena. To ensure that the meshes for the models considered in this chapter were fine enough, the mesh element sizes were varied to determine a maximum size needed to obtain results to within a few percent of those for a very fine mesh. In 2D, the linear systems are solved with the UMFPACK solver [47], while in 3D either the direct PARDISO solver or iterative FGMRES solver [47] are used, selecting the fastest of the two for every model. The timestepping algorithm for the transient models is the generalized-α method [47], with $\alpha = 0.75$. Lastly, axial and circumferential (anti-) symmetry are used where possible both for the 2D and 3D cases.

3.3 2D calculation performance

This section demonstrates the performance of the method in 2D with a number of hypothetical benchmark machines, designed to emphasize the various rotor loss aspects. Concentrated non-overlapping windings are used in most cases, as the richer space-harmonic content induces higher rotor losses.

The rotor losses are computed four times for each test case:

A. with an accurate transient simulation of the entire machine over one full electrical period, providing the baseline value for the rotor losses for comparison. A relative tolerance of 1% is used to control the stepsize of the transient solver algorithm.

B. with a fast transient simulation of the entire machine, to demonstrate the minimum time required to compute the rotor losses with reasonable accuracy using a full machine model. Half an electrical period is simulated to allow start-up transients to damp out. A relative tolerance of 2.5% is used.

C. with the proposed method over one full electrical period. A relative tolerance of 0.5% is used.

D. as with the proposed method, but using an A_z boundary condition to demonstrate the limits of this approach. A relative tolerance of 0.5% is used.

To summarize: the goal of this work is to find a method that approximates the rotor losses computed with an accurate FE transient simulation of the full machine model, yet requires less time. Whether the FE computed losses match the losses in an actual machine is beyond the scope of this work, and no practical validation is therefore performed. Note that the time-harmonic model is not used in 2D. Generally, it was found to have less accuracy than the transient rotor-only model, as will be shown for the 3D case.

Table 3.1 System specifications

Property	Specification
Rated power	100 kW
Rated speed	20000 RPM
Winding	12 slots, 10 poles, double layer
Laminations	M250-35A
Rotor yoke	Ideal, μ_r=800
Magnets	μ_r = 1.05, ρ=1 μΩm, B_r = 1.0 T
Sleeve	Low cond.: μ_r = 1, ρ=100 μΩm High cond.: μ_r = 1, ρ=1 μΩm

3.3.1 Baseline machine

A baseline machine is used, with specific adjustments for each loss aspect. Figure 3.2 shows the geometry and Table 3.1 provides relevant details. A 12 slot 10 pole double layer winding is used, as this layout has both lower and higher order asynchronous space-harmonics. This machine is not a realistic design in terms of power, speed and size, but the sole goal is to provide a test case to compare the methods. Zero total axial current is imposed per magnet, to more correctly represent the current flows inside individual magnets. The magnet conductivity specified in the FE models is not modified to account for the finite length or segmentation [48]. Either a poorly conducting sleeve, constructed with e.g. carbon fiber reinforced plastic, or a metallic sleeve, made from e.g. Inconel, is considered.

3.3.2 Space-harmonic losses only

The first case considers resistively limited eddy currents, mainly induced by asynchronous space-harmonics. A 1.5 mm airgap is used, together with reasonably wide tooth tips. The geometry shown in Figure 3.2 is used. Figure 3.1 shows the current density distribution computed with the full and rotor-only models. The most important observation is that the current density is almost identical in the two plots, in terms of both distribution and magnitude. An additional observation with regards to rotor losses in general, is that the eddy currents in the yoke mostly reveal a two-pole field, while the losses in the sleeve and magnet are caused by a 14-pole field, which follows directly from the space-harmonic spectrum of the 12/10 winding. Of these two harmonics, two-pole field can more easily cross the magnetic airgap to induce losses in the yoke, but since the magnet pitch is much shorter than the two pole pitch, less current is induced in the magnets. In other words, the magnets are segmented with regards to the two-pole field.

Figure 3.3 shows the sleeve and magnet losses as function of time, computed with the proposed method and the slow and fast transient full machine models. The magnet losses are approximately

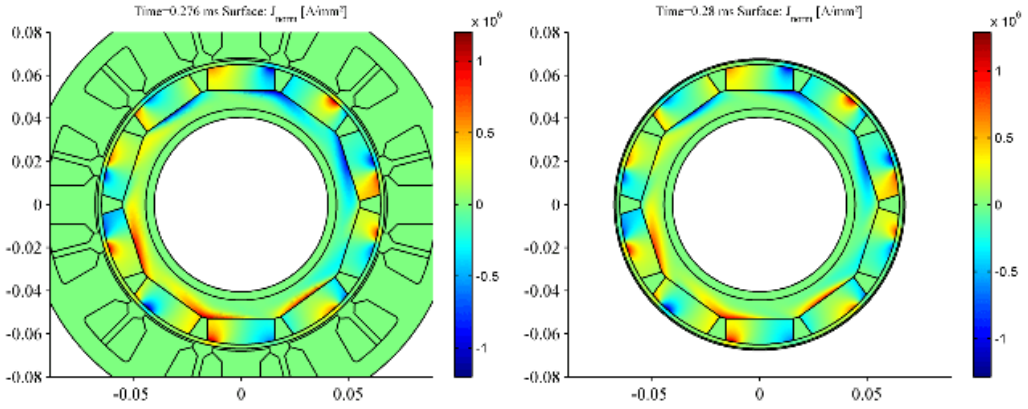

Figure 3.1 Current density distribution computed with the transient full (a) and rotor-only (b) models. For these plots, the material resistivities were adjusted to have losses in all rotor parts.

5 kW, while the sleeve losses are a negligible 100 W. The proposed method correctly predicts both the magnitude and time-variation of the losses. Table 3.2 summarizes the average losses computed and time required. The stated times include model and mesh creation in case of the rotor-only models. The proposed method is faster (10 vs 15 s, while simulating a full electrical period instead of a half) and more accurate (1% vs 5%) than a coarse simulation with the full model. Figure 3.3 shows that simulating a full electrical period is not strictly necessary for this specific case, as the solution reaches steady state after $1/6^{\text{th}}$ electrical period. However, this settling time increases if the eddy currents become inductance limited, and before deciding to use a shorter simulation time, convergence of the solution should be checked.

Selection of n

The number of static simulations that provide the boundary condition for the rotor-only model, n, needs to be chosen sufficiently high. To demonstrate this, Figure 3.4 shows the total rotor losses, computed with the proposed method, as function of n. With too few steps the losses are underestimated. For this case $n = 20$ yields an accurate prediction of the rotor losses. Unless indicated otherwise, $n = 24$ is used in the remainder of this chapter.

Choice of boundary condition

The proposed method uses a surface current density boundary condition for the rotor model, instead of a magnetic potential boundary condition, as is reported in other works [43, 44]. With

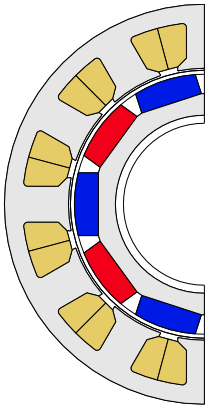

Figure 3.2 Machine geometry for space-harmonic losses only.

Table 3.2 Summary of computed losses and time required, with predominantly winding space harmonic losses

Case	Model	Sleeve (kW)	Magnets (kW)	Sum (kW)	Error (%)	Time (s)
CFRP sleeve	A	0.1	5.2	5.3		69
	B	0.1	4.9	5.0	-5.3	15
	C	0.1	5.2	5.3	-0.2	10
	D	0.1	8.1	8.3	+55.5	11
Metallic sleeve	A	10.3	3.9	14.2		94
	B	9.9	3.7	13.6	-4.2	24
	C	9.7	3.7	13.5	-5.1	23
	D	21.2	8.0	29.2	+105	23
Solid back iron	A	0.1	5.0	5.3		6243
	B	0.1	4.7	5.1	-4.2	817
	C	0.1	4.9	5.3	+0.2	140
	D	0.1	8.1	9.1	+73.4	106

purely resistance limited eddy currents, both methods will yield similar results, but with a magnetic potential boundary condition the rotor losses are overestimated in the presence of strong shielding effects, because both the radial and tangential flux density are constrained.

To illustrate this, Figure 3.5 shows the magnet and sleeve eddy current losses versus sleeve conductivity, computed with an accurate transient simulation of the entire machine (providing a reference) and rotor-only models with either a J_s or A_z boundary condition. Initially the eddy currents are resistance limited; increasing the sleeve conductivity linearly increases the sleeve losses, while the magnet losses do not significantly decrease. With conductivities above σ=1 MS/m, the eddy currents gradually become inductance limited, the sleeve losses reach a maximum before stabilizing (not shown in the plot) and the magnet losses go towards zero. With a poorly conducting sleeve, all methods show good agreement. In fact, transient FE simulations are not necessary for this specific case, as postprocessing methods can also give correct results. For a sleeve conductivity of σ=1 MS/m, which is the order of magnitude for metallic sleeves like Inconel, the losses are overestimated by 100% when using an A_z boundary condition, while with a J_s boundary condition, the error is negligible. With higher conductivities the J_s method will start to underestimate the losses by 40%, but still correctly captures the trends in both the magnet and sleeve losses, while the A_z method overestimates the losses 4–5 times. Therefore, using a J_s boundary condition is preferred over an A_z boundary condition.

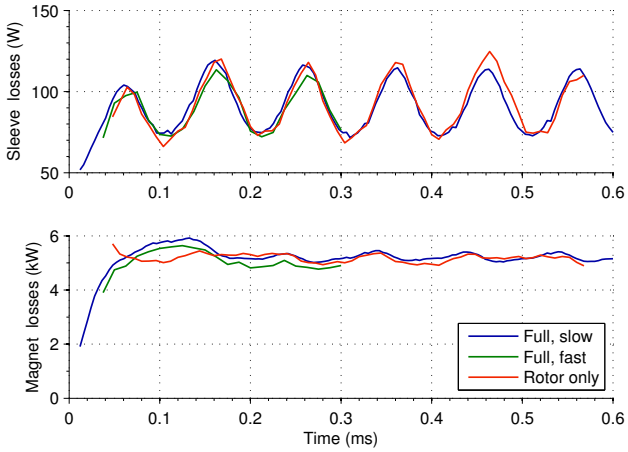

Figure 3.3 Magnet and sleeve losses in the presence of space-harmonics.

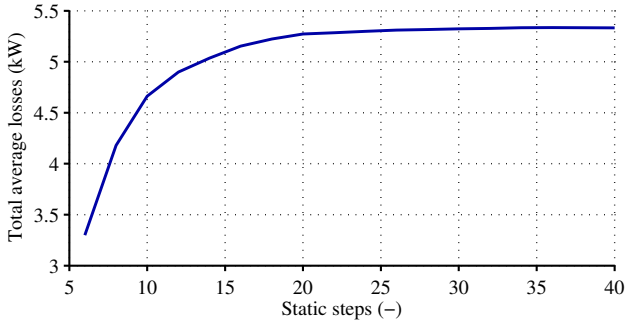

Figure 3.4 Total rotor losses as function of n.

3.3.3 Space-harmonic losses and shielding

In this case a conductive retaining sleeve with ρ=1 μΩm (e.g. Inconel) is assumed. Eddy-currents in the sleeve can develop to such an extent that the AC magnetic field and losses in the magnets are reduced. The geometry from Figure 3.2 is used and $n = 40$.

The results are included in Table 3.2. In this specific case, both the coarse transient simulation with the full machine geometry and rotor-only model underestimate the losses by about 5%. However, the rotor-only model is twice as fast, because a full electrical period is simulated, compared to half a period for the full machine model. Lastly, when using an A_z boundary condition, the total losses are overestimated by 100%.

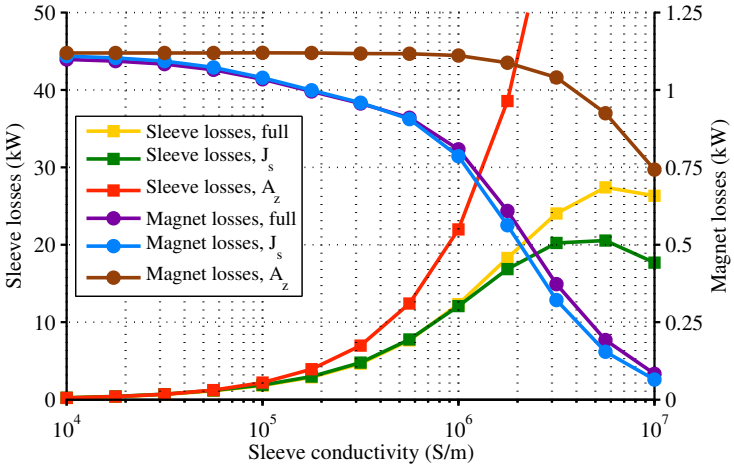

Figure 3.5 Magnet and sleeve losses as function of sleeve conductivity, computed with three different models.

3.3.4 Solid back-iron

A solid rotor yoke brings significant mechanical and cost benefits, but is also susceptible to eddy current losses. Estimating whether a solid yoke can be used in a certain design requires computation of the yoke eddy current losses. The low skin-depth in the rotor yoke requires a locally dense mesh in FE calculations, increasing the time required to calculate the losses. To estimate the consequences for the rotor loss calculation, the rotor yoke resistivity of the baseline design (Figure 3.2) is set to ρ=1 μΩm. The low-conductivity sleeve is assumed to maximize the AC-field inside the yoke and $n = 24$. The maximum mesh element size at the yoke-magnet interface is set to 0.4 mm.

The results are again summarized in Table 3.2. The yoke losses are computed as 238 W with the accurate transient model of the full machine, while with the proposed method 215 W is computed, a 6% underestimation. The coarse transient full model overestimates the yoke losses by 25% and is 12 times slower than the rotor-only model. With an A_z boundary condition, the yoke losses are overestimated threefold. Also note that the magnet losses are slightly reduced compared to the baseline case, due to shielding.

3.3.5 Slotting losses

Slotting or permeance variation induced losses are caused by a varying permeance experienced by the magnets as they rotate past individual stator teeth. The extent of this effect strongly depends on the tooth tip shape and airgap length, with shorter airgaps and straight teeth increasing the

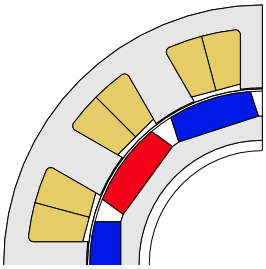

Figure 3.6 Machine geometry with pronounced slotting losses.

Table 3.3 Summary of computed losses and time required with high slotting losses

Case	Model	Sleeve (kW)	Magnets (kW)	Sum (kW)	Error (%)	Time (s)
CFRP sleeve	A	0.2	35.7	35.9		441
	B	0.2	34.7	34.9	-2.6	128
	C	0.2	32.8	33.0	-7.9	36
	D	0.2	51.4	51.6	+43.9	36
Metallic sleeve	A	27.1	32.9	60.0		446
	B	26.0	31.9	57.9	-3.5	126
	C	23.3	28.1	51.4	-14.4	46
	D	32.4	51.0	83.4	+38.9	46

losses. Figure 3.6 shows the geometry used; a 0.4 mm airgap and 0.9 mm thick retaining sleeve are assumed, $n = 40$. To emphasize the slotting losses, zero stator current is specified.

In this case, the proposed method underestimates the losses by 8%, while the coarse full simulation underestimates the losses by only 3%. However, due to the short airgap the full machine model requires a dense mesh inside the airgap, increasing the required computation time. This does not apply to the rotor-only method, making it 6–7 times faster than the coarse full simulation. With an A_z boundary condition the losses are overestimated by 44% in this case.

Aside from the differences between the calculation method, this example shows that the slotting losses can be excessive, even in no-load. Compared to the baseline case (Table 3.2) under full load, the losses have increased over sixfold. This should be kept in mind when designing fractional slot tooth-coil machines without tooth-tips.

3.3.6 Slotting losses with shielding

When a conducting sleeve is used with the 'high slotting losses' geometry, the proposed method underestimates the losses by 14% and the speed gain is decreased to about 6 times. Increasing n does not significantly reduce the error. With an A_z boundary condition, the losses are overestimated by 39%.

3.3.7 Strong stator saturation

Strong stator saturation can occur during a torque overload, but also in an optimization process, where unrealistic machine designs may need be evaluated. Transient simulations with heavily

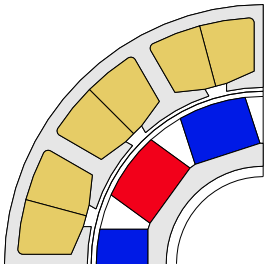

Figure 3.7 Machine geometry for pronounced stator saturation.

Table 3.4 Summary of computed losses and time required under strong stator saturation

Model	Sleeve (kW)	Magnets (kW)	Sum (kW)	Error (%)	Time (s)
A	0.2	15.2	15.4		1009
B	0.2	14.2	14.4	-6.7	375
C	0.2	12.8	13.0	-16.0	14
D	0.4	23.4	23.9	+55.0	14

saturated machines require small time steps to prevent divergence of the solution, increasing the time required. By performing a transient simulation with only the rotor and assuming linear materials, this problem is avoided.

To demonstrate the performance under heavy saturation, the yoke and teeth are made narrower, the stack length is halved and the output torque is doubled. Figure 3.7 shows the adjusted geometry. For this case, the coarse transient simulation requires 375 s and underestimates the losses by 7%. The proposed method requires only 14 s, but underestimates the losses by 16%. Given the roughly 25 times speed gain, this loss of accuracy is deemed acceptable.

3.3.8 Low magnet span

As part of an optimization process, very unrealistic designs need to be correctly evaluated. One extreme is a very low magnet pole span, as shown in Figure 3.8. The performance of the proposed method is in this case very similar to the initial case; a comparable error and approximately twice as fast as a course simulation with a full model. With an A_z boundary the losses are still overestimated, although to a lesser extend due to the smaller magnets.

3.3.9 Distributed windings

Distributed integer pitch windings have a significantly cleaner airgap space-harmonic spectrum than concentrated fractional pitch windings, which strongly reduces rotor losses. Correctly accounting for the eddy currents induced by the low amplitude asynchronous space-harmonics requires accurate transient solver settings, slowing down the solution process. In addition, the higher number of teeth simply requires more mesh elements, further increasing the solving time. To estimate the performance of the proposed method under these circumstances, a distributed winding machine with 36 slots and 6 poles ($q = 2$) is considered. The geometry is shown in Figure 3.9, the poorly conducting sleeve is assumed and $n = 50$.

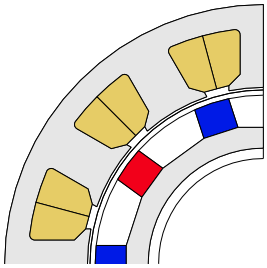

Figure 3.8 Machine geometry with low relative magnet span.

Table 3.5 Summary of computed losses and time required with a low magnet span

Model	Sleeve (kW)	Magnets (kW)	Sum (kW)	Error (%)	Time (s)
A	0.2	4.5	4.8		66
B	0.2	4.4	4.7	-3.3	10
C	0.2	4.5	4.8	+0.6	11
D	0.2	5.0	5.3	+10.6	11

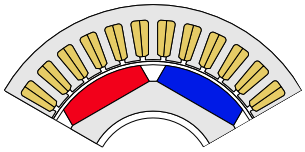

Figure 3.9 Machine geometry for a distributed winding.

Table 3.6 Summary of computed losses and time required with a distributed winding

Model	Sleeve (kW)	Magnets (kW)	Sum (kW)	Error (%)	Time (s)
A	0.008	0.15	0.16		136
B	0.006	0.12	0.13	-20.4	30
C	0.009	0.18	0.19	+16.5	16
D	0.007	0.15	0.16	-1.6	16

The results are summarized in Table 3.6. The rotor-only model executes about four times faster than the coarse transient full model. However, the rotor-only model overestimates the losses by 17%, wile the coarse full model underestimates the losses by 20%. With the A_z boundary condition the losses are underestimated by only 2%, but this is believed to be coincidence.

3.3.10 Tangential magnet segmentation

Two dimensional FEA can directly account for tangential magnet segmentation (unlike axial segmentation). The baseline geometry is modified to have three isolated magnets per pole, see Figure 3.10, and the losses are computed. In this case the proposed method overestimates the losses by 2% and is twice as fast as the coarse transient full machine model.

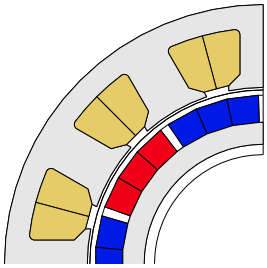

Figure 3.10 Machine geometry with tangentially segmented magnets.

Table 3.7 Summary of computed losses and time required with tangentially segmented magnets

Model	Sleeve (kW)	Magnets (kW)	Sum (kW)	Error (%)	Time (s)
A	0.1	3.7	3.8		79
B	0.1	3.6	3.7	-3.2	16
C	0.1	3.8	3.9	+2.2	15
D	0.1	4.0	4.0	+5.6	15

3.4 3D calculation performance

The method is now demonstrated with 3D models, followed by the determination of two rotor loss trends. Both the transient and time-harmonic rotor-only models will be compared to the full machine model. Contrary to the rotor-only models, which are solved using the magnetic vector potential formulation A (and scalar electric potential for time harmonic models), the full model is solved using a magnetic scalar potential V_m in the airgap region, as this allows a moving boundary between the rotor and stator to be accounted for via interpolation [47]. Additionally, the V_m formulation introduces fewer degrees of freedom per mesh element. However, a V_m formulation can only be used in domains that are both free of current and simply connected. To maintain a simply connected air domain, the stator iron and air around the end-windings (which carry current, so require the A formulation) are also solved with the A formulation.

A slightly different baseline machine design is used for the 3D simulations, relevant details of this machine are provided in Table 3.8, while Figure 3.11 shows an impression of this machine.

3.4.1 Loss calculation

First, to demonstrate that all three methods can indeed approximate the losses, Figure 3.12 shows the eddy currents computed with the transient full geometry and rotor-only models. The eddy current pattern and magnitude appear mostly identical. Figure 3.13 shows the instantaneous magnet losses versus time, computed with all three models and using a relatively high number of steps. Compared to the full machine model, the transient rotor-only model overestimates the losses by 3%, while the time-harmonic model, using the 81 most significant spatial harmonics, underestimates the losses by 18%. Figure 3.14 shows how the losses and solution time vary versus inclusion threshold. Increasing the number of harmonics considered only marginally improves the calculated losses, while this increases the calculation time well beyond that of the full model.

The motivation for using the transient rotor-only model is to save time, and Figures 3.15–3.17

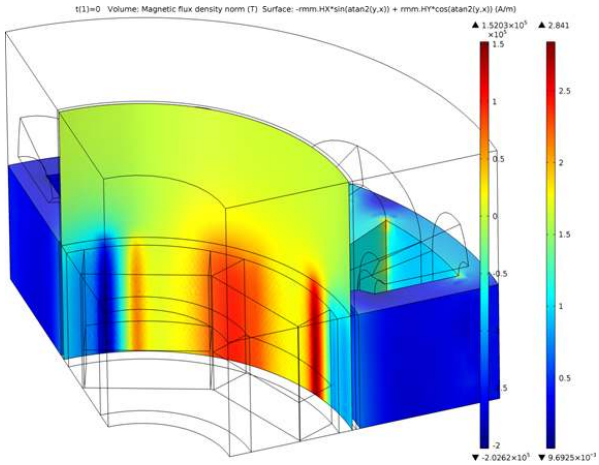

Figure 3.11 Example 3D machine geometry. The lamination surface color indicates flux density; the airgap surface shows the tangential magnetic field strength.

Table 3.8 Machine specifications

Requirement	Specification
Power	10 kW
Speed	16,000 RPM
Pole pairs	4
Stator teeth	12
Magnets	B_r = 1 T ϱ = 1 μΩm
Retaining sleeve	Carbon fiber ϱ = 200 μΩm
Rotor yoke	Laminated non-conducting

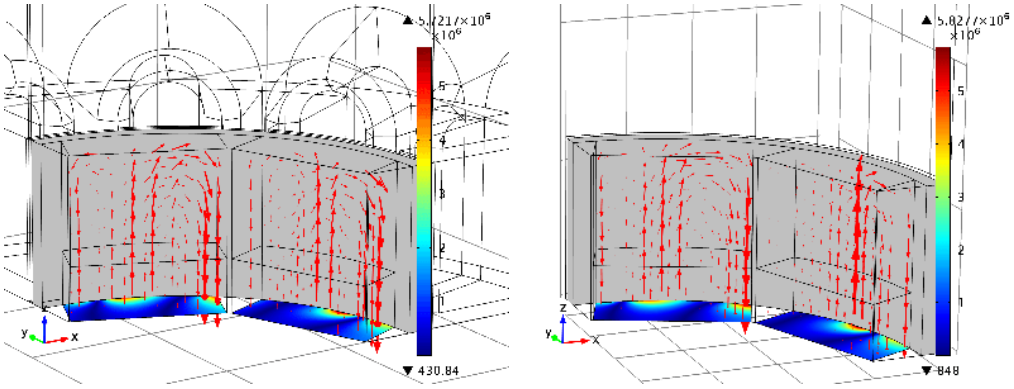

Figure 3.12 Eddy-current flow patterns (arrows) and density (color at bottom) computed with the transient full (a) and rotor-only (b) models, without magnet segmentation.

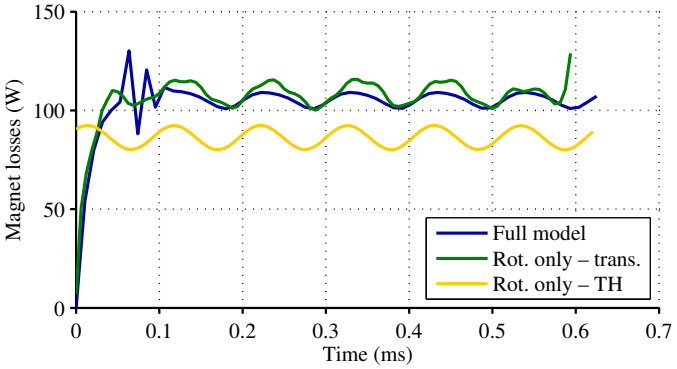

Figure 3.13 Magnet losses versus time, computed with three different 3D models.

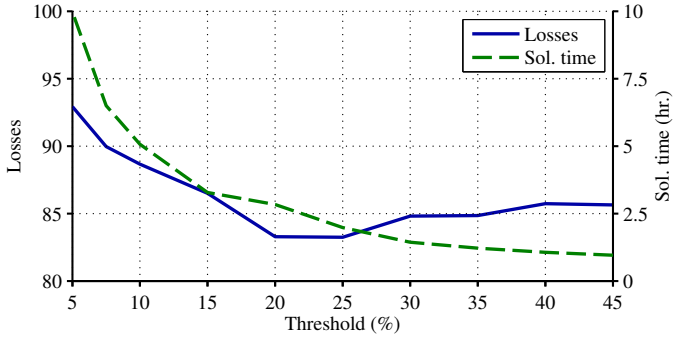

Figure 3.14 Solution time and losses versus harmonic inclusion threshold for the TH rotor-only model.

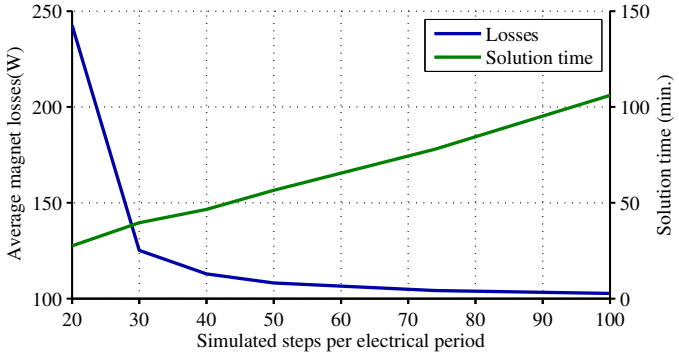

Figure 3.15 Computed losses and solution time for the full machine model.

elaborate on this. Figure 3.15 shows that 40 transients steps with the full model are needed to calculate the losses to within 10% of the final value, taking about 50 minutes on a given computer. Next, Figure 3.16 shows that for the rotor-only model the number of time steps is more important than the number of static steps with the full model (which provide the boundary conditions). Twenty steps with the full model plus 75 steps with the rotor-only model are needed to obtain losses to within 10% of the final value, taking in total 27 minutes on the same computer, as shown in Figure 3.17. Hence, the proposed approach is approximately two times faster than a direct solution of the full model.

3.4.2 Inductance limited currents

An important requirement of a rotor loss calculation method, is the ability to correctly account for shielding effects caused by inductance limited eddy currents. This allows the method to be used

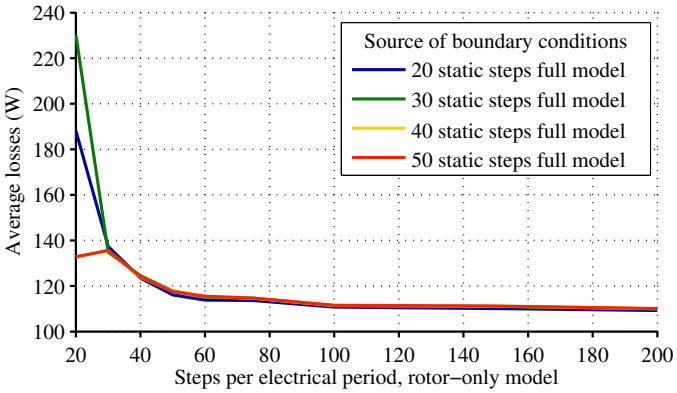

Figure 3.16 Losses computed with the transient rotor-only model versus number of steps.

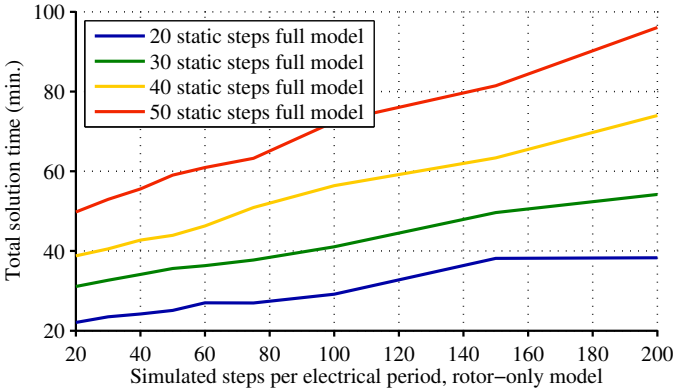

Figure 3.17 Combined solution time for the static full machine model and transient rotor-only model.

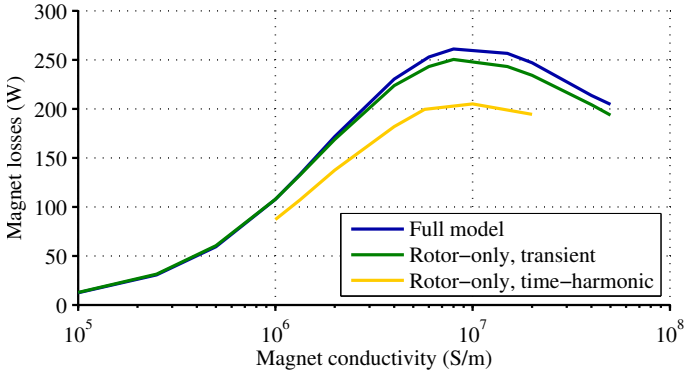

Figure 3.18 Rotor losses versus magnet resistivity.

on machines with shielding cylinders or metallic retaining sleeves, but also when the magnets are large with respect to the expected skin-depths. More generally, the method can be applied without the need to check the limiting cause of the eddy currents, which simplifies a machine analysis tool and reduces the risk of modeling errors.

To determine the accuracy in the presence of inductance limited eddy currents, the magnet resistivity is varied between 10 µΩm and 25 nΩm. Figure 3.18 shows the computed magnet losses; the transition from resistance to inductance limited eddy currents is clearly visible and correctly captured by the transient rotor-only model. The time-harmonic model underestimates the losses by 20% throughout the entire range, but also correctly captures the trend.

3.4.3 Effect of magnet segmentation

A benefit of both proposed methods is that for a given machine geometry, the full machine model only needs to be solved once, after which the same boundary conditions can be applied to rotor models with different numbers of magnet segments or magnet resistivities. This is useful to, for instance, determine the minimum number of segments needed to reduce rotor losses to an acceptable level.

To demonstrate this, the losses are computed for 1–14 segments per pole in either axial or tangential direction with magnet resistivities in the range of 50 nΩm to 1 µΩm; Figure 3.19 shows the result. As expected, the magnet losses reduce with increasing numbers of axial or tangential segments, but only for high values of resistivity. With low values, segmentation is at first ineffective or even adverse. This is a well known effect, and extensively described in literature [38, 49]. The difference between axial and tangential segmentation is generally small, but for high numbers of segments, the losses will settle at a non-zero value with tangential segmentation, while with axial segmentation the losses continue to decrease. The reason is that the magnetic field in the rotor has mostly radial and tangential components. Axial segmentation is effective for both

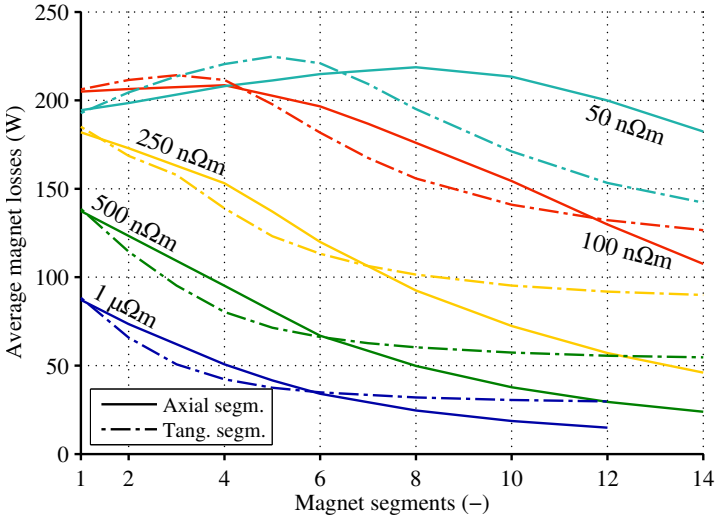

Figure 3.19 Rotor eddy current losses versus axial and tangential magnets segments, for multiple values of magnet resistivity.

components, but tangential segmentation only for the radial component. A simply solution, if needed, is obviously to combine axial and tangential segmentation, or even radial segmentation.

Note that for this analysis the magnet resistivity was altered, which is perhaps unrealistic, but a similar trend can be obtained if the machine properties would be altered instead, since eddy current problems are characterized by the geometry dimensions, material conductivity and permeability, and frequency. This also means that the losses in any machine will generally follow the trends shown in Figure 3.19, but to determine where specifically a given design is located and the scaling of both axes, separate calculations will still be required.

3.4.4 Alternate winding layouts

With different winding layouts, the airgap space-harmonic content changes. Generally, a reduction in slots per pole per phase (q) increases the number of asynchronous space-harmonics and their amplitude relative to the torque producing harmonic, which potentially increases the rotor losses. The proposed method will now be tested on several single and double layer tooth-coil winding layouts, as summarized in Table 3.9. Note that some of the considered winding layouts are unrealistic for the given application; these windings are only included to demonstrate the proposed method. To obtain the results in Table 3.9, 20 static steps and 50 transient steps were conducted with the full model and 100 steps with the transient rotor-only model. For the time-harmonic model, an inclusion threshold of 0.15 was used. The performance could be improved by including a frequency and pole-count dependent threshold, since higher frequencies and lower

Table 3.9 Calculation performance with other winding layouts

Slots/Poles	Full model		Rot. only, trans.		Rot. only, TH	
	Loss (W)	Time (min.)	Error (%)	Time (%)	Error (%)	Time (%)
9/6	244	103	+0.8	-53	-21.6	-51
9/8	565	448	-4.6	-28	-33.8	-83
12/8	108	57	+2.0	-48	-19.4	-5
12/8 SL[1]	278	326	-3.0	-51	-40.2	-68
12/10	129	228	+2.1	-33	-21.9	-61
12/10 SL[1]	263	304	-1.7	-33	-51.4	-68
12/16	405	72	-0.3	-32	-28.0	+6
12/16 SL[1]	584	318	-0.2	-29	-33.3	-6

[1] Single Layer (ie. alternate teeth wound).

pole counts contribute more strongly to the losses.

Generally, the proposed method based on a transient rotor-only model estimates the losses to within ±5%, while the total time needed for the static plus rotor-only models is about 30–50% less than that for the transient full model. The time-harmonic rotor-only model underestimates the losses by 20–55%, but needs up to 75% less time than the full model. However, the time gain strongly depends on the harmonic content of the airgap, which can be seen as a disadvantage. Due to these larger variations in both time gain and error, the time-harmonic model is considered to be inferior to the transient rotor-only model.

As a side note to the loss calculation performance, this table confirms some general trends on rotor losses also found in literature [50]: space-harmonics of lower orders than the synchronous harmonic are particularly harmful to the rotor losses. Especially the 9/8 slot/pole combination –which has two sub-harmonics– and single and double layer 12/16 combinations –which have a sub-harmonic of larger magnitude than the synchronous one– have high rotor losses, but also the single layer versions of 12/8 and 12/10 have higher rotor losses than the double layer versions.

Lastly, the loss reduction obtained by axially segmenting the magnets is also calculated for some of the winding schemes in Table 3.9, using the time-harmonic model. Figure 3.20 shows the resulting losses, normalized to the losses with 10 segments. This shows that for resistance limited eddy currents, the effectiveness of segmentation for a larger number of segments is very similar between the different winding layouts.

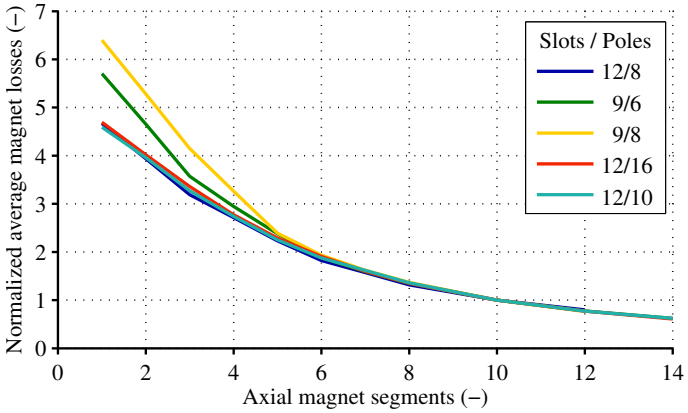

Figure 3.20 Normalized rotor eddy current losses versus axial magnets segments, for several winding layouts.

3.5 Conclusion

This chapter proposed two FE-based methods to compute rotor eddy current losses in surface mounted PM machines. The primary motivation to use those methods is to reduce calculation time. A secondary motivation is to work around software limitations. Both methods 'revolve' around a model containing only the rotor geometry and airgap, excited with a surface current boundary condition obtained from static solutions of the full machine model. This makes the method ideally suited to optimization applications, where static solutions are also needed for e.g. torque and iron loss calculations. The methods differ in the modeling domain, with one model being solved in the time domain and the other model in the complex frequency domain. Both methods can correctly account for inductance limited eddy currents (ie. with shielding effects occurring), in addition to both slotting and winding harmonic induced losses. In other words, the methods can be applied unconditionally, an important aspect in a flexible machine optimization approach.

In terms of performance, the transient rotor-only model is superior to the time-harmonic model. The error in calculated losses varies from -16 to +2%, while the time-harmonic model underestimates the losses by 30 to 50%. The time gain with the transient model varies between 2 and 25 times compared to a full machine model, with particularly high gains achieved in heavily saturated machines, or with machines having very short airgaps. While the time-harmonic method can be up to 80% faster, it is an order of magnitude slower if an accurate answer is needed. The inconsistent performance of the time-harmonic model makes it less attractive. Although this was only demonstrated for the 3D models in this chapter, this also applies to the 2D models. However, the time-harmonic model is the only means to account for magnet segmentation when using COMSOL Multiphysics and the independent nature of each harmonic makes it well suited to a

parallel computing environment.

Using the proposed methods, the effect of magnet segmentation was demonstrated and common winding layouts were analyzed, confirming general trends also described in literature and showing the general correctness of the methods.

CHAPTER 4

AC winding losses in high-speed PM machines

The electrical frequency in high-speed machines can easily exceed 1 kHz. As a result, few turns per coil will be needed to obtain sufficient back-emf to interface with the inverter. In low voltage battery fed systems this effect is even more pronounced. Therefore, the cross-sectional area per turn increases, making the turns susceptible to eddy current losses. The high electrical frequency enhances this problem. To reduce these additional losses, individual turns can be constructed with multiple insulated strands and the placement of those strands in the slots can be varied. However, analyzing suitable configurations is non-trivial, particularly with very few turns in non-square slots, while this is a necessary step in the design of a new machine. Hence, this chapter presents a modeling method to estimate the current distribution across parallel strands using simplified 3D FE models. After experimentally confirming the models, a number of design guidelines with regards to strand placement are determined.

Based on

- M. van der Geest, H. Polinder, J. Ferreira, and D. Zeilstra, "Current sharing analysis of parallel strands in low voltage high speed machines," *IEEE Trans. Ind. Electron.*, vol. 61, no. 6, pp. 3064–3070, Jun. 2014; and
- M. van der Geest, H. Polinder, J. A. Ferreira, and D. Zeilstra, "Stator winding proximity loss reduction techniques in high speed electrical machines," in *IEEE Int. Electric Machines Drives Conf. (IEMDC)*, 2013, pp. 340–346.

4.1 Introduction

Obtaining a high slot fill factor is very desirable in any electrical machine, since it reduces both the copper losses and thermal resistance, which ultimately increases the achievable power density [51,52]. However, measures against skin and proximity effects oppose a high fill factor. This applies to measures such as using several thinner strands in parallel, optionally with twisting, or even litz wire [53], but also in very large machines with bar windings, where discrete displacements are used (Roebel winding) [54]. The fill factor is also reduced when strands close the slot opening are omitted, as they incur high losses due to leakage fields [53, 55–57], particularly at the frequencies present in high-speed machines. Therefore, such measures should only be applied to the extent necessary to sufficiently reduce the winding AC losses. Hence, calculation of the AC losses, both due to unequal current sharing and proximity effects is necessary. This chapter starts with the calculation of the losses due to unequal current sharing between parallel strands, as these losses dominate in low voltage high-speed machines, followed by an overview of various loss mitigation methods and their effectiveness.

Before commencing, a few words will be spent on terminology. All induced currents are the result of a varying linked magnetic flux, but the associated losses can be separated in two groups based on the source of the flux.

- First, additional losses in a strand due to a bulk AC current in that strand itself are referred to as skin effect losses. A 'discrete' skin effect occurs when using parallel strands, and this will be the topic of the next section.

- Secondly, additional losses in a strand due to an externally imposed field on that strand are typically called proximity losses. The source of the proximity losses is often divided again based on the cause, with small differences depending on the research topic. When analyzing the performance with litz wires, which consist of twisted bundles of twisted strands, a distinction is often made between strand-level and bundle-level losses, as this allows modeling simplifications [58]. In regular electrical machines that have solid copper strands, a distinction can be made between armature field proximity losses (either due to other turns of the same coil, or other phase coils) and excitation field proximity losses.

Excitation field induced losses are mainly a problem in slotless machines, since in such machines the windings are directly exposed to the field flux. Axial flux machines are often based on slotless designs and a simple method to compute the field induced losses is presented in [59]. In high-speed machines without tooth tips these losses may also need to be considered [60], but the presence of tooth tips can nearly diminish these losses. Proximity losses induced by the armature field are mainly the result of slot leakage flux. A high permeability material completely enclosing a winding, except for a small gap, enhances the field near that gap and proximity losses will occur at lower frequencies than in an identically shaped air core coil. This effect is clearly pointed out in e.g. [53, 55, 61]. Section 4.3 will discuss and compare methods to reduce both proximity losses and bundle level skin effect losses.

4.2 Current sharing analysis

4.2.1 Overview

In low voltage high-speed machines, the necessarily low turn count and consequential large cross section per turn further exacerbate the problems of induced winding losses [62]. Using parallel strands wound straight through the slots does not solve the problem, because of unequal current sharing and circulating currents [61, 63, 64]. In the extreme case, segmenting one solid turn into n isolated parallel strands, but connecting those strand together at the coil ends, will not reduce the losses at all. Similar problems can occur in high frequency magnetic components [65, 66]. Displacing or twisting the conductors inside a slot can reduce the effects, but at the expense of a reduced fill factor, and should therefore be used only when necessary.

To assess the necessity of twisting the strands and by how much, a model is required that can predict the current imbalance. Conventionally, analyzing strand twisting is a topic within high frequency transformer and inductor design. Analytical methods on simplified geometries are often used to predict effective resistances and losses [58, 67–69]. Such methods also clearly demonstrate that litz wire is only beneficial over a limited frequency range [70, 71]. A specific model where the effects of twisting the strands is considered is presented in [72], where the effect on the resistance of the longitudinal magnetic field resulting from twisting the strands is computed. To account for the losses in end-windings or other complex structures where an analytical model is infeasible, FEA can provide a solution [65, 73, 74]. FEA is also used in [75], where the AC resistance of core-less planar windings is computed. In such a winding the copper is exposed to a significant magnetic field, increasing the AC loss density in the copper. Similarly, machines may have a large amount of leakage flux may exist inside the slots. Note that in the majority of the work on this topic, the litz wire is assumed to be ideal. That is, each strand carries the same net current.

In the field of machines little research exists on this topic, although one particular series of papers specifically discusses this topic [63, 64, 76, 77]. In this work, fully analytical models are derived to compute the magnetic field inside the slot, the current distribution and the induced losses. However, 3D effects related to the end-windings cannot be taken into account and while analytical methods are certainly faster than FE simulations, implementing the equations takes time and FEM verification is usually applied to confirm the equations. Also, the use of analytical models requires expertise. For single case studies, it can then be attractive to accept the longer time required for FE simulations. When using FEA to compute the winding losses, both transient and time-harmonic calculations can be used, but if only the steady state solution is of interest, time-harmonic simulations can provide the same answer as a transient simulation in less time, as is demonstrated in [60] for the no-load eddy current losses.

The aim of this section is to compute the current distribution across parallel strands with full account of the actual geometry. A simple method is proposed, based on the turn-level impedance matrix of the windings, which is extracted from 2D or 3D FE simulations, and basic circuit

Table 4.1 Machine specifications

Requirement	Specification
Rated power	10 kW
Speed	32,000 RPM
RMS phase current	200 A
Pole pairs	5
Stator teeth	15
Stack length	50 mm
Turns/tooth	5

equations. Complex 3D models are avoided by simulating only individual strands and using the superposition principle, allowing otherwise too complex 3D structures to be modeled on desktop computers. A machine with concentrated non-overlapping windings serves as an example, although the method can also be applied to distributed windings. The only difficulty with the latter type is the description of the end-winding shape.

4.2.2 Problem elaboration

Solid bars cannot be used as conductors in low voltage high frequency machines due to skin and proximity effects. As an alternative, regular circular wires connected in parallel may be used. To maintain a high fill factor, these strands are preferably wound straight (i.e. without twisting or displacements) around the teeth. Figure 4.1 shows four possibilities for such a winding, each having seven parallel strands and five turns of 1.5 mm diameter copper wire. More permutations are possible, but the four depicted here are considered reasonably manufacturable. In the 'grouped strands' style, the parallel strands are wound one at a time and all turns of one strand physically touch each other, while with 'grouped turns', all strands are wound simultaneously. In all cases the fill factor is 51%.

To assess the performance of these winding configurations in terms of copper losses, they are analyzed with transient 2D FEA. Table 4.1 summarizes the specifications of the machine used in all analyses. The seven strands of each phase are connected in parallel and a total current is imposed. Table 4.2 reports the resulting steady-state strand currents. Large differences exist between the strand currents; strands close to the slot-opening carry significant current in particular. Do note that this table reports RMS currents; the vector sum of the currents will always equal the phase current. At first sight these values may even seem erroneous and experiments will have to confirm these results.

Also listed in Table 4.2 are the copper losses computed with the transient FE simulations and the copper losses based on the strand currents only. The former includes all AC and DC losses, while

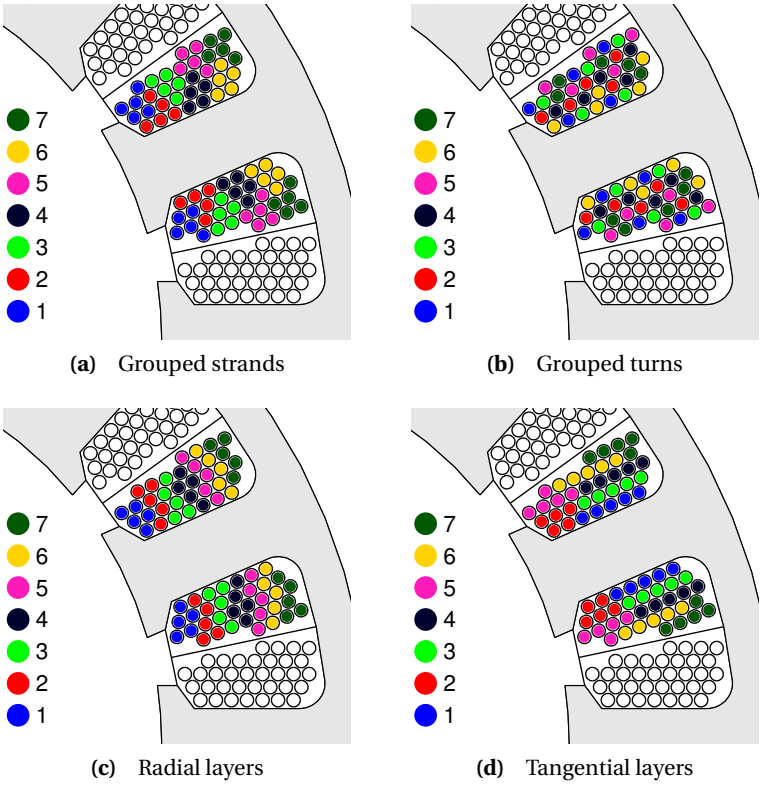

(a) Grouped strands **(b)** Grouped turns

(c) Radial layers **(d)** Tangential layers

Figure 4.1 Straight winding styles for a concentrated fractional pitch winding with 5 turns. Each color represents one strand. The strand diameter is 1.5 mm.

Table 4.2 Transient FE results for the winding schemes of Figure 4.1. The ideal strand RMS current would be 6.4 A with conduction losses of 31 W.

Winding style	Strand currents (A_{rms})	Total copper losses (W)	Conduction copper losses (W)
Grouped strands	42.5, 11.6, 7.2, 3.6, 2.5, 0.8, 1.2	260	213
Grouped turns	37.1, 15.1, 9.1, 11.7, 9.2, 9.6, 6.8	299	217
Radial layers	35.7, 15.7, 6.7, 1.4, 0.8, 0.6, 1.0	216	167
Tangential layers	7.5, 4.7, 14.3, 36.7, 6.4, 12.6, 5.2	255	196

the latter is computed solely with strand resistances and currents, that is, it accounts for the DC and unequal sharing losses only. The difference between these two values are losses due to strand level skin and proximity effects. These induced losses can be eliminated with sufficiently thin strands or even litz wire, while the losses due to the current imbalance can only be reduced by altering the layout of the coil. For this reason, the induced losses are not considered further and the focus lies solely on the current imbalance.

Of the four winding schemes shown, the one labeled 'Grouped turns' seems to have a reasonable strand current distribution, with most strands carrying around 10 A, yet the conduction losses are 30% higher than the 'Radial layers' scheme, which has strand currents ranging from 1 A to 35 A. Given that the ideal strand current is 6.4 A, the 'Grouped turns' scheme still has a fairly high imbalance, but predominantly in the current angles.

The total losses reported in Table 4.2 are high with respect to the volume, but could be cooled with adequate measures if they would be distributed uniformly. However, in the current imbalanced situation, local current densities can be in excess of 20 A/mm², leading to unavoidable hot-spots. The impact on the machine efficiency may also be considered too severe and alternatives are thus required. To quickly consider many options in a short time, a fast analysis method of the current distribution is needed, since transient models with many strands are too slow or even impossible to solve. In the remainder of this section, such a model is proposed and applied to this machine.

4.2.3 Model development

This section presents a fast means to obtain the current distribution computed with (slow) transient FEM in the previous section.

Circuit based current distribution

From a circuit perspective, the current distribution across the parallel strands depends on the self and mutual inductance between the strands, the strand resistances and the linked field flux from e.g. magnets or an excitation winding, i.e.:

$$\mathbf{u} = j\omega\mathbf{L}\mathbf{i} + \mathbf{R}\mathbf{i} + j\omega\boldsymbol{\lambda}_{\text{exci}}. \tag{4.1}$$

Here $\mathbf{u}$, $\mathbf{i}$ and $\boldsymbol{\lambda}_{\text{exci}}$ are vectors representing the strand voltages, currents and linked excitation field fluxes, respectively, $\mathbf{L}$ is the inductance matrix and $\mathbf{R}$ is a diagonal matrix holding the strand resistances. Note that in this case the vectors have length 21, since each strand of each phase is individually modeled. Computing $\mathbf{L}$ and $\boldsymbol{\lambda}_{\text{exci}}$ is the most difficult step. In [76, 78] the parameters are computed completely analytically. Although such an approach is fast, it requires simplifications to be made, reducing the accuracy.

The impedance matrix and linked flux can also be computed with FEA. Any desired two or three dimensional detail can be included, at the cost of computation time. 3D FE models containing hundredths of individual strands in close proximity are extremely memory intensive, but

multiple simple models each having only one strand can provide the same answer by using the superposition principle.

The flux linked with a turn can be computed by using a line integral of the tangential magnetic vector potential (MVP) along the path of that turn. That is,

$$\lambda_i = \oint_{l_i} A_t dl_i \tag{4.2}$$

where λ_i, l_i and A_t are the flux linked with turn i, the path of turn i and the tangential MVP, respectively. This is valid only when the average A_t in each perpendicular cross section of a conductor is sufficiently constant, which implies that the strands must be thinner than the skin depth. An advantage of this approach is that the strands where the flux is to be determined do not need to be present in the modeled geometry, significantly reducing the mesh complexity. Also note that this approach is equally applicable to distributed and concentrated windings and that any end-winding shape can be analyzed.

Summarizing, the following approach can be used to predict the current distribution:

1. Solve the machine model with only the excitation field present and compute the fluxes linked to all strands.
2. Either with static or time-harmonic simulations, compute the inductance matrix as follows:
   (a) In a model containing all strands, assign a current to one strand and compute all linked fluxes. Repeat for each strand.
   (b) Alternatively, solve a model containing one current carrying strand and extract all linked fluxes. Repeat for all other strands. In this case the modeled slots are largely empty, significantly reducing the mesh complexity.
3. Form the circuit equations and solve.

Parameter considerations

It may not be necessary to include all parameters with the same level of detail. Three main aspects are now checked for necessity of inclusion, based on 2D analyses, using the winding of Figure 4.1(a) as benchmark. In all cases the conductors of each phase are tied together at the ends and each phase is current driven, which is standard in vector controlled machines.

DC versus AC impedance matrix In practical machines the impedance matrix depends on frequency. Induced currents in the copper and iron parts increase the effective resistance and reduce the effective inductance at higher frequencies. To consider the significance of these effects, an impedance matrix is extracted from both a static simulation and a time-harmonic simulation at the rated frequency. For reference, the static inductance matrix is shown in Table 4.3. Note the large differences in both self and mutual inductance between the strands: strands 6 and 7, which lie near the bottom of the slot, have a 60% higher self inductance than strand 1, which lies

Table 4.3 Inductance matrix (µH) for the winding in Figure 4.1(a)

		Strand →						
		1	**2**	**3**	**4**	**5**	**6**	**7**
↓ Strand	**1**	5.10	5.22	5.03	5.01	4.91	4.94	4.90
	2		6.13	5.74	5.85	5.56	5.67	5.54
	3			6.27	6.26	6.11	6.15	6.05
	4				7.25	6.65	7.10	6.72
	5					7.08	6.97	7.04
	6						8.22	7.54
	7							7.97

Table 4.4 Winding properties and strand currents computed with different parameters

		Strand currents under nominal load current (A)					No-load currents	
Strand	Linked flux (mWb)	Transient FEM	With DC Z-matrix	With AC Z-matrix	One phase	Without field	Transient FEM	With AC Z-matrix
1	1.805	42.55	43.88	43.75	37.49	43.80	2.52	2.64
2	1.808	11.60	14.05	14.05	12.54	14.86	0.83	0.82
3	1.813	7.23	7.87	7.90	8.05	4.96	2.98	3.14
4	1.812	3.58	4.44	4.45	4.40	3.64	0.72	0.81
5	1.814	2.45	2.27	2.28	4.94	1.28	1.50	1.60
6	1.812	0.76	1.40	1.41	1.38	0.57	0.81	0.91
7	1.813	1.19	1.04	1.04	2.45	1.05	0.20	0.22

at the top of the slot. Next, the current distribution is computed for both cases and the results are presented in Table 4.4 for a winding with seven strands. Also included are the currents computed with a full transient FEM simulation, which serve as baseline.

A small discrepancy exists between the currents computed with the transient FE model and those computed with the impedance matrices, even though the same FE model was used to obtain the impedance matrices. The AC-inductance matrix should better capture the behavior of the transient FE model, but the underlying behavior of the transient model is more complex and the accuracy is not significantly improved. The currents computed with both the AC and DC impedance matrices are generally within 10% of the FE-predicted currents. This also holds for windings with a different number of parallel strands.

Inclusion of neighboring phases Throughout this work it is assumed that all phases are wound identically, that the mutual coupling between all phases is identical and that the machine is perfectly symmetrical. It then suffices to only excite the coils of phase A and duplicate the results to other phases to form the full inductance matrix. Completely neglecting the mutual coupling

between the phases could however further reduce the computation complexity.

To determine the feasibility of this assumption, the strand currents are computed based solely on the circuit of a single phase coil and the results are also included in Table 4.4. The deviation from the FE results is in this case more severe and it is recommended to always solve the full system including all phases.

Inclusion of excitation flux Although certainly relevant from a global circuit perspective, the effect of the excitation flux may not be as relevant on the current distribution. More specifically, if the relative differences in inductance are larger than the relative differences in linked field flux, the linked flux simply induces a total voltage across the winding, without influencing the current distribution.

To verify this assumption, the current distribution is again computed, now setting the excitation flux to zero in the circuit equations, and the results are again given in Table 4.4. The predicted distribution still agrees with the baseline FE results. This assumption is further supported by the linked fluxes and self inductance; the variation in PM flux linked with the strands is only 0.5% (see Table 4.4) while the variation in self and mutual inductance between the strands is over 50% (Table 4.3).

This further implies that circulating currents will pose no problem. The last two columns of Table 4.4 show the no-load strand currents and the magnitude is indeed insignificant compared to the loaded currents. Also observe the close match between the transient FE and impedance based results for this load case.

Summary of the proposed model

This section presented a simple modeling approach to determine the strand currents in the case of parallel strands. Some conclusions are

- Basing the calculations on the DC or AC impedance matrix gives similar results.
- The mutual coupling between phases should be included for the highest accuracy. If the phases are wound identically, the results can be copied between the phases and no additional simulations are required.
- Field flux can be ignored. The variation in linked flux between the conductors is typically far smaller than the variation in inductance. This also implies that there are no significant circulating currents.

4.2.4 Experimental validation

The proposed method is now to be verified on a test stator. The previous section concluded that the field flux can be ignored, which implies that a stationary test setup without rotor is justified.

It was also concluded that in a three phase system, all phases should be considered in the calculations. However, only one phase will be tested and modeled to minimize the experimental complexity. Since this is an intrinsically one phase system and will be modeled as such, there are no consequences.

These considerations led to the creation of a stator with a single wound tooth. To this end, the windings and short circuit rings were removed from a 50 mm long single phase shaded pole induction machine stator with 0.65 mm thick laminations, and the stator was rewound with nine five-turn coils of 1.5 mm diameter copper, as depicted in Figure 4.2(a). A FE model of this setup was created, with the strand assignment shown in Figure 4.2(b). A 3D model is depicted in Figure 4.2(c). Such a model is too complex to solve directly and 45 models with one current carrying turn were solved instead. In models with only one strand, computing an AC impedance matrix would not reflect the actual situation, since induced currents in other strands are not included. However, as shown in the previous section, the DC impedance matrix may be used without penalty.

In the models with only one strand present, the mesh is coarser in the slots than it would be if all strands are included, and as a result the accuracy is slightly reduced. A measure of the accuracy is the symmetry of the computed inductance matrix, which should be symmetrical. For the validation model, the average deviation between two symmetrical components is 0.01%, which indicates that the numerical accuracy poses no problem.

The modeled inductances are frequency independent, while in reality inductance reduces at high frequencies, or the winding even behaves capacitive due to parasitic capacitances. Hence, an error between the expected and measured current distribution is to be expected at high frequencies. To estimate the frequency at which this deviation starts to occur, the impedance of the coils is measured with an impedance analyzer (HP 4294A with fixture 16047E). The length of the connection leads is 10 cm, which is negligible compared to the actual coil length. The current magnitude used in such a measurement will not saturate the iron, but since linear iron is assumed throughout all computations and measurements, this is acceptable. Figure 4.3 shows the result of such a measurement where coil A was excited. Since each coil consists of the same number of turns and mutual coupling is never perfect, the self inductance will always have a larger magnitude than the mutual inductances. Although there is no definite region of constant inductance (which is not uncommon in machines), the measured inductance starts to reduce noticeably above 2 kHz and the predicted current distribution may start to deviate significantly.

Next, the actual current distribution is measured by exciting the parallel coils with a current and measuring the individual strand currents with current probes (Yokogawa 701929) and an oscilloscope. The total current is measured as well and provides a reference for the relative magnitude and phase of the individual strand currents. Figure 4.4 shows a schematic representation of the setup. At the connection side the conductors were slightly separated to allow access of the probes, as shown in Figure 4.2(d). The effect of the parasitic impedance of the current probes (0.3 μH) and the bends in the strands was found to be negligible. A total peak current of 8 A was used, keeping the iron well out of saturation.

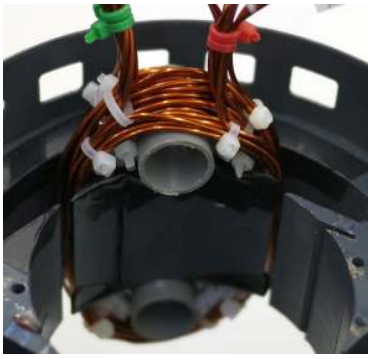

(a) Photo of the actual stator

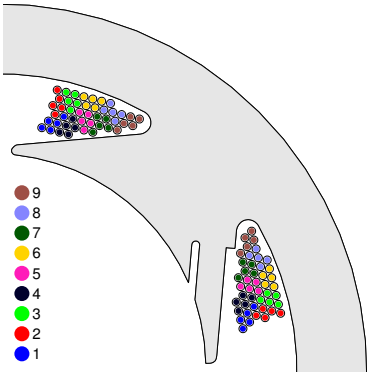

(b) Strand assignment

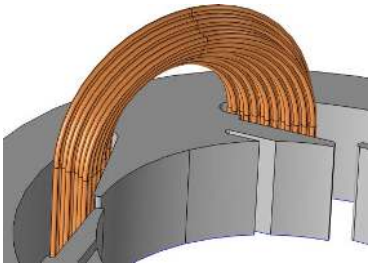

(c) 3D model of the setup

(d) current measurement

Figure 4.2 Models and setup used for the validation test.

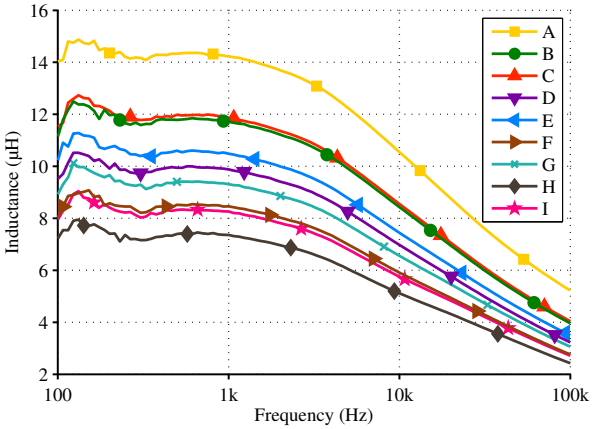

Figure 4.3 Measured self and mutual inductance with coil A excited. Parasitic effects start to reduce the inductance above 2 kHz.

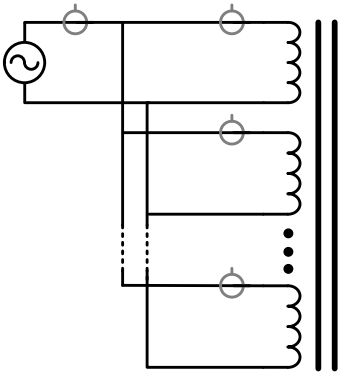

Figure 4.4 Schematic representation of the measurement setup. The actual setup has nine parallel coils.

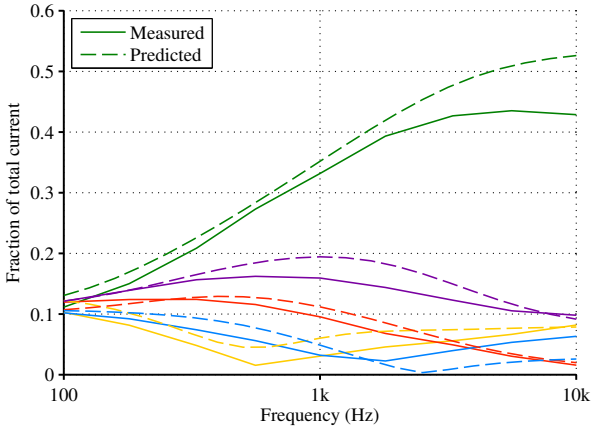

Figure 4.5 Measured (solid) and predicted current distribution for five of the nine strands.

The measured and simulated current distributions versus frequency are presented in Figures. 4.5 and 4.6. Only the five most current carrying strands are shown for clarity. At low frequencies the resistance of the conductors determines the distribution, and most strands carry approximately the same current. With increasing frequency, the inductive part of the impedance becomes significant and dictates the current distribution.

Figure 4.7 shows the relative error for the five strands of Figure 4.5 and the combined error for all strands, weighted by the strand currents. The predicted distribution matches the measured distribution generally within 15–20%, even for frequencies near 10 kHz, where the actual inductance starts to deviate from the computed inductance. The largest error occurs with the strands carrying the least current, which is not important from a loss perspective. In fact, the combined error weighted by the square of the strand currents never exceeds 15%. Note that some strands indeed carry a factor ten more current than others at high frequencies, as predicted in earlier transient simulations, which are therefore deemed credible.

4.2.5 Effect of strand twisting

The proposed method is now demonstrated by analyzing the effect of a single 360° twist of each turn along the stack length. Twisting or conductor displacements are common and proven technologies to equalize imbalances. Such a winding requires a 3D approach for a correct analysis and numerically analyzing such a layout is infeasible with a direct approach, where the full machine geometry is modeled.

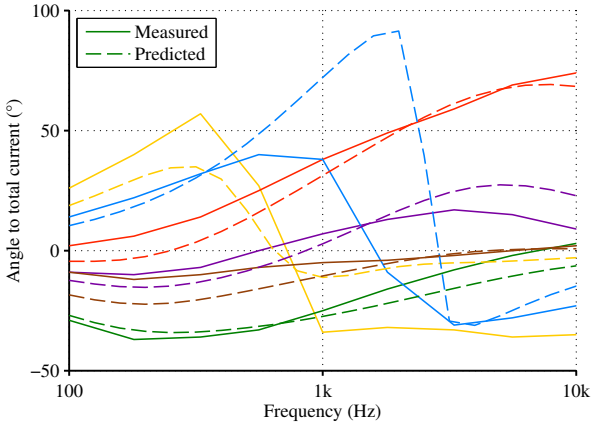

Figure 4.6 Measured (solid) and predicted current-angle distribution.

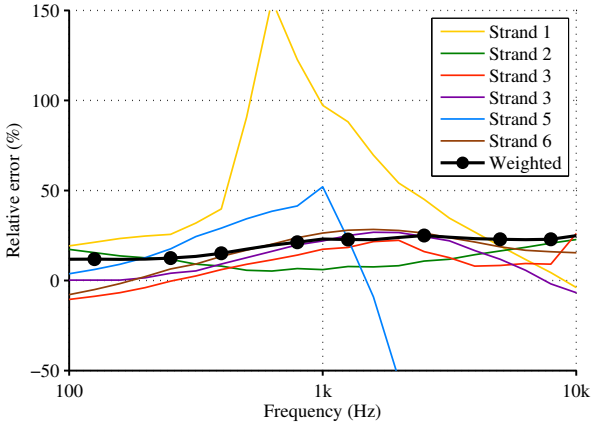

Figure 4.7 Relative error of the predicted currents in Figure 4.5, and the weighted relative error for all nine strands.

Model creation and solving

Twisting the strands introduces complexities in both the manufacturing and modeling of the windings. For simplicity, five circular bundles are assumed and sized such to exactly fill the slot. Within each bundle various conductor sizes and layout options were considered, leading to the selection of 0.84 mm diameter strands in a 1-6-11 arrangement, as shown in Figure 4.8. The resulting copper fill factor is 36%. By forcing the bundles in the slot, a higher fill factor may be obtained in reality, but the strand shapes become highly irregular and creating the models becomes tedious.

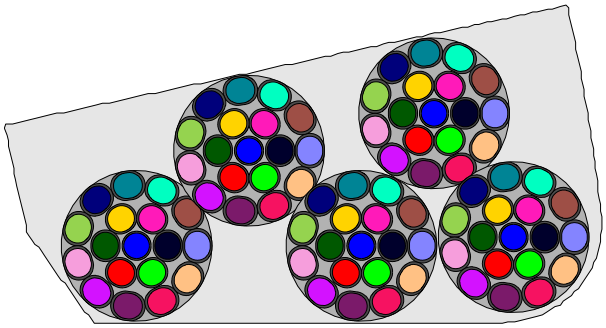

Figure 4.8 Cross-sectional view of a slot-side containing five 18-strand bundles. Each color represents the same conductor.

Figure 4.9 shows a 3D impression of the resulting five turn winding with 18 parallel strands per bundle. Directly solving such a model is deemed impossible and only one strand is actually modeled at a time (thus requiring 90 simple models), as shown in Figure 4.10. This greatly reduces the memory requirements. Circumferential symmetry is exploited to further reduce the problem size. The models typically had 3.5 million degrees of freedom, and solving all models took 24 hours on a 4 core desktop pc. A rather fine mesh was used to ensure accurate results; the same results could be obtained in less time with a more carefully selected mesh size.

Results

After solving all models, the fluxes linked to each turn and strand are merged and duplicated between the phases to form the full 54×54 inductance matrix, the strand resistances are computed and the circuit equations are solved. The resulting current distribution as function of frequency is shown in Figure 4.11, along with the distribution for the straight winding layout from Figure 4.1(a).

The effect on the current equalization is obvious; the currents start to diverge from the DC distribution only after 1 kHz for the twisted winding, while for the straight coils this occurs already at 80 Hz. Inspecting the results more closely reveals that the currents in the seven inner strands go to zero for high frequencies, as expected due to the bundle level skin effect. At the rated frequency for the target design, 2.67 kHz, the worst and average strand current deviations from the DC distribution are 38% and 4.4%, respectively. At this frequency the conduction copper losses are 79 W, while with a DC current distribution they are 71 W, an acceptable increase and still lower than the 200 W computed for the straight windings.

This result shows that for low voltage high-speed machines strand twisting will be necessary, but a single twist per stack length suffices. The impact of this on the manufacturing process of the windings is however considerable. Moreover, the reduction in fill factor may reduce the low speed high torque performance of machines in e.g. electric vehicles. All in all, the results indicate that in low voltage machines the windings should receive special attention early in the design.

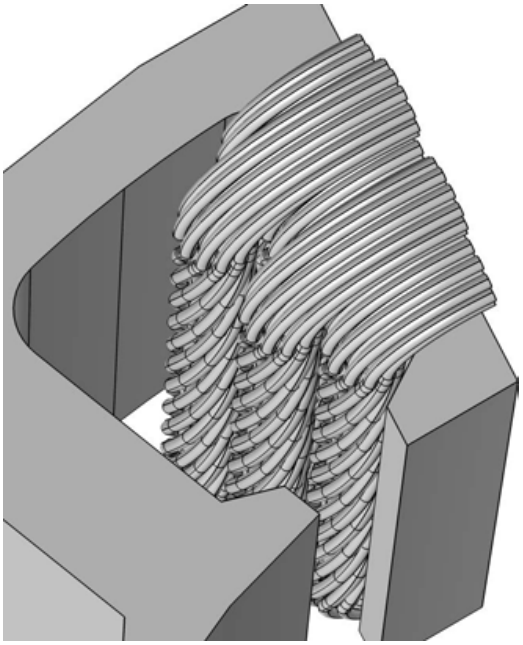

Figure 4.9 Depiction of the full 3D model, showing five 19-strand bundles twisted 360° inside the slot.

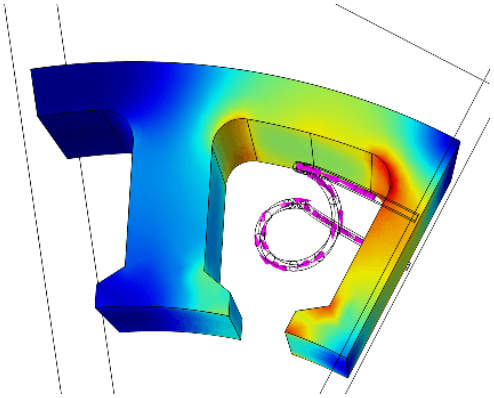

Figure 4.10 Example solved single strand model with exaggerated strand twisting.

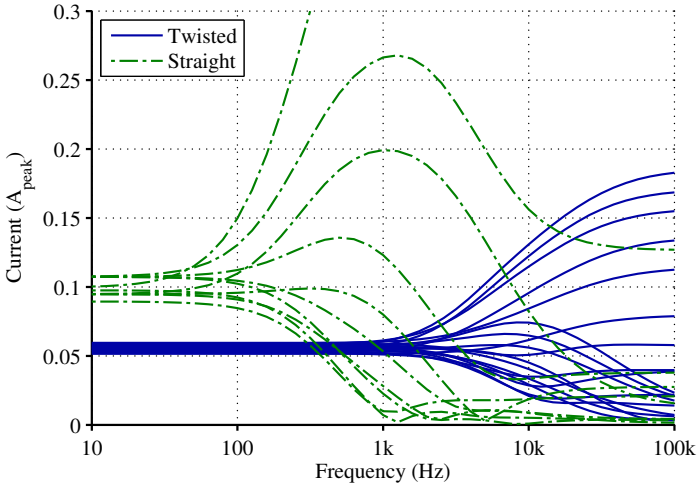

Figure 4.11 Strand currents as function of frequency for one straight and one twisted winding.

Additional observations

Having determined the 2D and 3D inductance matrices for both twisted and non-twisted windings, a few perhaps interesting observations can be made.

For a non-twisted layout, the self inductance of each coil increases for the machine considered by some 20–22% due to the end-windings. The mutual inductance between parallel coils on the same tooth increases slightly less; 18–20%. The mutual inductance between coils of neighboring phases increases by only 6–10%. As a result, the end-windings will act to equalize the current distribution across the strands. However, the extent of this effect is insignificant and cannot be seen as a method to equalize the strand currents, unless an unrealistically short machine is considered.

4.3 Loss reduction techniques

The goal of this section is to summarize winding loss reduction methods and numerically compare the benefits. The focus lies on small high-speed machines.

4.3.1 Background

The additional winding losses due to skin and proximity effects have been known since machines are widely being used [79]. Various models to compute these losses have been proposed and applied to show, for instance, the effects of segmentation [80], tooth tip shape [55], parallel strands [76], PWM [57], or the use of foil windings [81].

Using litz wire is a well known strategy from high frequency transformer design and is sometimes also applied to machines. When using litz wire the number of strands and bundles still needs to be determined. The individual strands should be no thicker than necessary as the effective copper area decreases with decreasing strand diameter due to the space required for the insulation. For high-frequency transformers approaches to determine the optimum are presented in [68, 82]. High frequency magnetic components are mostly designed with no or small airgaps and, as a result, have little leakage field inside the slot. The results obtained are then not directly applicable to machines.

Most examples found in literature concern single cases, obscuring the exact benefits and drawbacks of the measures. The aim of this section is to provide more insight into the problem of eddy current loss reduction methods in high-speed PM machines by systematically analyzing the consequences of using parallel strands, a reduced slot filling or slot size, or an increased fill factor. A high-speed fractional pitch concentrated non-overlapping winding machine is used as example and analyzed with 2D finite element (FE) analysis.

Table 4.5 Machine properties

Property	Value
Rated power	10 kW
Rated speed	36,000 RPM
Poles	6
Turns/tooth	18
Copper losses	33 W (in-slot)
Iron losses	83 W
Dimensions	Outer radius: 70 mm Yoke thickness: 12 mm Slot height: 23 mm Tooth width: 12.3 mm Stack length: 41 mm Tooth tip height: 1.2 mm Tooth tip span: 75%

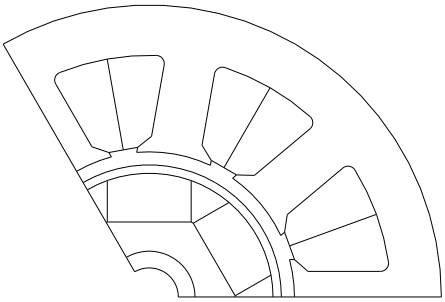

Figure 4.12 Cross section of the basic machine.

4.3.2 Example machine

This section presents the SPM machine that will be analyzed. Table 4.5 gives the basic specifications and Figure 4.12 shows a cross section. The rotational speed and power level are those of e.g. an auxiliary generator for a gas turbine. The electrical frequency was deliberately chosen fairly high (1.8 kHz) to enhance eddy current losses in the winding, but it is not unrealistically high.

The initial machine is assumed to have perfect litz wires, and the copper losses are computed with a fill factor of 30%. This gives rise to 33 W of copper losses inside the slots. Only the in-slot copper losses are considered, because the magnetic field strength inside the slots is higher than in the end-windings, leading to far stronger pronounced loss effects [83]. In addition, the losses inside the end-windings can be neglected compared to the in-slot part for longer machines, especially for machines with tooth-coil windings.

The following sections aim to find design modifications that allow regular solid strands, placed inside the slots without twisting, to be used. This enables a cost reduction and an increased fill factor.

4.3.3 Analytical models

The strand level AC copper losses can also be computed analytically, as is demonstrated in e.g. [55, 76]. The difficulty with analytical modeling is to obtain the distribution of the magnetic field inside the slots. FE modeling does not suffer from this drawback, but creating and solving models

with a large number of strands inside the slots can take a long time. Also, rotor motion cannot be accounted for with standard time-harmonic models, and transient or multiple specially prepared time-harmonic models are required instead [60].

An intermediate solution is to use FE models with bulk strand domains to compute the magnetic field inside the slots and compute the AC copper losses afterwards. This allows a quick evaluation of the AC losses for various strand dimensions and slot fill styles. It also allows AC losses to be accounted for in automated FE-based optimization strategies, where on the one hand the FE models should be as simple as possible, while on the other hand all loss mechanisms should be taken into account.

In the field of high-frequency magnetic components, much research exists on AC losses in windings. The induced losses inside a strand subjected to an external magnetic field H_e are for instance given by [66]:

$$P_{str} = \rho l \hat{H}^2 D_s \quad \text{with} \quad D_s = 2\pi \text{Re}\left\{ \frac{\alpha r I_1(\alpha r)}{I_0(\alpha r)} \right\} \tag{4.3}$$

where P_{str} is the power in one strand, ρ the resistivity, l the length, $\hat{H}$ the peak of the magnetic field, $\alpha = \frac{1+j}{\sqrt{2\rho}}\sqrt{\omega\mu}$, r the radius of the strand and I_0 and I_1 are modified Bessel functions.

To demonstrate the applicability of such an approach, the AC copper losses were computed with a FE model containing the individual strands and using eq. (4.3) together with a simpler FE model. Figure 4.13 shows a strand layout inside the slot along with the losses for each strand, computed in the two ways. A close match can be observed. The asymmetry between the slot sides is the result of the selected load angle. The total analytically computed losses are 11% less than the FEM predicted losses. Although this is a close match, FEM will be used to calculated strand level proximity losses throughout the rest of this chapter for maximum accuracy.

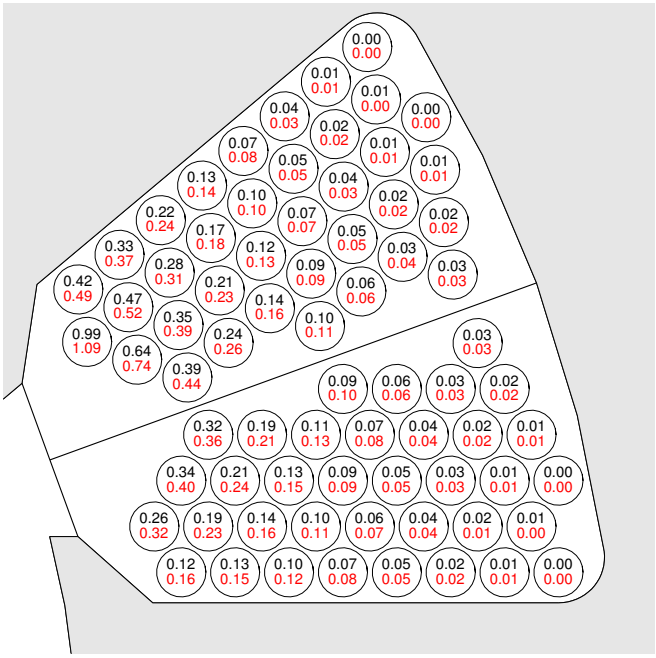

Figure 4.13 Individual average strand losses computed semi-analytically (top, black) and with transient FEM (bottom, red). Total losses: FEM: 5.08 W, Analytical: 4.54 W.

4.3.4 Loss reduction mechanisms

This section considers the effects of the proposed loss reduction schemes.

Parallel strands

If the diameter of a single strand is close to the skin depth, employing several thinner strands in parallel may sufficiently reduce the additional losses. Two disadvantages of using parallel strands are increased manufacturing complexity and an uneven current distribution across the stands. Advantages over pre-fabricated litz wire are a higher fill factor and reduced cost.

The uneven current sharing among the strands has two causes as pointed out in the previous section: circulating currents, which are the result of imbalances in the linked field flux; and variations in mutual coupling between the parallel strands, which depend on the winding geometry and cause the imposed current to distribute unevenly. For small machines the differences in the inductance matrix are greater than those in the linked field flux and circulating currents present no significant problem. To minimize both effects, the impedance of all strands should be as similar as possible, which can be achieved by placing each strand in various positions inside the

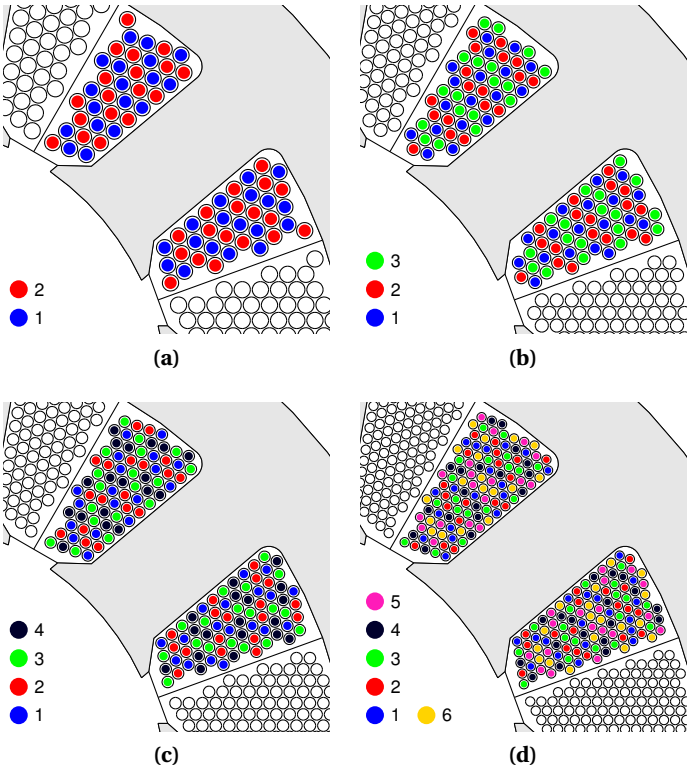

Figure 4.14 Four slot fill schemes with 18 turns and an increasing number of parallel strands.

slot. Twisting the bundle of strands was shown to be a very effective method, but reduces the fill factor. This section considers the case where the strands are placed in the slot without twisting, which allows high fill factors to be obtained and can be analyzed with 2D computations. The best averaging of the impedances can in this case be obtained by winding all strands simultaneously, as shown in Figure 4.14, where the slot layouts for increasing numbers of strands are shown.

The strand arrangements of Figure 4.14 are analyzed with transient FEA to consider both the induced losses and the current imbalance. Each case is analyzed with the same number of turns (here: 18) and total phase current. In the FE models the total phase current is imposed on the windings and the individual strand currents are added as a degree of freedom, allowing for an uneven current distribution across the strands to exist, as well as circulating currents. The average induced voltage and resistive voltage drop across each strand are used in the formulation of the parallel connection, which is only valid if the single strands are thinner than the skin depth.

Figure 4.15 shows the ratio of AC to DC copper losses across the operating range of the machines.

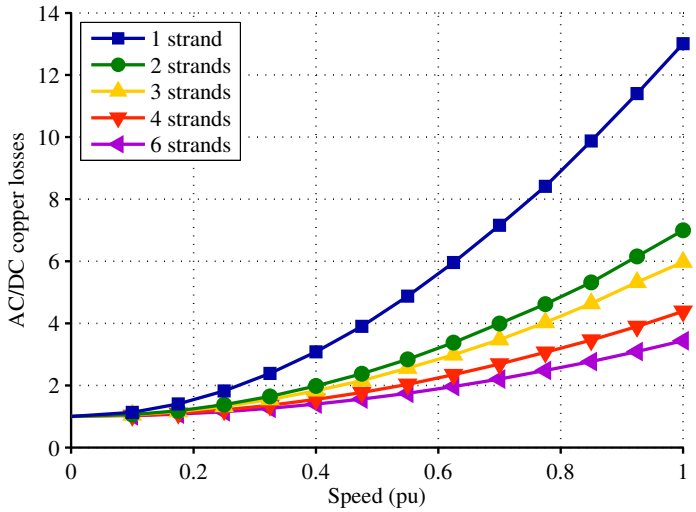

Figure 4.15 Computed ratios of AC to DC copper losses for increasing numbers of parallel strands.

Without parallel strands the total copper losses at full speed are 13 times the DC losses. Introducing parallel strands reduces this, although with diminishing returns. For the case with six strands, the AC losses are still 3.4 times the DC losses, which amounts to 64 W. This is still 193% of the baseline litz design.

The increased losses are partly due to an imbalance among the strand currents, caused by differences in mutual and self inductance of the individual turns, and partially due to strand level eddy current losses. Table 4.6 shows the strand current deviation from DC at nominal speed. With six strands, the imbalance alone gives rise to a 1.58 times loss increase. This table also shows that large variations between different numbers of parallel strands exist as a result of differences in slot filling. This implies that a high number of parallel strands is unattractive, because small differences in strand placement lead to large loss variations.

To further demonstrate the effect of current imbalance, the current distributions are computed for various winding styles and parallel strand numbers, each having 48 strands inside the slot. 48 was selected because it allows many integer divisions, so that many parallel strand combinations can be considered. Table 4.7 shows the computed loss increases solely due to current imbalance. Even with three parallel strands, a fivefold increase may result, while the worst case exceeds 12 times. The winding style denoted 'Grouped turns, tang layers' has the lowest loss increase factor and is the one used for the windings in Figure 4.14.

Looking at Table 4.7, it appears that using 12 turns with four parallel strands is still feasible (loss ratio 1.4), while using 8 turns with six parallel strands is not (loss ratio 4). Considering also the results from Table 4.6, a safe initial rule-of-thumb for the maximum number of parallel strands

Table 4.6 Relative strand current deviations from the ideal DC distribution and resulting loss increase

Number of strands	Strand current deviation from ideal (%)						Additional losses (%)
1	0						0
2	-2	+6					5
3	+103	-1	+30				126
4	+44	+3	+8	+22			45
5	+126	+45	-3	-3	+50		128
6	+2	+4	+33	+16	+4	+78	58

Table 4.7 Loss increase factors due to unbalanced currents for four winding schemes (all with 48 strands per tooth).

fill type	Parallel strands								
	2	3	4	6	8	12	16	24	48
Grouped cond., random (Fig. 4.1(a))	3.2	4.4	4.7	6.3	6.2	7.6	8.1	8.6	9.0
Grouped turns, random (4.1(b))	2.9	5.0	7.1	9.8	8.7	10.0	10.6	10.8	9.0
Grouped turns, tang layers (4.14)	1.3	1.7	1.4	4.0	6.7	5.2	6.9	12.6	9.0
Grouped cond., tang layers (4.1(d))	2.8	6.5	6.8	6.3	7.6	8.1	8.5	9.1	9.0

when not using equalization methods, would be to use at most half the number of turns as number of parallel strands.

Partially filled slots

With semi-closed slots, most leakage flux exists near the slot opening. In addition, a part of the PM flux also leaks close to the slot opening. By using only the rear side of the slot, the total losses may then be reduced, despite a decrease in slot fill factor. Moreover, to maintain the same number of turns, thinner strands will be required, further reducing the AC losses. For machines which require transient high-torque operation, such as machines in electric vehicles, this measure may not be attractive as the thermal capacity of the windings is reduced.

The main benefit of this solution is the reduction of the production cost, since less material is required, and regular round enameled wires and simple automatic winding techniques can be used.

The shape of the tooth tips greatly affects the field distribution near the slot opening and therefore also the AC copper losses. The effect of the main tooth tip dimensions, the span and height, on

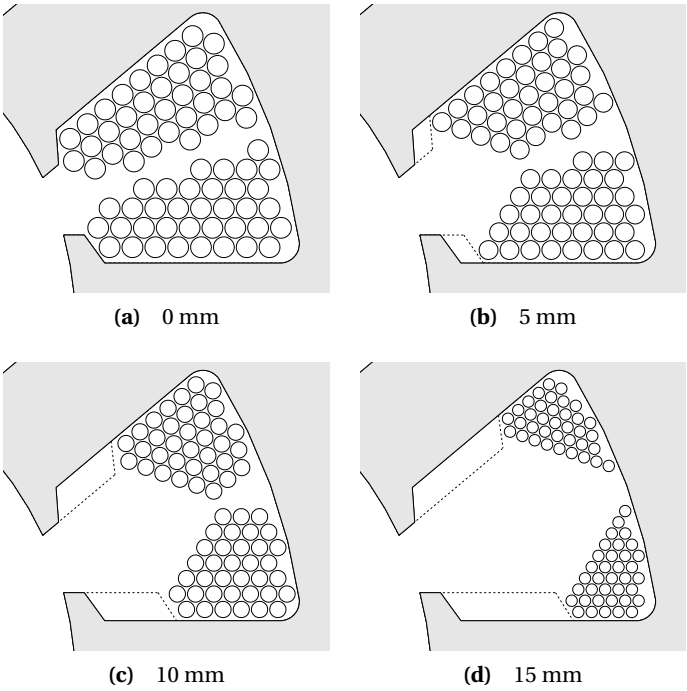

(a) 0 mm **(b)** 5 mm

(c) 10 mm **(d)** 15 mm

Figure 4.16 Slot fill schemes with additional air near the slot opening. They are created by moving a virtual line, which runs parallel to the strand sides, gradually to the right. The height of the tooth is 22 mm.

the copper losses is demonstrated in e.g. [55]. Besides the copper losses, the span of the tooth tips also affects other machine parameters, such as cogging torque or inductance and is therefore kept constant in this analysis. The height of the tips can be changed with less consequences and the effect on the winding losses will be considered.

Figure 4.16 shows several strand arrangements with increasing distance to the slot opening. Both fixed and variable height tooth tips are indicated. In each case the winding has 18 turns with two parallel strands, thus keeping the voltage rating constant. The previous sections showed that two parallel strands pose no problem for the current sharing, while still reducing the losses significantly. To accommodate the same number of strands, the strand diameter is gradually reduced.

Figure 4.17 shows the resulting AC and DC copper losses, computed with transient FEA. For small distances away from the slot-opening, the decrease of the induced losses is greater than increase in DC losses, and it is beneficial to not fill the complete slot. The optimum lies near 11 mm, when only half the slot is filled. Increasing the tooth tip height along with the strands can be seen to

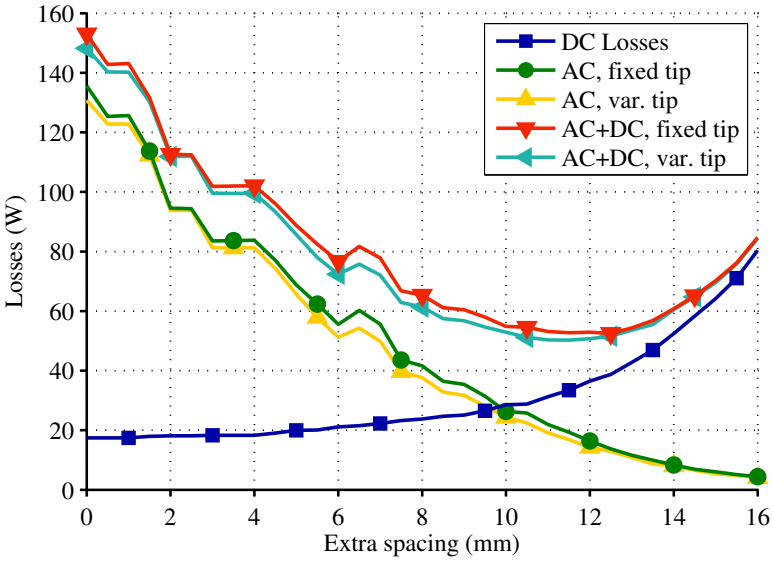

Figure 4.17 DC only and total losses as function of extra slot clearing.

result in slightly lower AC losses, but the difference is negligible. At the height with the lowest combined losses, the total losses are about 50 W, which still equals 1.5 times the losses with ideal litz wire.

Effect of strand shape and fill factor

In an attempt to increase the fill factor, a coil with circular strands may be compressed, leading to a hexagonal cross-section [84]. Rectangular wires may also be used to obtain a high fill factor. The effect of these strand shapes on the losses is analyzed in this section.

Five cases are considered:

- A winding with circular strands as reference, with a fill factor of about 55%.
- Two windings with hexagonal strands, one having the same total cross-sectional copper area as the reference case and one having a maximized cross-section with a minimum space between the conductors of 50 µm. In the latter case the fill factor was in the order of 75%.
- Two windings with square strands, but otherwise identical the hexagonal case.

For each case the number of strands was varied between 18 and 108. Figure 4.18 shows how the strands are placed inside the slots and the current distribution inside the strands for a strand cross-sectional area of 2 mm².

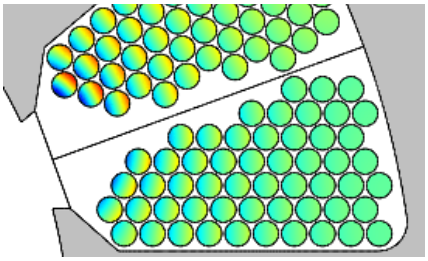

(a) circular

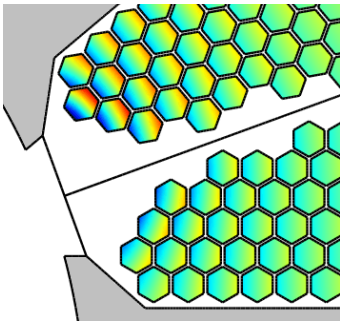

(b) hexagonal

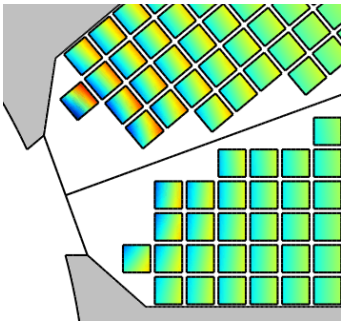

(c) square

Figure 4.18 Current densities in the strands under full load.

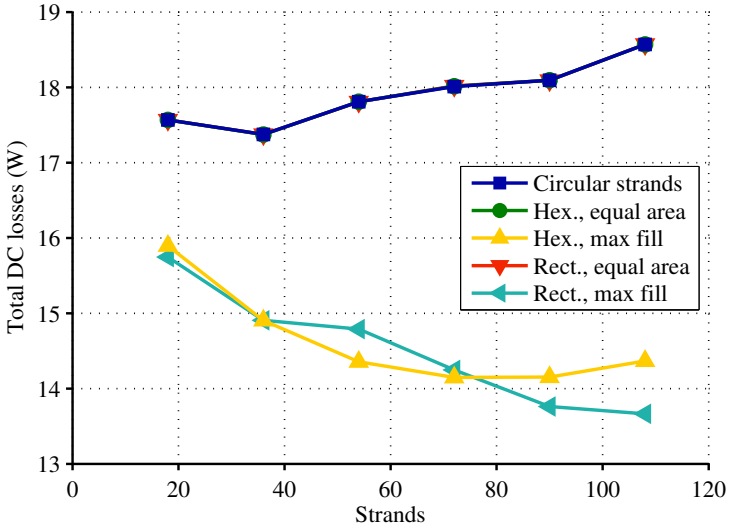

Figure 4.19 DC losses for windings with circular, square and hexagonal shape.

Figures. 4.19 and 4.20 show the DC and AC losses for the analyzed strands. The DC losses are obviously identical for strands with identical surface area, while for the maximum fill windings the DC losses are up to 20% less. The AC losses in strands with the same area are virtually identical. That is, using hexagonal or square strands instead of circular strands does not increase the losses. However, in windings with a high fill factor the AC losses are consistently 20 W larger than in the lower fill factor counterparts.

This shows that in a case where the AC losses form a substantial part of the copper losses, maximizing the fill factor is not immediately beneficial. To still benefit from a larger fill factor, design modifications as proposed in the other sections will be required.

Decreasing the slot size

The previous sections showed that maximally filling the slot with windings may result in higher copper losses. Instead of partially filling the slot, the total losses can perhaps also be reduced by using narrower slots. An added benefit of wider teeth is a lower thermal resistance from the windings to the stator, allowing a higher current density. To investigate this assumption, this section considers the effect of tooth width on the copper and iron losses.

Narrowing the slots causes in two opposing effects on the induced copper losses: on the one hand, the strand diameter has to be reduced to fit the same number of turns in the slot, thus reducing the losses, while on the other hand the magnetic field strenght inside a narrower slot increases,

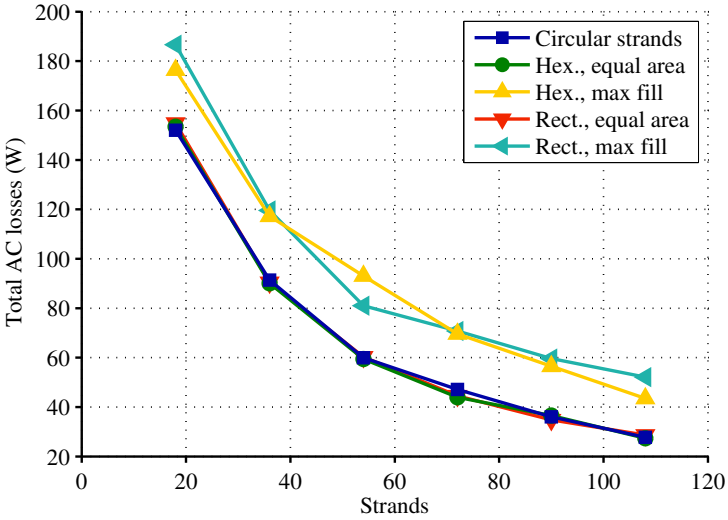

Figure 4.20 AC losses for windings with circular, square and hexagonal shape.

thereby increasing the losses. Apart from this, the DC losses will logically increase while the iron losses will decrease. The key question is whether there is a benefit in terms of total losses.

Figure 4.21 shows various loss components as function of tooth width. Two fill cases were considered: one where the entire slot was filled and one where, for each tooth width separately, the fill height of the slot was chosen to give the minimum total copper losses. About 70% of the slot height was typically filled in the second case, which slightly increases for narrower slots. Forty series-connected turns were considered, so that no uneven distribution between parallel strands can occur.

Considering the total copper losses, a small reduction can be observed for the fully filled slot case; from 110 W for a narrow tooth to 80 W for a wide tooth. In the optimally filled slot case, the total losses show a slight increase, from 40 to 55 W. This result shows that the effects of changing the tooth width on the total copper losses is small compared to the other methods.

The copper losses in the best case are still 50 W; 17 W more than the baseline design. Compared to that same design, the iron losses are however reduced by 15 W, giving this design a similar efficiency at full load and reduced no-load losses.

4.3.5 All methods combined

To demonstrate the benefits of combining the proposed methods, a final design incorporating all modifications is created. A tooth width of 16 mm was selected and only the lower 12 mm of the

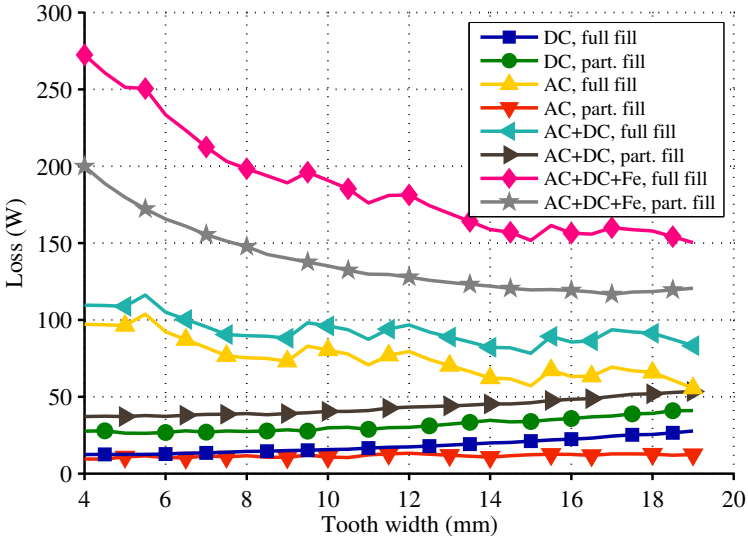

Figure 4.21 Loss components as function of tooth width.

slot was used to place 5 parallel strands. Figure 4.22 shows this machine and the strand placement. The strand diameter is 0.97 mm and the total copper area per slot-side is 66 mm², with a local fill factor of 62%. The baseline design presented in section 4.3.2 has an almost identical copper area (65 mm²), but a fill factor of only 30%. The performance of the new design will therefore be better at low frequencies.

The total in-slot copper losses are 46 W, which is 1.4 times the DC losses, of which 1.09 times due to current unbalance. Compared to the baseline design, iron losses are reduced by 13 W, which exactly equals the increase in copper losses. In the end, this new design with solid non-twisted strands offers similar full load performance and reduced no-load losses compared to the initial design. This shows that it is not always necessary to use litz wires in high-speed machines, as long as appropriate measures are taken.

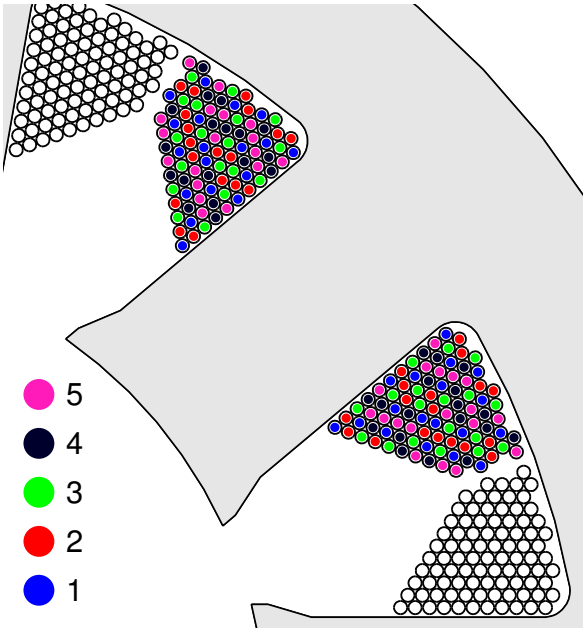

Figure 4.22 Cross section and strand placement of the final design.

4.4 Conclusion

This chapter focussed on winding losses in low-voltage high-speed machines. The need for very few turns in combination with a high electrical frequency is problematic for the AC copper losses. Using litz wire may provide a solution, but suffers from a somewhat poorer fill factor. Discrete parallel strands may be used as an alternative, but this solution is susceptible to bundle level skin effects ('discrete skin effect').

A simple approach was presented to predict the current distribution across parallel strands in low voltage high-speed machines by using the inductance matrix obtained from FE simulations. Basic experiments were performed to confirm the modeling method. The use of two or three dimensional FE analysis requires little set up time and allows any desired detail to be included, trading run time for simplicity. Any distributed or concentrated winding style can be considered, including strand displacements or twisting. Using the method it was demonstrated that including a 360° twist per stack length very effectively equalizes the strand currents, reducing the copper losses from 200 W for a non-twisted winding to 79 W. The example further indicated that the current imbalance is the result of variations in the mutual inductance between the strands, and that circulating currents pose no problem, because the linked field flux shows far less variation.

After having demonstrated the correctness of the strand level FE models, a number of more

general loss reduction methods were compared, starting from a baseline design using litz wire. Considered were the use of parallel strands, partially filling the slot and changing the tooth width. Of these, the most promising technique is to only partially fill the slots in radial direction. In the example case, filling only the lower half of the slots limits the copper losses to 150% of those with ideal litz wire. Although this is not interesting when a high efficiency is essential, this approach can be cheaper and has a lower thermal resistivity from the winding core to the ambient than litz wire. When using parallel strands the best case losses were 193% of the ideal winding losses. However, compared to partially filling the slots, this approach gives a better total fill factor and hence a larger thermal capacity and lower DC losses, which are beneficial for sustained low-speed or transient operation modes. The benefits of this approach diminish for larger numbers of parallel strands due to an increasing current imbalance across the strands. A rough rule of thumb to avoid problems with an uneven current distribution across non-twisted parallel strands, is to keep the number of parallel strands below half the number of turns. For example, with ten turns, no more than five parallel strands should be used. Lastly, using wider teeth hardly changes the copper losses, but does lower the iron losses and can bring a small benefit in this way.

Techniques to maximize the fill factor are of limited use if they are not combined with the other methods considered here, because the increased strand area gives rise to more AC copper losses. If however all of the proposed methods are combined, a design results that has similar performance as the baseline design with litz wires. This shows that solid copper strands, wound without twisting or displacements, can be used in high-speed machines.

Lastly, this chapter only considered the losses at the fundamental frequency, neglecting any time-harmonics in the phase currents. Considering that high-performance machines are commonly driven by an inverter, the effect of time-harmonics should be given some consideration. This is further motivated by the results from Figure 4.11, which shows that even with twisted windings, the strand currents start to diverge above a few kHz. Therefore, the consequences of time-harmonics in the phase currents are given further consideration in Chapter 6.

CHAPTER 5

Inter-turn faults – modeling, detection and consequences

In fail-safe and fault-tolerant applications, a thorough understanding of all possible faults is necessary to minimize the risk of those faults occurring. Some faults cannot be intrinsically avoided by proper design and additional measures are needed to reduce the consequences if those faults occur. Turn-to-turn or inter-turn short circuits in PM machines are an example of such faults. Even though the use of heavy grade multi-layer insulation materials can reduce the likelihood of a turn-to-turn short circuit, this may not suffice and fault detection and mitigation systems will be needed.

This chapter is a detailed study of turn-to-turn faults. Starting with a modeling and analysis section, the consequences of various fault types and turn-turn combinations are considered. The fault currents, losses and other properties are computed for an idealized or complete drive system, allowing the severity of various faults to be compared. Next, a short series of experiments is performed to determine the failure mode and behavior of electrical coils. Finally, a fault detector concept is presented, demonstrated with the models from the earlier sections, and validated with lab experiments on two different machines.

Based on

- M. van der Geest, H. Polinder, J. A. Ferreira, A. Veltman, J. J. Wolmarans, and N. Tsiara, "Analysis and Neutral Voltage Based Detection of Inter-Turn Faults in High-Speed Permanent Magnet Machines with Parallel Strands," *IEEE Trans. Ind. Electron.*, vol. 62, no. 6, pp. 3862–3873, Jun. 2015; and
- M. van der Geest, H. Polinder, and J. A. Ferreira, "Short-circuit faults in high-speed pm machines with parallel strands and coils," in *Int. Conf. Power Electron. Machines Drives (PEMD)*, 2014; and
- M. van der Geest, H. Polinder, and J. A. Ferreira, "Experimental determination of stator winding failure behavior," in *16th European Conf. Power Electron. Appl. (EPE-ECCE Europe)*, 2014.

5.1 Introduction

Electrical drives in safety critical applications, such as those in automotive or aerospace systems, should exhibit a high system availability. One approach to achieve a high availability is to design for a high reliability of the individual components that make up a system by using overrating. Examples are employing a higher grade winding insulation material than strictly necessary, or over-dimensioning the cooling system. In addition to, or as an alternative to overrating, a system can be made fault-tolerant. A fault-tolerant system can continue to (partially) function in the presence of faults. To achieve this, possible failure modes are identified and the design is adapted to handle such faults. Aerospace drive systems are a clear example of fault-tolerant systems. In these systems, both the electrical machine and the inverter can be implemented as multiple isolated and independent single or three phase subsystems [85–87]. By ensuring a complete thermal, magnetic and electrical isolation between those systems, the failure of one subsystem does not affect other subsystems. Still, when a fault occurs, taking corrective actions can further reduce post fault risks such as fire hazards; improve performance, such as reducing torque ripple or power loss; or generally ensure a predictable post-fault state.

A particular problem with PM generators are short circuits, since the magnets cannot be disabled. Turn-to-turn (inter-turn) short circuits are especially dangerous, because the local short circuit currents can greatly exceed those caused by terminal short circuits [88], leading to rapid machine failure. In many fault-tolerant drive systems inter-turn faults are dealt with by designing the machine to have a one per-unit inductance, leading to a terminal short circuit current equal to the rated current. After the occurrence and detection of an inter-turn fault, the affected phase is short circuited at the terminals, ideally reducing the fault current to the nominal value [81, 86, 89, 90]. An alternative approach is to not act after an inter-turn fault and relying on the design to reach a safe, non-functional steady state.

So, in the development of a fail-safe or fault-tolerant machine, a number of questions must be answered:

- How large are the expected short circuit currents and how do they affect the total drive system?
- How does an unmitigated fault evolve? And, strongly related;
- How much time is available to detect a fault?
- How can faults be detected?
- How effectively can a terminal level short circuit suppress the local short circuit currents?

This chapter will address these topics. To this end, models will be created, partially based on the modeling method described and tested in Chapter 4, and used to estimate the fault currents and losses for turn-to-turn faults in single strands, between parallel strands and between neighboring phase coils, with account of the position of the short circuit inside the slot. Contributions are the level of detail that is considered and the fact that short circuits between parallel strands are also considered. Next, experiments are performed on coils to determine basic failure behavior,

providing insight into the failure process of coils. Lastly, a novel fault detector is proposed, which is simple enough for hardware implementation as an independent observer, but cannot locate or identify faults. The detection concept is demonstrated with simulations and experiments. The results presented in this chapter will ultimately improve the understanding of (the detection of) turn level faults in electrical machines.

All of these items have been addressed in literature in one way or another. What now follows is an overview of relevant work with regards to modeling, detection and mitigation of faults.

5.1.1 Modeling of short circuits

Short circuits at a turn level can be modeled in various ways, with a tradeoff between simplicity and level of detail. At the simplest level, the impedances of the healthy and faulty parts of the winding are computed as a fraction of the total healthy impedance. Although this approach does not consider the effect of strand shape and position inside the slot, it can be used to quickly estimate faulted machine performance. For a more detailed analysis, fully analytical methods [91–93], magnetic equivalent circuits [88, 94, 95], or finite element analysis (FEA) [96–98] can be used. Analytical models accounting for individual layered turns are described in [78, 89], and show that vertical strip layers can very effectively suppress fault currents, but are prone to proximity effect losses. Ref. [76] presents a model to compute turn level windings properties with circular strands, but does not compute fault behavior.

5.1.2 Fault detection

For the detection of short circuits, a large variety of systems has been proposed, differing in complexity, sensitivity and fault identification abilities [99]. A somewhat older approach is to compute the negative sequence component of the line currents for voltage fed machines, or the voltages for current fed machines [100]. Instead of computing the negative sequence component from the terminal quantities, the zero sequence component may be measured at the neutral point of the machine, which is simpler and slightly more sensitive [101–103]. Other frequency components in the synchronous reference frame can also indicate faults, particulary for multi-phase machines[104]. Applying time-frequency or wavelet methods to the terminal quantities yields a more sensitive system, but is also computationally intense [105–107]. Nature inspired methods such as neural networks [108] or ant clustering [109] potentially offer high sensitivity with limited complexity. Model based fault detection is yet another approach, but requires extensive knowledge about the machine parameters [97, 110], although Kalman filtering can improve performance[111].

Many detection methods are passive, using only existing terminal level voltages or currents to determine the state of the machine. Such a method can be added to an existing drive system with few modifications, but perhaps the major disadvantage is the dependency of the sensitivity on motor speed. By injecting excitation signals, faults can be detected even at stand-still [112, 113],

which is particularly attractive in e.g. electric vehicle applications. Instead of measuring or injecting signals at the machine terminals, faults can also be detected with search coils, either internal [114] or external to the machine [115]. Although these methods are invasive, they are among the most effective approaches.

Ultimately though, the question is not if a method *can* detect a fault, but if it can detect the fault *fast enough* [86].

5.1.3 Fault mitigation

After detection of a fault, corrective actions have to be taken to minimize damage. For non-PM machines, electrically disconnecting the machine will obviously suffice, but with externally driven or fault-tolerant PM machines, which need to function in the presence of faults, other actions are required. A typical approach is to design the machine with a 1 pu phase inductance and short circuit the affected phase(s) at the machine terminals, ideally limiting the short circuit to the rated current [85]. Due to leakage flux inside the machine slots, the current equalization is not perfect and short circuits near the slot opening will maintain a higher than nominal fault current [89, 116, 117].

An additional choice is the number of phases to be used. The highest level of modularity is obtained if each phase is individually fed by a full bridge converter. By appropriately driving the remaining phases, a reduced but ripple free torque may still be obtained in the presence of a fault. Disadvantages of this approach are that non-standard bridges will be needed, as well as non-standard vector control during faulted operation. Moreover, since each phase is a single phase load with pulsating power requirements, filter capacitors may be needed in the converters. To avoid all of those problems, it can be attractive to utilize multiple independent three phase lanes [85].

5.2 Modeling of short circuit faults

This section briefly presents the various models that will be used to compute short circuit currents and estimate fault-detector performance.

5.2.1 Machine

The machine considered is a non-salient surface mounted PM machine, Figure 5.1 shows a cross section. Intended for aerospace applications, the machine has a 16,000 RPM nominal rotational speed and an 18 slot 12 pole tooth-coil winding layout. The six coils of each phase are connected in parallel to meet the voltage constraints, which can lead to circulating currents between the parallel teeth, especially during short circuits. In addition, each tooth is wound with three parallel solid

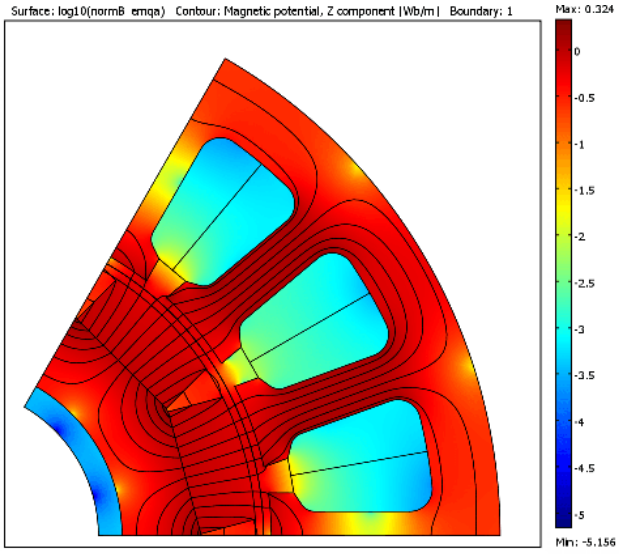

Figure 5.1 Field distribution of the considered machine, on a logarithmic scale to emphasize the distribution inside the slots.

strands (no twisting or displacements) to reduce strand level eddy current losses. This can lead to unequal current sharing between the strands and allows short circuits between parallel strands to occur, which needs to be correctly taken into account. Because of the various imbalances that can exist, it is believed that the usual benefits of modeling the machine in the synchronous dq-frame are reduced and all models are formulated entirely in the stationary abc-frame.

5.2.2 Circuit

Figure 5.2 shows a part of the circuit that is solved. Each phase consists of t parallel teeth and each tooth carries a coil with s parallel strands and N turns. The machine is connected in star, but the modeling approach can also be used for delta connected machines. Each turn is described by an inductance, a resistance and an electromotive force (emf). The short circuit is applied between turns n_a and n_b. The values of the self and mutual inductance as well as the emf are obtained from 3D FEA using Comsol Multiphysics. To minimize computational complexity, each strand is modeled individually and the linked flux is obtained by post-processing the result as described in Chapter 4. The three short circuit types that are considered are indicated: 1, a turn-to-turn short circuit in one strand; 2, a short circuit between two parallel strands around the same tooth; and 3, a short circuit between neighboring conductors of different phases.

A number of assumptions is made:

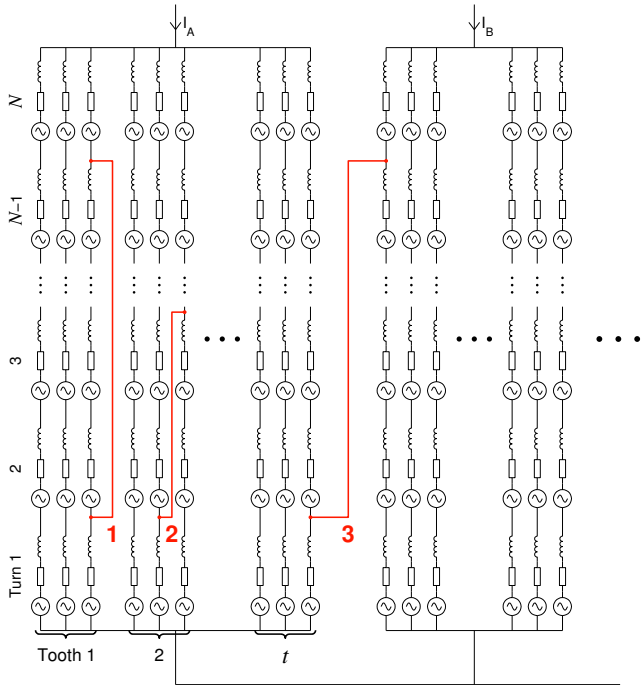

Figure 5.2 Partial machine circuit with parallel strands and teeth, including the following short circuits:
1: turn-to-turn short circuit in one strand;
2: turn-to-turn between parallel strands;
3: turn-to-turn short circuit between two phases.

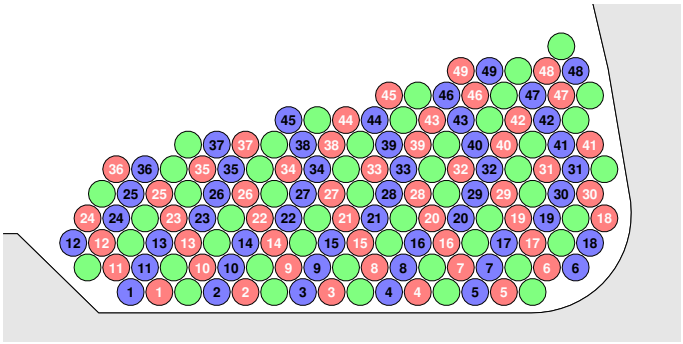

Figure 5.3 Strand and turn locations inside the slot. Blue, red and green turns belong to strands 1, 2 and 3, respectively.

- Only one simultaneous short circuit is considered.
- The external short circuit impedance is described by a resistance with value R_s (in addition to the turn resistance).
- The temperature (resistance) is held constant and fault propagation is not considered. This represents a short circuit immediately after it occurred.
- In the FE models, each turn is modeled as a closed loop. That is, the small diagonal displacements present in an actual winding are ignored.
- The short circuit is assumed to exist, without considering the cause.
- The number of parallel teeth, t, is 6, the number of parallel strands, s, is 3 and turns/tooth N=49.
- The back-emf is sinusoidal.
- The iron is considered to be linear and constant inductance terms are used, based on the fact that a short circuit current opposes the inducing flux.
- Eddy current losses in the winding are ignored.

All combinations in terms of start turn and end turn of the fault will be considered. To this end, the turns are numbered as shown in Figure 5.3. In reality the exact position of each turn can vary by a few strand diameters, changing the short circuit properties, but this approach still allows trends to be identified.

5.2.3 Time-harmonic model

Time-harmonic (frequency domain) models at the synchronous frequency with ideal current source excitation allow a quick estimation of the steady state currents and losses for all short

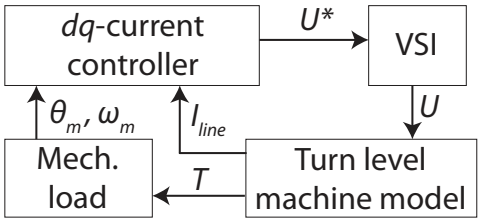

Figure 5.4 Top level transient system model.

circuit combinations of n_a and n_b. The voltage across each turn is given by:

$$\mathbf{u} = \mathbf{R}\mathbf{i} + j\omega\mathbf{L} + \mathbf{e} \tag{5.1}$$

Here, vectors **u** and **i** hold the turn voltages and currents, **R** is the diagonal resistance matrix, **L** the self and mutual inductance matrix and **e** the back-emf vector. By equating the strand voltages for each phase and imposing a total current for each phase, the strand currents can be solved for. The losses per turn are then simply obtained from:

$$\mathbf{p}_{\text{turn}} = \mathbf{R}(\mathbf{i} \circ \mathbf{i}) \tag{5.2}$$

5.2.4 Transient models

Simulink models are used to consider transient behavior, the effect of PWM switching and to model the proposed fault detector. The circuit in Figure 5.2 is re-written to state space form:

$$\frac{\mathrm{d}\mathbf{i}}{\mathrm{dt}} = \mathbf{L}^{-1}(\mathbf{u} - \mathbf{R}\mathbf{i} - \mathbf{e}) \tag{5.3}$$

and combined with either an ideal voltage source inverter (VSI) or a switching VSI, as shown in Figure 5.4. The controller is entirely conventional [118]: the measured line currents are converted to the *dq*-frame where two PI controllers regulate the *dq*-currents by adjusting the *dq*-voltage references. Feed-forward terms for the back-emf and inductive voltage drops are also added. These set points are then converted back to the *abc*-frame. It is assumed that the rotor position is known to the control system and zero-sequence injection is used to maximize the phase to phase output voltages.

The ideal VSI is modeled as a perfect linear amplifier between 0 and the DC-link voltage, having only a delay of 50 µs to somewhat account for the limited bandwidth of an actual power stage, while the switching inverter switches at 16 kHz. In either case, the DC-link voltage is 500 V.

5.3 Analysis of short circuit faults

Now, the various short circuit cases will be compared in terms of severity and the time-harmonic and transient models are compared.

5.3.1 Parametric exploration

Three measures are relevant when considering the faulted copper losses. Firstly, the total losses are important as they determine the expected braking torque and torque ripple (remember that a short circuit is a single phase load, and as such will always cause a 100% torque ripple). Secondly, the maximum losses per turn are relevant because these relate to the localized temperature rise, which in turn determines the time available for detection of the fault. Lastly, if a terminal short circuit is used as safety measure in fault-tolerant or fail-safe applications, the per-turn losses after applying a terminal short circuit are relevant because they indicate how effectively the fault current can be suppressed. These aspects will now be discussed individually for the three short circuit cases shown in Figure 5.2.

Single strand short circuit faults

A short circuit inside a single strand is indicated in Figure 5.2 by number 1 and is the most likely turn-to-turn short circuit to occur in machines with one solid strand.

Figure 5.5(a) shows the total copper losses for this short circuit under nominal load and with a perfect short circuit ($R_s = 0$) for all combinations of n_a and n_b, with the short circuit occurring in strand 1. Refer to Figure 5.3 for the turn and strand numbers. The diagonal in Figure 5.5(a), $n_a = n_b$, indicates that only that turn is shorted. All turn combinations are shown, even though a short circuit will most likely occur for turns directly adjacent to each other inside the slot.

In this example, the maximum total losses are 8 kW and occur for a difference of $|n_a - n_b| = 6$, and are largely independent of the location of the short circuit along the length of the coil. With less turns involved, the turn resistance limits the fault current and a short circuit across more turns leads to linearly increasing losses. For larger $|n_a - n_b|$, the inductance becomes the limiting impedance and both the short circuit current and total losses reduce due to the squared relationship between inductance and the number of shorted turns. As an indication, the single turn impedance at the synchronous frequency is 6.8–8 mΩ + j3–5 mΩ.

Figure 5.5(b) shows the maximum losses per turn for all turn-to-turn combinations. For single turn short circuits, the largest losses are in the range of 1.7—1.9 kW/turn, with current densities in the range of 0.8–1 kA/mm². The electrical position of the short circuit along the strand again has little impact on the magnitude of the losses.

To emphasize these numbers, the initial temperature rise of the shorted turn is in the order of several thousands K/s when assuming adiabatic heating. If a temporary 200 K increase is

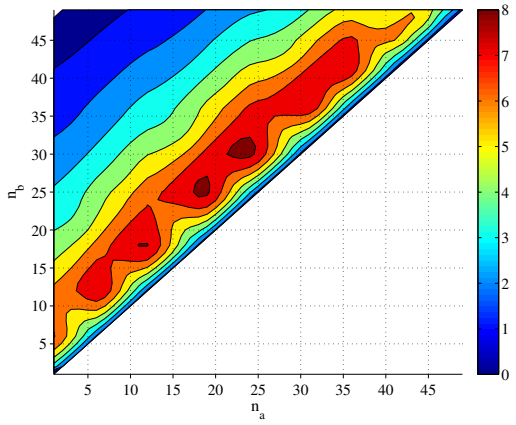

(a) Total losses (kW) under nominal load

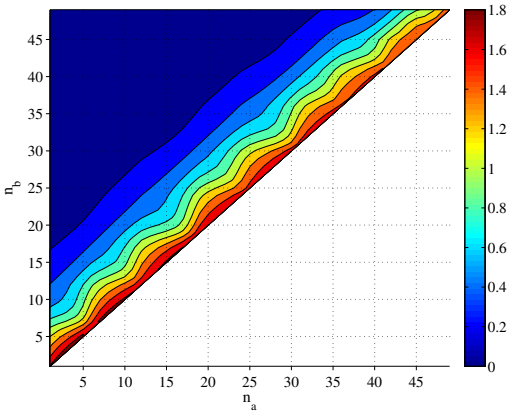

(b) Maximum per strand losses (kW) under nominal load

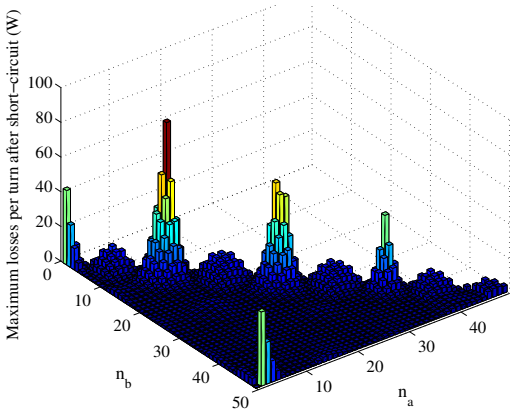

(c) Maximum per-turn losses (W) after mitigation action (terminal short circuit)

Figure 5.5 Copper losses in the presence of a single strand turn-to-turn short circuit, versus start turn and end turn of the short circuit. The axis numbers refer to the turn numbers in Figure 5.3.

acceptable, the available detection time is in the order of 100 ms, or 160 electrical periods. These numbers clearly show that assuming a constant resistance will quickly overestimate the faulted losses. However, the models are still useful to compare all short circuit cases and provide a rough figure for the available detection time. It should be noted that this specific machine has a fundamental frequency of 1600 Hz. Since the turn resistance limits the fault current with very few turns involved, the losses depend on the square of the frequency and in e.g. line-connected machines the temperature rise rate will be considerably lower.

These losses are partially so large because the healthy and shorted parts of the affected strand behave as an autotransformer, with the healthy phase coils on the other five teeth acting as an excitation source, in addition to the PM flux directly linked with the faulted tooth. Therefore, a few amperes from the healthy coils may induce several tens of amperes in the shorted strands, depending on which turns are affected. If the inverter is driving current into the machine, this will even further increase the losses. Note that with a short circuit across nearly all turns (from e.g. 1 to 48 of 49) the losses in the shorted strands are nearly nominal as the inductance is leading in limiting the fault current magnitude. The other teeth of the same phase will however be short circuited by the few remaining turns. Because the impedance of a single turn is far smaller than the impedance of an entire coil, the current is limited by the feeding coils. Hence, increasing the number of parallel machine sections increases the short circuit losses. With 1, 2, 3 or 4 sections, the losses are 2, 11, 29 and 55 W/turn, respectively. This should be kept in mind when machines with a very large number of parallel sections are considered. One solution would be to drive each section from an individual inverter with independent current control.

Strand-to-strand short circuits

A strand-to-strand short circuit between parallel strands around one tooth is indicated in Figure 5.2 by number 2. The fault current is driven by a voltage difference between the turns that come into contact; in an ideal machine, a short circuit between two strands at the same turn does not lead to any fault current. With this specific fault, the short circuit current forms a closed path via the terminals and is therefore limited by the resistance and leakage inductance of each turn encountered. As a result, a short circuit with a turn difference of e.g. five turns will lead to a larger fault current if it occurs between turns 1 and 6 than between turns 20 and 25. In the latter case the total losses may be higher though, as more turns carry the fault current.

Figure 5.6(a) shows the total copper losses for all possible turn-turn combinations between the first two strands. Along the diagonal line $n_a = n_b$ –where the voltage difference between the turns will be minimal– the losses are indeed near zero. When the difference in turn number $|n_a - n_b|$ increases, the fault losses increase as well, indicating that the short circuit current is still (partially) limited by ohmic resistance. The maximum losses are again in the order of 8 kW and occur for $|n_a - n_b|$ =10–13, but only near the electrical middle of the coil.

Figure 5.6(b) shows the maximum per-turn losses. Note the large differences to Figure 5.5(b). The largest loss is now 1 kW, about half that of a single strand short circuit, and only occurs for

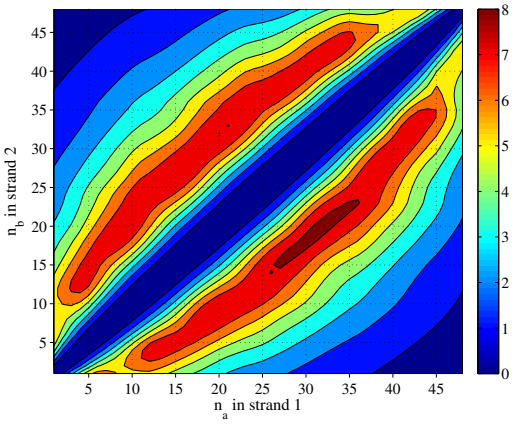

(a) Total losses (kW) under nominal load

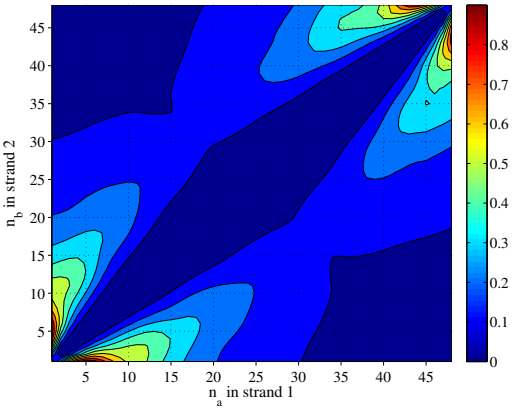

(b) Maximum per turn losses (kW) under nominal load

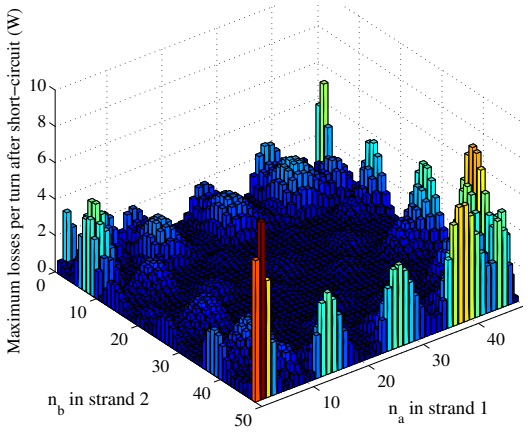

(c) Maximum per turn losses (W) after mitigation action

Figure 5.6 Copper losses versus start turn and end turn of a short circuit between parallel strands around one tooth.

a turn difference of 4–7 turns close to the terminals, which is in line with the explanation given above. The distribution is highly symmetrical about both diagonals, which indicates that only the number of affected turns and electrical distance to the terminals determine the faulted losses, rather than the exact strand that is involved or whether the fault occurs near the neutral or supply side of the coil.

Phase-to-phase short circuits

A phase-to-phase short circuit is indicated in Figure 5.2 by number 3. Proper manufacturing techniques can make the likelihood of this short circuit far smaller than the previous two cases, especially when a single layer fractional pitch tooth-coil winding is employed.

Figure 5.7(a) shows the total copper losses during the fault under rated load. The peak of the total losses is 7.3 kW; almost identical to both other cases, and occurs for $n_a = n_b = 5$. When moving away from the neutral point (increasing n), the total losses decrease strongly. This is caused by the orientation of the fault current and mutual coupling between consecutive teeth, giving a high effective inductance.

The losses per turn are shown in Figure 5.7(b). The maximum losses occur for a short circuit between turn 1 of both phases and are about 1.7 kW. This is more than in the strand-to-strand case, but less than the turn-to-turn case. All in all, phase-to-phase faults are less severe than short circuits within in one coil.

Fault mitigation actions

In safety critical applications a machine should not catastrophically fail, or is even required to continue operating in the presence of faults. Applying a short circuit at the terminals of the affected phase or machine section is a typical approach to meet this requirement, as this approximately equalizes the current in all turns [117]. To estimate the effectiveness of this remedial action for this specific machine, a three phase terminal short circuit was imposed for the three fault cases considered, with the machine being mechanically driven (generator mode).

Figure 5.5(c) shows the worst per-strand losses remaining in the presence of both a single strand inter-turn short circuit and a terminal level short circuit. The highest losses are still 86 W/turn for a short circuit in turn 12, which is a turn located close to the slot-opening, while the average loss is 3 W/turn. Other peaks also occur for short circuits involving strands close to the slot-opening, an effect also described in [89, 117] for single strand short circuits. The cause is an increased leakage flux of strands in the slot back and the effect can be reduced by using strip windings, but at the cost of increased eddy current losses [117]. As an alternative, negative d-axis current exceeding the short circuit current could be injected [116].

Some imbalance exists for parallel strand short circuits (Figure 5.6(c), max 8 W/turn), but it is negligible compared to single strand short circuits. This suggests that having multiple parallel

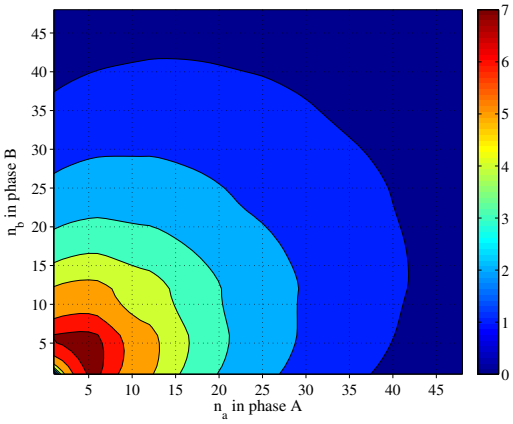

(a) Total losses (kW) under nominal load

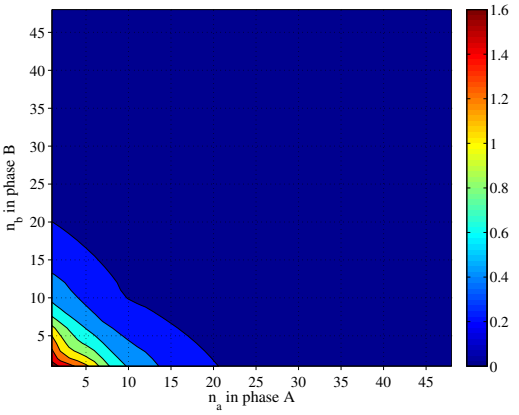

(b) Maximum per turn losses (W) under nominal load

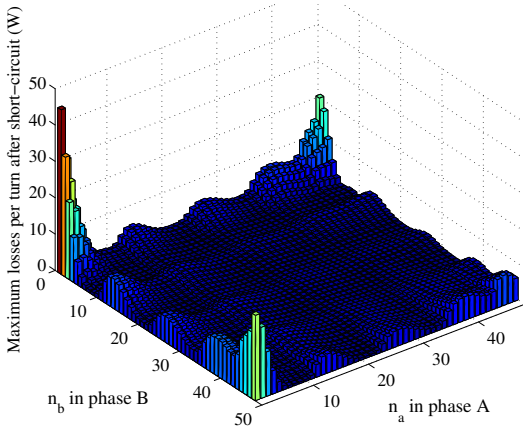

(c) Maximum per turn losses (kW) after mitigation action

Figure 5.7 Copper losses versus start turn and end turn of a short circuit between neighboring phases.

strands or even litz wire increases the post-fault safety aspect of the machine. Finally, phase-to-phase short circuits (Figure 5.7(c)) can still induce 45 W/turn if the short circuits occur close to the terminals.

Summary

Comparing the various short circuits, the following can be said:

- A short circuit between turns of a single strand is the worst case. Without external short circuit resistance, the initial losses can reach 1.9 kW in a single turn. Moreover, the short circuit current is not completely equalized after applying a terminal short circuit, especially for short circuits involving turns close to the slot-opening.
- A turn-to-turn short circuit between parallel strands is less severe: the peak per-strand losses can reach 1 kW and only occur for specific combinations of shorted turns. In addition, good current equalization is obtained after applying a terminal short circuit. The maximum total losses before applying a terminal short circuit are of the same magnitude as a single strand short circuit, but occur for a larger difference in number of shorted turns. This implies a larger physical distance between the turns, which reduces the likelihood of a critical short circuit occurring.
- A turn-to-turn short circuit between neighboring teeth falls between the other two cases in terms of severity. The total peak losses are again in the order of 7 kW, but occur for far fewer short circuit combinations. The worst per-strand losses are 1.7 kW and 34 W without and with a terminal short circuit applied. Because of the medium severity and the fact that this fault can be prevented comparatively easy with tooth-coil windings, it is not considered any further.

5.3.2 Number of parallel strands

The baseline machine is designed with three parallel strands as a trade-off between manufacturability, eddy current losses and fill-factor, but the short circuit losses also depend on the number of parallel strands. This section will consider the effects on the fault losses of using 1–4 parallel strands. The strand and turn placement in the slot for all strand numbers follows the same pattern as for the three strand case given in Figure 5.3.

Figure 5.8 shows the worst total and per-turn losses during a single strand short circuit under nominal load as function of the number of turns shorted (note that the data for the '3 strands' lines is a subset of the data in Figures 5.6(a)&(b)). With just a few turns shorted, the short circuit current will be resistance limited, giving a constant current density. In this case, using less but thicker strands will cause larger losses. With more turns shorted (the threshold depending on R and L, in this case about 4–5 turns), the short circuit current becomes inductance limited, causing a constant current behavior. Now, using less parallel strands becomes a benefit. For this machine, a peak in the worst total losses occurs for a short circuit with 7–12 turns difference,

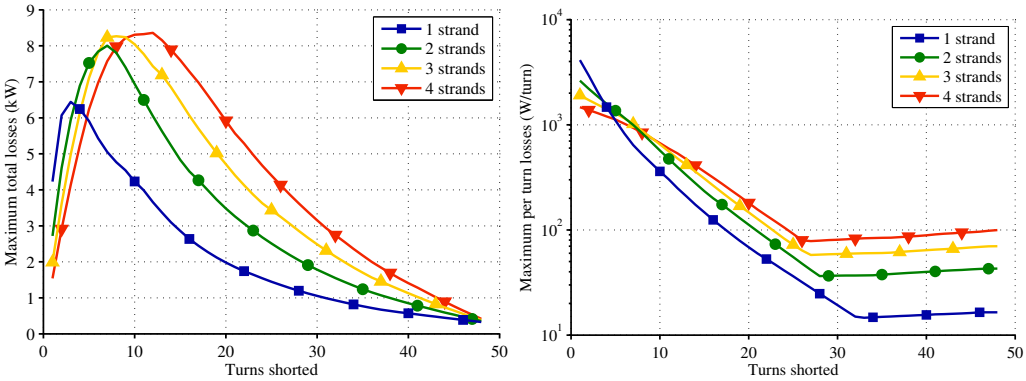

(a) maximum total losses **(b)** maximum per-turn losses

Figure 5.8 Losses as function of shorted turns for different parallel strand numbers and a short circuit across turns of one strand.

slightly depending on the number of parallel strands. When manufacturing the coils, a close proximity of turns separated by this distance should be avoided, although that may be difficult in a layered coil.

As a side note, the 'suddenly' increasing losses beyond 26–32 turns in Figure 5.8(b) are the result of using multiple machine sections connected in parallel. In this case, when a short circuit across a large fraction of a coil occurs, the short circuit will, through the few remaining 'healthy' turns, short circuit the entire phase. As a consequence, those few remaining turns will carry the short circuit current from all other phase coils, and have larger per-turn losses than the directly shorted turns. This could be an argument against using parallel connected phase coils, but do note that the plot is shown on a logarithmic scale: the worst losses under this condition are still an over order of magnitude less than those for a short circuit across only a few turns.

The previous analysis is repeated for short circuit between parallel strands in Figure 5.9. In this case a short circuit across a small number of turns causes far less losses (and even negligible losses with 0 turns difference), while a peak exists around 4–6 turns difference. This peak is however still lower than with a single strand short circuit. For a short circuit across many turns, constant current behavior applies and fewer parallel strands will again gives less losses per-turn and less total losses.

Whether or not to use parallel strands from a safety perspective is therefore a non-trivial question. In a coil wound with regular layers, consecutive turns are often in close physical proximity, which increases the likelihood of a short circuit across just a few turns and hence suggests the use of more parallel strands. However, a short circuit between consecutive layers is less severe with fewer parallel strands. Additional insulation between winding layers could reduce the occurrence of this specific short circuit, but at the cost of copper area and thermal conductivity. When also

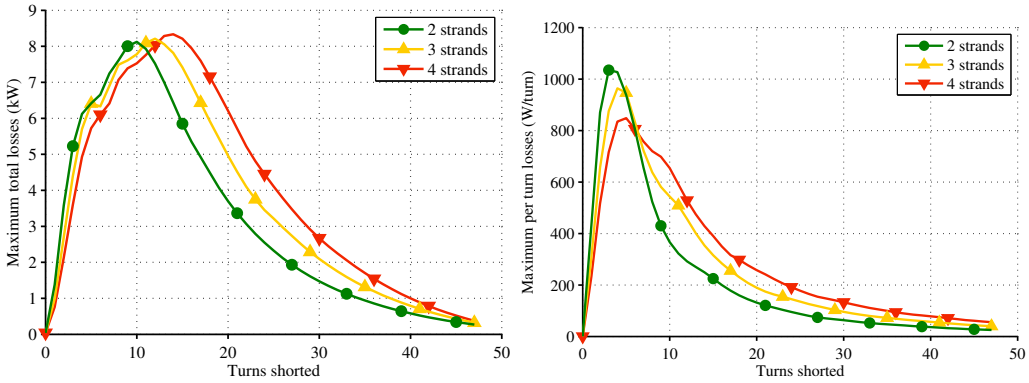

(a) maximum total losses **(b)** maximum per-turn losses

Figure 5.9 Losses as function of shorted turns for different parallel strand numbers and a short circuit between parallel strands.

considering that a short circuit between parallel strands can be neutralized more effectively with a terminal short circuit, using more parallel strands is perhaps desirable from a safety viewpoint, although it should be kept in mind that using more parallel strands increases the chance of a short circuit occurring.

5.3.3 Closed loop drive model

A few of the short circuit cases are now analyzed with the transient circuit model to consider the effects of real current controllers and PWM switching.

Figure 5.10 shows the results for a single strand short circuit being applied across turn 24 (2% of the coil) at t=0.1 s. Subfigure (a) shows the line-neutral voltage of phase A. Since the currents are controlled and the short circuit reduces the apparent impedance and back-emf in that phase, the terminal voltage will reduce, but for this specific short circuit, the reduction is only 4%. Subfigure (b) shows the *dq* line currents. Until the short circuit occurs, the currents predicted by the continuous and switched model show good agreement and are constant, but during the short circuit the limited bandwidth of the controllers causes an AC component in the *dq* currents at twice the fundamental frequency, which could be used as fault indicator [119]. Subfigure (c) shows the current through the shorted turn. The RMS current in the shorted turn computed by the continuous and switched source models is 483 A and 486 A, respectively, indicating that the ripple in the short circuit current does not significantly increase the losses for this short circuit case. The time-harmonic model predicts a current of 487 A.

Figure 5.11 shows the same quantities, but for a single strand short circuit across turns 24–34 (20% of the coil). The fault current is now mainly inductance limited and therefore has a much larger

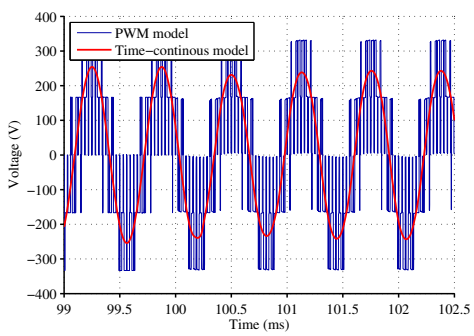

(a) Phase A line to neutral voltage

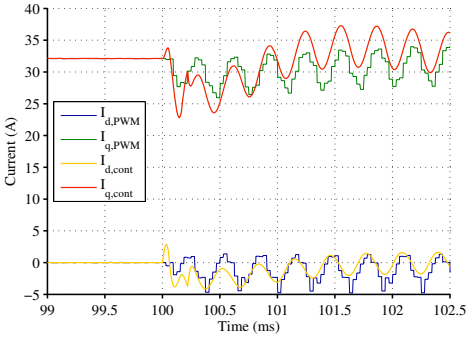

(b) *dq*-currents

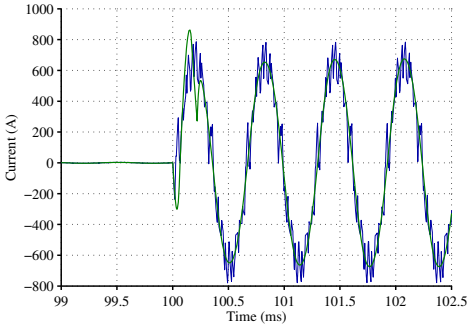

(c) Current in shorted turns

Figure 5.10 Selected system signals under nominal load, with a single strand short circuit being applied in phase A across turn 24 at t=0.1 s

impact on the magnetic fields inside the machine. The reduction in terminal phase voltage is significant, as is the increase in the *dq*-current ripple. The RMS current through the shorted turns is 294 A, 341 A and 270 A, computed by respectively the continuous time model, switching model and time-harmonic model. The increased coupling between the faulty and healthy part of the coil causes an increased ripple in the fault current that can no longer be neglected. The discrepancy between the system models and the time-harmonic model is caused by the poor regulation of the currents in the system models, which shows that the interaction between the machine and inverter cannot be neglected under all circumstances. If nearly the entire winding is shorted, the time-harmonic model may underestimate the current by 50%.

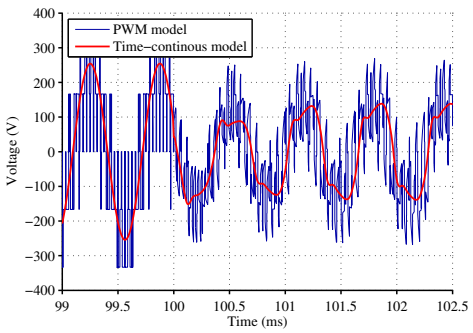

(a) Phase A line to neutral voltage

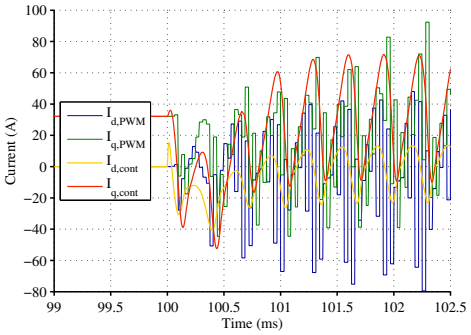

(b) *dq*-currents

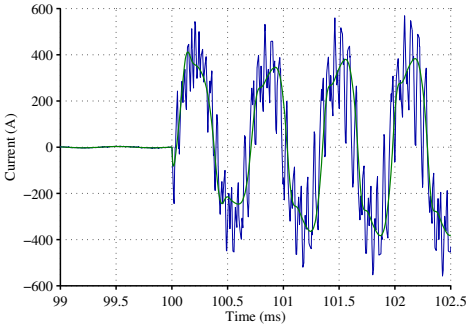

(c) Current in shorted turns

Figure 5.11 Selected system signals under nominal load, with a single strand short circuit being applied in phase A across turns 24–34 at t=0.1 s

5.4 Turn-level short circuit current measurement

Rudimentary experiments are now performed to validate part of the short circuit current calculations.

5.4.1 Test setup

The prototype starter/generator (to be fully presented in Chapter 7) was equipped with two additional wires around two different teeth to mimic single turn short circuits. Due to the risks involved, this was preferred over modifying the actual winding. The wires have diameters of 1 mm and 2 mm diameter, with measured resistances of 8.7 mΩ and 4.6 mΩ, and represent smaller and larger faults, respectively. The inductance of both turns is about 650 nH, approximately twice that

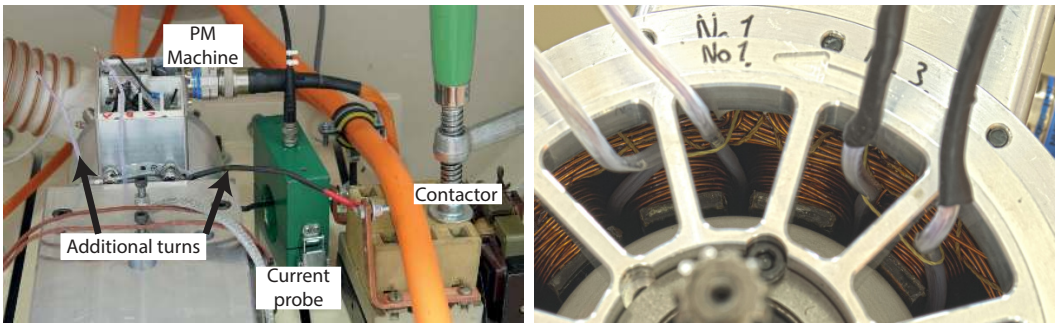

Figure 5.12 (a) Test setup showing the prototype starter/generator machine with two additional short circuit turns, a contactor and a current transformer; (b) detail of the short circuit turns.

of a normal turn due to the additional external length. Only one short circuit is applied at any time, for a predetermined safe duration using a mechanical contactor outside the machine. No further impedance is added to limit the fault current, which is measured with a current transformer and logged on an oscilloscope. Figure 5.12 shows the described test-setup.

5.4.2 Results

Figure 5.13 shows the initial short circuit current density versus speed. The *initial* short circuit current density is considered, because the current noticeably reduces (with e.g. 10% over 0.1 s in the thin wire at nominal speed) due to heat-up of the wire. The additional impedance of the external relay and connection leads never allows the fault current to be completely limited by the turn resistance. As a result, the thin wire shows the largest current density under all conditions. At nominal speed the measured initial current density is 451 A_{rms}/mm^2, while the worst case predicted in section 5.3.1 reaches 1 kA_{rms}/mm^2. Considering that the measurement setup approximately doubles the inductance of the circuit, this result suggests that the losses and current densities predicted in section 5.3 are realistic.

Figure 5.13 also shows the initial short circuit current density with a three phase short circuit applied at the terminals. This should ideally reduce the fault current density to the average winding current density (11 A_{rms}/mm^2), but depending on the position of the shorted turns in slot, larger current densities may remain. In this case, the current densities in the thick and thin wire are reduced by 3.6 and 13 times to 40 and 33 A_{rms}/mm^2, respectively. This is a consequence of the position of the extra turns close to the slot opening, as discussed in Section 5.3.1.

The short circuit current in the separate turns was also simulated with 2D models, with the extra end-winding inductance of the main winding included. Figure 5.14 shows one of the solved

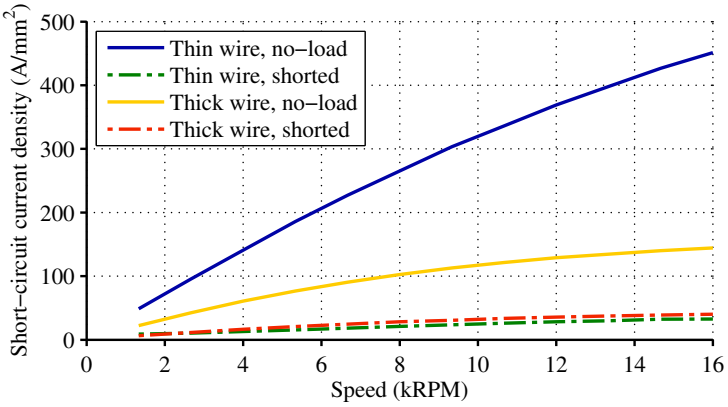

Figure 5.13 Measured short circuit current density versus speed in the thin and thick wires, under open circuit and terminal short circuit conditions.

FE models. Table 5.1 summarizes the simulated and measured short circuit current densities at nominal speed. The largest error, a threefold overestimation, occurs for the thin wire with a terminal level short circuit applied. This error can be reduced by adjusting the position of the simulated turn and the assumed external impedance, but due to a lack of information, this is not done. A more important result is that a shorted turn close to the slot-opening will have a higher than nominal remaining fault current density after application of a terminal level short circuit.

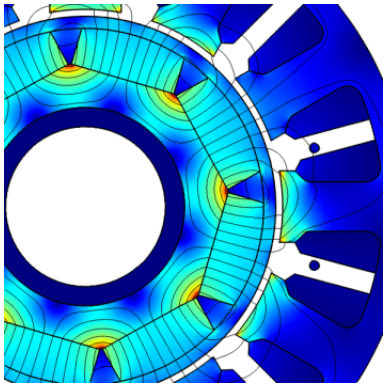

Figure 5.14 Field distribution with a terminal short circuit applied and a separate shorted turn.

Table 5.1 Short circuit current densities (A/mm²) in the separate wires at nominal speed, simulated and measured

	Simulated		**Measured**	
Terminals	Open	shorted	Open	shorted
Thin wire	424	97	451	33
Thick wire	177	42	144	40

5.5 Consequences of short circuit faults

The previous section considered the short circuit currents and losses immediately after occurrence of the short circuit, but did not address how the fault could progress if no action is taken. This section will investigate the propagation of unmitigated faults, focussing on the following topics:

Ultimate failure mode The ultimate failure mode is defined as the steady state reached when all failure propagations have occurred, but with any voltage or current excitation still present.

Time to initial failure (T_{IF}) This aspect is particularly relevant for the design of fault detection systems, as it gives upper limits for the available detection time. In addition, under high overloads the time to failure can be predicted using the thermal capacity and current density. These experiments provide confirmation of such predictions.

Emissions Due to the high temperatures involved, smoke, fire or liquid materials may be ejected from the coil. Knowledge on this aspect is needed to design a proper enclosure for the coil or machine.

Predictability If the failure behavior is sufficiently consistent, it can be taken into account during the design stage to ultimately create more reliable machines.

5.5.1 Test setup

This section details the test and measurement setup used for the experiments. Figure 5.15 schematically shows the setup. A stepwise DC current source is used because this corresponds best with instantaneous short circuits in electrical machines. The wire current is measured through a shunt resistor and the wire voltage is measured with a differential probe to exclude any voltage drop across the connectors. The voltage and current are logged on a 12 bit oscilloscope for further processing.

The coils are wound on a ceramic coil former, as this material can withstand high temperatures. A winding machine is used to ensure a consistent wire tension, but the strand is only fixed to the former at the ends. During heat up, it may therefore expand and detach from the former. All tested coils have three layers and about 100 turns. An untested coil is shown in Figure 5.16. The tests are conducted in a closed chamber to capture smoke and ejected particles as well as preventing undesirable air flow. The coil is suspended in air to minimize interaction with the surroundings.

The wire tested is 0.8 mm diameter round copper wire according to IEC 60317-13 and NEMA MW 35 (Magnetemp® CA-200, grade 2). This wire is intended for high-temperature operation up to 200 °C and can withstand temporary overloads to 240 °C [120].

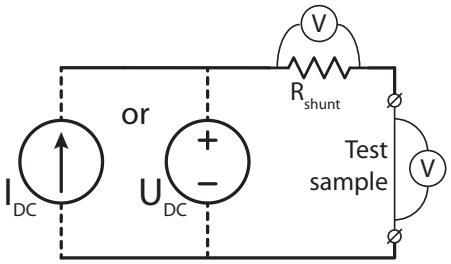

Figure 5.15 Schematic of the test setup. Only a current source is used in this work.

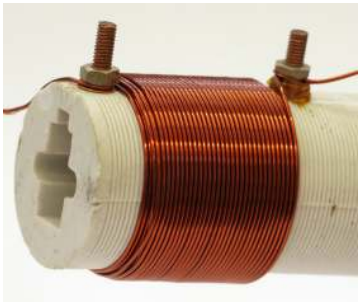

Figure 5.16 Untested three layer coil on ceramic former.

5.5.2 Results

Time to initial failure

Figure 5.17 shows the coil resistance versus time for four different terminal currents, derived from the terminal voltages and currents. Multiple traces per current level are shown to demonstrate the differences between coil samples due to e.g. manufacturing. For clarity, the traces are truncated after initial failure to avoid clutter. The time between applying the current step and initial failure (T_{IF}), clearly recognized by a sudden drop in voltage caused by interlayer short circuits, is surprisingly consistent. The terminal resistance has increased almost threefold just before the initial failure, implying an *average* coil temperature rise of about 450–500 K.

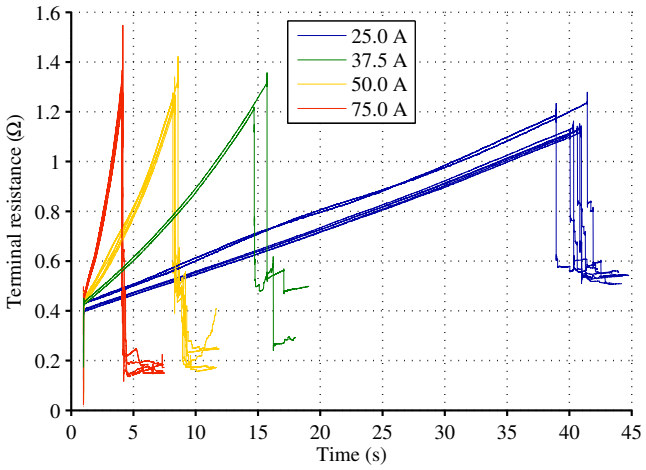

Figure 5.17 Coil voltage resistance versus time under constant current excitation.

Figure 5.18 shows the distribution of T_{IF} versus current level for the various coil samples. The consistency of the T_{IF} increases with current magnitude, suggesting that this is a purely adiabatic process at higher currents, as was to be expected. To confirm this assumption, an elementary thermal model was created, accounting only for the resistive losses, copper specific thermal capacity and dependency of copper resistivity on temperature. The T_{IF} obtained with this model using a threshold temperature of 1100 K is also shown in Figure 5.18. The adiabatic model predicts a six times resistance increase at the time of failure, while only a three times increase is measured. This discrepancy is attributed to an unequal heating of the three layers in the actual coil; the layer closest to the former will initially stay cooler due to the heat capacity of the former. Generally though, this shows that for large current densities a simple adiabatic model can be used to accurately predict the time to failure, but it does need to be calibrated to the specific coil geometry.

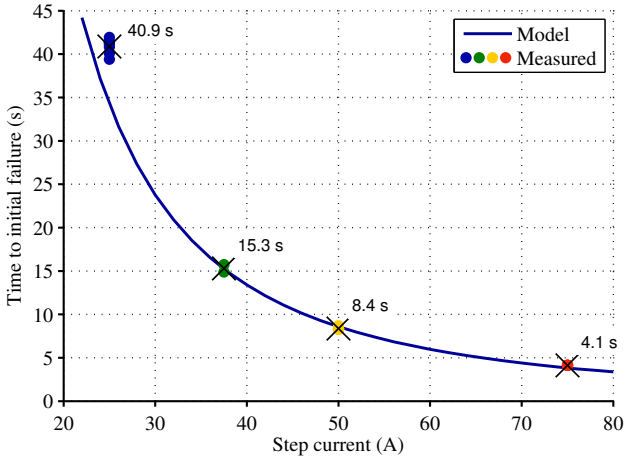

Figure 5.18 Time to initial failure (T_{IF}) versus step current magnitude.

Fault progression

Figure 5.19 shows a detail of the resistance versus time in the first seconds after the initial failure occurred. In all cases the resistance reduces in smaller stepwise changes after the initial larger step. In this period, inter-turn and inter-layer contacts are formed. The exact magnitude and time of occurrence of the individual steps varies (this phase is a somewhat stochastic process), but after 1.2 s and 0.3 s for respectively 50 A and 75 A (initially 100 A/mm² and 150 A/mm²), all coils reach a similar low resistance state, with a terminal resistance lower than the initial resistance. This suggests that the failure behavior immediately following the initial failure is also fairly predictable.

The ultimate steady state behavior of faulted coils depends entirely on the environment, e.g. core material acting as heat sink, presence of forced cooling, or the medium surrounding the coil.

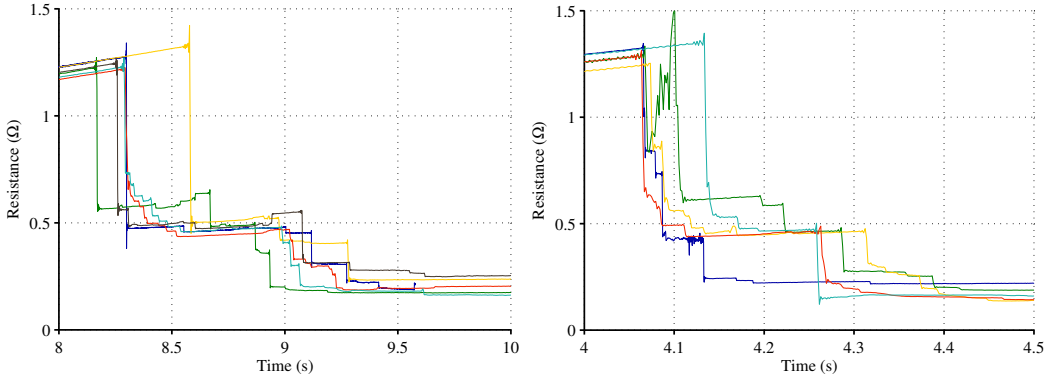

(a) 50 A **(b)** 75 A

Figure 5.19 Coil resistance versus time immediately after initial failure. Different lines correspond to different coils.

Hence, the results on the steady state behavior presented here will only be an indication.

Figure 5.20(a) shows the coil resistance over a longer period of time for a terminal current of 25 A. All but one coil show similar behavior over the course of 6 minutes, with a sharp but repeatable decrease in resistance after 250 s. It is suspected that this is related to insulation failure of the bottom layer, which is cooled via the coil former. Figure 5.20(a) shows the coil resistance for a terminal current of 50 A. At this current, one out of 6 coils failed to an open circuit after 36 s, while the other coils sustained this current for at least 90 s, when the test was stopped. With a terminal current of 75 A, all samples failed to an open circuit within 10–17 s, typically with electrical arcs occurring and liquid copper drops being ejected, potentially damaging the coil surroundings. Inspection of the samples showed that all failures occurred at the connection terminals, thus not providing fully realistic data.

These results show that short circuits between the coil layers can reliably be formed at moderate current densities, reducing the effective current density and allowing the coils to sustain larger terminal currents. Although the coils did repeatedly fail at 75 A, this failure occurred near the connection terminals. To realistically determine the failure behavior after the initial failure for larger initial current densities, more elaborate setups will be necessary, using e.g. magnetically induced currents.

The above results allow some predictions about fault progression in PM machines to be made. Short circuits in PM machines across few turns are typically resistance limited, allowing a maximum current density to be determined, based on per-turn resistance and induced voltage, from which the time to failure can be estimated. Machines with a high per-turn voltage will therefore exhibit a faster failure process. As the fault spreads after the first failure, more turns (conductor area) will carry the fault current and the current will become inductance limited (ie. the fault

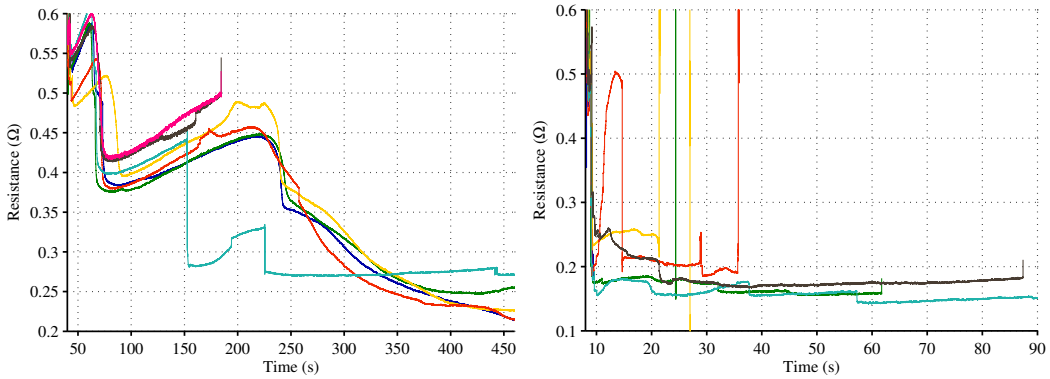

(a) 25 A **(b)** 50 A

Figure 5.20 Coil resistance versus time after initial failure. Different lines correspond to different coils, some measurements were stopped early.

current fully opposes the inducing flux), reducing the local current densities. The reduction in locally dissipated power will slow down this process. It is therefore not unlikely that a steady state is reached where parts of the coil carry a current, but guaranteeing that a minimum fraction of turns carries this current (to impose a maximum on the power loss) will be difficult.

5.6 Fault detector: concept

This section proposes a synchronous fault detector and investigates its performance, using the circuit models and machine presented in Section 5.2.

5.6.1 Detector description

The goal of the fault detector is to measure the voltage difference between the machine and supply neutral voltages, at the synchronous machine frequency. This neutral voltage spectrum contains many harmonics, including many PWM related harmonics and the third harmonic of the fundamental frequency when using zero sequence injection, but the synchronous harmonic will only be non-zero if the machine in not balanced. For small imbalances, such as single-turn short circuits, the synchronous neutral voltage will be small, so it is necessary to properly filter this signal.

Refs. [101–103] also consider the difference between the supply and machine neutral voltage, but propose a tunable band-pass filter or a Fourier transform to determine the fundamental

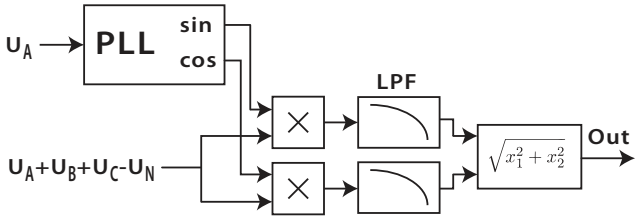

Figure 5.21 Block level model of the proposed fault detector.

component, which are complex to implement. Instead, ref. [119] uses the amplitude of the 2nd harmonic in $u_{dq,ref}$ as measure of imbalance, and applies synchronous detection to determine the amplitude. Although this requires no additional hardware and few processor cycles, the close integration with the controller can pose a safety issue.

Synchronous detection is based on the property that when a signal is multiplied with a signal of frequency ω_{shift}, the signal is shifted in the frequency domain by ω_{shift}:

$$f(t)a^{j\omega_{\text{shift}}t} = \hat{f}(\omega - \omega_{\text{shift}}) \tag{5.4}$$

where $f(t)$ is an input signal and $\hat{f}(\omega)$ its Fourier transform. By choosing ω_{shift} equal to a frequency of interest, that frequency shifts to dc. The amplitude of the signal can then by obtained by a simple fixed low-pass filter. If the frequency of interest changes, only ω_{shift} needs to be adjusted. The advantage of this approach is that narrow low-pass filters are simpler to implement than equally narrow adjustable band-pass filters.

The key elements of the actual fault detector are shown in Figure 5.21. The difference between the machine neutral voltage and the inverter neutral voltage (created with three equal impedances) is multiplied with the sine and cosine of the fundamental frequency and the result is low pass filtered, squared and added. This performs amplitude detection around the synchronous frequency with the bandwidth of the low-pass filter. A phase-locked loop (PLL) is used to obtain the fundamental frequency independently of the motor controller.

The drawback of the topology proposed here is that it cannot identify faults; it merely provides an indication of the system imbalance. Still, this topology is chosen because it can be implemented in relatively simple microcontrollers and can operate as an independent observer of a drive system, which is beneficial in safety critical applications.

5.6.2 Basic operation

To demonstrate the fault detector operation, a single strand short circuit is applied across turn 24 of the first strand and coil of phase A (arbitrarily chosen) at t = 0.1 s, with the machine operating under nominal conditions. Figure 5.22(a) shows the computed machine neutral voltage. The time-continuous model clearly shows the triangular voltage at $f = 3f_e$, with f_e the fundamental

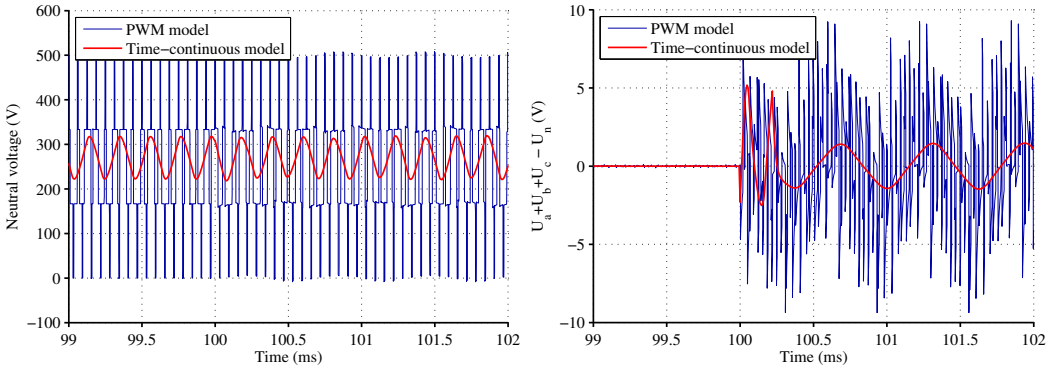

(a) Absolute voltage **(b)** Neutral voltage difference

Figure 5.22 Machine neutral voltage computed with two models. A short circuit is applied at t = 0.1 s.

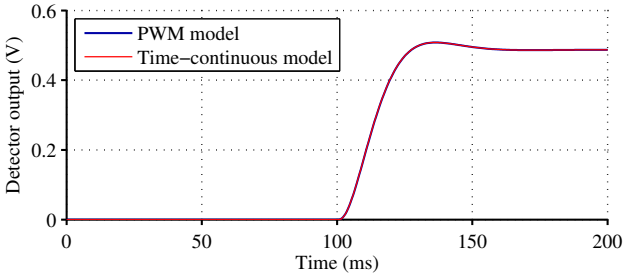

Figure 5.23 Simulated detector output.

electrical frequency, due to zero-sequence injection. The difference between the two neutral voltages is shown in Figure 5.22(b). After the fault occurs a fundamental component exists, and in the case of PWM also sideband harmonics at $f = f_s \pm 2kf_e, k = 1,2,3,\ldots$, with f_s the switching frequency, because the machine is imbalanced at all frequencies. Note that the difference voltage can be small with respect to the zero-sequence component. In this specific case 0.8 V on a 45 V signal, or 1.8%. This implies that the subtraction hardware should have adequate common mode rejection. The output of the detector is shown in Figure 5.23; both models give a nearly identical response, since only the fundamental component is considered by the detector. Because of the good match between the ideal and PWM VSI models and the fact that the ideal VSI model runs about ten times faster, the ideal VSI model is used for the remaining simulations.

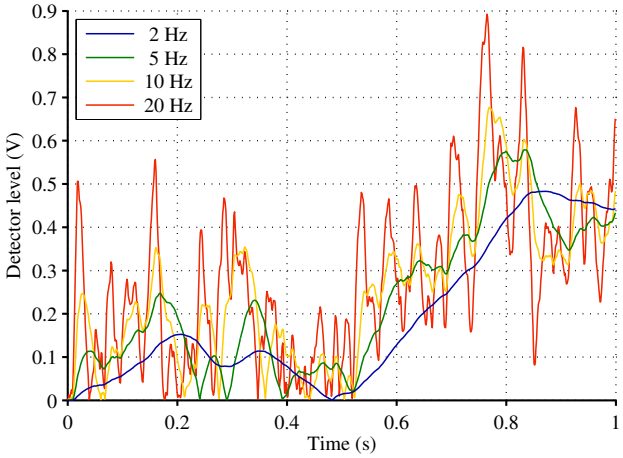

Figure 5.24 Simulated detector output in a noisy system for multiple detector bandwidths. A single turn short circuit is applied at t = 0.5 s.

5.6.3 Low pass filter tuning

The cutoff frequency and, to a lesser degree, the order of the two low pass filters are the only critical parameters that affect the performance of the detector, and directly represent the trade-off that needs to be made for any fault detector: a high cutoff frequency allows a quick detection of faults, but also makes the detection more susceptible to noise and essentially reduces the sensitivity.

To demonstrate this effect, white noise is added to the simulated neutral voltage and the detector response is computed for different bandwidths, using fourth order Butterworth filters. The effect of interfering signals, such as unintended supply grid leakage, will be similar in nature. Figure 5.24 shows the detector responses for increasing bandwidths with a single turn short circuit applied at t = 0.5 s. This specific fault can only reliably be detected with a bandwidth of at most 5 Hz. The detection time is in the order of 0.25 s, which can already cause damage to the machine. In a following section, experiments are performed to determine the impact of noise in an actual system.

5.6.4 Fault detection performance versus short circuit position

Figure 5.25 shows the detector output level range versus the number of shorted turns for a single strand fault and the shorted turns difference for a parallel strand fault. For a given number of shorted turns, the detected imbalance varies due to the position of the short circuit along the coil, as indicated by the shaded areas of possible fault levels. With a short circuit across a given number

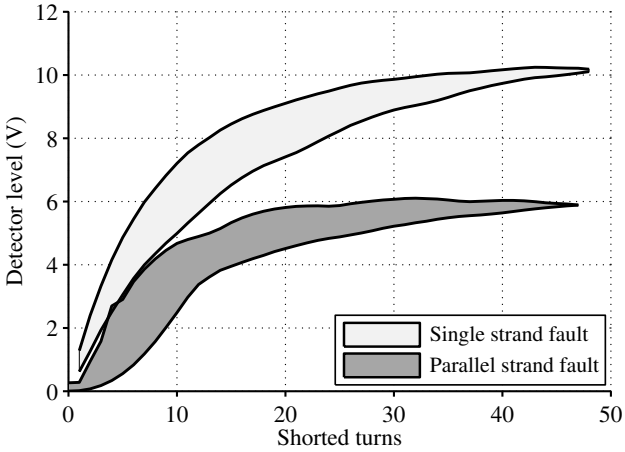

Figure 5.25 Detector output level range versus shorted turns.

of turns, the lower range of the detector output occurs for short circuits close to the slot opening. This is somewhat unfortunate, since it was shown earlier that those faults also exhibit the highest short circuit current densities. This is inherent to the nature of the short circuit though, and any fault detection scheme will suffer from this. A final important observation in Figure 5.25 is that a short circuit between parallel strands causes roughly half the detector output compared to a single strand fault.

Ideally, high losses in the machine lead to high detector output to enable fast detection of the fault. Figure 5.26 shows the detector level versus the total copper losses for a single strand short circuit, which indeed increases with increasing total losses. This figure also shows that resistively and inductively limited fault currents can both cause e.g. 2 kW of total losses, but the detector output is larger in the latter case. Figure 5.27 shows the detector output versus the maximum per turn losses. Unfortunately, the detector output decreases with increasing per-turn losses.

5.6.5 Open circuit faults

The machine under consideration has 18 parallel strands per phase (3 per tooth) and an open circuit fault of one strand is not immediately critical (the copper losses will increase by $\frac{1}{17}$), but may indicate the start of a larger fault and detection is still desirable. The detectability of open strand failures is therefore considered.

Table 5.2 summarizes the detector output when one, two or all three parallel strands of one coil are disconnected. With two of the three strands disconnected the detector output is 0.05 V, still below any of the short circuit faults. Only the disconnection of a complete tooth produces a strong error indication. This was to be expected, since at nominal speeds the voltages in the machine

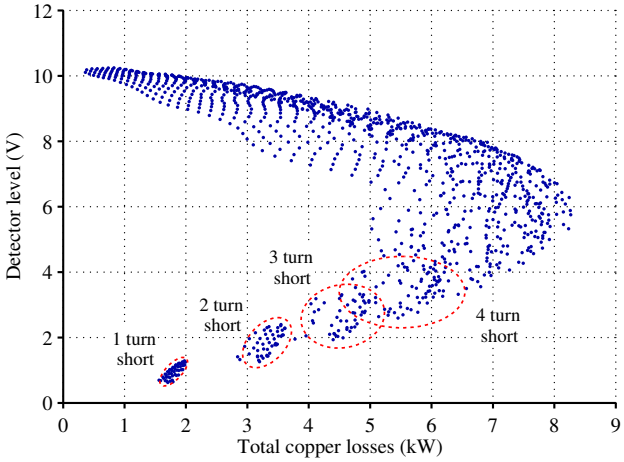

Figure 5.26 Detector output versus total copper losses for a single strand short circuit.

Table 5.2 Simulated fault detection level for various faults

Failure	Level (V)
Single turn turn-to-turn short circuit	0.48–1.2 V
Ten turn turn-to-turn short circuit	5–7 V
One open strand	0.013 V
Two open strands	0.051 V
Three open strands (full tooth)	1.5 V
Partial demagnetization	~0 V
Dynamic rotor misalignment	~0 V
Static rotor misalignment	0.021 V

mainly depend on the back-emf and phase inductance, neither of which significantly changes when one or two parallel strands disconnect.

5.6.6 Other faults

Partial demagnetization

Large negative d-axis currents, high temperatures, overspeed situations or manufacturing faults may lead to partial magnet failure, ie. situations with differing pole magnetization. This introduces additional harmonics in the machine emf and attenuates the synchronous emf.

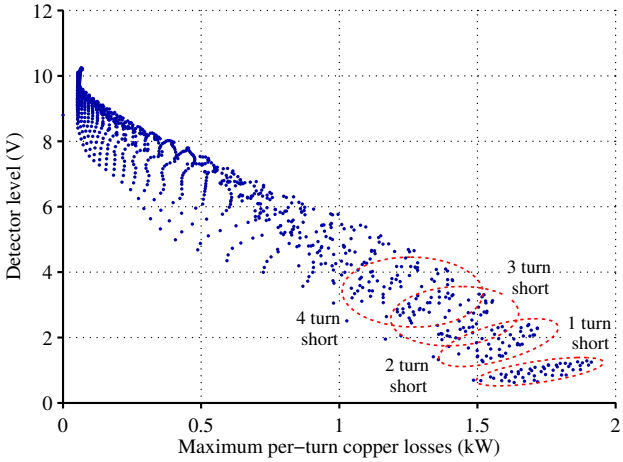

Figure 5.27 Detector output versus maximum per turn copper losses for a single strand short circuit.

Since the proposed detector only measures the fundamental frequency voltage, lower or higher order harmonics will not be detected, provided that the additional harmonics fall sufficiently outside the passband. The fundamental emf amplitude will reduce, but since the machine remains balanced at the fundamental frequency, this will not lead to detector output. To validate this, a model is created having one partially demagnetized pole, as shown in Figure 5.28. The simulation indeed predicts no output, which is also summarized in Table 5.2. Note that by changing the detector center frequency to one of the additional emf harmonics, this fault can be detected.

Mechanical faults

The most common mechanical fault is a bearing failure, which causes misalignment between rotor and stator [109]. Rotating misalignment, where the position of the shorter airgap side is fixed with respect to the rotor, induces additional lower and higher order harmonics in the machine emf and circulating currents between any parallel connected phase coils. This failure mode is highly similar to partial demagnetization. With static misalignment, the position of the shorter airgap side is fixed with respect to the stator. No additional harmonics appear in the emf, but the magnitude of the emf will differ between the phases, leading to some imbalance and thus fault detector output. The largest three phase imbalance occurs for a two pole machine, because this maximizes the difference in relative rotor displacement between the phases.

To estimate the detected imbalance levels, a model of a misaligned machine is created, using coil field flux linkages obtained from a FE model with static or rotating offset. An offset length of 70% of the mechanical airgap length is used. Figure 5.28 shows the field flux linkages versus rotor angle for one coil. Table 5.2 summarizes the simulated fault detector level. As expected, rotating

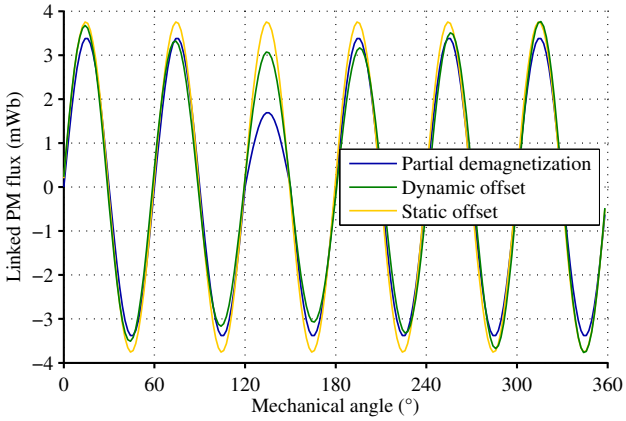

Figure 5.28 PM field flux linked with one tooth coil versus rotor position for three mechanical faults.

misalignment does not produce significant detector output. Static misalignment produces output an order of magnitude smaller than a single turn turn-to-turn short circuit. This demonstrates that the proposed method cannot readily detect mechanical failures.

5.7 Fault detector: experimental validation

The fault detector concept will now be experimentally validated. To this end, two different machines will be used: the prototype high-speed starter/generator machine also considered in sections 5.2–5.4, to demonstrate basic performance on a high-speed machine; and an industrial off-the-shelf machine, to analyze the detection capability of small faults and compare the natural imbalance of identical machines.

5.7.1 Test on the prototype machine

Test setup

To perform the test on the starter/generator, the same setup described in Section 5.4.1 and Figure 5.12 is used again. In addition, for tests under motor operation, a standard two-level IGBT inverter is used, switching at 18 kHz. The fault detector is implemented on a dedicated circuit board, shown in Figure 5.29, which scales the voltages and filters the switching harmonics before final processing using a TI TMS320F28069F microcontroller.

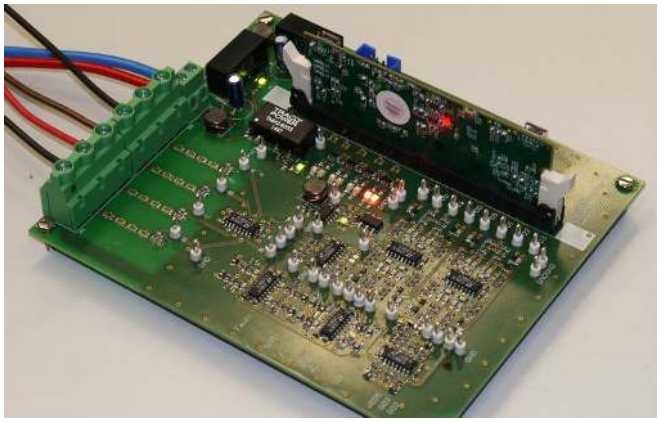

Figure 5.29 Prototype fault detector circuit.

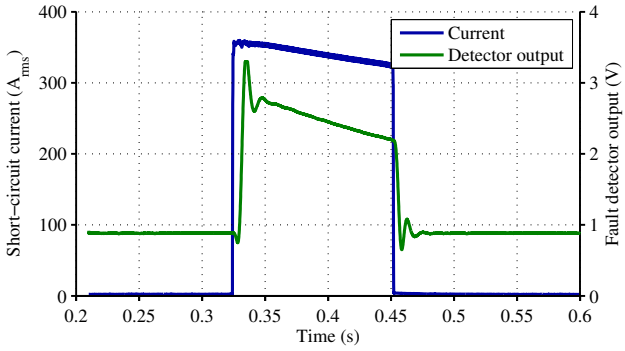

Figure 5.30 Measured short circuit current and detector output versus time, for a short circuit in the thin wire at nominal speed.

Fault detection

First, a 0.13 s short circuit during no-load, steady state, nominal speed operation is considered, using the thin wire to create the short circuit. Figure 5.30 shows the short circuit current and detector output around the short circuit. A fourth order Chebyshev type II filter with 80 dB stopband attenuation at 500 Hz is used. The fault is clearly detected, with a delay of 6 ms. Observe that the fault indication level is non-zero even when no fault is present, which is the result of natural imbalance, ie. small differences between the phases in machine properties, inverter components and detector circuit. Further notice that the reduction of short circuit current over time also reduces the detected imbalance level, as one would expect.

The dependency of the imbalance level on the operating conditions is also demonstrated in

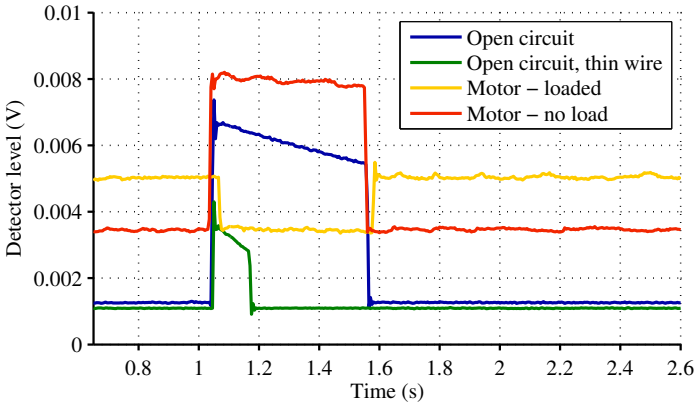

Figure 5.31 Measured detector output level at rated speed during various operating modes.

Figure 5.31, which shows the detector output under various operating conditions at nominal speed. Between no-load generator mode, no-load motor mode and loaded motor mode, the detected imbalance during healthy conditions increases and even exceeds the detected level of imbalance during a small fault under no-load conditions. Moreover, under loaded motor operation the detected imbalance level reduces during a fault. This suggests that to detect small faults under all conditions, more involved approaches may be required, such as using a lookup table of the healthy system imbalance. It should be noted that this is not specific to this system, since any imbalance can be seen as a fault and may trigger a fault detection system.

Finally, the detector performance during a speed ramp of 1300 RPM/s is considered. For proper detection during speed transients, the PLL should be able to track the motor frequency to within the filter bandwidth. Hence, a low filter bandwidth requires a more accurate and faster PLL. Figure 5.32(a) shows the machine speed. The short circuit, applied between t=0.5–1 s with the thicker wire, slightly disturbs the machine speed due to the instantaneous additional losses. Figure 5.32(b) shows the short circuit current and detector output. Unlike the steady state case, the increasing frequency compensates the current reduction due the increasing resistance, leading to an approximately constant fault current. The fault detector correctly detects the fault throughout the entire short circuit, although both the healthy and faulted imbalance level increase with speed, as pointed out earlier.

5.7.2 Test on the industrial machine

Setup

Additional tests are performed on commercial off-the-shelf PM machines to determine the detection performance of small faults and compare the healthy imbalance of identical machines.

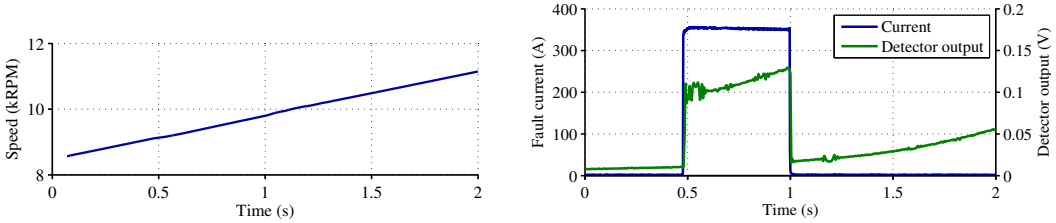

Figure 5.32 Fault detection during speed transients: (a) machine speed; (b) short circuit current and fault detector output.

Table 5.3 Commercial test machine specifications

Property	Specification
Type	SEW K37 DY71S
Rated power (S1)	0.8 kW
Rated speed	3,000 RPM
Rated current	2 A_{rms}
Short circuit current	6.2 A_{rms}
Layout	36 slots, 6 pole, single layer
Stack dimensions	40.5 × 110 mm (l×dia)
Wire diameter	0.7 mm

Table 5.3 provides the details of the tested machines. Figure 5.33(a) shows one machine with five additional taps on the winding to create various short circuits, as indicated in Figure 5.33(b). The smallest short circuit covers 0.4% of the winding, based on DC resistance. For this machine the detector algorithm is run in a realtime Simulink model, because this allows greater flexibility in comparing filters and storing measured signals.

Detection of small faults

Figure 5.34 shows the detector output versus time for a two filter bandwidths and a small fault (0.4%, taps 4&5) and larger fault (2.2%, taps 3&5). Firstly, this graph demonstrates that a short circuit across 0.4% of the winding can be detected, although the margin is small (40% detection level increase). Secondly, it is a clear demonstration of the trade-off between detection sensitivity and speed. For example, if a warning is issued above a detection level of 0.3 V, a large fault (taps 3&5) can be detected correctly within 8 ms using a 100 Hz bandwidth, but a small fault is not detected at all. With warning level of 0.15 V small faults can also be detected, but only with a low

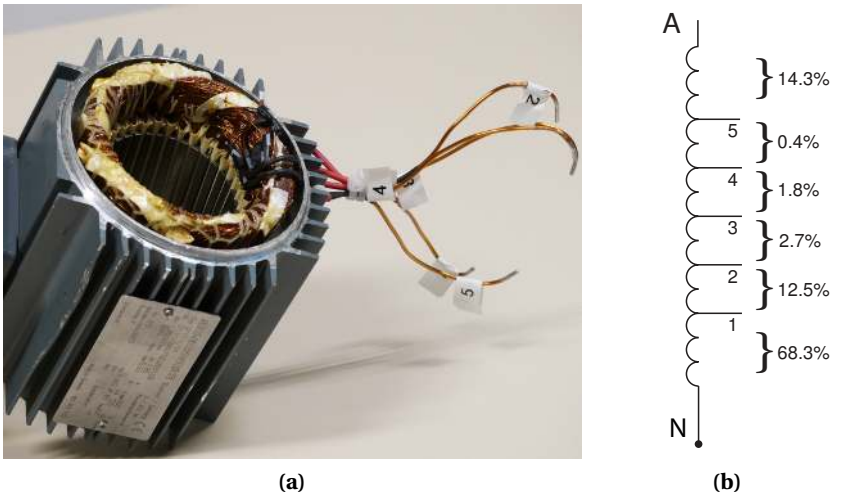

Figure 5.33 (a) Photo of the commercial test machine with additional taps; (b) relative location of the taps.

bandwidth to avoid false positives due to noise. The detection time is now in the order of 100 ms. This problem is partially fundamental in nature, and will apply to any detection scheme.

Speed and load dependency

As with the starter/generator machine, the detector output will vary with speed, i_d, and i_q, amongst other factors, both for a healthy and faulted machine. Figure 5.35 shows the healthy and faulted detector output and the ratio between those versus speed for a fault between taps 4&5. The increase of the imbalance level when going from no load to full load exceeds or equals the increase due to a short circuit in no-load. Moreover, the variation of the imbalance level with speed has the same order of magnitude. The relative output level, which can be seen as an indication of the detectability, slightly decreases with an increase in machine load, suggesting that fault detection is more difficult in heavily loaded machines.

These results indicate that detection of the 0.4% fault requires a very carefully designed system. On the other hand, the detection level during a larger 2.2% fault (tap 3&5, see Figure 5.34) exceeds any of the changes due to speed and load variations. So, by sacrificing some sensitivity, a much simpler fault detection scheme could be considered.

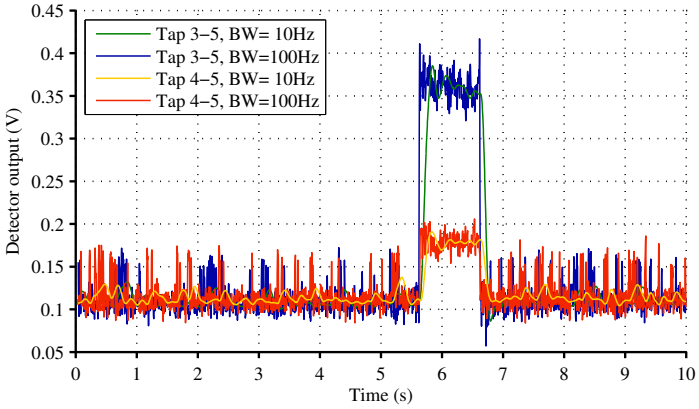

Figure 5.34 Measured detector output for two short circuits and two detector bandwidths. During t=5.6–6.6 s a short circuit is applied.

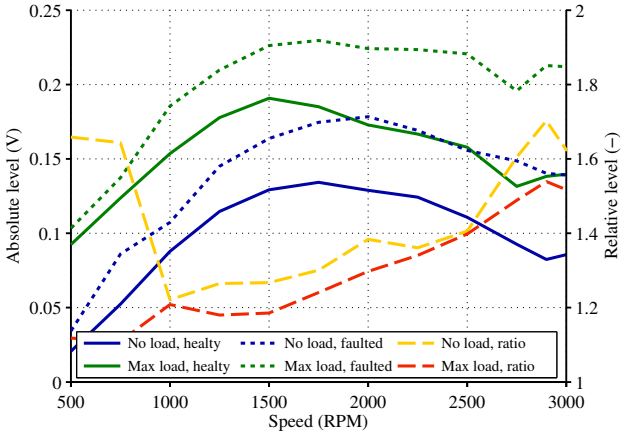

Figure 5.35 Measured detector output for a short circuit between taps 4&5.

Natural imbalance

Previous sections have shown that even a healthy machine can exhibit an imbalance level larger than the change caused by short circuits across a small fraction of the winding. To obtain an impression of the natural imbalance between identical production machines, the healthy detector level of four machines is measured. All six possible phase connection orders per machine are compared, because the inverter imbalance also affects the natural imbalance.

Figure 5.36 shows the healthy detector output versus speed. The measured imbalance is asym-

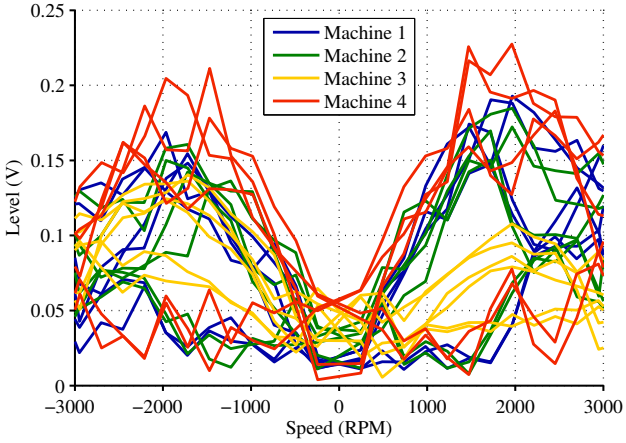

Figure 5.36 Healthy level detector output for all possible connection orders for four different machines of one type.

metrical for forward and reverse rotation; for unidirectionally operated machines, the sensitivity can be maximized by using the phase order with the smallest healthy imbalance. In a production environment, where pairing machines with inverters is undesirable, such an approach is infeasible. Fortunately, the maximum measured imbalance is comparable for all machines and a possible solution would be to use a slightly higher warning level, again sacrificing sensitivity for less complexity.

5.8 Conclusion

This chapter focussed on turn-level short circuit faults, covering all areas including modeling, analysis, progression, detection and mitigation.

To analyze the effects of inter-turn faults, idealized but fast time-harmonic as well as more realistic but slower transient circuit models were used. The properties of each turn were obtained from 3D FEM, so that all turn-turn combinations can be considered, fully accounting for the position of the fault inside the slot. Important observations are that, when increasing the number of parallel strands the *total* faulted copper losses do not significantly change, but the worst case *per turn* losses do decrease and occur for fewer turn-turn combinations. Because faults between parallel strands can also be better suppressed with a remedial three phase terminal short circuit, using parallel strands may be beneficial in safety critical applications. Furthermore, faults near the slot-opening lead to higher losses, and are more difficult to suppress with a remedial terminal short circuit.

The idealized time-harmonic circuit model was compared to transient circuit models of a com-

plete closed loop drive system, using either an idealized VSI or switching VSI. It was found that for short circuits across a small fraction of the winding, all models yield highly similar numbers. This shows that involved models are not necessary to estimate the worst case current densities. With larger parts of the winding short circuited, neglecting the limited bandwidth of actual current regulators and the switching nature of real VSIs will cause an underestimation of the losses, although in practical cases this is unlikely to cause any issues.

A further observation is that single-turn short circuits remain resistance limited up to very high speeds. This implies that turn-to-turn faults in high-speed machines can be more severe than in line frequency machines. Experiments on the starter-generator underline this, with measured fault current densities up to 450 A_{rms}/mm^2, still partially being limited by the measurement setup. This highlights the need for a fast fault detection system in safety critical applications.

Brief experiments were performed to determine the basic failure behavior of coils in the presence of unmitigated faults. Three layer dummy coils were subjected to a current step until steady state breakdown was achieved. Important observations include that at moderate initial current densities, the inter-layer contacts formed due to failing insulation allow the coil to carry higher currents for extended periods of time; and that at high current densities, a simple adiabatic thermal model can predict the time to initial breakdown.

Lastly, a fault detector is proposed that can provide an indication of the three phase system imbalance, based on synchronous detection of the machine and inverter neutral voltage difference. The main benefit is the simplicity of implementation. The concept was demonstrated on two different machines, showing that short circuits across 0.4% of the winding can be detected with a carefully designed detector system. The design of this fault detector entails two tradeoffs: one, the detection speed is fundamentally limited by noise; that is, detecting smaller faults requires more time. Two, imbalances in practical systems cause fault detector output during healthy conditions of a similar order of magnitude as small faults, leading to a tradeoff between a simple but less sensitive system on the one hand, and a more involved and more sensitive detection system on the other hand. These considerations apply to any fault detection system to some degree.

Concerning the detectability it is shown that short circuits between parallel strands are more difficult to detect than single strand short circuits. In the case of parallel strands, open-circuit faults are even more difficult to detect, but are also far less dangerous. Short circuits across a given number of turns are more difficult to detect if they occur close to the slot-opening. This is somewhat unfortunate, as those faults also exhibit the highest losses. Mechanical faults or partial demagnetization cannot be detected without changes to the proposed detector.

CHAPTER 6

Analysis of additional losses due to PWM induced current ripple

The previous chapters of this thesis occasionally considered the problem of matching a machine to an inverter, but considered only the primary aspect: relative inductance. The impact of the current ripple caused by the pulse width modulated inverter output voltages was neglected. This brief chapter considers the impact of this current ripple on the rotor losses, iron losses and winding losses. These losses are calculated for one machine, allowing their relative magnitude to be compared. A different, larger machine is used instead of the S/G to better highlight the potentially large losses.

Based on

- M. van der Geest, H. Polinder, and J. A. Ferreira, "Influence of PWM switching frequency on the losses in PM machines," in *Int. Conf. Electrical Machines (ICEM)*, 2014, pp. 1243–1247.

6.1 Introduction

Electrical machines are increasingly used in combination with an inverter due to obvious benefits, such as energy savings or improved dynamic behavior. One of the side effects of inverter driven machines is a high frequency current ripple, which induces additional losses in all parts of the machine. If these additional losses are neglected during the design stage, the machine may run warmer or even fail in operation.

The magnitude of the current ripple depends on three factors: firstly, it is inversely proportional to switching frequency, secondly, it is inversely proportional to the machine inductance and lastly, it is proportional to the dc-link voltage. When designing a complete drive system, at least some care should taken to optimize these factors. Not only can this minimize the current ripple, it can also reduce the total system size and/or inverter rating, ultimately saving cost.

The effect of the current ripple on the iron losses has received considerable attention in e.g. [121–124]. Compared to an ideal sinusoidal supply voltage, using a PWM power supply increases the losses only marginally (10-20%) if the switching frequency and modulation index are sufficiently high. At high modulation indexes but low switching frequencies, only a small loss increase of about 15% occurs, compared to high switching frequencies. With a decreasing modulation index, which implies an increase in dc-link voltage and current ripple, the additional iron losses at low switching frequencies can exceed 50%. This emphasizes the importance of a good match between the machine voltage level and dc-link voltage. As a side note, although many models have been proposed to accurately compute iron losses under various conditions, they are of limited use because a large spread in actual iron losses can exist, even between identical motors [125].

The high frequency current ripple also induces losses in the machine windings. In a machine with parallel strands (bundles) inside the coils, four components can be recognized (as explained in Chapter 4): skin and proximity effects inside individual strands, and skin and proximity effects between parallel strands [63, 126]. At the strand level, the skin-effect can be ignored if there are many strands inside a slot, as the proximity effect will dominate. At bundle level, the variations in (leakage) inductance between strands are often far greater than variations in linked magnet flux, and the proximity effect can be ignored instead. Due to these effects, the distribution of high frequency currents in the strands and bundles, as well as the corresponding AC/DC loss ratio, can be significantly worse than for the fundamental current component. In [57] up to 15% additional losses are reported due to PWM switching. In [127] it is however demonstrated that the use of litz wire removes the dependency on switching frequency.

High frequency stator currents also create asynchronous airgap harmonics, which induce rotor eddy current losses. At lower frequencies the induced currents are resistively limited and the losses depend on the square of both the frequency and field strength. At higher frequencies, the skin-effect provides shielding, limiting the loss increase [127, 128].

This chapter considers the additional losses as function of switching frequency with a case study on a 500 kW machine (ie. not the starter/generator). Losses in the stator laminations, windings

(proximity and unequal current sharing) and rotor are considered. Ultimately, this demonstrates the sensitivity of these loss sources to the current ripple.

This chapter is structured as follows: the first section presents the system model that is used to obtain the current ripple. In the following sections, this ripple is used to compute the additional lamination, winding and rotor losses, respectively.

6.2 System model

6.2.1 Introduction

A Simulink model of the complete drive system, containing the machine, inverter and closed loop *dq*-current control, is used to obtain an estimate for the current ripple. Note that this approach assumes that the machine impedance is independent of frequency, which is true if the magnitude of the eddy currents is sufficiently small. A conventional six-switch inverter with ideal switches and dc-link voltage is assumed. The controller is a sampled time, continuous amplitude system, consisting of two PI-controllers to regulate the *dq*-currents. The machine is connected in star and modeled in the *abc*-domain, with the inductance matrix and shape of the PM flux linkage obtained from 2D FEM, while the phase resistance is based on the winding dimensions. A single constant inductance matrix is used; saturation or high-frequency effects are ignored. Asynchronous carrier based PWM is used, with zero sequence injection to maximize the use of the dc-link voltage.

The geometry of the machine is shown in Figure 6.1. The machine is a 72 slot, 12 pole single layer distributed winding surface mounted PM machine, rated for 500 kW. The stator winding consists of 5 turns/coil with 25 parallel strands/turn to reduce AC-winding losses and facilitate manufacturing, but the strands are not intentionally twisted or displaced. The rotor has a non-conductive non-magnetic retaining sleeve and laminated back iron. Further details are provided in Table 6.1.

6.2.2 Current ripple

The machine currents are computed under nominal load in steady state for dc-link voltages of 450 V (well matched to the machine emf) and 650 V (higher than needed). Figure 6.2 shows the three phase currents in the time and Figure 6.3 in the frequency domain, for a low and high switching frequency and U_{dc}=450 V. The typical spectrum can be recognized, with harmonics occurring at $f = mf_s \pm nf_e$, where $m, n = 1, 2, 3, \ldots$ and f_s and f_e are respectively the switching and fundamental frequency. At f_s=3 kHz the peak ripple harmonic has an amplitude of 5.6% of the fundamental. At 12 kHz, the worst peak reduces to 1.4%.

In the following sections, these current trajectories are used as input to the loss calculations.

Table 6.1 System specifications

Property	Specification
Rated power	500 kW
Rated speed	1800 RPM
Rated current	1100 A
Inductance	0.25 pu
Winding	72 slots, 12 poles, single layer 5 turns/coil, 25 parallel strands
Laminations	M270-35A
Magnets	μ_r = 1.05, ϱ=1 $\mu\Omega$m, B_r = 1.16 T
Ideal losses	Lamination: 4.8 kW Windings: 4.5 kW Rotor: 600 W

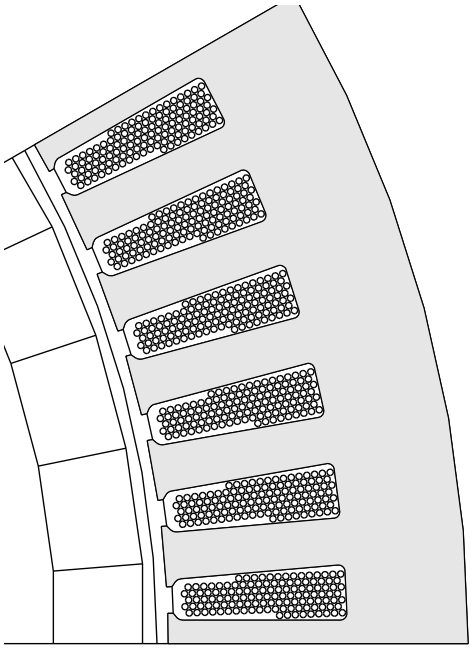

Figure 6.1 Machine geometry.

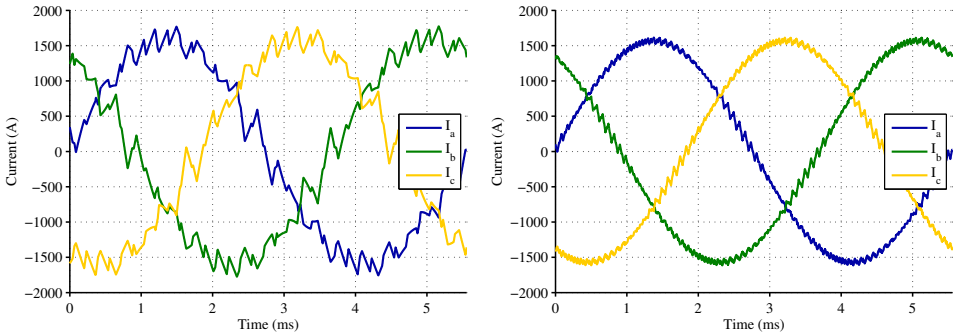

Figure 6.2 Phase currents with U_{dc}=450 V: (a) f_s=3 kHz; (b) f_s=12 kHz.

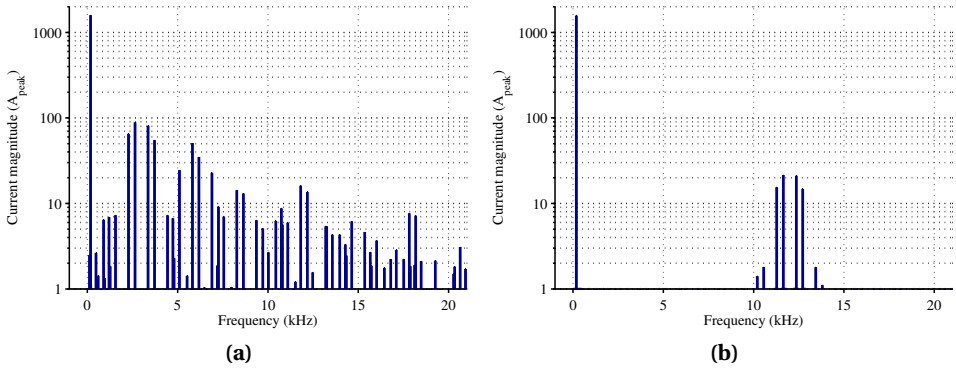

Figure 6.3 Phase current spectra with U_{dc}=450 V: (a) f_s=3 kHz; (b) f_s=12 kHz.

6.3 Stator lamination losses

The effectiveness of laminations reduces at higher frequencies, potentially leading to higher losses. This section attempts to quantify the additional losses. To this end, the field distribution is computed over one electrical period for every time harmonic in the current, including the synchronous harmonic. The field distribution is converted to the loss distribution and integrated over the lamination volume to obtain the total losses. Given that the non-synchronous harmonics are small compared to the fundamental harmonic and occur at higher frequencies (Figure 6.3), only the eddy current loss component is computed for those harmonics, while at the synchronous frequency the PM field is also included and both hysteresis and eddy current losses are computed. The eddy current losses are computed with two functions as means of confirmation. Firstly via a function fitted to manufacturer data, using separate terms for the hysteresis and eddy current components, and secondly via an analytical approach based on the lamination thickness and resistivity [129].

Figure 6.4 shows the additional iron losses as function of switching frequency and dc-link voltage. Firstly, the expression fitted to manufacturers data corresponds well with the theoretical expression. Secondly, as expected from other works, the increase in iron losses seems insignificant. Compared to the ideal iron losses (4.8 kW), the worst case increase is only 16%, which occurs for f_s=3 kHz and a dc link voltage of 650 V. Generally, the dependency on the switching frequency is far smaller than the dependency on the dc-link voltage.

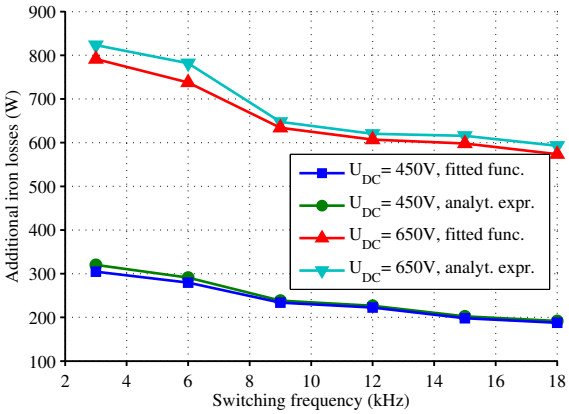

Figure 6.4 Additional iron losses due to the current ripple as function of switching frequency and two dc link voltages.

6.4 Winding losses

This machine is wound with 5 turns/coil, each turn having 25 parallel strands, but without intentional strand twisting or displacements. Using parallel strands possibly introduces imbalanced currents inside the windings, with the extent of the imbalance strongly depending on layout of the strands (straight or twisted/displaced) and operating frequency, as demonstrated in Chapter 4. At higher frequencies the effect is typically stronger and a large harmonic content in the current may thus induce large losses. In addition to imbalanced currents, 'regular' proximity losses in individual strands may also occur, but those depend solely on the strand thickness.

This section will analyze the additional losses due to both causes. The current distribution across the parallel wires can be evaluated in two ways, either completely with time-harmonic or transient FEA, or by extracting the inductance matrix at turn level from a FE calculation, and solving time-harmonic or transient circuit equations using this inductance matrix, as described in Chapter 4. The latter is obviously much faster and used here, but assumes a single, constant value for all inductance terms, while FEM can also account for strand level skin- and proximity effects.

Figure 6.5 shows the position of each strand and turn inside one slot. For simplicity, all slots are assumed to be wound identically. The fill factor obtained is 0.47 and a 2D model is used.

6.4.1 Current imbalance

As a first step, the current imbalance is computed with the inductance matrix method, the result of which is shown in Figure 6.6. The inductance is based on 2D FEM data, but the wire resistance (length) is adjusted to also account for the end-winding copper losses. This adjustment shifts the point where the wire currents start to diverge by a few 100 Hz to higher frequencies. At high frequencies a significant imbalance exist due to the bundle level skin-effect: some strands carry 20 times the DC current, while other strands carry almost no current. Note that thermal effects

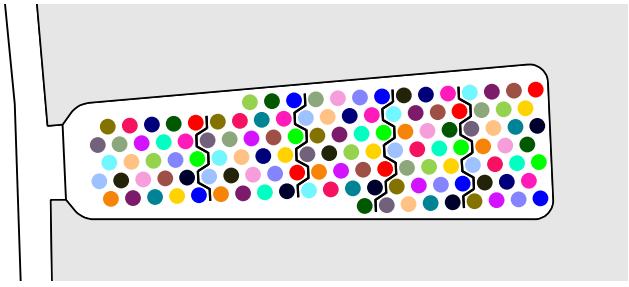

Figure 6.5 Strand and turn positions inside one slot. The black edges indicate boundaries between turns, while each color represents one specific strand.

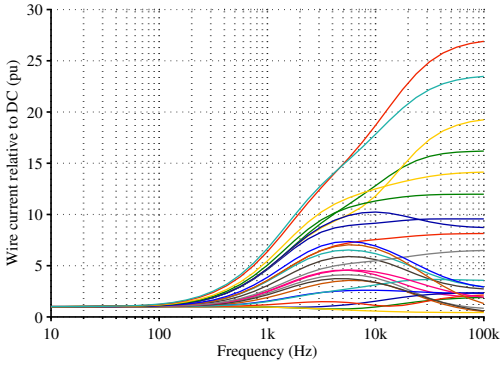

Figure 6.6 Strand current distribution relative to the ideal DC-distribution. Each line represents one strand.

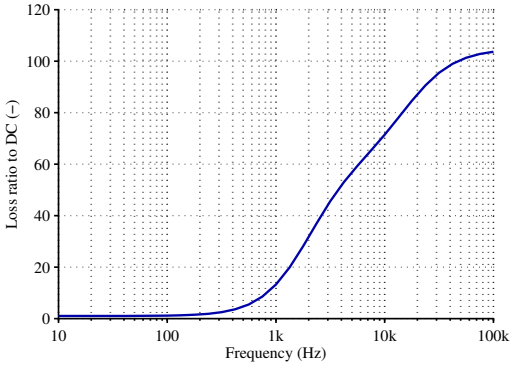

Figure 6.7 Loss ratio compared the ideal DC-distribution.

and end-winding inductance were not included; in reality both will act to equalize the current distribution.

Figure 6.7 shows the associated loss increase due to the unequal current sharing compared to the ideal DC distribution. At the fundamental frequency, the AC/DC loss ratio is about 1.5, which could be improved by displacements or twists inside the slot. At 3 kHz, the AC/DC loss ratio is about 40, which indicates the loss potential for high-frequency currents.

Figure 6.8 shows the additional losses due to the unequal division of the high frequency ripple currents, obtained by combining the current spectrum (Figure 6.3) with the AC/DC loss ratio (Figure 6.7). At f_s=3 kHz and dc-link voltages of 450 and 650 V, the switching ripple causes 2.2 kW and 4.5 kW of additional losses, respectively, on ideal fundamental DC-losses of 4.5 kW. Using a higher switching frequency is beneficial, since this linearly reduces the ripple amplitude (and thus quadratically the loss contribution), while the AC/DC loss ratio saturates at higher frequencies. These results show that if parallel strands are used in combination with a low switching frequency, care should be taken to sufficiently twist or displace the strands.

6.4.2 Induced losses (classical proximity effect)

The copper losses due to the proximity effect are computed using 2D FEA. Note that the winding AC losses mainly occur inside the stack, which is the only part considered here.

Figure 6.9 shows the winding proximity losses versus switching frequency. Some proximity losses occur at the fundamental frequency. At f_s=3 kHz, 730 W, or 16% of additional proximity losses occur. The proximity losses depend more strongly on the dc-link voltage than on the switching frequency, compared to the losses due to unequal current sharing.

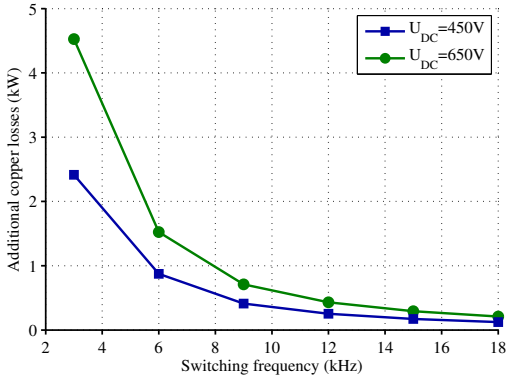

Figure 6.8 Additional copper losses due to ripple currents unequally dividing over parallel strands.

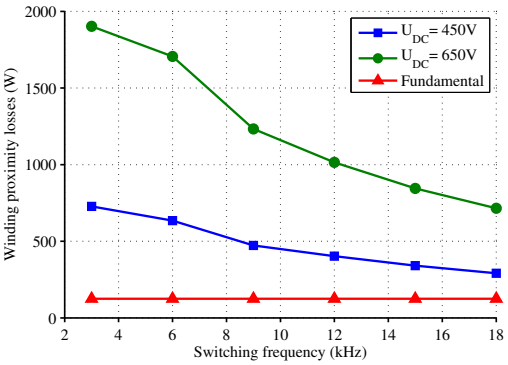

Figure 6.9 Additional copper losses due to the proximity effect.

6.5 Rotor eddy current losses

Harmonics in the machine supply current also create pulsating or asynchronously rotating space harmonics in the airgap, which induce eddy current losses in the conducting parts of the rotor. This section analyzes these additional losses. To this end, accurate transient FEM simulations (with a fine mesh and small time-steps) with and without supply current harmonics are compared. A large insight can be obtained by considering one time harmonic at a time, but this is very time consuming and not undertaken at this point.

Figure 6.10 shows the instantaneous total magnet losses over 1/3 of the electrical period, for multiple switching frequencies. The switching harmonics can be recognized from their pulsation frequency, which is approximately twice the switching frequency. Figure 6.11 shows the average total magnet losses versus switching frequency for two dc link voltages. Increasing the switching frequency strongly reduces the losses: at f_s=3 kHz and 15 kHz the rotor losses are respectively nine and two times the losses with ideal stator currents. Besides increasing the switching frequency (which to some extent shifts the losses to the inverter), the rotor losses could of course also be reduced with magnet segmentation.

Figure 6.12 shows the average loss distribution inside the magnets for f_s=3 kHz and 9 kHz at U_{dc}=450 V. Note that the magnets are tangentially segmented in three pieces. At the higher switching frequency, the losses are concentrated near the surface of the magnets (the skin-effect is already pronounced for this harmonic), while at f_s=3 kHz the losses occur over the entire magnet height.

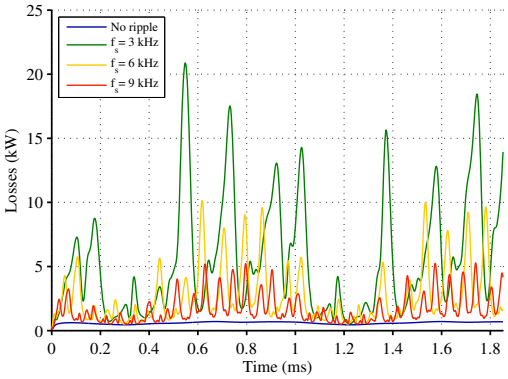

Figure 6.10 Instantaneous rotor losses for various switching frequencies, U_{DC}=450 V.

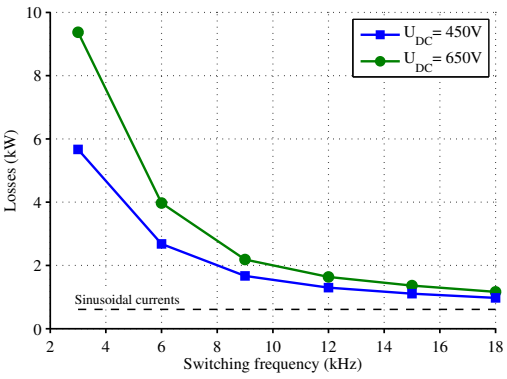

Figure 6.11 Rotor losses as function of switching frequency.

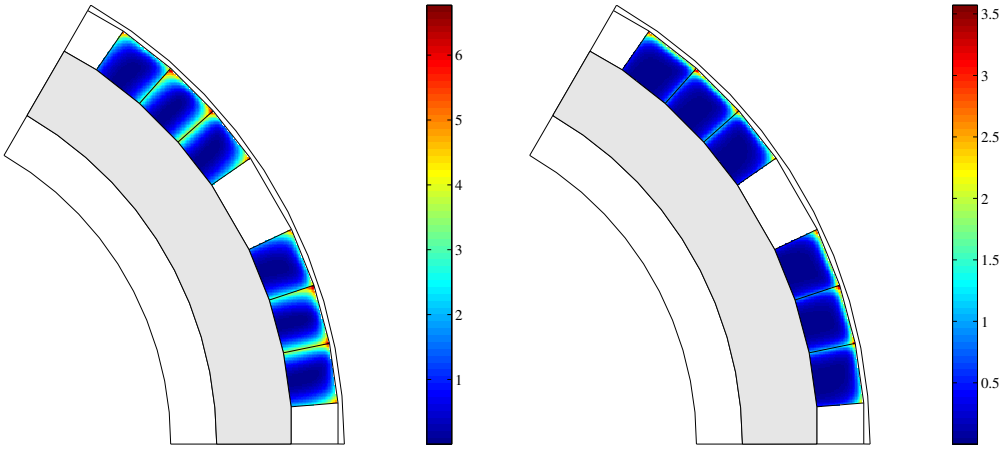

(a) f_s=3 kHz, U_{dc}=450 V **(b)** f_s=9 kHz, U_{dc}=450 V

Figure 6.12 Time averaged magnet eddy current loss distribution (W/cm³)

6.6 Conclusion

This chapter considered the additional iron, winding and rotor losses occurring in a PM machine due to time harmonics in the phase currents. A range of switching frequencies and two dc link voltages were considered in a machine with a 0.25 pu inductance.

Based on literature, the increase in the stator lamination losses was expected to be small, which was confirmed. The largest increase obtained was 16%. Moreover, the additional iron losses depend much stronger on the dc-link voltage than the switching frequency. The rotor losses were found to be the most sensitive to the switching frequency: compared to ideal sinusoidal supply currents, the ripple at low switching frequencies causes a ninefold loss increase, while at higher switching frequencies the losses only double. The winding losses were analyzed separately for proximity effect losses and unequal current sharing between parallel strands. The winding proximity losses due to the ripple currents depend more strongly on the dc-link voltage than the switching frequency, but always remain a fraction of the dc copper losses for the machine considered. However, unequal current sharing can cause significant AC/DC loss ratios, which needs attention when used in combination with a low switching frequency, although it can be very effectively counteracted by increasing the switching frequency.

Comparing the different loss mechanisms, two groups can be identified. On the one side are the resistively limited eddy current losses –in this case the lamination and winding proximity losses– which barely depend on the switching frequency but strongly depend on the dc-link voltage. On the other side are the inductively limited eddy current losses –here the rotor and winding current sharing losses– which depend strongly on both dc-link voltage and switching frequency. Those aspect have to be kept in mind when deciding on a (new) switching frequency for a new or given machine.

All in all, the results emphasize the importance of performing a system wide initial design of a drive system, where upper and lower limits on the machine inductance, inverter switching frequency and system voltages are determined, to avoid excessive machine losses.

CHAPTER 7

Design and testing of the prototype permanent magnet starter/generator

This chapter discusses the basic design of the prototype starter/generator (S/G) and experimentally validates the performance. After a brief overview of existing S/Gs, the impact of the starting, generating and safety requirements on the machine and inverter sizing is discussed. Then, some detailed design aspects are described, such as the use of parallel wires and magnet segmentation, using the models and results covered in detail in the earlier chapters. Finally, the machine is assembled and the basic functionalities are tested.

Based on

- M. van der Geest, H. Polinder, J. A. Ferreira, and D. Zeilstra, "Machine selection and initial design of an aerospace starter/generator," in *IEEE Int. Electric Machines Drives Conf. (IEMDC)*, 2013, pp. 196–203; and
- M. van der Geest, H. Polinder, J. A. Ferreira, and D. Zeilstra, "Design and testing of a high-speed aerospace permanent magnet starter/generator," in *3rd Int. Conf. Electrical Systems Aircraft, Railway, Ship propulsion and Road Vehicles (ESARS)*, 2015.

7.1 Introduction

Large aerospace turbines are traditionally started with pneumatic motors, powered by bleed air from the auxiliary power unit. Electrical starters are used in smaller aircraft, where no bleed air may be available. An electrical generator is often connected in addition to the starter, to supply power to the avionics and other on-board electronics. Combining these functions into a starter/generator (S/G) possibly saves weight and space, ultimately reducing the cost of ownership.

A combined S/G is not a new concept in aerospace applications though. Brushed DC machines have been in use for decades at lower power levels [130]. The armature of these machines can be connected directly to the DC-bus without power electronics and voltage control in generating mode can be achieved with a straightforward DC-controller, leading to a very simple system. The major downside however, is the periodic maintenance that the brushes require. In addition, these machines have only a moderate power density and the uncontrolled torque transient during turn-on may require special mechanical dampers. Therefore, to further reduce the operating cost of an aircraft, brushless alternatives are sought.

The possibilities of using brushless machines as S/G has been explored before, especially in the automotive industry, where much research exists on this topic. Since the mid 1990s virtually all machines types have been or are being considered for use as a S/G. In [131] a switched reluctance machine (SRM) is compared to an induction machine (IM), after dropping PM machines based on qualitative reasons. The IM generally performs better as a S/G. In [132] on the other hand, a SRM is developed and tested, resulting in system efficiencies of 80–90%. The described system uses a double clutch system to spin up the SRM before connecting it to the engine, providing a torque pulse to overcome static friction without having to significantly increase machine size. SRMs are also considered in [133]. A wound rotor synchronous machine was compared to an interior (or buried) PM machine (IPM) in [134]. Both machines have similar specific power densities, but the IPM has a higher efficiency. The benefits of an adjustable field, such as a better power factor and increased safety, are also mentioned.

In automotive S/G research the main focus lies on PM machines, due to the potentially high power density those machines offer. For automotive applications where the S/G is connected to main drive engine, the operational shaft speed may vary over a 10:1 speed range, which is why usually IPMs are used. (Range extender combustion engines usually have a narrower operating speed range, which slightly affects S/G design [135]). IPMs have a magnetically salient rotor, which, combined with properly dimensioned magnets, allows a theoretical infinite constant power speed range [22, 136]. Examples of research on IPM S/Gs are [137–140]. PM flux switching machines (PMFSM) are also considered as S/G [141], but these have a salient stator and rotor (i.e. doubly salient), which, combined with high field strengths close to saturation, makes them prone to torque ripple. This is not desirable in automotive S/Gs from a comfort and noise perspective and a range of skewing methods is required to minimize the torque ripple [142]. Depending on the available space, axial flux machines can be an attractive option. However, AF machines with

iron-less stators have a very low inductance and electrical flux weakening is therefore ineffective. An alternative may be to use mechanical flux weakening [143].

Compared to automotive S/Gs, less research is published on brushless alternatives to the aerospace DC S/G. In the research that exists, the main focus lies on SRMs, which are usually chosen due to the very harsh environment and safety requirements [87, 144]. In older work from the early 90s system efficiencies while generating of 80–85% are reported [145–147], which can be seen as a downside of this machine type. In [148] an embedded (incorporated in the turbine) SRM is discussed. Because the machine is embedded, the inner and outer radius were constrained and a segmented rotor is used, which provides a higher power density, but also presents manufacturing issues.

Wound rotor machines are also considered. Although their efficiency is perhaps less than that of PM machines, the ability to control the field current allows unity power factor operation over a wide speed range [149] or even the use of a simple bridge rectifier instead of a full inverter. Also, in case of faults the machine can be electrically switched off. A brushless exciter may be used to avoid brushes; the design, testing and control of such a machine are the topic in [150–152]. A wound-field doubly salient machine is presented as potential aerospace S/G in [153]. However, the doubly salient nature of this machine causes severe torque ripple. No comparison to other machine types is made.

Recently, surface mounted PM machines have also been considered [154–156]. The simple mechanical structure of a surface mounted PM rotor allows operation up to very high speeds, offering significant power density improvements.

This chapter presents the implementation of a surface mounted permanent magnet (SPM) machine for use as a S/G to fulfill the project specifications. For this specific application the starting torque is approximately five times higher than the generator torque. Furthermore, the specification requires a fail-safe design, where failures during generator operation, such as short circuits, do not lead to catastrophic failure with any significant probability. Since the magnets cannot be switched off, this is achieved by designing for a specific phase inductance together with adequate cooling capacity. However, the safety and high starting torque requirements directly oppose each other and strongly affect both machine and inverter design, which is the topic of the first section of this chapter. The second section discusses the actual implementation of the machine, using the models and conclusions from the earlier chapters, and the third section describes experimental tests on the machine to validate the performance and models.

7.2 Design considerations

7.2.1 Requirements

Table 7.1 summarizes the main requirements. Note that this is (of course) a strong abstraction of the actual set of requirements, which in reality is far more verbose with regards to limits,

procedures and safety requirements. In addition to the straightforward starter and generator requirements, the machine also needs to be fail-safe. In this context fail-safe means that the machine may cease to function, but only in a predictable, non-catastrophic way. Internal turn-to-turn short circuits are particularly dangerous, as the high local current densities can easily overheat the windings if the machine is not switched off in time (see Chapter 5). Since the PM excitation cannot be disabled, the local short circuit current is minimized by applying a three phase terminal short circuit during faults in the machine. This equalizes all short circuit currents inside the machine and by designing for a 1 per-unit phase inductance, the copper losses remain equal to the rated losses [85]. However, a large phase inductance may conflict with the starting requirement due to more pronounced iron saturation effects and increased inverter VA-ratings.

Hence, three interacting requirements drive the design:

- starting torque, duration and speed range;
- generator power and speed range;
- short circuit losses.

The magnitude of each requirement determines the impact on the design. That is, it determines whether a machine can for example be considered as 'fail-safe starter with additional generating possibilities' or a 'generator that is also used for starting'.

The design is constrained by the machine and inverter weight. Quantifying the inverter weight based on VA-rating goes beyond the scope of this work, and instead, the minimum VA-rating accounting for all operating conditions is considered. Therefore, the design should aim to minimize the following targets:

- machine weight;
- required inverter VA-rating.

The remainder of this section analyzes how the requirements affect the targets.

Table 7.1 Summarized Starter/Generator requirements

Property	Requirement
Generator power	5 kW
Nominal speed	24,000 RPM
Generator speed	50–100 %
Generator efficiency	> 93%
Starting torque	20 Nm
Cooling	Shaft mounted fan

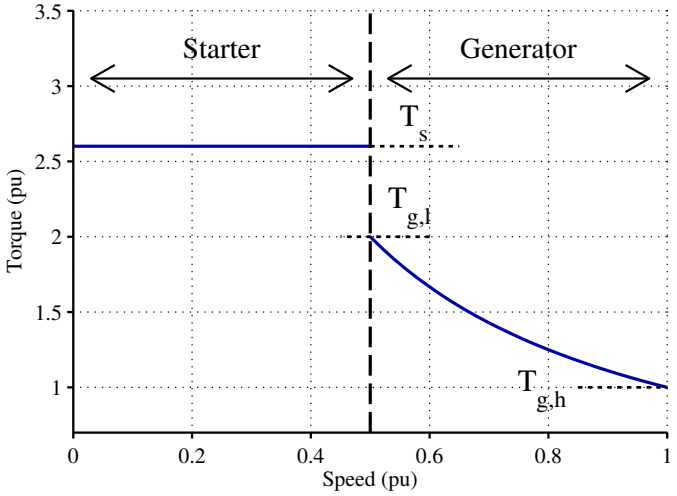

Figure 7.1 Definition of generic S/G torque speed curve.

7.2.2 Inverter considerations

To demonstrate the impact of the requirements on the system design, an abstract torque speed curve is first defined in Figure 7.1. The machine operates as starter with constant torque T_s up to 50% speed and as a generator with constant power load between 50% and 100% speed. The generator quantities at full speed serve as 1 pu base. The pu three phase short circuit current is $I_{sc,pu}$. For convenience, the starting torque is normalized to the maximum generator torque:

$$T_{s,rel} = \frac{T_s}{T_{g,l}} \tag{7.1}$$

Hence, for $T_{s,rel} = 1$ the starting torque requirement does not increase the machine or inverter current ratings, except from the thermal perspective in case of a shaft mounted fan. Lastly, the maximum losses that can be sustained indefinitely are set equal to the short circuit copper losses.

Next, the minimum theoretical inverter VA-rating is computed for different values of $T_{s,rel}$ and $I_{sc,pu}$, under the assumption that semiconductor devices with arbitrary ratings can be used. This requires the dq-currents versus speed to be determined. The required q-axis current is defined by the torque-speed requirement, but the d-axis current can be chosen freely. In the following analysis, the d-axis current versus speed is chosen to either minimize the inverter VA-rating, or as zero.

Figure 7.2 shows the resulting minimum inverter rating versus short circuit current, normalized to the nominal generator power. For large values of $T_{s,rel}$ and low values of $I_{sc,pu}$, the inverter rating rises sharply; a 1 pu short circuit current for the target machine would imply an inverter

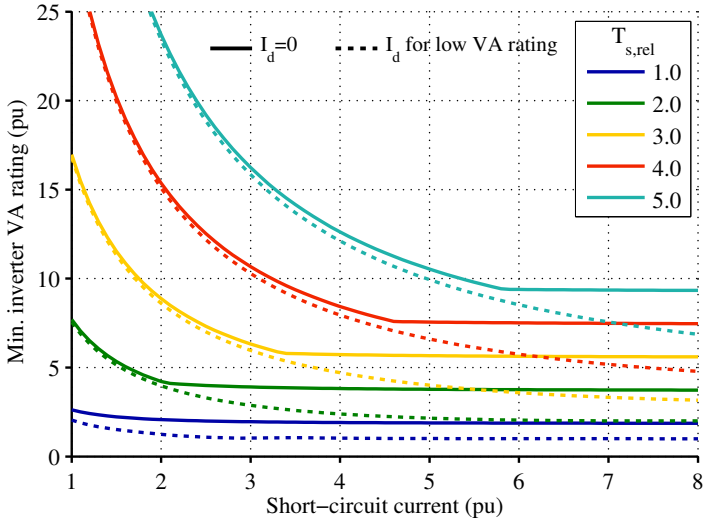

Figure 7.2 Minimum inverter VA rating relative to nominal generator power, versus machine short circuit current and starter-to-generator torque ratio.

rating of roughly 40 times the generator power. Clearly, short circuit currents larger than the nominal current are desirable, but how much larger? Figure 7.2 suggests as a rule of thumb to use $I_{sc,pu} = T_{s,rel}$, which avoids the need for excessively high inverter ratings, even with $I_d = 0$. For $I_{sc,pu} > T_{s,rel}$, the inverter rating can be further reduced if flux weakening is used near the end of the starting phase and during generator operation. It should be noted that from a safety perspective the use of field weakening may be undesirable, because a failure in the inverter (control) may lead to hazardous DC-link voltages or uncontrolled generator operation.

7.2.3 Machine considerations

The previous section demonstrated that from the inverter perspective, the machine should have a large pu short circuit current. This section will consider how this affects the machine design by performing a Pareto based multi-objective optimization.

Modeling

The modeling and optimization procedure as described in Chapter 2 will be used. To also account for the starting and short circuit behavior, the following additional properties are determined for each machine design:

- The q-axis current needed to reach the required starting torque, accounting for saturation.

- The adiabatic temperature rise rate (K/s) during starting, to compare the starting performance of different machines. The adiabatic temperature rise is based solely on the copper losses and weight, which may not be fully realistic, but avoids the need for more accurate thermal models.
- The copper, lamination and rotor losses during a three phase short circuit.

The optimization variables are the nine most important geometric dimensions, including stack length, outer radius and airgap length. Further relevant assumptions are: a winding fill factor of 50%; 0.1 mm FeCo stator laminations (due to the high saturation flux density); magnets with B_r=1 T; a carbon fiber retaining sleeve for low rotor losses and a 15 slot 10 pole concentrated non-overlapping winding layout.

The optimization targets were the following:

- minimize machine weight;
- maximize per-unit short circuit current;
- minimize short circuit losses;
- minimize starting temperature rise rate.

Note that the generator mode efficiency is not included as target; earlier exploratory optimizations (partially described in Chapter 2) indicated that when designing for both low fault losses and good starting performance, acceptable generator performance will result, as will be shown here as well. Further note that the S/G example optimization in Chapter 2 used the starting copper losses as target, instead of temperature rise rate. Focussing on the copper losses favors FSMs, as those machines typically have lower copper losses than SPMs, but operate at higher current densities. Hence, when also accounting for the temperature rise rate, the benefits of FSMs reduce.

Lastly, to obtain the results in this section, 330 generations with 20 particles were used in two trails with different starting conditions, so that in total over 13,000 machine designs were analyzed.

Optimization outcome

Figure 7.3 shows several side views to the Pareto optimal front, divided based on the starting temperature rise rate, as indicated in Figure 7.3(a). Each point represents a machine design that is optimal in some way in the 4D target space. Figure 7.3(a) clearly shows that a good starting performance requires a high short circuit current. For the specifications considered here, designing a machine with a 1 pu inductance is practically impossible, while with $I_{sc,pu} = 4$, temperature rise rates below 2 K/s are possible. Figure 7.3(b) shows that machines with good starting performance (ie. yellow triangles) are heavy machines. This was to be expected, since larger machine have more copper mass to both carry the current and absorb the starting losses.

Figure 7.3(c) shows the short circuit losses versus $I_{sc,pu}$. Unsurprisingly, increasing $I_{sc,pu}$ also increases the short circuit losses, which conflicts with the fail-safe requirement of having low

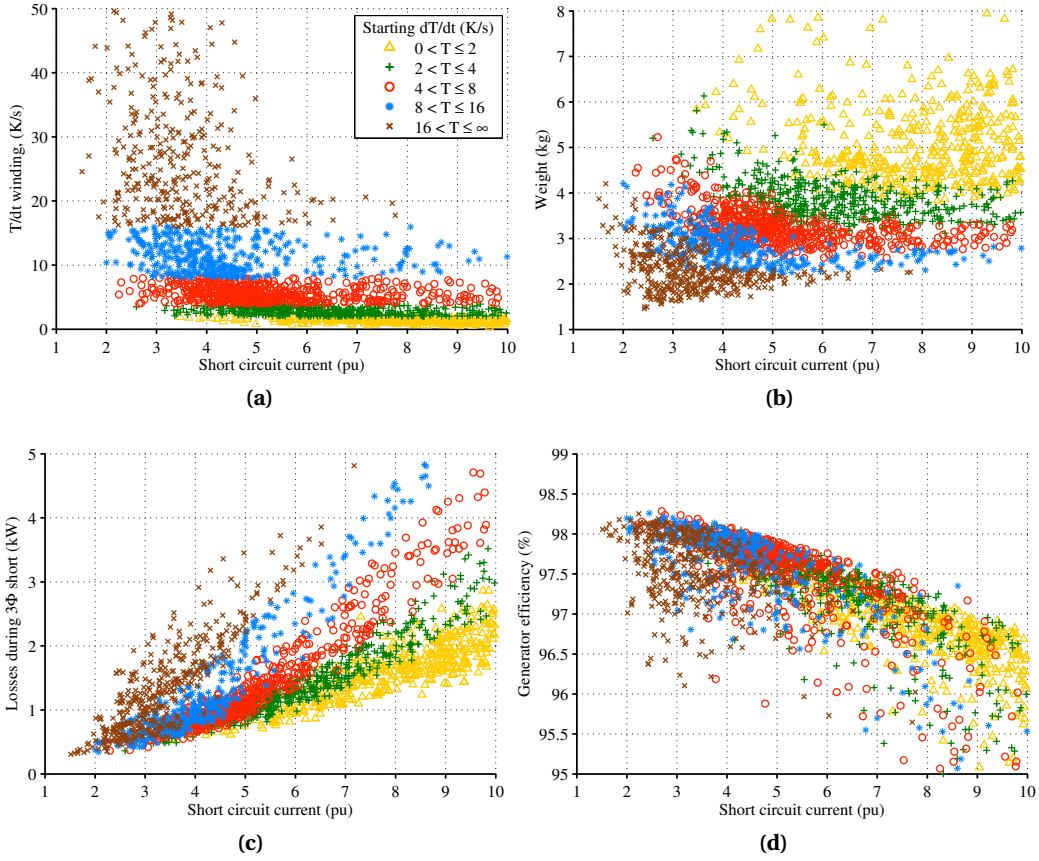

Figure 7.3 Side views to the Pareto optimal front, with colors and shapes indicating the starting temperature rise rate.

short circuit losses. On the other hand, for a given value of $I_{sc,pu}$, machine designs with good starting performance also offer low faulted losses.

Finally, Figure 7.3(d) shows the generator efficiency. Although this was not an optimization objective, the values do not turn out problematically low, because the requirements on low short circuit losses and high $T_{s,rel}$ inherently lead to acceptable generator performance. However, the generator efficiency does slightly decrease with increasing $I_{sc,pu}$, which is caused by increasing iron losses. Put differently, machine designs with both acceptable starting performance and faulted losses will be oversized for generator operation in this specific application.

7.3 Detailed electromagnetic design

Using the design considerations presented above as guidance, additional particle swarm optimizations were undertaken to arrive at a set of candidate designs suitable for implementation. Further FE analyses were performed on those machines to estimate additional winding losses (Chapter 4), demagnetization risks, potential unbalanced forces, rotor insertion force, and 3D effects including magnet flux leakage, additional inductance and rotor losses (Chapter 3), some of which are briefly discussed here specifically for this machine. Ultimately, one design was chosen for manufacturing, of which a cross-section is shown in Figure 7.4.

7.3.1 Winding considerations

Due to the high electrical frequency, eddy current losses may occur in the windings. Moreover, relatively few turns are needed to obtain sufficient back-emf, potentially worsening the eddy

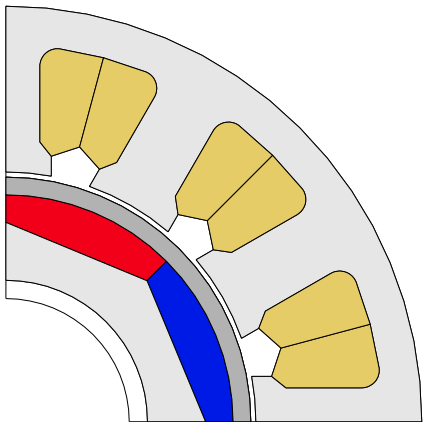

Figure 7.4 Cross section of the designed machine, showing only magnetically active materials.

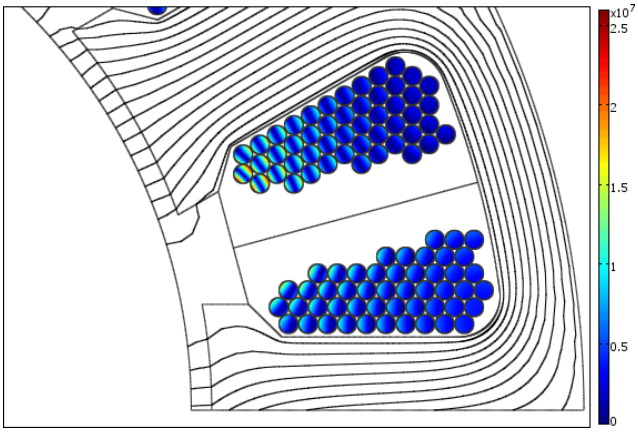

Figure 7.5 Example of proximity losses in the solid strands. Colors indicate absolute current density (A/m²).

current losses. Using litz wire or multiple parallel strands with sufficient twisting can reduce these losses, but will also reduce the fill factor and increase production cost. The use of standard solid wire without additional twisting or displacement was therefore desired.

Figure 7.5 shows an example FE model with individual strands. The majority of the winding AC losses originate near the slot opening and are caused by slot leakage flux. Therefore, these losses are virtually absent under no-load conditions. Given the distribution of the losses, the total losses can be reduced by only partially filling the slots with conductors, which is common with higher electrical frequencies [53]. However, this reduces the total slot fill factor, which was deemed undesirable. As an alternative, the winding AC losses are reduced by using several thinner non-twisted enameled strands in parallel, as demonstrated in Figure 7.6. For the machine considered, using four parallel strands per turn instead of one reduces the AC/DC loss ratio from 1.6 to 1.2. The effectiveness of adding parallel strands reduces for larger numbers of strands, and when also considering the increasing manufacturing complexity and cost, high numbers of discrete parallel strands may be unattractive.

7.3.2 Rotor eddy current losses

The use of tooth-coil windings introduces asynchronous airgap space-harmonics, which potentially induce rotor eddy current losses. To reduce those losses, the magnets are axially segmented and a carbon fiber retaining sleeve is used. To determine the number of required magnet segments, the average magnet losses are computed with 3D FEM simulations using the approach presented in Chapter 3. Figure 7.7 shows such a solved model, while Figure 7.8 shows the expected losses versus the number of axial segments. With six or more magnet segments the losses become suitably low for the given machine.

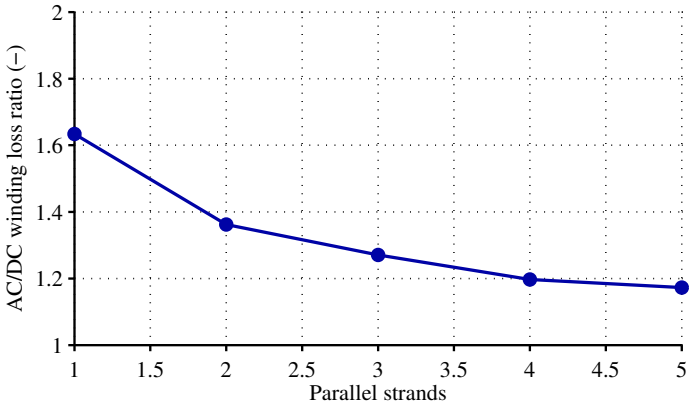

Figure 7.6 Winding AC/DC loss ratio versus number of parallel strands.

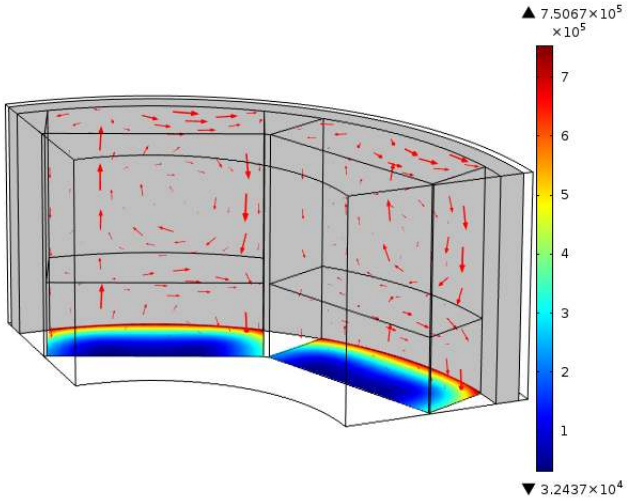

Figure 7.7 Example rotor eddy currents with three axial magnet segments. Arrows show current direction and magnitude, colors average current density (A/m²).

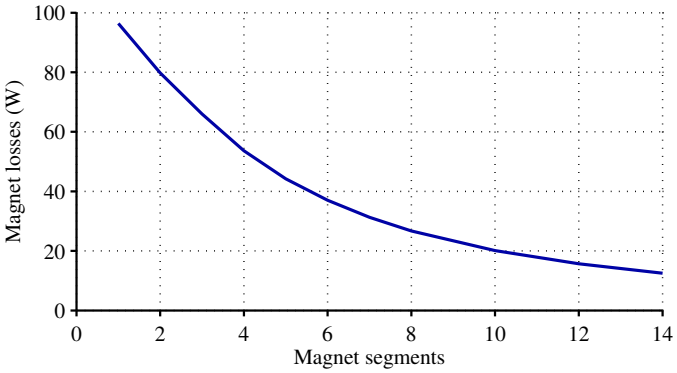

Figure 7.8 Magnet eddy current losses.

7.3.3 Demagnetization check

Although the machine may be able to thermally withstand short circuits, demagnetization may still occur. The transient phase currents immediately after occurrence of a short circuit may reach twice the steady state short circuit current, potentially damaging the magnets. A simulation was conducted where a three phase short circuit is applied during nominal generator mode, and the worst magnet working point was determined, as shown in Figure 7.9. The minimum flux density obtained was 0.38 T, which is above the knee point of the selected magnet grade, even at slightly elevated temperatures.

7.3.4 Realization

A prototype of the design described above was manufactured, shown in Figure 7.10. Test results obtained with this machine are presented in the next section.

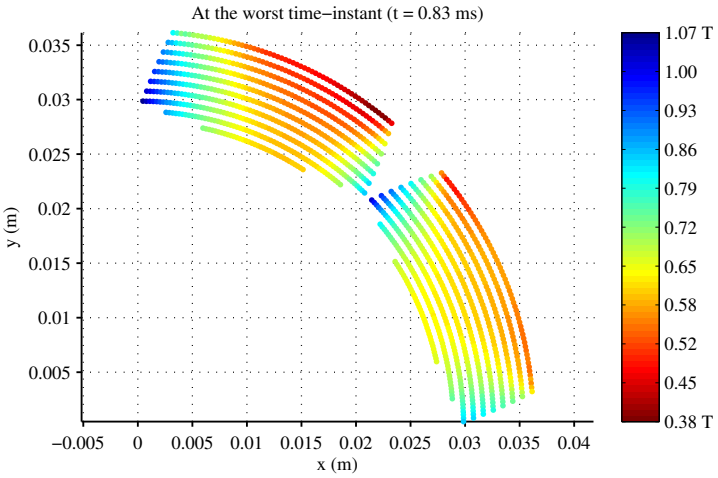

Figure 7.9 Magnetic flux density in the magnets in the magnetization direction, showing the worst case situation after application of a short circuit.

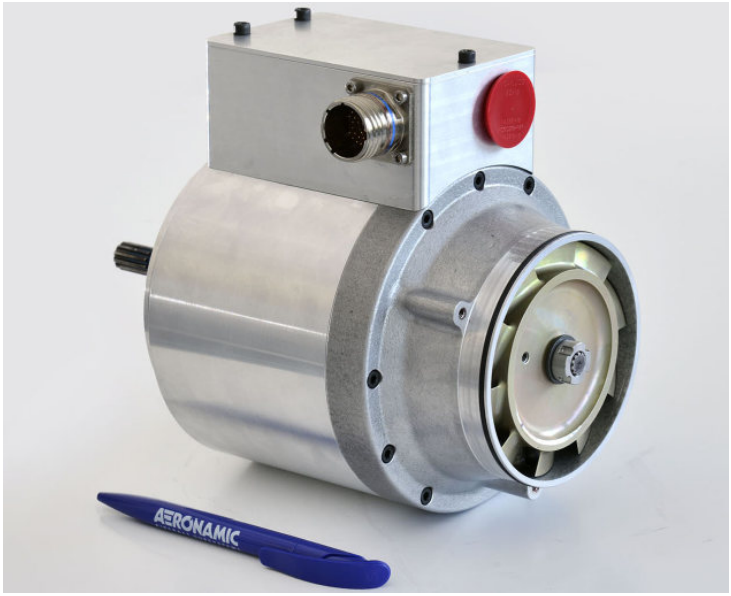

Figure 7.10 Realized S/G machine.

7.4 Testing

7.4.1 Basic performance

Table 7.2 shows the basic machine properties. The back-emf amplitude is 1.5% less than simulated. Due to the long magnetic airgap and the tooth-coil windings, the back-emf is highly sinusoidal (and therefore not shown); the total harmonic distortion, both simulated and measured, is only 0.8%, which is mostly caused by the 5^{th} harmonic with 0.7% amplitude of the fundamental. The actual inductance is 2–3% smaller than designed, leading to a marginally higher short circuit current. The simulated torque ripple is negligible, and was too low to be accurately measured.

As part of the safety requirements, the machine must be able to withstand indefinite three phase terminal short circuits under nominal operating conditions, without failing or demagnetizing. To validate this, the steady state winding temperature during a short circuit is measured. Under ambient conditions, the measured winding temperature rise is approximately 90°C, and matches reasonably well with the predicted steady state temperature of approximately 100°C. This shows that the slightly larger short circuit current is not problematic. With the measured temperature rise, short circuit operation is also possible at elevated ambient temperatures or higher altitudes (where the air density and cooling effectiveness reduce), if suitable isolation materials are used. Lastly, there was no evidence of demagnetization after performing these tests.

7.4.2 Saturation performance

To validate that the required starting torque can be reached, the torque versus I_d and I_q is measured and compared with the calculated torque. The measurement is conducted for a blocked rotor case, but the connecting shaft –which includes the torque transducer– has a non-negligible

Table 7.2 Basic machine properties

Property	Simulated	Measured
Back-emf (20 °C)(3D)	195 V_{rms}	192 V_{rms}
Inductance (3D)	L: 0.186 pu	0.177 pu
	M: -0.072 pu	-0.068 pu
Phase resistance (20 °C)	22 mΩ	27 mΩ
Cogging torque	0.10 Nm_{pp}	-
Generator torque ripple	0.12 Nm_{pp}	-
Starting torque ripple	0.34 Nm_{pp}	-
Short circuit current	3.9 × I_{nom}	4.1 × I_{nom}
Short circuit temperature	100°C rise	90°C rise

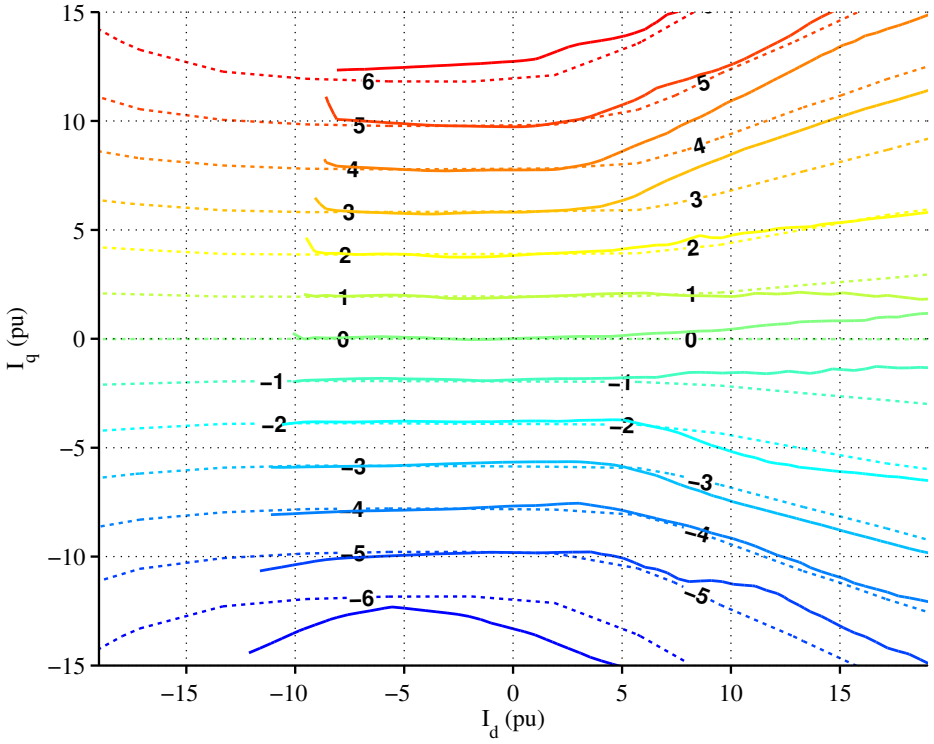

Figure 7.11 Measured (solid lines) and calculated torque (in pu) versus I_{dq}.

flexibility, so the actual rotor position varies with applied torque. As a result, the position of the d-axis can slight shift under high torque conditions, increasing measurement uncertainty.

Figure 7.11 shows the resulting torque map. The limitations of the measurement setup are evident from the slight asymmetry between the upper and lower halve planes (positive and negative I_d) and distortion near the edges. Nonetheless, within the linear region the predicted and measured torque match closely, as was to be expected from the matching back-emf. The five times nominal torque can be obtained with no saturation, as expected, but beyond this the model underestimates the saturation effect and overpredicts the torque by 9% at 15 times nominal current.

7.4.3 Starting performance

To determine the temperature rise during starting, the rated starting current is injected for several starting cycles and the temperature rise is monitored. Figure 7.12 shows the result, along with the simulated temperature rise. This figure shows a measured temperature rise of about 1–

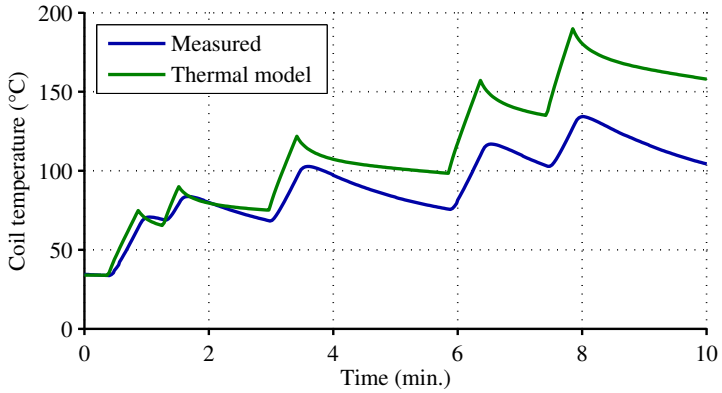

Figure 7.12 Measured and simulated winding temperature during repeated starting cycles.

1.5 K/s, which is sufficiently low to allow multiple repeated start attempts without overheating. Within each starting cycle the model overpredicts the temperature rise by about 10%, which is considered to be sufficiently accurate. The thermal model over-predicts the average temperature rise after some time, because it partially neglects heat conduction to the machine's surroundings at standstill.

7.5 Conclusion

This chapter discussed the implementation of a surface mounted PM machine as an aerospace starter/generator. Unique in this design is the five times larger starting torque than the maximum generator torque. Furthermore, the machine is required to be fail-safe, which is achieved by limiting the short circuit current. However, a low short circuit current directly opposes the starting performance, as it increases both the minimum inverter VA-rating and the temperature rise during starting, and a compromise needs to be found. Ultimately, the implemented machine will be over-dimensioned for the generator requirement, while still having only a limited safe starting duration.

Multidimensional particle swarm based optimization was again used to consider the important trade-offs that affect the machine design and find suitable candidate machines. Further detailed analyses were performed, demonstrating the impact of rotor and winding eddy current losses specifically for this machine. A prototype was built and tested. The back-emf, inductance, short circuit current and temperature, and starting performance all show a good match to simulated performance, ultimately demonstrating that a surface mounted PM machine may be successfully used as starter/generator. Additionally, the tests verify the outcome of the FE models used throughout this thesis.

CHAPTER 8

Power density limits and design trends of high-speed permanent magnet synchronous machines

In the previous chapters, optimization methods were introduced and models were presented and tested, eventually leading to the prototype starter/generator. In this final chapter, those models and optimization methods are used at a large scale to determine more general but still quantitative design trends and limits related to the specific power density of high-speed permanent magnet machines. To this end, eighty individual optimizations are executed, covering a range of rotor surface speeds, power levels and cooling systems. Afterwards, machines are selected from each front and relevant performance criteria and properties are plotted, demonstrating various trends in machine design. This chapter may be used in two ways: as a demonstration of a method to find accurate yet generic design trends and limits; and as an actual overview of power density limits and the associated design trends.

Based on

- M. van der Geest, H. Polinder, J. A. Ferreira, and M. Christmann, "Power density limits and design trends of high-speed permanent magnet synchronous machines," *IEEE Trans. Transportation Electrification*, vol. 1, no. 3, pp. 266–276, Oct. 2015; and
- M. van der Geest, H. Polinder, J. A. Ferreira, and M. Christmann, "Quantitative power density limits of aerospace permanent magnet synchronous machines," in *More Electric Aircraft Conference*, 2015.

8.1 Introduction

Electrical machines are inherently part of a larger system. They should therefore be designed together with the other parts of the system to arrive at a global optimum. This is particularly important for aerospace systems, where a low system weight and volume are essential to obtain a competitive system. In the early design phase of new systems, many different concepts and configurations may be considered. It is usually infeasible to consider all possible options in detail, so a selection of the most promising systems to proceed with needs to be made. To facilitate this early selection, figures of merit or sufficiently accurate yet fast models are required for all major subcomponents in the system.

For electrical machines, many simple analytical scaling laws and rules of thumb exist, but these can only provide a rough initial guess for the machine size, which may be insufficient for the design of high performance systems [157]. For example, [158] uses very basic analytical equations to establish a generic torque-per-volume parameter. This provides a high-level estimate of machine performance in this parameter, but may not offer the level of detail that is required for early machine selection. Similar arguments apply to [159], where a more detailed sizing equation for volumetric power density is developed, but a detailed loss analysis is necessarily omitted. Determining volumetric power density limits is the focus of [160]. However, the modeling and optimization methods have limitations, because the analytical models neglect saturation and rotor losses, while these effects are considered in the method proposed in this thesis. The machines are loaded by a passive *RL* load, while an inverter drive would commonly be used in high performance applications today. Nonetheless, quantitative results for the volumetric power density are presented and compared for a range of PM machine types. Ref. [161] determines speed limits for electrical machines. To this end, analytical expressions are used to correlate mechanical, thermal and magnetic limits, providing a high level theoretical support of empirically obtained power-speed limits. Ref. [162] quantifies power limits of surface mounted permanent magnet (SPM) machines for five rotational speeds between 20–100 kRPM and a given set of mechanical and thermal constraints. The emphasis lies on modeling however, and few underlying details of the five resulting machines are provided. A finite element based sizing approach for interior PM machines with consideration of the magnetic and thermal domains is proposed in [163]. In a two step process, a generic optimal machine cross-section is first created with PSO, which is then transformed into a final design via a scaling exercise. Hence, manual interaction is still necessary to obtain the final machine design. Most of these examples implicitly also illustrate that when determining limits of electrical machines, a balance needs to be found between generality and level of detail.

Another approach is to use a database with existing machine designs to identify trends and limits [164, 165], but this approach has several drawbacks as well: very few comparable designs may exist (in terms of application, power and speed levels, design intent); or little specific data is published for a given machine, such as constraints, dimensions, weight or used materials. Ultimately, a literature study allows global limits such as power-speed curves to be identified, but an in-depth analysis of underlying machine properties is generally not possible.

The desired level of detail and accuracy can be obtained with finite element analysis (FEA). In itself, FEA is an analysis method, but by combining FEA with optimization algorithms, it can be part of a design method ([16, 166],Chapter 2). By using magnetic, thermal and mechanical simulations, all relevant performance data can be obtained, at the cost of computation time. This computational cost prohibits the direct application of FE-based optimization methods in an early design stage.

This chapter attempts to bridge the gap between inaccurate scaling laws, underpopulated databases and time consuming FE-based optimizations, by filling a database with systematically chosen and individually FE-based optimized machine designs. Advantages of this approach include that all machine properties –such as dimensions, losses or electrical parameters– are known and that each resulting machine is optimized with identical targets, constraints and materials. This allows both global trends such as power density, and underlying trends such as machine dimensions and performance, to be determined and quantified. The results can serve as a direct starting point for new designs, as a reference for comparison with existing designs, or as a means to gain insight into fundamental design tradeoffs of surface mounted permanent magnet (SPM) machines.

In this work, the ultimate goal is to determine the maximum specific power density (kW/kg) of SPM machines, as function of four rotor surface speeds, five power levels and four cooling scenarios. For each of these 80 design points, an individual multi-objective FE-based optimization is executed, with minimization of weight and peak winding temperature and maximization of efficiency as objectives, and the machine geometry as variable. Qualitatively, the relation between the specific power density and the main variables is well known. The contribution of this work is the proposal and application of a method to quantify and present design trends and limits with a very high level of detail. A second contribution is the presentation of useful design relations and trends that can be used as a starting point for new machine designs or gain general insight into sizing trends.

One major limitation of a design study as proposed here is validation of the results. Although the underlying FE models used here have been successfully validated in the previous chapters, this does not imply that the trends determined here are also correct. Validation of the design trends could for example be achieved by pursuing the same goal (ie. dependencies of specific power density), but using a different optimization strategy and work flow. A simpler alternative will be undertaken in this case though: the properties of the optimal designs obtained here are compared with those from existing designs found in literature [161, 164].

This chapter is structured as follows: Section 8.2 explains and motivates the proposed optimization approach, while Section 8.3 briefly presents the models and assumptions used. Section 8.4 presents and explains the results. Lastly, Section 8.5 discusses the results with a comparison to literature values and a thermal sensitivity analysis.

8.2 Optimization approach

8.2.1 Choice of main target and independent variables

The main goal of this work is to determine the dependency of specific power density on rotor surface speed, power level and cooling effort. This is motivated by the following arguments:

- Specific power density is chosen because in aircraft, and particulary rotorcraft, low weight is essential to increase range and reduce operating costs.
- Constant rotor surface speeds of 25, 50, 100 and 200 m/s are considered. A constant surface speed is chosen over a constant rotational speed, because the former represents a roughly constant mechanical design effort. For example, a machine with v_{surf}=200 m/s will always require detailed mechanical analysis, regardless of the rotational speed or rotor diameter. In applications where the rotational speed is imposed, the results from this work can be used in two ways: with given surface and rotational speeds the rotor diameter can be estimated and compared with a target design envelope. Alternatively, the results can be combined with gearbox data to compare direct drive systems to geared solutions.
- Power levels of 50, 100, 200, 500 and 1000 kW are considered. A small dependency of power density on power level is expected and multiple levels are considered to confirm this.
- The achievable machine performance strongly depends on cooling intensity and a wide range of cooling options exist, ranging from passive convection cooling to complex liquid cooling with flow paths inside the magnetically active parts. This implies that the cooling system must be a parameter to obtain sufficiently generic results, but it also implies that cooling solutions cannot easily be compared. Therefore, four cooling scenarios are defined, as will be described in a few pages.

8.2.2 Implementation

Due to the wide range of power, speed and cooling levels considered, properties such as optimal flux and current densities, pole count and dimensions will all vary between the considered cases. To ensure that each design in the database is indeed optimal, an individual multi-objective optimization is executed for each design point. The variables in this optimization are the machine dimensions, while the targets are high efficiency, low winding temperature rise and low weight.

The result of each optimization is a Pareto optimal front (POF), which captures the fact in the presence of conflicting targets, no single optimum exists ([16, 167],Chapter 2). In this study, each of the 80 resulting three dimensional POFs shows the trade-off between weight, efficiency and winding temperature for a given design point. These are considered *local* trade-offs, since they correspond to a single machine specification.

To determine high level *global* trends (the dependencies of the power density), the results from all POFs have to be compared. A direct comparison of the POFs is however infeasible, as each front contains hundredths of individual designs. Therefore, the n lightest designs meeting a set of given temperature constraints are selected from each POF and the performance and properties are averaged and plotted. n designs are selected and averaged instead of just selecting the lightest design, because the Pareto optimal fronts contain small local variations, but the designs are sufficiently similar to allow averaging. Alternatively, the averaging step can be omitted, thus providing an impression of the uncertainty, but also resulting in less clear plots.

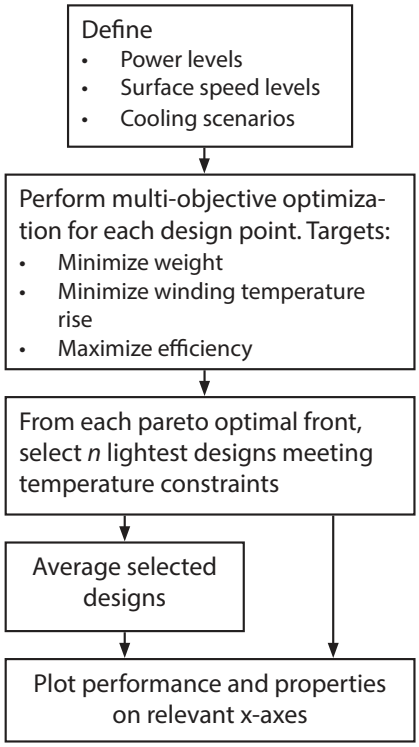

Figure 8.1 Proposed design approach.

Figure 8.1 schematically summarizes this approach. As an example, Figure 8.2(a) shows the resulting POFs for all rotor surface speed levels for the 200 kW optimistically air cooled design point. As shown, and in line with expectations, lighter machines operate at higher temperatures due to increased current and flux densities. Highlighted in each POF are the n=6 designs meeting a 150 °C temperature constraint. For these designs relevant properties are computed, optionally averaged, and plotted against e.g. rotor surface speed, as demonstrated in Figure 8.2(b). This plot already demonstrates the diminishing returns in specific power density with increasing rotor surface speeds. Plots like Figure 8.2(b) will be extensively shown and discussed in the results section.

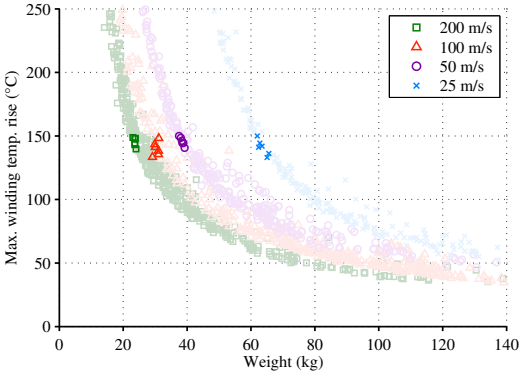

(a)

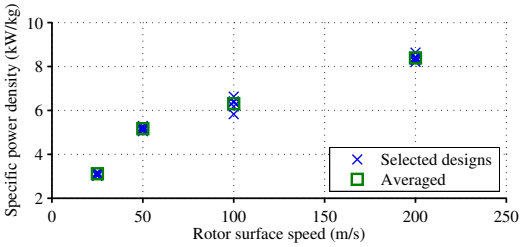

(b)

Figure 8.2 Design selection and averaging: (a) complete POFs for the 200 kW, optimistically air cooled design point, with the 6 selected designs highlighted in each POF; (b) performance of the selected designs versus rotor surface speed.

8.3 Modeling, assumptions & material properties

This section describes all constants and assumptions, as well as the models used in the optimizations.

8.3.1 Electrical domain

Assumptions

To keep the number of variables manageable, a number of assumptions must be made. With the emphasis on higher speed machines and high performance, SPM machines are considered. At high speeds SPM machines are more attractive than interior PM machines, because the latter rapidly require thicker magnetic bridges at higher speeds, which in turn requires more magnet material to maintain sufficient airgap field strength [164, 168]. In addition, increasing surface speeds require increasing mechanical airgap lengths due to mechanical considerations, which in turn reduces the saliency ratio and with that, the benefits of interior PM machines.

Only concentrated non-overlapping windings are considered, because this offers the benefits of short end-windings and simple manufacturing. With such windings, asynchronous space-harmonics can induce problematic rotor eddy current losses, especially at high speeds. To minimize these losses, only windings from the 3 slot, 2 pole family (q=0.5) are chosen, as these have no space-harmonics below the synchronous harmonic and the first higher order harmonic has already twice the pole count of the synchronous harmonic. To further reduce rotor losses, a carbon fiber retaining sleeve is assumed, together with axial magnet segmentation in 8 pieces.

Lastly, (costly) iron-cobalt laminations are assumed, because they allow high flux saturation levels (2.4 T) and are available as thin sheets to reduce losses. Further material properties, constants and variables are summarized in Table 8.1.

Modeling

Each machine is analyzed entirely with 2D FEA, allowing saturation, rotor eddy current losses and all geometric details to be accounted for. The basic machine properties and losses, such as linked flux, inductance, torque ripple; and iron, copper and rotor losses are computed, as described in Section 2.2.1. Note that losses, temperatures or current and flux densities are not explicitly constrained in this approach. Instead, by optimizing for a low temperature rise and selecting final designs based on temperature, the optimal current and flux densities will result. This removes the need for the user to specify 'optimal' current densities a priori. Next, because only 2D models are used, the machine performance may be overestimated for very short machines. To avoid this, a minimum axial stack length of 40 mm is used for all cases.

Table 8.1 Relevant material properties

	Stat./Rot. Lam.	Winding	Magnets	Retain. Sleeve
μ_r	FeCo	1	1.05	1
Losses[1]	0.15 mm	fill 50%	ϱ=1 $\mu\Omega$m	ϱ=100 $\mu\Omega$m
B_r	-	-	1.2 T	-
Density[2]	8120	5185	7500	1597
Therm. cond.[3]	29 / 0.7	1.2 / 195	7.5 / 2.5	0.77

[1] Respectively sheet thickness, fill factor, resistivity
[2] In kg/m^3; [3] In W/(m·K), in-plane / axial

8.3.2 Mechanical domain

At the considered rotor surface speeds, the mechanical design of the machines –consisting of static stress analysis and rotor dynamic analysis– must be considered to some extend. Other authors suggest that the stress analysis is of primary concern for high power density designs [169]. In this work, this is dealt with by using a fixed sleeve thickness of 2.5 mm for the carbon fiber sleeve. At higher speeds this may be insufficient, but the results will show that at these speeds the optimal magnetic airgap length increases, allowing thicker sleeves to be used if needed.

8.3.3 Thermal domain

Assumptions

A wide variety of cooling systems exists and quantifying a complete cooling system is difficult. Therefore, the following four cooling scenarios are defined:

- **C1 – Pessimistic air cooling** The machine is cooled only by ambient air forced through the airgap; the only heat exchange occurs in the airgap and around the end-windings. The stator yoke outside surface is assumed to be insulated. This case represents electrical machines built into large structures, where cooling from the machine outer periphery towards the environment is not possible (e.g. engine bays).
- **C2 – Optimistic air cooling** has increased flow rates compared to the previous case, as well as forced cooling on the stator yoke outside surface.
- **C3 – Liquid jacket, totally enclosed** The stator outside is cooled by a liquid jacket. The machine is closed, but air is circulated in the machine to transfer rotor heat to the stator.
- **C4 – Liquid jacket & rotor air cooling** Is similar to the previous case, but ambient air is forced through the airgap, although at lower rates than in the pessimistic air cooling case.

Table 8.2 Heat transfer coefficients for the four cooling cases

		HTC (W/(m^2 K))			
Description	**Face**	**C1**	**C2**	**C3**	**C4**
Stator yoke outside	A	-	65	1610	1610
End-winding outside	B	-	25	-	-
End-winding topside	C	40	80	15	15
End-winding rotor side	D	50	80	20	20
Tooth front (airgap)	E	150	200	50	50
Winding at slot opening	F	50	75	15	10
Rotor surface (airgap)		150	200	50	50
Rotor end-plates		-	15	10	10

The main purpose of this airflow is to cool the rotor, which can pose an issue when only using a liquid jacket.

These four scenarios are implemented as different surface heat transfer coefficients (HTC) to ambient air that are applied as boundary conditions on a model of the solid machine parts. Figure 8.3 shows the surfaces considered and Table 8.2 summarizes the corresponding HTC values. In the case of a liquid jacket, the yoke HTC represents the total effective resistance from yoke surface to liquid, the flow rate is adjusted to obtain a 40 K temperature rise, starting from an inlet temperature equal to the ambient temperature. Lastly, the weight of the jacket and liquid are included in the machine weight.

The HTCs represent convection and radiation cooling and are therefore non-linear, but by assuming forced cooling, constant values may be used. The values used are based on previous projects and [170–173].

With the aim on high performance applications, the baseline maximum temperature rise is 150 K for the windings (50 °C ambient with 240 °C rated wire) and 80 K for the carbon fiber sleeve, due to the limited maximum temperature of such sleeves. The effect of lower limits will be considered in a later section.

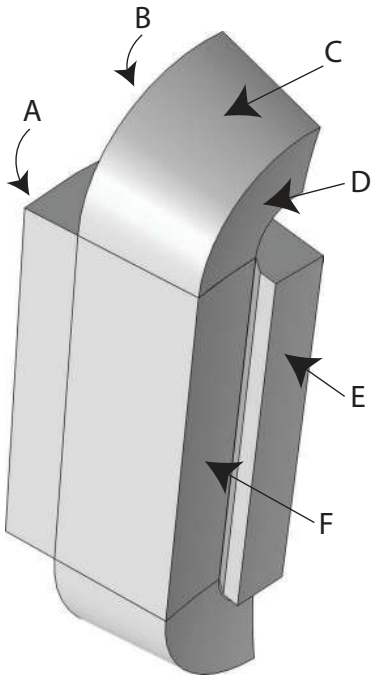

Figure 8.3 Machine interfaces with thermal heat transfer coefficients.

Modeling

The temperatures are computed with a 3D lumped element network, which is faster than FEA, but still provides sufficient accuracy compared to FEA, given the uncertainty associated with typical HTCs [170]. The use of a 3D model allows an axial temperature rise across the airgap or liquid jacket, as well as cooling of the end-windings, to be accounted for. Lastly, the lumped element network was validated with 3D FEM on a number of benchmark machines; the computed temperatures were always within 10 K. See appendix A for more details on the thermal model.

8.3.4 Optimization

Particle swarm optimization (PSO) is used to determine the POF for each design point. PSO is a gradient free, heuristic optimization algorithm, used on electrical machine problems before [31, 174]. For each design point, 200 iterations with 20 particles are executed, so that ultimately 320,000 machines have been analyzed to arrive at the final data set. Each optimization run takes about 1–2 days using a workstation with a Xeon E5-1620 processor, analyzing 4000 machine designs in the process.

8.4 Results

The results are now discussed in four parts. First, all unfiltered and processed POFs are shown, serving as a bridge between the optimization results and more abstract trends. Then, the main goal –specific power density– is discussed. Next, derived parameters for the same machines are presented, split into parameters relevant at system level, such as efficiency or frequency, and those only relevant to the machine designer, such as flux densities and loss distributions.

8.4.1 Individual fronts

Contrary to the procedure described in Section 8.2.2, the full POFs will now briefly be considered. This is done to demonstrate the amount of data that was generated and to underline the need for the proposed additional processing steps to determine actual trends.

Figure 8.4 shows the efficiency versus weight side-view to the POF for the purely air cooled machines. The typical behavior –increasing efficiency with weight– is visible for all machines. The most important observation is that the machine efficiency should not be a problem; a value of 97% is easily obtainable for most machines. The general fronts for the liquid cooled machines are very similar and hence not shown.

Figure 8.5 shows the winding temperature rise versus weight for the air cooled machines (the liquid cooled machines are again similar). Individual power levels can roughly be identified. The

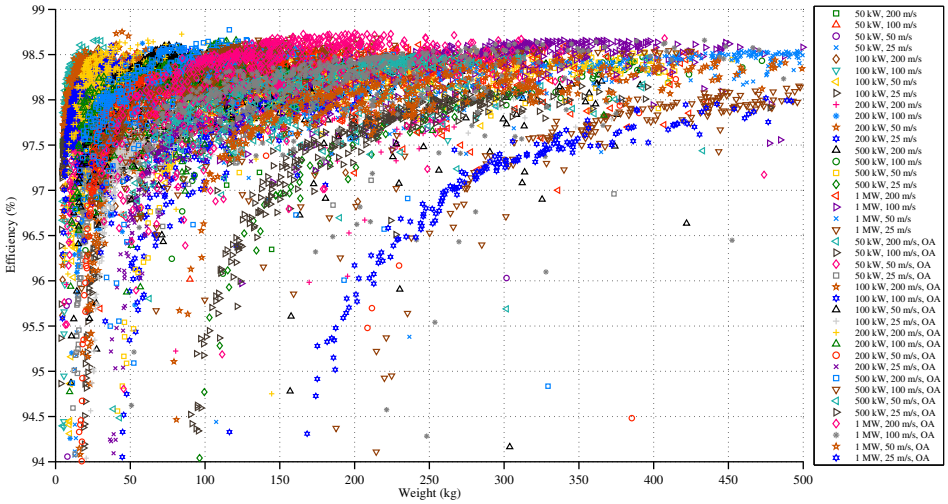

Figure 8.4 Full POFs: Efficiency versus weight for the air cooled cases.

general trends are again in line with what one would: heavier machines remain cooler.

Although Figures 8.4 and 8.5 contain a wealth of information, they also demonstrate that this information is difficult to comprehend. Therefore, they are not further discussed and the remaining sections apply the proposed processing approach to highlight specific trends.

8.4.2 Specific power density

Figure 8.6 shows the specific power density versus rotor surface speed and so fulfills the main goal of this chapter. Discussing the dependency on the main variables individually:

- Improving the cooling system is most beneficial for improving the power density. Compared to pessimistic air cooling, optimistic air cooling increases the specific power density by 1.5–2.5 times, the totally enclosed system with liquid jacket by 1.2–1.6 times and the mixed cooling system by 2–3 times. The totally enclosed system performs worse than the optimistically air cooled system, mostly due to the limit on the rotor temperature, which will be discussed later. All power levels and rotor surface speeds benefit from an improved cooling system, but the gain is greater at higher rotor surface speeds.
- Increasing the rotor surface speed also increases the power density, but with diminishing returns. This is attributed to the iron and rotor losses, which remain constant or increase with speed. For the pessimistic air cooling case, the specific power density doubles from 25 to 200 m/s, while for the mixed cooling case it triples. This demonstrates that with increasing surface speed, the importance of a good cooling system increases.

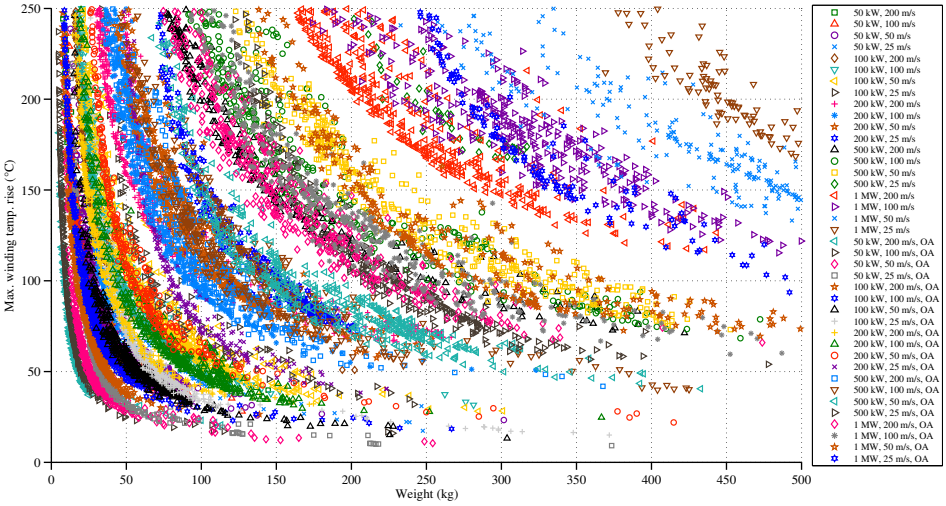

Figure 8.5 Full POFs: Peak winding temperature rise versus weight for the air cooled cases.

- The dependency of the power density on the power level is small, compared to the cooling system or speed, but distinguishable. Machines with higher power ratings occupy the lower end of the power density range for most cooling/speed design points. The difference in power density is at most 20% across the considered power range. This trend is believed to be correct, since the machine volume, where the losses originate, scales with n^3, while the area, which dissipates the losses, scales with n^2, necessitating lower loss densities for larger machines.

Note that in these results, some of the 50 or 100 kW machines have an equal or slightly lower power density than the 200 kW machines, which is the result of the minimum stack length imposed in the optimizations.

8.4.3 Detailed results – interface level

This sections presents detailed properties of the optimal machines, focussing on properties relevant for system level design considerations. The aim is to provide as generic trends as possible, to allow the results to be used in other applications as well. Yet, the machines considered here are optimized for power density without any constraints on e.g. rotational speed, outer diameter or length. When fixing such parameters to match a target application, the results may not represent the true optimum for that application.

Figure 8.7 shows the efficiency versus rotor surface speed. Higher power machines and higher rotational speeds will lead to higher efficiencies. This is a fundamental relation, because as the

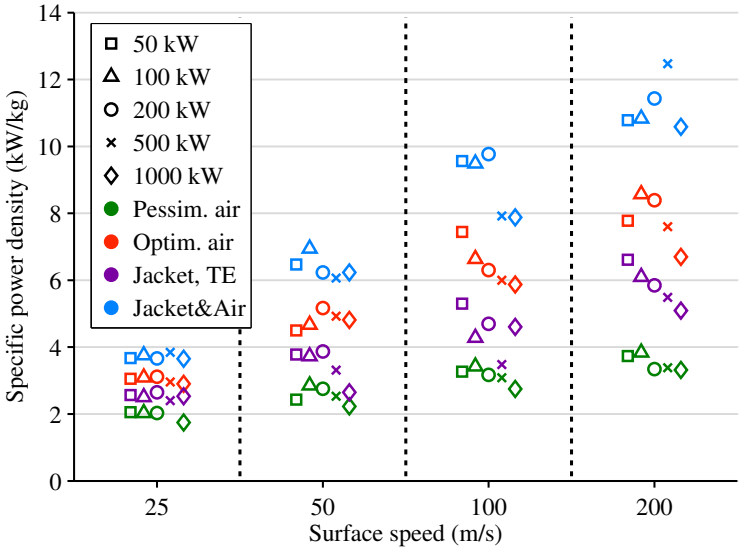

Figure 8.6 Specific power density versus rotor surface speed.

speed increases, the machine size and so the surface area through which the losses are dissipated decrease, ultimately requiring lower losses to maintain acceptable temperatures Most designs fall in the range of 96.5–98.5%. With increased cooling effort, higher loss densities can be accepted and the efficiency will reduce.

Figure 8.8 shows the hot spot winding and magnet temperatures of the selected machines. For the purely air cooled machines, the winding temperature is the limiting factor. This is beneficial, as it allows the power density to be increased by improving the stator cooling, which is generally simpler than improving the rotor cooling. With the mixed cooling system at higher surface speeds, neither the magnet nor winding temperature is clearly limited. For the totally enclosed machine the magnet temperature was by far the limiting factor, regardless of the rotor surface speed. This implies that to improve the power density of totally enclosed machines, it is essential to minimize the rotor losses (by e.g. using magnet segmentation or suitable winding schemes) or to improve the heat transfer away from the rotor. Extreme examples of these approaches can be found in [154] respectively [175].

Directly comparing most dimensions of the greatly different machines considered here is not possible. Instead, the stack outer envelope aspect ratio is considered. Figure 8.9 shows the aspect ratio; a value of 0.5 means that the axial length equals half the stator (machine) outer diameter. A clear preference for short and wide machines is visible. Especially for the pessimistically cooled machines aspect ratios of 0.1 are not uncommon. When increasing the cooling effort, it is attractive to decrease the radius, rather than the length. Only a handful of the 25 m/s machines have an aspect ratio greater than 1.

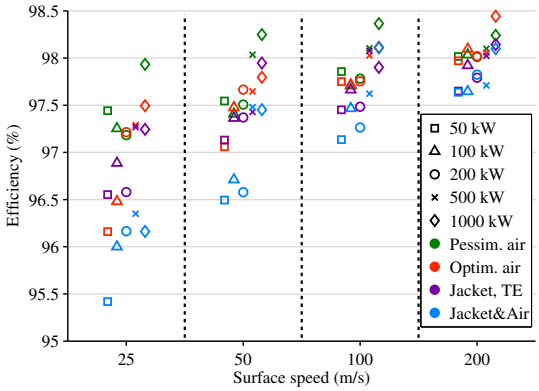

Figure 8.7 Efficiency versus rotor surface speed.

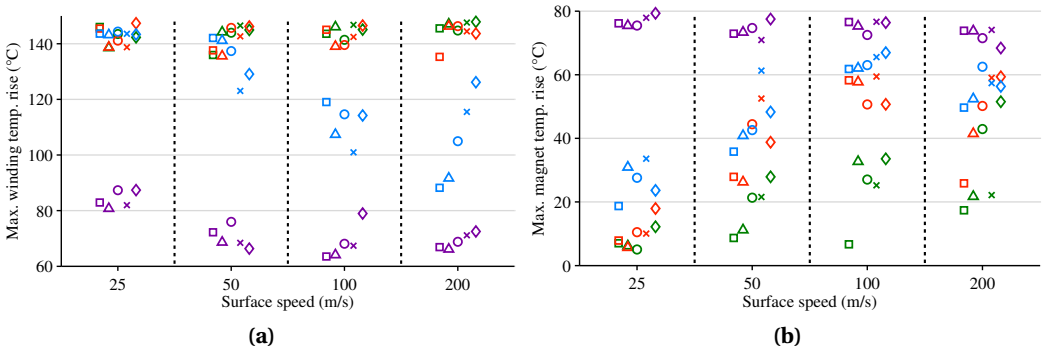

Figure 8.8 Predicted maximum temperature: (a) winding; (b) magnets.

Figure 8.10(a) shows the mechanical airgap length. Note that the magnetic airgap is an additional 2.5 mm longer due to the retaining sleeve. Most machine designs at v_{surf}=25 or 50 m/s have the minimum airgap of 1.5 mm specified in the optimizations. Hence, when performing optimizations at those surface speeds using a fixed, low airgap length can yield satisfactory results. With increasing surface speed, the optimal airgap length increases. This is driven by the need to have a lower flux density in the iron at higher speeds and to maintain acceptable rotor eddy current losses, which would otherwise increase with frequency. A longer optimal airgap is also beneficial in several ways: it reduces windage losses and allows a thicker sleeve to be used if this is mechanically necessary. Therefore, the fixed sleeve thickness used in this work does not lead to infeasible designs. In addition, a longer airgap alleviates the mechanical requirements. To demonstrate this, Figure 8.10(b) shows the airgap length normalized to the rotor outer diameter, which accounts for the fact that shorter airgap lengths are more difficult to accurately maintain in

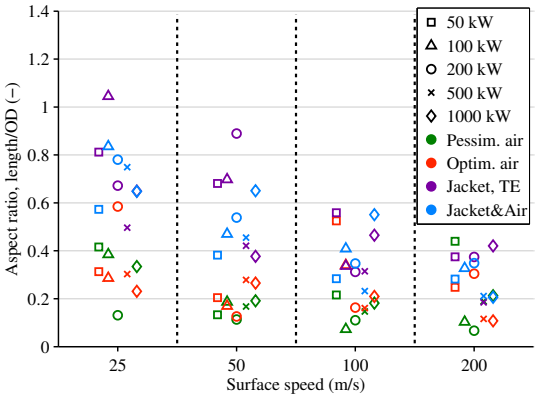

Figure 8.9 Stack aspect ratio versus rotor surface speed.

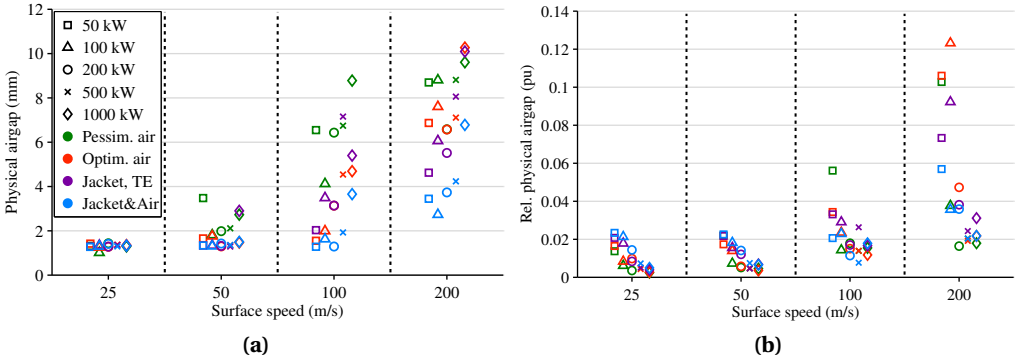

Figure 8.10 Mechanical airgap length versus rotor surface speed: (a) absolute length; (b) relative length (gap length divided by rotor outer diameter).

larger machines. Fortunately, many of the high-speed machines have physical airgap lengths in excess of 2%.

Figure 8.11 shows the rotational speed versus surface speed. Since force density is limited by the airgap flux density, higher output torque requires a larger airgap surface area, reducing the rotational speed. The 50 kW machines rotate about 5–6 times faster than the 1 MW machines for all design variations. Further observe that the optimal rotational speed increases with cooling effort, which is attributed to the higher tolerable loss densities. The lowest speed is 450 RPM for the 1 MW pessimistically air cooled machine at v_{surf}=25 m/s. For the mixed jacket/air cooled system, this increases to 890 RPM. The highest speed occurs for a 50 kW, 200 m/s, mixed jacket/air cooled machine: 31.5 kRPM. Figure 8.12 shows the specific power density versus rotational speed.

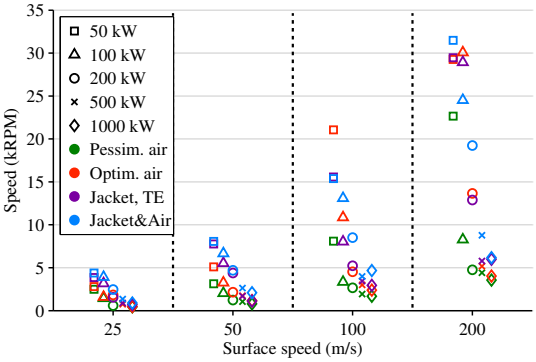

Figure 8.11 Rotational speed versus rotor surface speed.

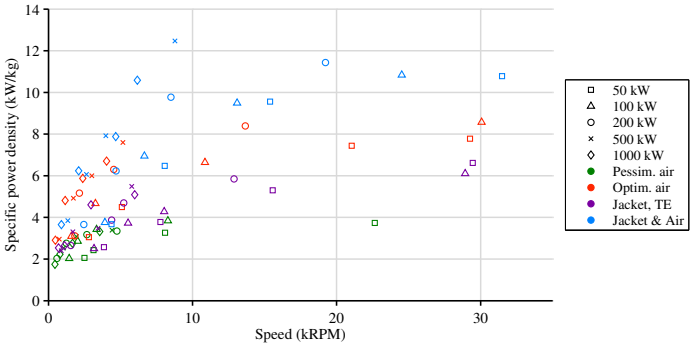

Figure 8.12 Specific power density versus rotational speed.

This shows mostly that high rotational speeds are not necessary to obtain high power densities; no major improvements are observed beyond 10–12 kRPM, regardless of the cooling scenario.

Fig 8.13 shows the electrical frequency. For v≥50 m/s the frequency increases approximately linearly with surface speed. The designs with higher cooling effort (and so higher tolerable loss densities) have higher frequencies. Since the number of poles was an optimization variable, no direct relation to the rotational speed exists: for a given cooling case and surface speed the rotational speed varies over a roughly 10:1 ratio, while the frequency only varies over a 2:1–3:1 ratio. In addition, a fairly large spread exists in the electrical frequency (this becomes even more apparent when considering the non-averaged version of Figure 8.13 (b) (not shown to preserve space)). All in all the results imply that no ideal frequency exists, even for a given power and speed level.

Note that the frequency is considered an external parameter, because it affects the inverter design. With increasing power level and thus inverter size, the achievable switching frequencies reduce

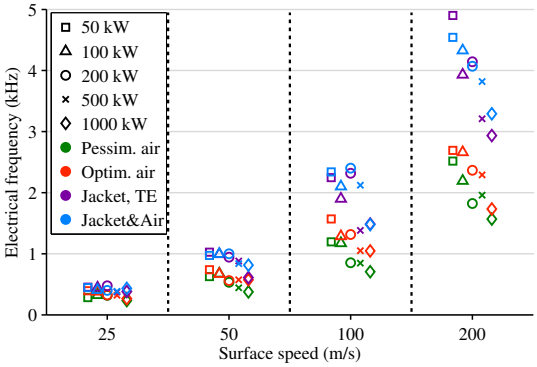

Figure 8.13 Frequency versus rotor surface speed.

and consequently the maximum fundamental electrical frequency. Alternatively, inverters could be derated, increasing cost and size.

Figure 8.14 shows the relative (or per-unit (pu)) synchronous inductance. The design of a machine is linked to the inverter sizing through the pu inductance (besides electrical frequency). Higher inductances require either a larger inverter (when assuming $I_d = 0$; the inverter supplies the reactive magnetizing power) or a larger machine ($I_d < 0$; machine supplies reactive power). On the other hand, a larger inductance also reduces current ripple, which reduces parasitic losses in the machine ([57], Chapter 6). Additionally, the pu inductance is also a rough indication of the magnetic machine utilization. A one per-unit inductance implies that the armature current field has the same order of magnitude as the PM field, leaving less room for transient high torque operation.

The pu inductance is mostly dependent on cooling effort. Machines with high cooling capacity have higher pu inductances, reaching unity inductance for some of the low power low speed machines. This is caused by the maximum electric loading of the machines. In a simple case, increasing the maximum permissible current density of a given machine design, without further adjusting the design, will reduce the pu base impedance and increase the pu phase inductance.

In fault-tolerant applications a machine must be able to withstand permanent short circuits during operation [85]. A typical approach to achieve this is to design machines with a 1 pu inductance. Figure 8.14 shows that machines with optimal power density have an inductance in the range of 0.25–0.6 pu, suggesting that constraining the inductance to 1 pu would reduce the power density. However, a proper quantification would require further optimizations.

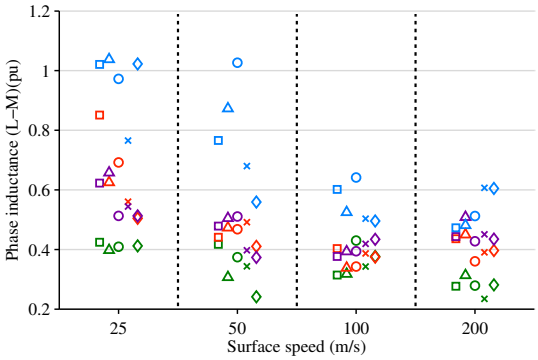

Figure 8.14 Per-unit inductance versus rotor surface speed. A 1 pu inductance would limit the short circuit current to the nominal current.

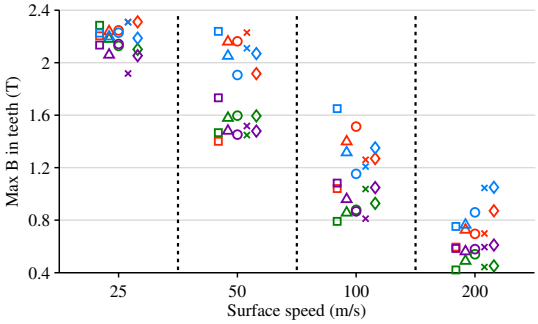

Figure 8.15 Teeth magnetic flux density versus rotor surface speed.

8.4.4 Detailed results – machine level

This section presents further machine properties, focussing on quantities mainly relevant for the design of the machine.

Figure 8.15 shows the peak flux density in the teeth of the selected machines (the yoke flux densities are very similar). Notice that the saturation level of 2.4 T of the FeCo laminations is reached but not exceeded, suggesting that heavily saturating the machines is not attractive. With increasing speed (and so frequency), the flux densities decrease to maintain the loss density acceptable. In fact, the flux density for many machines at v=100 m/s or v=200 m/s is well below 1.4 T, allowing substantially cheaper FeSi laminations to be used instead of FeCo. Moreover, high silicon content FeSi steel types can have lower specific losses than FeCo types for a given sheet thickness, allowing further performance improvements [164].

Figure 8.16 shows the airgap stress (torque divided by rotor radius and surface area), a quantity

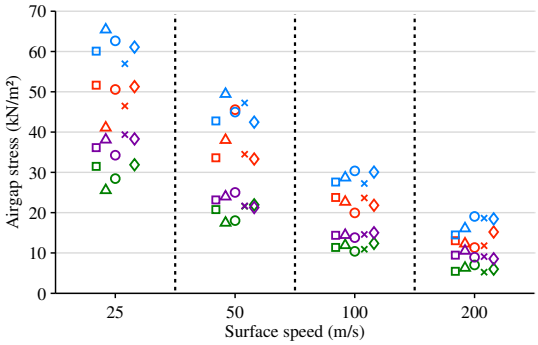

Figure 8.16 Shear force versus rotor surface speed.

often used to compare or dimension electrical machines. The values show a very low dependency on power level –which is desirable for a dimensioning parameter–, but do strongly depend on both surface speed and cooling approach, so this value should always be quoted with those parameters to be useful.

Figure 8.17 shows the distribution of the copper, stator iron and rotor eddy current losses versus cooling scenario. The results are perhaps unsurprising. At v_{surf}=25 m/s the majority of the losses (60–80%) are copper losses (which are mostly frequency independent), with iron losses making up the rest. Hence, these machines are highly electrically loaded, with the iron saturation flux density limiting machine performance. At v_{surf}=200 m/s the situation is inverted, with just 30–40% of the losses in the windings. This again shows that using a low loss lamination type is critical at higher surface speeds. Another conclusion is that in low speed machines, the cooling system should aim at effectively removing heat from the windings, while at high speeds, overall machine cooling becomes more important. The rotor loss share is higher (up to 15% for the highest speed machines) for the purely air cooled machines than the jacket cooled machines (up to 5%), which follows directly from the cooling assumptions. Generally, the loss distribution depends more strongly on surface speed than cooling scenario. Hence, when designing a machine for a given surface speed, aiming for a certain loss distribution is a valid approach.

Figures 8.18 and 8.19 show the RMS current density and linear RMS current density versus surface speed, respectively. The former varies between 6 and 20 A/mm^2, mostly depending on cooling scenario. In simple machine design approaches without thermal models, a fixed value is often assumed for the current density. This figure suggests that this could lead to acceptable results, if an appropriate value is chosen. On the other hand, the linear current density varies over a wider range (10–70 kA/m), strongly depending on the surface speed, but shows less variation for a given surface speed and cooling scenario. Hence, if these quantities are known for a new design, the linear current density may provide a better starting point.

Figure 8.20 shows the specific power density versus cooling scenario (compare to Figure 8.6). This figure very clearly demonstrates that increasing the rotor surface speed becomes more attractive

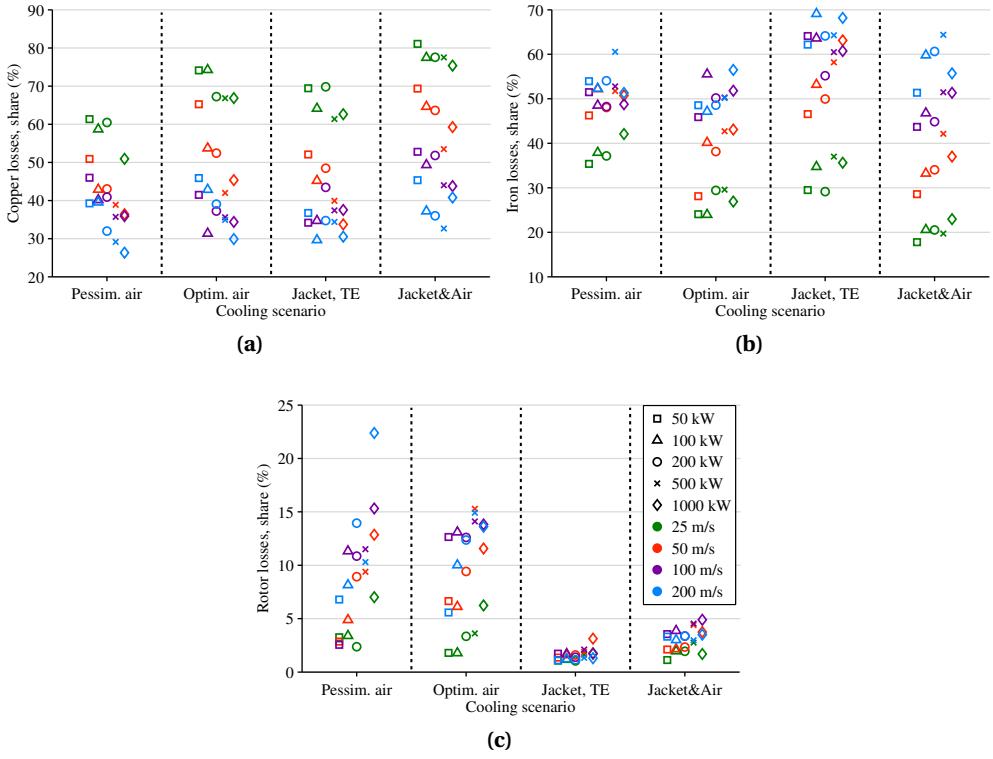

Figure 8.17 Distribution of the main electrical losses: (a) copper losses; (b) stator iron losses; (c) rotor losses.

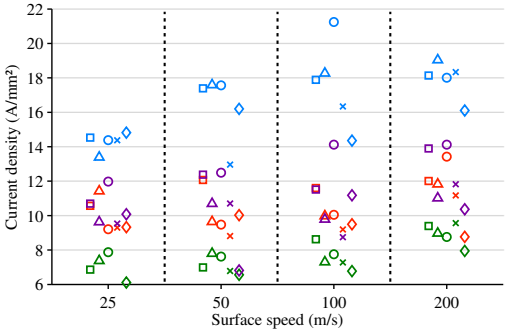

Figure 8.18 RMS current density versus rotor surface speed.

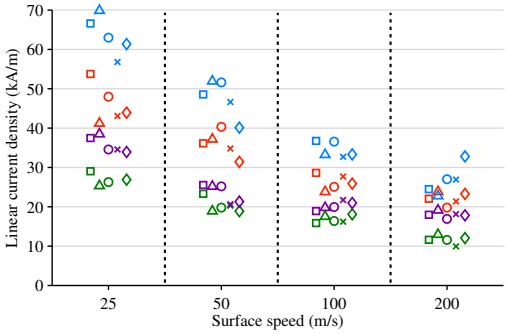

Figure 8.19 Linear RMS current density versus rotor surface speed.

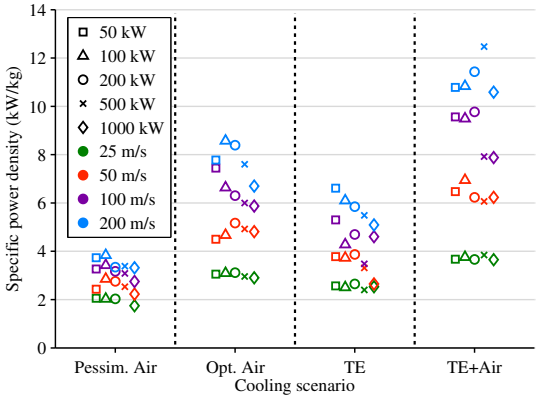

Figure 8.20 Specific power density versus cooling scenario (compare to Figure 8.6).

with better cooling: the power density doubles when increasing v_{surf} from 25 to 200 m/s for the pessimistically cooled machines, but more than triples for the intensively cooled machines.

8.4.5 Lower temperature constraints

The temperature constraints used in the previous section are based on the use of expensive, high performance materials. To investigate the impact of lower permissible temperature rises, Figure 8.21 shows the specific power density versus maximum winding and magnet temperature. The results are averaged over all power levels for this plot, because the power level has only a small impact on power density. It appears that the specific power density follows an almost linear trend with maximum temperature, in particular for the air-cooled machines. This was to be expected, since for a given machine design, increasing the temperature rise by a factor f, requires

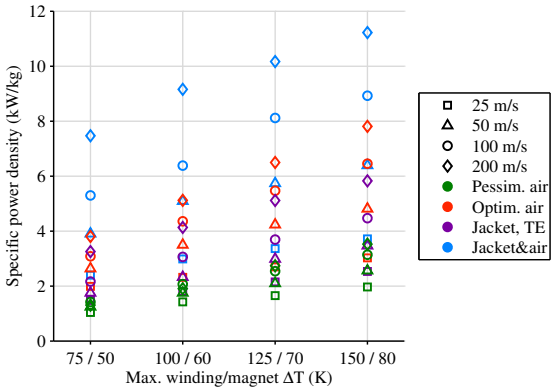

Figure 8.21 Specific power density versus winding and magnet temperature limit, averaged over all power levels.

an increase in losses by the same factor (assuming temperature independent cooling). When all loss mechanisms follow a squared relationship (which holds at high frequencies, where the iron losses are dominated by eddy current losses), an increase by a factor of $\sqrt{f}$ of e.g. current and flux density, or current density and speed, will double both the losses and output power (and so power density). Hence, the power density figures presented in this chapter may be scaled linearly with the acceptable temperature rise to inter- or extrapolate the results. For the totally enclosed liquid cooled and mixed liquid/air cooled machines, this clear relation does not exist; a twofold increase in maximum temperature increases the specific power density by only 1.5 times.

8.5 Discussion

The optimal machines presented and discussed in the previous sections are now compared to designs obtained from literature and a thermal sensitivity analysis is performed.

8.5.1 Literature comparison

Validating the range of machines considered here by constructing prototypes is impossible. As an alternative means to determine the realism of the optimized machines, the results are compared to examples from literature.

Ideally, the specific power density is compared with values obtained from literature. However, most references provide insufficient information to determine the specific power density. This is partially due to most applications having a fixed rotational speed, and the machine design is focussed on obtaining a feasible and efficient machine for this speed, rather than directly

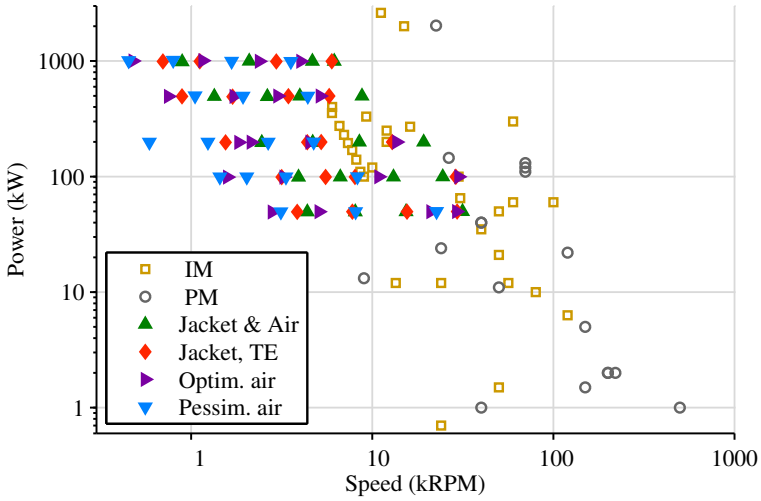

Figure 8.22 Power-speed graph of the optimized machines (solid markers), compared to existing literature examples (hollow markers) [161, 164].

maximizing power density. As an alternative, the machine designs are compared in terms of power and rotational speed, keeping in mind that this is a somewhat unfair comparison. Still, if the optimized machine designs have significantly too low or high power-speed products, it is an indication that the models and assumptions used here were too pessimistic or optimistic.

Figure 8.22 compares the designs presented in the previous sections to examples of induction machines and PM machines from literature. Note that many of the reference designs have surfaces speeds in excess of 200 m/s. The five individual power levels can be clearly recognized. The designs with v_{surf}=200 m/s are in the region of existing machines, especially for the lower power levels. Hence, the designs presented here are not deemed to be unrealistic.

8.5.2 Thermal sensitivity analysis

Thermal constants, especially those related to solid-gas, solid-liquid or non-perfect solid-solid interfaces, have a larger uncertainty than most electrical properties. This is caused by uncertainties in for example the flow regime or surface finish. Consequently, the calculated temperatures will also have a larger uncertainty than the electromagnet properties.

A sensitivity analysis is performed to estimate the impact of variations in the thermal properties. All HTCs in Table 8.2 as well as the thickness and thermal conductivity of the slot liner and the conductivity of the winding insulation and impregnation are randomly varied with a uniform distribution of ±40% span to obtain 10,000 sets of boundary conditions. For each set, the tem-

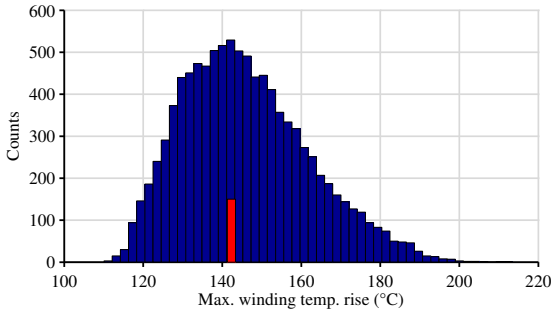

Figure 8.23 Distribution of the winding hot-spot temperatures due to uniformly distributed random variations in thermal properties by ±40%. The red bar indicates reference design.

peratures are computed for the lightest optimistically air cooled machine of 100 kW and 100 m/s (arbitrarily chosen).

Figure 8.23 shows the results, with the red bar indicating the baseline value for the selected design. The standard deviation is 16 K or 11%. This information together with the dependency of power density on the temperature limits (Figure 8.21) can be used to estimate the consequences due to uncertainty in thermal parameters. For example, if the maximum temperature rise of 150 K is to occur for +2 standard deviations as a safety margin, the maximum design temperature should be about 120 K, which reduces the power densities by roughly 20%.

8.6 Conclusion

This chapter proposed and demonstrated a method to determine machine capabilities, bridging the gap between inaccurate but fast analytical design methods and literature based studies. By individually optimizing a range of machines, high and low level trends can be determined. Accurate FEA and lumped element models were used to account for all relevant geometrical, magnetic and thermal effects, providing more detailed results than analytical models.

The proposed method was demonstrated by quantifying the dependency of specific power density on rotor surface speed, power level and cooling effort, demonstrating that increasing the cooling capacity can improve the power density more strongly than increasing the rotor surface speed. The maximum specific power densities obtained are approximately 4 kW/kg for pessimistically air cooled machines, 9 kW/kg for optimistically air cooled machines, 7 kW/kg for totally enclosed jacket cooled machines, and 11–12 kW/kg for machines with both airgap cooling and a liquid jacket. These values refer to the active mass only, plus the mass of the cooling jacket where applicable.

The influence of the power level on the specific power density is very small. At the lowest power

level of 50 kW, the constraint on the minimum stack length slightly limited the performance of these machines. For each surface speed and cooling scenario combination, peak power density was generally obtained for the 200 kW machines. At the highest power level of 1 MW the specific power density marginally reduces, by about 10%. Compared to the impact of rotor surface speed or cooling effort, the specific power density could be considered to be independent of the power level for the range considered in this work.

By further inspection of the results, it is shown amongst others that at high speeds the high saturation flux density offered by FeCo laminations is not needed; that the optimal mechanical airgap length increases up to 1 cm, allowing thicker retaining sleeves to be used or reducing windage losses; and that the airgap stress or linear current densities are (indeed) good machine dimensioning parameters, but only if quoted together with cooling level and rotor surface speed.

Ultimately, using the results (and approach) presented here can be used at several levels: 1. as a reference when performing a similar study for a different case; 2. as a reference work to determine the capabilities of PMSMs for conceptual targets applications or comparisons with existing designs; and 3. as a starting point for new machine designs, using the basic dimensioning parameters given in Figures 8.16–8.19.

CHAPTER 9

Conclusion

The primary goal of the research project leading to this thesis was to provide a candidate design for a prototype starter/generator. For the specific application, a balance had to be found between weight, starting performance, short circuit losses and generator performance. Due to the magnitude of the starting torque and the requirement for low short circuit losses, generator performance is of secondary importance and will generally be sufficient if the other requirements are met. However, good starting performance directly opposes low fault losses and weight, which are the main tradeoffs to be made. The faulted losses are strongly dependent on the per-unit phase inductance, which in turn determines a minimum inverter rating. Ultimately, a prototype machine was designed and built having a short circuit current of 4 pu, which is roughly equal to the starting-to-generating torque ratio. Lower short circuit currents would sharply reduce both machine and inverter feasibility. The prototype was tested, showing a good match between simulations and measurements. Afterwards, the prototype S/G (and associated power electronics) were successfully tested at the clients' facilities. All in all this demonstrates that surface mounted PM machines may be successfully used as starter/generator.

However, before the final S/G design was established, several modeling and analysis steps were necessary.

As a first step, a Pareto based multi-objective optimization strategy was developed, based on PSO and FEA. Such a tool serves two purposes: at first it helps to find machine designs that 'optimally' meet the target specifications and allows various topologies to be compared. However, any real engineering problem has multiple –most likely conflicting– objectives and no single optimal design exists. The designer then has to decide on a specific compromise, but this requires insight into the tradeoffs between the various targets. Gaining insight into a design problem is the second purpose of an optimization algorithm. When using an optimization algorithm it is extremely important that the user and his audience become confident in the results, and can explain various trends that emerge. As a rule of thumb, one should maybe spent as much time checking the output of an optimization run as it took to set it up.

In the analysis and optimization of high-speed machines, rotor losses must be accounted for. If the eddy currents are expected to be inductance limited, calculating the inducing field and the eddy currents becomes a coupled problem. This strongly increases the solution complexity regardless of the modeling approach. A FEM based method was proposed that fits well into the optimization approach proposed earlier. By using a linear model of only the rotor geometry, the mesh can have fewer elements; rotation does not need to be accounted for; and stator saturation, the most likely cause of saturation in SPM machines, does not have to be considered in a transient simulation. All in all this leads to a speed gain of 2–20 times, depending on the machine operating conditions, while still accurately estimating the losses even with pronounced shielding effects. An added benefit is that the method is flexible with regards to rotor shapes, due to the use of FEM.

The high-speed nature of the S/G also requires the additional winding losses to be considered. The initial starter/generator specification called for an extremely low voltage, requiring only a few turns per tooth at most. Regular solid strands were to be used, optionally with discrete parallel strands, and it is well known from literature that this may lead to strand level proximity effects and bundle level skin effects. To accurately estimate the bundle level skin effect (unequal current sharing), including 3D effects such as twisting and the end-windings, no adequate models were found, so a simplified 3D FEM based method was developed and experimentally tested. Using the method, it was demonstrated that even a single twist over the machine length can increase the frequency where current start to diverge by over an order of magnitude. Then, using those models together with transient FEM models, the effects of various loss reduction mechanisms were compared, showing that by carefully using discrete non-twisted strands, performance similar to that of a winding made with an ideal but lower fill factor litz wire may be obtained.

A fourth and last important step was the analysis of turn level, or inter-turn, short circuit faults. This is a broad topic, including estimation of short circuit currents and losses, detection of the fault and post-fault operation. The strand based models from the previous chapter were used for the short circuit calculations. Compared to most existing works, this offers a very high level of detail and easily allows the impact of using parallel strands to be considered. Trends described in literature were confirmed, such as the increased fault losses for short circuits in turns located close to the slot opening, even after applying a terminal level short circuit. Worst case fault current densities approaching 1000 A/mm² were calculated, while in experiments values up to 450 A/mm² were recorded, still limited by the measurement setup. Using parallel strands in safety critical applications brings both benefits and disadvantages. Major advantages include the reduced likelihood of high localized losses and the better fault current suppression by a terminal level short circuit. A disadvantage is that the worst case total losses may be somewhat higher than with a single strand.

The potentially high fault current densities in high-speed machines stress the importance of a fault detection system. In this thesis, a simple fault detection system is proposed, suitable for implementation as an independent observer of a drive system. The system applies synchronous detection at the fundamental frequency to the difference between the ideal inverter neutral voltage and actual machine neutral voltage. As such, it provides an indication of the three phase system imbalance. The performance was characterized by simulations and measurements on two

totally different systems. With a careful system design, faults down to 0.4% of the winding can be detected, albeit only at sufficiently high speeds. The strong dependency of the sensitivity on speed is a disadvantage of the method. A second disadvantage is that no real system is perfectly balanced. Changes in speed, i_d, i_q or connection order will change the natural imbalance. These changes may exceed the imbalance level caused by small faults, making the reliable detection of small faults difficult. This fundamental limitation will affect any fault detection scheme, as every imbalance can be seen as a fault.

After having confirmed the correctness of the machine models with the prototype machine, they were applied one last time to determine power density limits for PMSMs versus rotor surface speed, power level and cooling system. An approach is proposed and demonstrated to find highly detailed trends and limits from a set of carefully selected optimization runs. Main findings include that increasing the cooling capacity can improve the power density more strongly than increasing the rotor surface speed and that peak power densities beyond 10 kW/kg are possible with a mixed liquid/air cooling system. The method also confirms well known machine design trends, such as the suitability of the linear current density as a design parameter. The fact that such trends and expectations were not included in the optimization algorithms, partially confirms the modeling and optimization approach. Further confirmation was obtained by comparing the results to a range of designs from literature.

Contributions

Since the work in this thesis is motivated by a technical research project, the contributions can be divided in two groups. First, the scientific contributions of this thesis can be summarized as follows:

- The suitability of multi-objective optimization methods as a tool to systematically compare and select machine topologies was demonstrated. Additionally, such methods are a means to gain insight into design problems.
- A finite element based rotor loss calculation method for surface mounted PM machine was proposed. The method offers a speed improvement over a direct transient solution of a full machine model, without losing generality.
- A FE based method to estimate unbalanced current sharing effects between parallel strands was proposed and demonstrated. With this method, individual strands can be accurately accounted for with 3D FEA, using only very moderate computing resources.
- The short circuit losses for turn-to-turn faults were computed with full account of parallel strands and the position of the strands in the slots. The findings suggest that using parallel strands is beneficial in safety critical applications, because the peak per-turn losses are less than those with a single strand winding and because a better current equalization is obtained after applying an all-phase terminal short circuit.

- The potential dangers of turn-to-turn short circuits in high-speed machines were experimentally demonstrated, with measured current densities up to 450 A/mm² for a single turn short circuit.
- A fault detector scheme aimed at a simple implementation was proposed and tested. When properly adjusted, short circuit faults covering less than 1% of the winding can still be detected.
- A large scale optimization approach to quantify limits and trends of electrical machines was demonstrated.
- Power density limits and associated design trends were quantified.

Then, a number of engineering contributions can be identified:

- A surface mounted PM machine was successfully designed for a starter/generator application, meeting conflicting requirements for starting torque, generator efficiency, short circuit losses and weight.
- Various winding AC loss reduction mechanisms were quantitatively compared, showing that by carefully selecting the wire sizing and winding style, the use of litz wire can be avoided.
- Finally, all chapters together perhaps demonstrate that finite element modeling of electrical machines has matured to a point that it may be used throughout the entire design cycle of electrical machines, varying from large scale exploratory optimization applications to highly detailed parasitic loss analyses.

Recommendations

Although the methods proposed in this thesis were successfully used to design a prototype machine, further improvements are possible:

- The optimization approach as presented in this thesis uses 2D estimations for the inductance and linked PM flux, because direct 3D calculations are too time consuming. In the design of the S/G, the value of the phase inductance is critical, because it determines both the short circuit losses and inverter VA rating. An accurate and fast 3D estimate of the phase inductance will further reduce the design time, since no post-optimization 3D checks are required anymore. An important requirement of such an estimation method is that it should be flexible with regards to the machine type and geometry, and be based on little assumptions.
- While at an abstract level the design approach can be applied to any machine type, the analysis time for a single model may become prohibitive. In practise, an analysis time in the order of 1 minute per design allows one to obtain satisfactory results in a few days. If the approach is to be used for other machine types, such as induction machines, modeling

simplifications may need to be investigated to obtain sufficiently fast, yet still accurate performance estimates for those machines.

- In high speed machines, mechanical rotor dynamics and static forces cannot always be fully neglected. A logical step would then be to include sufficiently accurate estimates of those properties in the modeling steps.
- While a fault detection and mitigation scheme are presented in this thesis and many others can be found in literature, it remains difficult to easily and reliably detect single turn faults, especially with higher turn counts. For high reliability applications, research into completely different safety approaches may ultimately lead to a higher reliability than existing fault detection methods.

APPENDIX A

Thermal model

This appendix briefly describes and demonstrates the thermal model used in the main part of this thesis.

A.1 Introduction

The maximum temperatures inside the various machine parts, along with material types used, ultimately determine the rating of the machine. Correctly predicting these temperatures is thus import in the design stage if a high power density is the goal. This becomes even more important in transiently loaded machines, partially because an increased cooling effort to 'correct' for wrongly predicted temperatures after construction will be less effective than in the steady state case.

A 'classical' thermal modeling method is the lumped element network. Such a model can yield acceptable results and account for 3D heat flows, even with 10–20 nodes. At another end of the modeling spectrum is 3D FEA, which, although potentially very accurate, is computationally more intense. Two-dimensional FEM is of limited use, because of axial heat flows occurring in e.g. the windings, shaft or cooling medium. This is obviously more pronounced in relatively short machines ('pancake' machines).

A problem with any thermal model is the determination of heat transfer coefficients between the solid parts machine parts and the cooling medium (gas or liquid). Examples include the airgap, outer housing and end-winding regions. Moreover, small interface gaps, such as those between the stator lamination and housing or the winding and slot wall, introduce additional uncertainty in the model. Although an impression of expected values can be obtained from literature [170–172] or by using CFD (which is very computationally intensive)[176, 177], the actual values still depend strongly on the material type and finishing, processing steps and assembly techniques. As a

result, thermal models will typically have greater uncertainties than e.g. electromagnetic models. Therefore, the use of 'accurate' FEA is questionable, especially during initial design stages.

In this work, a lumped element network is therefore employed, as it is believed to offer sufficient accuracy at significant time savings. Different from some classical lumped element network models, the network in this work is not simplified to a bare minimum number of nodes, as such a simplification is based on assumptions that reduce the generality. Instead, a grid-like network of nodes, following the shape of the geometry is employed. It is believed that this approach ultimately offers more flexibility.

The model only considers the heat conduction in the solid parts. This is perhaps not fully realistic, but for the purpose of comparing machines this approach can still suffice, provided that identical and sufficiently realistic boundary conditions are used.

A.2 Model description

This section describes the various parts of the thermal model.

A.2.1 Heat conduction in solid parts

The thermal properties of solid materials are relatively well known and can be used directly to determine the lumped thermal resistances. When determining these parameters, the machine geometry is imaginarily divided in a grid of squares or a circular grid. Note that if the grid-size is small compared to the geometry, a square grid can even accurately describe a circular geometry. To trade-off accuracy and speed, the node-density in many parts is a parameter. In addition to the (unavoidable) heat load, a heat capacity is also computed to allow useful transient computations to be performed. The heat load may be made linearly temperature dependent, to account for e.g. temperature dependent copper losses. In addition, individual resistors may be set as non-linear resistors, using arbitrary equations involving any node-temperature available, so that e.g. non-linear passive convection can be included (although this feature is not used at this point).

In 2D models, only the in-stack cross sections of the stator and rotor are included. 3D modeling is not conceptually different than 2D modeling, but more time is needed to create, solve and validate the models. The 3D model consists of four separate regions:

- An in-stack stator part. Multiple stacked layers of the 2D network are used. The number of layers can be varied as desired.
- An 'upstream' end-winding part. This part is connected to the winding part of the in-stack network. If an axial airflow with temperature gradient is imposed, this part is near the entrance.
- A 'downstream' end-winding part. The network is a mirrored copy of the upstream part, but the boundary conditions may differ.

- An in-stack rotor part. Multiple stacked layers of the 2D network are used.

This network describes the solid, magnetically active part of the machine. Additional constructional or housing parts, such as a stator casing, end-plates, shaft and bearings, may be added to the boundaries of the model as needed.

A.2.2 Application of boundary conditions

Boundary conditions are needed to fully specify a model. The following boundary conditions are available:

Insulation This is the default boundary condition that naturally results from a thermal network if no further actions are taken.

Temperature source A hard temperature source may be specified, implying that the node temperature at this node is no longer an unknown.

Temperature source through Heat Transfer Coefficient In this case the node is connected to a temperature source through a constant resistor, its value depending on a given HTC and the area of the node face.

To model an actual machine, the last boundary condition is typically used. To this end, individual temperatures and HTC values are assigned to all surfaces subjected to a cooling medium; see Figure 8.3 on page 165 and the associated table for an example. The values for the HTCs are in many cases obtained from literature.

A.2.3 Special nodes

To enable a number of advanced modeling options, two special nodes are created:

- a temperature and heat flow dependent temperature source, and
- a temperature and heat flow dependent heat source.

Those nodes can be used to account for e.g. axial temperature rise of a coolant, or to couple rotor and stator side models that span a different tangential fraction of the machine (ie. practically all machine models, since the number of rotor magnets or bars rarely equals the number of stator slots). In the latter case, a uni-directional transformer is used[1], with a $1:1$ ratio for the temperature and a $1:x$ ratio for the heatflow.

[1] remember that an ideal transformer can be modeled with back-to-back connected controlled voltage and current sources.

A.3 FEM validation

In this section the thermal model is compared to thermal FE models to estimate the accuracy, both in 2D and 3D.

A.3.1 2D validation

A transient 2D simulation of the actual geometry is executed. Care was taken to ensure a correct heat load for both the LE and FE models. Since only the solid parts are of concern, a temperature source of 300 K is specified on the stator outer boundary and shaft inner boundary, while the airgap is made inactive (ie. the rotor and stator models are completely independent). All models are linear.

Figure A.1 shows the steady state solution of the network. The machine considered for this test is realistic in terms of flux density, but intended for short-duration operation, hence the ΔT of 200 K for the winding, even with 300 K imposed on the stator surface. The largest relative error occurs in the tooth tip, but is still less than 10%. Inside the windings, an absolute deviation of 10 K exists, which is partly caused by the fact that the FE model does not consider the slot liner. The winding hot-spot temperature deviates by only 2%. Inside the rotor, the error is typically far less than 5%.

Figure A.2 shows the transient solution for both the LEM and FEM. Note that some temperatures have not yet settled, but only the first part is shown to better reveal the time constants. All time constants are correctly predicted.

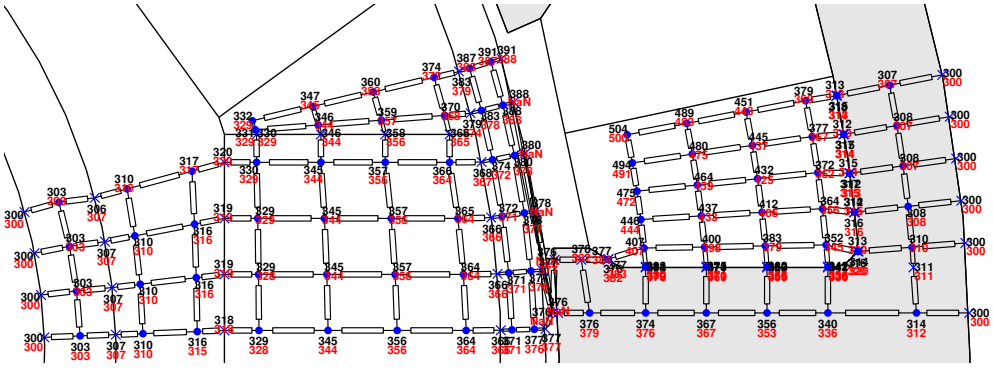

Figure A.1 Node temperatures in steady state. Black temperatures are those computed with the thermal network, red are obtain from FEM.

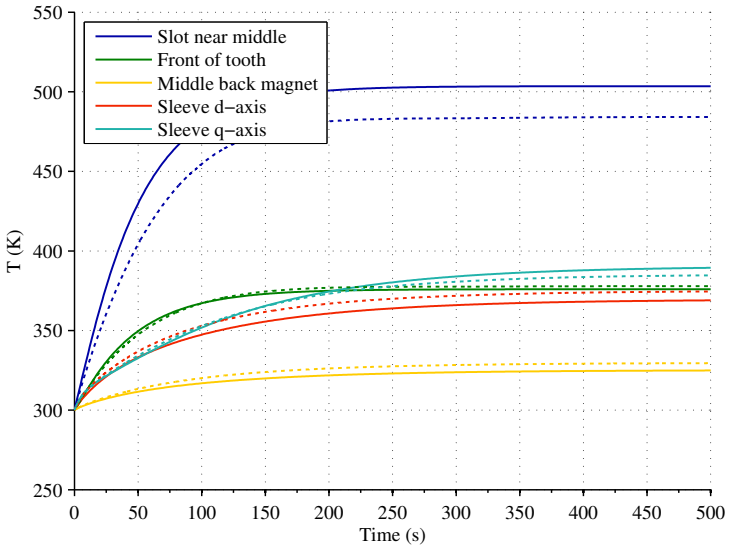

Figure A.2 Several node temperatures as function of time. Solid lines: lumped element network; dashed lines: FEM.

A.3.2 3D validation

It is not uncommon that the end-windings are the hottest part of a machine and they should therefore be considered in the thermal modeling process, requiring the use of 3D models. Moreover, axial temperature gradients in e.g. the forced cooling air also require a 3D model. The 2D model from the previous section was therefore extended to 3D, which will be detailed in this section. The 3D network is created by stacking 2D layers and adding the end-windings; an impression of the resulting network is given in Figure A.3.

To validate the correctness of the model, an equivalent 3D FE model was created for comparison. Figure A.4 shows the solved FE model in the same orientation as the lumped element network. To place emphasis on the thermal model inside the solid parts rather than the boundary conditions, a simple constant temperature of 300 K was enforced on the stator outer surface and the rotor inner surface (identical to the 2D case). With both the FEM and LEM, anisotropic conductivities were set in the laminations and windings for the in-plane and axial conductivities (lamination: respectively 29 and 0.6 W/(m·K), windings: 2 and 195 W/(m·K)).

Surface plots like Figure A.4 cannot easily be made with the LEM. For comparison, the temperatures at several locations along the length of the machine are plotted instead in Figure A.6. The worst absolute error in the winding is about 10 K, occurring at the back near the tooth/yoke intersection. This can possibly be explained by the fact that the slot rounding is not considered in the LEM, while the slot liner is ignored in the FEM. The relative error in this point is 25%. However,

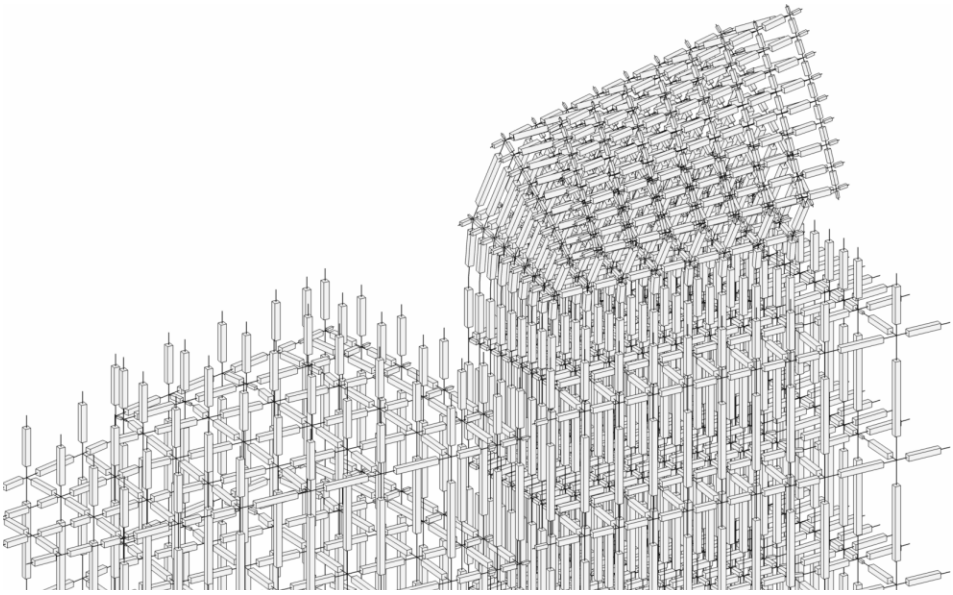

Figure A.3 Depiction of the 3D lumped element network.

since this is the coolest part of the winding, this is not seen as an issue. The hot-spot temperature is predicted to within 5 K, a relative error of 2 %, which is deemed acceptable.

The temperature profile along the tooth front is shown in Figure A.5. The absolute error is again 10 K, the relative error is about 12%.

The LEM was (partially) created to be faster than the FEM. The 3D LEM takes about 1.3 s (with 2232 degrees of freedom) to be created and solved from scratch, while the FEM takes about 20 s (6000 degrees of freedom, standard 'Coarse' mesh size). In a machine optimization with about 3000 function evaluations this equates to a time saving of 16 hours (with all electromagnetic analyses taking about 24–48 hours).

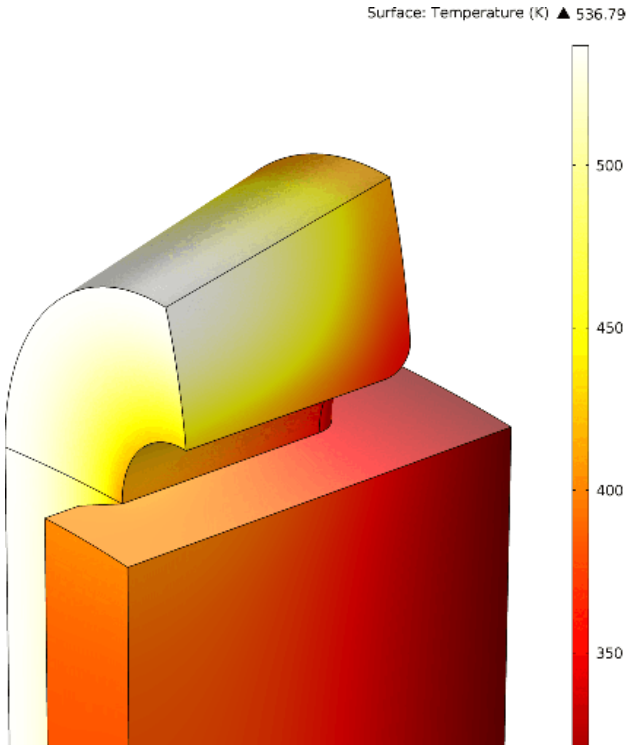

Figure A.4 Solution of the 3D FEM model.

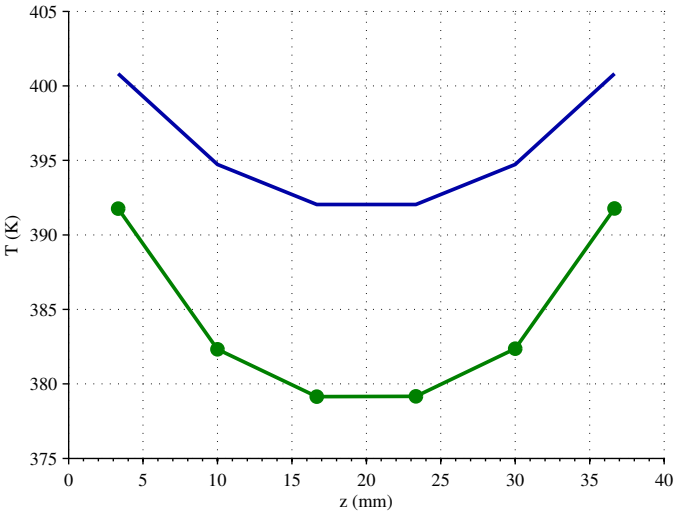

Figure A.5 Temperature profile along the middle front of the tooth. The dotted green line is the FEM result. In both models, the yoke outside surface was kept at 300 K.

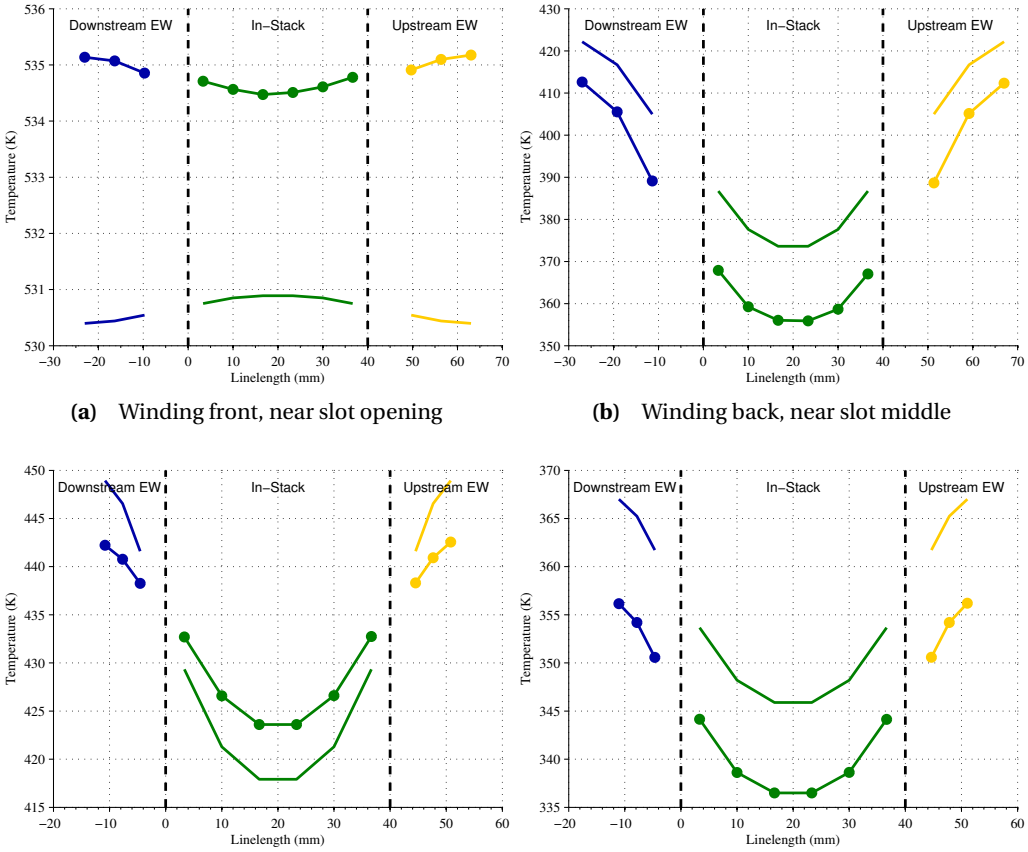

(a) Winding front, near slot opening

(b) Winding back, near slot middle

(c) Winding front, near tooth

(d) Winding back, near tooth

Figure A.6 Temperature at various locations inside the winding, along the path of the wires. The dotted lines are the FEM result, the solid lines the LEM.

Bibliography

[1] S. Palko and T. Jokinen, "Optimisation of squirrel cage induction motors using finite element method and genetic algorithms," in *Proc. Eighth Int. Electrical Machines and Drives Conf. (Conf. Publ. No. 444)*, 1997, pp. 21–25.

[2] J. Lahteenmaki, "Optimisation of high-speed motors using a genetic algorithm," in *Proc. Eighth Int. Electrical Machines and Drives Conf. (Conf. Publ. No. 444)*, 1997, pp. 26–30.

[3] S. Williamson and C. I. McClay, "Optimization of the geometry of closed rotor slots for cage induction motors," *IEEE Trans. Ind. Appl.*, vol. 32, no. 3, pp. 560–568, 1996.

[4] J. Legranger, G. Friedrich, S. Vivier, and J. C. Mipo, "Combination of finite-element and analytical models in the optimal multidomain design of machines: Application to an interior permanent-magnet starter generator," *IEEE Trans. Ind. Appl.*, vol. 46, no. 1, pp. 232–239, 2010.

[5] J.-H. Seo, S.-M. Kim, and H.-K. Jung, "Rotor-design strategy of IPMSM for 42V integrated starter generator," *IEEE Trans. Magn.*, vol. 46, no. 6, pp. 2458–2461, 2010.

[6] G. Pellegrino and F. Cupertino, "FEA-based multi-objective optimization of IPM motor design including rotor losses," in *Proc. IEEE Energy Conversion Congress and Exposition (ECCE)*, 2010, pp. 3659–3666.

[7] C. A. C. Coello, G. T. Pulido, and M. S. Lechuga, "Handling multiple objectives with particle swarm optimization," *IEEE Trans. Evol. Comput.*, vol. 8, no. 3, pp. 256–279, 2004.

[8] Y. Duan and R. G. Harley, "A novel method for multiobjective design and optimization of three phase induction machines," *IEEE Trans. Ind. Appl.*, vol. 47, no. 4, pp. 1707–1715, 2011.

[9] N. Bianchi and S. Bolognani, "Design optimisation of electric motors by genetic algorithms," *IEE Proceedings -Electric Power Applications*, vol. 145, no. 5, pp. 475–483, 1998.

[10] Y. Duan, R. G. Harley, and T. G. Habetler, "A useful multi-objective optimization design method for PM motors considering nonlinear material properties," in *Proc. IEEE Energy Convers. Congr. and Expo.*, 2009, pp. 187–193.

[11] S. A. Semidey, Y. Duan, J. R. Mayor, R. G. Harley, and T. G. Habetler, "Optimal electromagnetic-thermo-mechanical integrated design candidate search and selection for surface-mount permanent-magnet machines considering load profiles," *IEEE Trans. Ind. Appl.*, vol. 47, no. 6, pp. 2460–2468, Nov. 2011.

[12] A. Mahmoudi, S. Kahourzade, N. A. Rahim, and W. P. Hew, "Design, analysis, and prototyping of an axial-flux permanent magnet motor based on genetic algorithm and finite-element analysis," *IEEE Trans. Magn.*, vol. 49, no. 4, pp. 1479–1492, Apr. 2013.

[13] M. Rottach, C. Gerada, T. Hamiti, and P. W. Wheeler, "A computationally efficient design procedure for actuator motors using magnetic reluctance-and thermal resistance network models," in *XXth Int. Conf. Electrical Machines (ICEM)*, Sep. 2012, pp. 2526–2532.

[14] R. Wrobel and P. H. Mellor, "Particle swarm optimisation for the design of brushless permanent magnet machines," in *Conf. Rec. 41st IEEE IAS Annu. Meeting*, vol. 4, 2006, pp. 1891–1897.

[15] F. Bittner and I. Hahn, "Kriging-assisted multi-objective particle swarm optimization of permanent magnet synchronous machine for hybrid and electric cars," in *IEEE Int. Electric Machines Drives Conf. (IEMDC)*, 2013, pp. 15–22.

[16] P. Zhang *et al.*, "Multi-objective tradeoffs in the design optimization of a brushless permanent magnet machine with fractional-slot concentrated windings," *IEEE Trans. Ind. Appl.*, vol. 50, no. 5, pp. 3285–3294, Sep.-Oct. 2014.

[17] G. Sizov, D. Ionel, and N. Demerdash, "Modeling and parametric design of permanent magnet AC machines using computationally efficient - finite element analysis," *IEEE Trans. Ind. Electron.*, vol. 59, no. 6, pp. 2403–2413, Jun 2012.

[18] M. Popescu, D. M. Ionel, T. J. E. Miller, S. J. Dellinger, and M. I. McGilp, "Improved finite element computations of torque in brushless permanent magnet motors," *IEE Proc. Electric Power Appl.*, vol. 152, no. 2, pp. 271–276, 2005.

[19] J. Kennedy and R. Eberhart, "Particle swarm optimization," in *Proc. Conf. IEEE Int Neural Networks*, vol. 4, 1995, pp. 1942–1948.

[20] Y. del Valle, G. K. Venayagamoorthy, S. Mohagheghi, J.-C. Hernandez, and R. G. Harley, "Particle swarm optimization: Basic concepts, variants and applications in power systems," *IEEE Trans. Evol. Comput.*, vol. 12, no. 2, pp. 171–195, Apr. 2008.

[21] D. Ishak, Z. Q. Zhu, and D. Howe, "Comparison of PM brushless motors, having either all teeth or alternate teeth wound," *IEEE Trans. Energy Convers.*, vol. 21, no. 1, pp. 95–103, 2006.

[22] W. L. Soong and T. J. E. Miller, "Field-weakening performance of brushless synchronous AC motor drives," *IEE Proc. Electr. Power Appl.*, vol. 141, no. 6, pp. 331–340, 1994.

[23] Z. Q. Zhu and J. T. Chen, "Advanced flux-switching permanent magnet brushless machines," *IEEE Trans. Magn.*, vol. 46, no. 6, pp. 1447–1453, 2010.

[24] A. S. Thomas, Z. Q. Zhu, and G. W. Jewell, "Comparison of flux switching and surface mounted permanent magnet generators for high-speed applications," *IET Electrical Systems in Transportation*, vol. 1, no. 3, pp. 111–116, 2011.

[25] Y. Pang *et al.*, "Comparative study of flux-switching and interior permanent magnet machines," in *Proc. ICEMS Electrical Machines and Systems Int. Conf*, 2007, pp. 757–762.

[26] J. T. Chen, Z. Q. Zhu, A. S. Thomas, and D. Howe, "Optimal combination of stator and rotor pole numbers in flux-switching PM brushless AC machines," in *Proc. Int. Conf. Elect. Machines and Systems ICEMS*, 2008, pp. 2905–2910.

[27] JFE electrical steel. [Online]. Available: http://www.jfe-steel.co.jp/en/products/electrical/index.html

[28] G. Pellegrino, A. Vagati, P. Guglielmi, and B. Boazzo, "Performance comparison between surface mounted and interior PM motor drives for electric vehicle application," *IEEE Trans. Ind. Electron.*, vol. 59, no. 2, pp. 803–811, Feb. 2012.

[29] D. Evans, Z. Azar, L. J. Wu, and Z. Q. Zhu, "Comparison of optimal design and performance of PM machines having non-overlapping windings and different rotor topologies," in *Proc. IET Int. Power Electron., Machines and Drives (PEMD)*, 2010, pp. 1–7.

[30] J. J. Wolmarans, M. van der Geest, H. Polinder, J. A. Ferreira, and D. Zeilstra, "Composite materials for low loss rotor construction," in *IEEE Int. Elec. Mach. Drives Conf.*, 2011, pp. 295–299.

[31] L. dos Santos Coelho, L. Z. Barbosa, and L. Lebensztajn, "Multiobjective particle swarm approach for the design of a brushless DC wheel motor," *IEEE Trans. Magn.*, vol. 46, no. 8, pp. 2994–2997, 2010.

[32] A. Jassal, H. Polinder, and J. A. Ferreira, "Literature survey of eddy-current loss analysis in rotating electrical machines," *IET Electric Power Appl.*, vol. 6, no. 9, pp. 743–752, Nov. 2012.

[33] F. Deng, "Commutation-caused eddy-current losses in permanent-magnet brushless DC motors," *IEEE Trans. Magn.*, vol. 33, no. 5, pp. 4310–4318, Sep. 1997.

[34] Z. Q. Zhu, K. Ng, N. Schofield, and D. Howe, "Improved analytical modelling of rotor eddy current loss in brushless machines equipped with surface-mounted permanent magnets," *IEE Elect. Power Appl.*, vol. 151, no. 6, pp. 641–650, Nov. 2004.

[35] A. Jassal, H. Polinder, D. Lahaye, and J. A. Ferreira, "Comparison of analytical and finite element calculation of eddy-current losses in PM machines," in *Int. Conf. Elect. Machines (ICEM)*, Sep. 2010, pp. 1–7.

[36] L. J. Wu, Z. Q. Zhu, D. Staton, M. Popescu, and D. Hawkins, "Analytical model for predicting magnet loss of surface-mounted permanent magnet machines accounting for slotting effect and load," *IEEE Trans. Magn.*, vol. 48, no. 1, pp. 107–117, Jan. 2012.

[37] J. Pyrhönen, H. Jussila, Y. Alexandrova, P. Rafajdus, and J. Nerg, "Harmonic loss calculation in rotor surface permanent magnets—new analytic approach," *IEEE Trans. Magn.*, vol. 48, no. 8, pp. 2358–2366, Aug. 2012.

[38] F. Martin, M. E.-H. Zaïm, A. Tounzi, and N. Bernard, "Improved analytical determination of eddy current losses in surface mounted permanent magnets of synchronous machine," *IEEE Trans. Magn.*, vol. 50, no. 6, pp. 1–9, Jun. 2014.

[39] K. Yamazaki and Y. Fukushima, "Effect of eddy-current loss reduction by magnet segmentation in synchronous motors with concentrated windings," *IEEE Trans. Ind. Appl.*, vol. 47, no. 2, pp. 779–788, Mar. 2011.

[40] A. R. Tariq, C. E. Nino-Baron, and E. G. Strangas, "Iron and magnet losses and torque calculation of interior permanent magnet synchronous machines using magnetic equivalent circuit," *IEEE Trans. Magn.*, vol. 46, no. 12, pp. 4073–4080, Dec. 2010.

[41] N. Schofield, K. Ng, Z. Q. Zhu, and D. Howe, "Parasitic rotor losses in a brushless permanent magnet traction machine," in *Int. Conf. Elect. Machines and Drives (Conf. Publ. No. 444)*, Sep. 1997, pp. 200–204.

[42] P. Zhang, G. Y. Sizov, J. He, D. M. Ionel, and N. A. O. Demerdash, "Calculation of magnet losses in concentrated-winding permanent magnet synchronous machines using a computationally efficient - finite element method," *IEEE Trans. Ind. Appl.*, vol. 49, no. 99, pp. 2524–2532, Nov. 2013.

[43] F. Luise, A. Tessarolo, F. Agnolet, and M. Mezzarobba, "Use of time-harmonic FE analysis to compute rotor eddy-current losses in synchronous machines subject to distorted stator currents," in *Int. Conf. Elect. Machines (ICEM)*, Sep. 2012, pp. 1503–1509.

[44] K. Yamazaki and Y. Kanou, "Rotor loss analysis of interior permanent magnet motors using combination of 2-D and 3-D finite element method," *IEEE Trans. Magn.*, vol. 45, no. 3, pp. 1772–1775, Mar. 2009.

[45] T. Okitsu, D. Matsuhashi, Y. Gao, and K. Muramatsu, "Coupled 2-d and 3-d eddy current analyses for evaluating eddy current loss of a permanent magnet in surface pm motors," *IEEE Trans. Magn.*, vol. 48, no. 11, pp. 3100–3103, Nov. 2012.

[46] P. Zhang *et al.*, "Multi-objective tradeoffs in the design optimization of a brushless permanent magnet machine with fractional-slot concentrated windings," in *Energy Conversion Congr. Expo. (ECCE)*, 2013, pp. 2842–2849.

[47] *COMSOL Multiphysic Reference Manual*, COMSOL AB, 2014.

[48] K. Yamazaki *et al.*, "Reduction of magnet eddy-current loss in interior permanent-magnet motors with concentrated windings," *IEEE Trans. Ind. Appl.*, vol. 46, no. 6, pp. 2434–2441, Nov 2010.

[49] M. Mirzaei, A. Binder, B. Funieru, and M. Susic, "Analytical calculations of induced eddy currents losses in the magnets of surface mounted PM machines with consideration of circumferential and axial segmentation effects," *IEEE Trans. Magn.*, vol. 48, no. 12, pp. 4831–4841, Dec. 2012.

[50] N. Bianchi, S. Bolognani, and E. Fornasiero, "An overview of rotor losses determination in three-phase fractional-slot pm machines," *IEEE Trans. Ind. Appl.*, vol. 46, no. 6, pp. 2338–2345, Nov. 2010.

[51] A. M. El-Refaie, "Fractional-slot concentrated-windings synchronous permanent magnet machines: Opportunities and challenges," *IEEE Trans. Ind. Electron.*, vol. 57, no. 1, pp. 107–121, Jan. 2010.

[52] D. G. Dorrell *et al.*, "A review of the design issues and techniques for radial-flux brushless surface and internal rare-earth permanent-magnet motors," *IEEE Trans. Ind. Electron.*, vol. 58, no. 9, pp. 3741–3757, Sep. 2011.

[53] G. J. Atkinson *et al.*, "The analysis of losses in high-power fault-tolerant machines for aerospace applications," *IEEE Trans. Ind. Appl.*, vol. 42, no. 5, pp. 1162–1170, Sep.–Oct. 2006.

[54] M. Fujita *et al.*, "Circulating currents in stator coils of large turbine generators and loss reduction," *IEEE Trans. Ind. Appl.*, vol. 45, no. 2, pp. 685–693, Mar.-Apr. 2009.

[55] L. J. Wu, Z. Q. Zhu, D. Staton, M. Popescu, and D. Hawkins, "Analytical model of eddy current loss in windings of permanent-magnet machines accounting for load," *IEEE Trans. Magn.*, vol. 48, no. 7, pp. 2138–2151, Jul. 2012.

[56] A. S. Thomas, Z. Q. Zhu, and G. W. Jewell, "Proximity loss study in high speed flux-switching permanent magnet machine," *IEEE Trans. Magn.*, vol. 45, no. 10, pp. 4748–4751, Oct. 2009.

[57] S. Iwasaki *et al.*, "Influence of PWM on the proximity loss in permanent-magnet brushless AC machines," *IEEE Trans. Ind. Appl.*, vol. 45, no. 4, pp. 1359–1367, Jul.–Aug. 2009.

[58] J. A. Ferreira, "Improved analytical modeling of conductive losses in magnetic components," *IEEE Trans. Power Electron.*, vol. 9, no. 1, pp. 127–131, Jan. 1994.

[59] R.-J. Wang and M. J. Kamper, "Calculation of eddy current loss in axial field permanent-magnet machine with coreless stator," *IEEE Trans. Energy Convers.*, vol. 19, no. 3, pp. 532–538, Sep. 2004.

[60] A. Tessarolo, F. Agnolet, F. Luise, and M. Mezzarobba, "Use of time-harmonic finite-element analysis to compute stator winding eddy-current losses due to rotor motion in surface permanent-magnet machines," *IEEE Trans. Energy Convers.*, vol. 27, no. 3, pp. 670–679, Sep. 2012.

[61] P. H. Mellor, R. Wrobel, and N. McNeill, "Investigation of proximity losses in a high speed brushless permanent magnet motor," in *Proc. Ind. Applications Conf. 41st IAS Annu. Meeting.*, vol. 3, Oct. 2006, pp. 1514–1518.

[62] T. Noguchi and T. Komori, "Eddy-current loss analysis of copper-bar windings of ultra high-speed PM motor," in *3rd Int. Conf. Electrical Systems Aircraft, Railway, Ship Propulsion Road Vehicles (ESARS)*, 2015.

[63] P. B. Reddy, T. M. Jahns, and T. P. Bohn, "Transposition effects on bundle proximity losses in high-speed PM machines," in *IEEE Energy Convers. Congr. and Expo.*, Sep. 2009, pp. 1919–1926.

[64] P. B. Reddy and T. M. Jahns, "Analysis of bundle losses in high speed machines," in *Int. Power Electron. Conf.*, Jun. 2010, pp. 2181–2188.

[65] J. Sibue, J. Ferrieux, G. Meunier, and R. Periot, "Modeling of losses and current density distribution in conductors of a large air-gap transformer using homogenization and 3-D FEM," *IEEE Trans. Magn.*, vol. 48, no. 2, pp. 763–766, Feb. 2012.

[66] H. Rossmanith, M. Doebroenti, M. Albach, and D. Exner, "Measurement and characterization of high frequency losses in nonideal litz wires," *IEEE Trans. Power Electron.*, vol. 26, no. 11, pp. 3386–3394, Nov. 2011.

[67] P. L. Dowell, "Effects of eddy currents in transformer windings," *Proc. IEE*, vol. 113, no. 8, pp. 1387–1394, Aug. 1966.

[68] R. P. Wojda and M. K. Kazimierczuk, "Analytical optimization of solid–round-wire windings," *IEEE Trans. Ind. Electron.*, vol. 60, no. 3, pp. 1033–1041, Mar. 2013.

[69] J. Acero, R. Alonso, J. M. Burdio, L. A. Barragan, and D. Puyal, "Frequency-dependent resistance in litz-wire planar windings for domestic induction heating appliances," *IEEE Trans. Power Electron.*, vol. 21, no. 4, pp. 856–866, Jul. 2006.

[70] R. P. Wojda and M. K. Kazimierczuk, "Winding resistance of litz-wire and multi-strand inductors," *IET Power Electron.*, vol. 5, no. 2, pp. 257–268, Feb. 2012.

[71] M. Bartoli, N. Noferi, A. Reatti, and M. K. Kazimierczuk, "Modeling litz-wire winding losses in high-frequency power inductors," in *Proc. IEEE Power Electron. Spec. Conf., Baveno, Italy*, vol. 2, Jun 1996, pp. 1690–1696 vol.2.

[72] A. W. Lotfi, P. M. Gradzki, and F. C. Lee, "Proximity effects in coils for high frequency power applications," *IEEE Trans. Magn.*, vol. 28, no. 5, pp. 2169–2171, Sep. 1992.

[73] R. Wrobel, A. Mlot, and P. H. Mellor, "Contribution of end-winding proximity losses to temperature variation in electromagnetic devices," *IEEE Trans. Ind. Electron.*, vol. 59, no. 2, pp. 848–857, Feb. 2012.

[74] C. R. Sullivan, "Computationally efficient winding loss calculation with multiple windings, arbitrary waveforms, and two-dimensional or three-dimensional field geometry," *IEEE Trans. Power Electron.*, vol. 16, no. 1, pp. 142–150, Jan. 2001.

[75] J. Acero, P. J. Hernandez, J. M. Burdio, R. Alonso, and L. A. Barragdan, "Simple resistance calculation in litz-wire planar windings for induction cooking appliances," *IEEE Trans. Magn.*, vol. 41, no. 4, pp. 1280–1288, Apr. 2005.

[76] P. B. Reddy, T. M. Jahns, and T. P. Bohn, "Modeling and analysis of proximity losses in high-speed surface permanent magnet machines with concentrated windings," in *IEEE Energy Convers. Congr. and Expo.*, Sep. 2010, pp. 996–1003.

[77] P. B. Reddy and T. M. Jahns, "Scalability investigation of proximity losses in fractional-slot concentrated winding surface PM machines during high-speed operation," in *IEEE Energy Convers. Congr. and Expo.*, Sep. 2011, pp. 1670–1675.

[78] P. Arumugam, T. Hamiti, and C. Gerada, "Modeling of different winding configurations for fault-tolerant permanent magnet machines to restrain interturn short-circuit current," *IEEE Trans. Energy Convers.*, vol. 27, no. 2, pp. 351–361, Jun. 2012.

[79] W. Rogowski, "Über zusätzliche kupferverluste, über die kritische kupferhöhe einer nut und über das kritische widerstandsverhältnis einer wechselstrommaschine," *Archiv für Elektrotechnik*, vol. 2, no. 3, pp. 81–118, 1913.

[80] Y. Amara, P. Reghem, and G. Barakat, "Analytical prediction of eddy-current loss in armature windings of permanent magnet brushless AC machines," *IEEE Trans. Magn.*, vol. 46, no. 8, pp. 3481–3484, Aug. 2010.

[81] P. Arumugam, T. Hamiti, and C. Gerada, "Fault tolerant winding design — a compromise between losses and fault tolerant capability," in *XXth Int. Conf. Elect. Machines*, Sep. 2012, pp. 2559–2565.

[82] C. R. Sullivan, "Optimal choice for number of strands in a litz-wire transformer winding," *IEEE Trans. Power Electron.*, vol. 14, no. 2, pp. 283–291, Mar. 1999.

[83] H. Hämäläinen, J. Pyrhönen, and J. Nerg, "AC resistance factor in one-layer form-wound winding used in rotating electrical machines," *IEEE Trans. Magn.*, vol. 49, no. 6, pp. 2967–2973, 2013.

[84] A. G. Jack *et al.*, "Permanent-magnet machines with powdered iron cores and prepressed windings," *IEEE Trans. Ind. Appl.*, vol. 36, no. 4, pp. 1077–1084, Jul.-Aug. 2000.

[85] J. W. Bennett, G. J. Atkinson, B. C. Mecrow, and D. J. Atkinson, "Fault-tolerant design considerations and control strategies for aerospace drives," *IEEE Trans. Ind. Electron.*, vol. 59, no. 5, pp. 2049–2058, May 2012.

[86] A. M. El-Refaie, "Fault-tolerant permanent magnet machines: a review," *IET Electric Power Appl.*, vol. 5, no. 1, pp. 59–74, 2011.

[87] C. Wenping, B. C. Mecrow, G. J. Atkinson, J. W. Bennett, and D. J. Atkinson, "Overview of electric motor technologies used for more electric aircraft (MEA)," *IEEE Trans. Ind. Electron.*, vol. 59, no. 9, pp. 3523–3531, Sep. 2012.

[88] C. Gerada, K. Bradley, and M. Summer, "Winding turn-to-turn faults in permanent magnet synchronous machine drives," in *Conf. Rec. 40th IEEE IAS Annu. Meeting*, vol. 2, 2005, pp. 1029–1036.

[89] Z. Sun, J. Wang, D. Howe, and G. Jewell, "Analytical prediction of the short-circuit current in fault-tolerant permanent-magnet machines," *IEEE Trans. Ind. Electron.*, vol. 55, no. 12, pp. 4210–4217, Dec. 2008.

[90] A. M. El-Refaie, M. R. Shah, and K. Huh, "High-power-density fault-tolerant PM generator for safety-critical applications," *IEEE Trans. Ind. Appl.*, vol. 50, no. 3, pp. 1717–1728, May 2014.

[91] R. M. Tallam, T. G. Habetler, and R. G. Harley, "Transient model for induction machines with stator winding turn faults," *IEEE Trans. Ind. Appl.*, vol. 38, no. 3, pp. 632–637, May-Jun. 2002.

[92] L. Romeral, J. C. Urresty, J.-R. Riba Ruiz, and A. Garcia Espinosa, "Modeling of surface-mounted permanent magnet synchronous motors with stator winding interturn faults," *IEEE Trans. Ind. Electron.*, vol. 58, no. 5, pp. 1576–1585, May 2011.

[93] S. Nadarajan, S. Panda, A. Gupta, and B. Bhagnu, "Hybrid model for wound rotor synchronous generator to detect and diagnose turn-to-turn short circuit fault in stator windings," *IEEE Trans. Ind. Electron.*, vol. 62, no. 3, pp. 1888–1900, Mar. 2015.

[94] G. Y. Sizov, C.-C. Yeh, and N. A. O. Demerdash, "Magnetic equivalent circuit modeling of induction machines under stator and rotor fault conditions," in *Proc. Int. Elec. Machines Drives Conf. (IEMDC)*, 2009, pp. 119–124.

[95] B.-G. Gu, J.-H. Choi, and I.-S. Jung, "Development and analysis of interturn short fault model of PMSMs with series and parallel winding connections," *IEEE Trans. Power Electron.*, vol. 29, no. 4, pp. 2016–2026, Apr. 2014.

[96] B. Vaseghi, N. Takorabet, and F. Meibody-Tabar, "Fault analysis and parameter identification of permanent-magnet motors by the finite-element method," *IEEE Trans. Magn.*, vol. 45, no. 9, pp. 3290–3295, Sep. 2009.

[97] A. Sarikhani and O. A. Mohammed, "Inter-turn fault detection in PM synchronous machines by physics-based back electromotive force estimation," *IEEE Trans. Ind. Electron.*, vol. 60, no. 8, pp. 3472–3484, Aug. 2013.

[98] P. M. Tuohy, S. Djurovic, and A. C. Smith, "Finite element analysis of winding fault effects in a wound-rotor induction machine with experimental validation," in *Power Electron. Machines Drives Conf. (PEMD)*, 2012, pp. 1–6.

[99] A. Gandhi, T. Corrigan, and L. Parsa, "Recent advances in modeling and online detection of stator interturn faults in electrical motors," *IEEE Trans. Ind. Electron.*, vol. 58, no. 5, pp. 1564–1575, May 2011.

[100] R. M. Tallam, T. G. Habetler, and R. G. Harley, "Stator winding turn-fault detection for closed-loop induction motor drives," *IEEE Trans. Ind. Appl.*, vol. 39, no. 3, pp. 720–724, May-Jun. 2003.

[101] M. A. Cash, T. G. Habetler, and G. B. Kliman, "Insulation failure prediction in AC machines using line-neutral voltages," *IEEE Trans. Ind. Appl.*, vol. 34, no. 6, pp. 1234–1239, Nov.-Dec. 1998.

[102] J. Urresty, J.-R. Riba Ruiz, and L. Romeral, "Diagnosis of interturn faults in PMSMs operating under nonstationary conditions by applying order tracking filtering," *IEEE Trans. Power Electron.*, vol. 28, no. 1, pp. 507–515, Jan. 2013.

[103] M. Christmann, "Error detection method for electrical motors having one or more star points," EU Patent EP2 377 239 B1, Jul. 31, 2013.

[104] F. Immovilli, C. Bianchini, E. Lorenzani, A. Bellini, and E. Fornasiero, "Evaluation of combined reference frame transformation for inter-turn fault detection in permanent magnet multi-phase machines," *IEEE Trans. Ind. Electron.*, vol. 62, no. 3, pp. 1912–1920, Mar. 2015.

[105] J. A. Rosero, L. Romeral, J. A. Ortega, and E. Rosero, "Short-circuit detection by means of empirical mode decomposition and wigner–ville distribution for PMSM running under dynamic condition," *IEEE Trans. Ind. Electron.*, vol. 56, no. 11, pp. 4534–4547, Nov. 2009.

[106] A. G. Espinosa, J. A. Rosero, J. Cusido, L. Romeral, and J. A. Ortega, "Fault detection by means of hilbert–huang transform of the stator current in a PMSM with demagnetization," *IEEE Trans. Energy Convers.*, vol. 25, no. 2, pp. 312–318, Jun. 2010.

[107] J. Seshadrinath, B. Singh, and B. Panigrahi, "Incipient turn fault detection and condition monitoring of induction machine using analytical wavelet transform," *IEEE Trans. Ind. Appl.*, vol. 50, no. 3, pp. 2235–2242, May 2014.

[108] Y. Nyanteh, C. Edrington, S. Srivastava, and D. Cartes, "Application of artificial intelligence to real-time fault detection in permanent-magnet synchronous machines," *IEEE Trans. Ind. Appl.*, vol. 49, no. 3, pp. 1205–1214, May 2013.

[109] A. Soualhi, G. Clerc, and H. Razik, "Detection and diagnosis of faults in induction motor using an improved artificial ant clustering technique," *IEEE Trans. Ind. Electron.*, vol. 60, no. 9, pp. 4053–4062, Sep. 2013.

[110] N. Leboeuf, T. Boileau, B. Nahid-Mobarakeh, G. Clerc, and F. Meibody-Tabar, "Real-time detection of interturn faults in PM drives using back-EMF estimation and residual analysis," *IEEE Trans. Ind. Appl.*, vol. 47, no. 6, pp. 2402–2412, Nov.-Dec. 2011.

[111] B. Aubert, J. Regnier, S. Caux, and D. Alejo, "Kalman filter based indicator for on-line inter-turn short-circuits detection in permanent magnet synchronous generators," *IEEE Trans. Ind. Electron.*, vol. 62, no. 3, pp. 1921–1930, Mar. 2015.

[112] F. Briz, M. W. Degner, A. Zamarron, and J. M. Guerrero, "Online stator winding fault diagnosis in inverter-fed AC machines using high-frequency signal injection," *IEEE Trans. Ind. Appl.*, vol. 39, no. 4, pp. 1109–1117, Jul. 2003.

[113] J. Arellano-Padilla, M. Sumner, and C. Gerada, "Winding condition monitoring scheme for a permanent magnet machine using high-frequency injection," *IET Electric Power Appl.*, vol. 5, no. 1, pp. 89–99, Jan. 2011.

[114] Y. Da, X. Shi, and M. Krishnamurthy, "A new approach to fault diagnostics for permanent magnet synchronous machines using electromagnetic signature analysis," *IEEE Trans. Power Electron.*, vol. 28, no. 8, pp. 4104–4112, Aug. 2013.

[115] H. Henao, C. Demian, and G.-A. Capolino, "A frequency-domain detection of stator winding faults in induction machines using an external flux sensor," *IEEE Trans. Ind. Appl.*, vol. 39, no. 5, pp. 1272–1279, Sep. 2003.

[116] A. Mitcham, G. Antonopoulos, and J. J. A. Cullen, "Implications of shorted turn faults in bar wound PM machines," *IEE Proc. Elec. Power Appl.*, vol. 151, no. 6, pp. 651–657, Nov. 2004.

[117] P. Arumugam, T. Hamiti, C. Brunson, and C. Gerada, "Analysis of vertical strip wound fault-tolerant permanent magnet synchronous machines," *IEEE Trans. Ind. Electron.*, vol. 61, no. 3, pp. 1158–1168, Mar. 2014.

[118] R. De Doncker, D. W. J. Pulle, and A. Veltman, *Advanced Electrical Drives.* Springer, 2011.

[119] T. Boileau, N. Leboeuf, B. Nahid-Mobarakeh, and F. Meibody-Tabar, "Synchronous demodulation of control voltages for stator interturn fault detection in PMSM," *IEEE Trans. Power Electron.*, vol. 28, no. 12, pp. 5647–5654, Dec. 2013.

[120] Magnetemp CA-200. Superior essex. [Online]. Available: http://superioressex.com/magnetwire.aspx?id=3698

[121] A. Boglietti, P. Ferraris, M. Lazzari, and M. Pastorelli, "Change of the iron losses with the switching supply frequency in soft magnetic materials supplied by PWM inverter," *IEEE Trans. Magn.*, vol. 31, no. 6, pp. 4250–4252, Nov. 1995.

[122] R. Liu, C. C. Mi, and D. W. Gao, "Modeling of eddy-current loss of electrical machines and transformers operated by pulsewidth-modulated inverters," *IEEE Trans. Magn.*, vol. 44, no. 8, pp. 2021–2028, Aug. 2008.

[123] A. Boglietti *et al.*, "A general model to predict the iron losses in PWM inverter-fed induction motors," *IEEE Trans. Ind. Appl.*, vol. 46, no. 5, pp. 1882–1890, Sep. 2010.

[124] A. Krings, J. Soulard, and O. Wallmark, "Influence of PWM switching frequency and modulation index on the iron losses and performance of slot-less permanent magnet motors," in *Int. Conf. Elec. Machines Syst. (ICEMS)*, Oct. 2013, pp. 474–479.

[125] P. A. Hargreaves, B. C. Mecrow, and R. Hall, "Calculation of iron loss in electrical generators using finite-element analysis," *IEEE Trans. Ind. Appl.*, vol. 48, no. 5, pp. 1460–1466, Sep.–Oct. 2012.

[126] P. Mellor, R. Wrobel, D. Salt, and A. Griffo, "Experimental and analytical determination of proximity losses in a high-speed PM machine," in *Energy Convers. Congr. Expo. (ECCE)*, 2013, pp. 3504–3511.

[127] L. Schwager, A. Tüysüz, C. Zwyssig, and J. W. Kolar, "Modeling and comparison of machine and converter losses for PWM and PAM in high-speed drives," in *Int. Conf. Elect. Machines (ICEM)*, Sep. 2012, pp. 2441–2447.

[128] K. Yamazaki, T. Fukuoka, K. Akatsu, N. Nakao, and A. Ruderman, "Investigation of locked rotor test for estimation of magnet PWM carrier eddy current loss in synchronous machines," *IEEE Trans. Magn.*, vol. 48, no. 11, pp. 3327–3330, Nov. 2012.

[129] G. Bertotti *et al.*, "An improved estimation of iron losses in rotating electrical machines," *IEEE Trans. Magn.*, vol. 27, no. 6, pp. 5007–5009, Nov. 1991.

[130] V. B. Hart, "Starter-generator control system for a multijet airplane," *Trans. Amer. Inst. Elect. Engineers*, vol. 67, no. 2, pp. 1316–1318, Jan. 1948.

[131] J. M. Miller, A. R. Gale, P. J. McCleer, F. Leonardi, and J. H. Lang, "Starter-alternator for hybrid electric vehicle: comparison of induction and variable reluctance machines and drives," in *Conf. Rec. 33rd IEEE IAS Annu. Meeting*, 1998, pp. 513–523.

[132] N. Schofield and S. Long, "Generator operation of a switched reluctance starter/generator at extended speeds," *IEEE Trans. Veh. Technol.*, vol. 58, no. 1, pp. 48–56, Jan. 2009.

[133] B. Fahimi, "A switched reluctance machine based starter/generator for more electric cars," in *IEEE Int. Elec. Mach. Drives Conf.*, 2001, pp. 73–78.

[134] G. Friedrich, "Experimental comparison between wound rotor and permanent magnet synchronous machine for integrated starter generator applications," in *IEEE Energy Convers. Congr. Expo.*, Sep. 2010, pp. 1731–1736.

[135] C.-F. Wang, M.-J. Jin, J.-X. Shen, and C. Yuan, "A permanent magnet integrated starter generator for electric vehicle onboard range extender application," *IEEE Trans. Magn.*, vol. 48, no. 4, pp. 1625–1628, Apr. 2012.

[136] T. M. Jahns, G. B. Kliman, and T. W. Neumann, "Interior permanent-magnet synchronous motors for adjustable-speed drives," *IEEE Trans. Ind. Appl.*, vol. IA-22, no. 4, pp. 738–747, Jul. 1986.

[137] B.-H. Bae and S.-K. Sul, "Practical design criteria of interior permanent magnet synchronous motor for 42V integrated starter-generator," in *IEEE Int. Electric Mach. Drives Conf.*, vol. 2, 2003, pp. 656–662.

[138] L. Chedot, G. Friedrich, J.-M. Biedinger, and P. Macret, "Integrated starter generator: The need for an optimal design and control approach. application to a permanent magnet machine," *IEEE Trans. Ind. Appl.*, vol. 43, no. 2, pp. 551–559, 2007.

[139] L. Alberti *et al.*, "IPM machine drive design and tests for an integrated starter–alternator application," *IEEE Trans. Ind. Appl.*, vol. 46, no. 3, pp. 993–1001, May-Jun. 2010.

[140] M. Morandin, A. Faggion, and S. Bolognani, "Integrated starter–alternator with sensorless ringed-pole pm synchronous motor drive," *IEEE Trans. Ind. Appl.*, vol. 51, no. 2, pp. 1485–1493, Mar. 2015.

[141] Z. X. Fang, Y. Wang, J. X. Shen, and Z. W. Huang, "Design and analysis of a novel flux-switching permanent magnet integrated-starter-generator," in *IET Conf. Power Electron. Mach. Drives*, Apr. 2008, pp. 106–110.

[142] W. Fei, P. C. K. Luk, J. X. Shen, B. Xia, and Y. Wang, "Permanent-magnet flux-switching integrated starter generator with different rotor configurations for cogging torque and torque ripple mitigations," *IEEE Trans. Ind. Appl.*, vol. 47, no. 3, pp. 1247–1256, May-Jun. 2011.

[143] L. Del Ferraro, F. Caricchi, and F. G. Capponi, "Analysis and comparison of a speed-dependant and a torque-dependant mechanical device for wide constant power speed range in AFPM starter/alternators," *IEEE Trans. Power Electron.*, vol. 21, no. 3, pp. 720–729, May 2006.

[144] J. Borg Bartolo and C. Gerada, "Design and modeling of a 45kW, switched reluctance starter-generator for a regional jet application," in *SAE Aerospace Syst. Techn. Conf.*, 2014.

[145] C. A. Ferreira, S. R. Jones, W. S. Heglund, and W. D. Jones, "Detailed design of a 30-kW switched reluctance starter/generator system for a gas turbine engine application," *IEEE Trans. Ind. Appl.*, vol. 31, no. 3, pp. 553–561, May-Jun. 1995.

[146] E. Richter and C. Ferreira, "Performance evaluation of a 250 kW switched reluctance starter generator," in *IEEE Ind. Appl. Conf*, vol. 1, Oct. 1995, pp. 434–440 vol.1.

[147] S. R. MacMinn and W. D. Jones, "A very high speed switched-reluctance starter-generator for aircraft engine applications," in *IEEE Nat. Aerospace Electron. Conf. (NAECON)*, May 1989, pp. 1758–1764 vol.4.

[148] R. Hall, A. G. Jack, B. C. Mecrow, and A. J. Mitcham, "Design and initial testing of an outer rotating segmented rotor switched reluctance machine for an aero-engine shaft-line-embedded starter/generator," in *Proc. IEEE Int. Electric Mach. Drives Conf.*, 2005, pp. 1870–1877.

[149] G. Friedrich and A. Girardin, "Integrated starter generator," *IEEE Ind. Appl. Mag.*, vol. 15, no. 4, pp. 26–34, Jul.–Aug. 2009.

[150] R. Wrobel *et al.*, "Design study of a three-phase brushless exciter for aircraft starter/generator," in *Proc. IEEE Energy Convers. Congr. Expo.*, 2011, pp. 3998–4004.

[151] P. H. Mellor *et al.*, "Design considerations for aircraft generator with start function," in *Power Systems Conference*, 2008.

[152] A. Griffo, D. Drury, T. Sawata, and P. H. Mellor, "Sensorless starting of a wound-field synchronous starter/generator for aerospace applications," *IEEE Trans. Ind. Electron.*, vol. 59, no. 9, pp. 3579–3587, Sep. 2012.

[153] Z. Chen, H. Wang, and Y. Yan, "A doubly salient starter/generator with two-section twisted-rotor structure for potential future aerospace application," *IEEE Trans. Ind. Electron.*, vol. 59, no. 9, pp. 3588–3595, Sep. 2012.

[154] M. Degano *et al.*, "An optimized bi-directional, wide speed range electric starter-generator for aerospace application," in *7th IET Int. Conf. Power Electron. Machines, Drives (PEMD)*, April 2014.

[155] P. Arumugam *et al.*, "Comparative design analysis of permanent magnet rotor topologies for an aircraft starter-generator," in *Int. Conf. Intelligent Energy Power Syst (IEPS)*, Jun. 2014, pp. 273–278.

[156] B. S. Bhangu and K. Rajashekara, "Electric starter generators: Their integration into gas turbine engines," *IEEE Ind. Appl. Mag.*, vol. 20, no. 2, pp. 14–22, Mar. 2014.

[157] N. Bianchi, D. Durello, and A. Fasolo, "Relationship between rotor losses and size of permanent-magnet machines," *IEEE Trans. Ind. Appl.*, vol. 49, no. 5, pp. 2015–2023, 2013.

[158] K. J. Binns and D. W. Shimmin, "Relationship between rated torque and size of permanent magnet machines," *IEE Proc. - Electric Power Appl.*, vol. 143, no. 6, pp. 417–422, Nov 1996.

[159] S. Huang, J. Luo, F. Leonardi, and T. A. Lipo, "A general approach to sizing and power density equations for comparison of electrical machines," *IEEE Trans. Ind. Appl.*, vol. 34, no. 1, pp. 92–97, Jan. 1998.

[160] G. A. J. Amaratunga, P. P. Acarnley, and P. G. McLaren, "Optimum magnetic circuit configurations for permanent magnet aerospace generators," *IEEE Trans. Aerosp. Electron. Syst.*, vol. AES-21, no. 2, pp. 230–255, Mar. 1985.

[161] A. Borisavljevic, H. Polinder, and J. A. Ferreira, "On the speed limits of permanent-magnet machines," *IEEE Trans. Ind. Electron.*, vol. 57, no. 1, pp. 220–227, Jan. 2010.

[162] Z. Kolondzovski, A. Arkkio, J. Larjola, and P. Sallinen, "Power limits of high-speed permanent-magnet electrical machines for compressor applications," *IEEE Trans. Energy Convers.*, vol. 26, no. 1, pp. 73–82, Mar. 2011.

[163] J. L. Baker, D. Drury, and P. H. Mellor, "Sizing of concentrated-wound permanent-magnet machines using thermal analysis," in *7th IET Int. Conf. Power Electronics, Machines Drives (PEMD)*, Apr. 2014, pp. 1–6.

[164] D. Gerada *et al.*, "High-speed electrical machines: Technologies, trends, and developments," *IEEE Trans. Ind. Electron.*, vol. 61, no. 6, pp. 2946–2959, Jun. 2014.

[165] A. Tenconi, S. Vaschetto, and A. Vigliani, "Electrical machines for high-speed applications: Design considerations and tradeoffs," *IEEE Trans. Ind. Electron.*, vol. 61, no. 6, pp. 3022–3029, Jun. 2014.

[166] F. Cupertino, G. Pellegrino, and C. Gerada, "Design of synchronous reluctance machines with multi-objective optimization algorithms," *IEEE Trans. Ind. Appl.*, vol. 50, no. 6, pp. 3617–3627, Nov.-Dec. 2014.

[167] Y. Duan, Q. Sun, and D. M. Ionel, "Methods for studying the pareto-fronts in multi-objective design optimization problems of electrical machines," in *Energy Convers. Congr. Expo. (ECCE)*, Sep. 2013, pp. 5013–5018.

[168] A. Binder, T. Schneider, and M. Klohr, "Fixation of buried and surface-mounted magnets in high-speed permanent-magnet synchronous machines," *IEEE Trans. Ind. Appl.*, vol. 42, no. 4, pp. 1031–1037, 2006.

[169] D. Gerada, A. Mebarki, N. L. Brown, K. J. Bradley, and C. Gerada, "Design aspects of high-speed high-power-density laminated-rotor induction machines," *IEEE Trans. Ind. Electron.*, vol. 58, no. 9, pp. 4039–4047, Sep. 2011.

[170] A. Boglietti, A. Cavagnino, and D. Staton, "Determination of critical parameters in electrical machine thermal models," *IEEE Trans. Ind. Appl.*, vol. 44, no. 4, pp. 1150–1159, 2008.

[171] D. A. Staton and A. Cavagnino, "Convection heat transfer and flow calculations suitable for electric machines thermal models," *IEEE Trans. Ind. Electron.*, vol. 55, no. 10, pp. 3509–3516, Oct. 2008.

[172] N. Simpson, R. Wrobel, and P. H. Mellor, "Estimation of equivalent thermal parameters of impregnated electrical windings," *IEEE Trans. Ind. Appl.*, vol. 49, no. 6, pp. 2505–2515, Nov. 2013.

[173] O. Maloberti *et al.*, "Thermal modeling of a claw-pole electrical generator: Steady-state computation and identification of free and forced convection coefficients," *IEEE Trans. Ind. Appl.*, vol. 50, no. 1, pp. 279–287, Jan. 2014.

[174] Y. Duan, R. G. Harley, and T. G. Habetler, "Comparison of particle swarm optimization and genetic algorithm in the design of permanent magnet motors," in *Proc. 6th IEEE Int. Power Electron. and Motion Control Conf.*, 2009, pp. 822–825.

[175] B. C. Mecrow *et al.*, "Design and testing of a four-phase fault-tolerant permanent-magnet machine for an engine fuel pump," *IEEE Trans. Energy Convers.*, vol. 19, no. 4, pp. 671–678, Dec. 2004.

[176] C. Jungreuthmayer *et al.*, "A detailed heat and fluid flow analysis of an internal permanent magnet synchronous machine by means of computational fluid dynamics," *IEEE Trans. Ind. Electron.*, vol. 59, no. 12, pp. 4568–4578, Dec. 2012.

[177] M. Tosetti, P. Maggiore, A. Cavagnino, and S. Vaschetto, "Conjugate heat transfer analysis of integrated brushless generators for more electric engines," *IEEE Trans. Ind. Appl.*, vol. 50, no. 4, pp. 2467–2475, Jul. 2014.

Acknowledgements

The actual writing a of PhD thesis is something you do mostly alone, but all steps leading up to this involve a lot of other people. Here, I would like to take the opportunity to thank those people.

First of all I want to thank my co-promotor Henk Polinder. He offered me the possibility to do this PhD, and doing it with a great amount of freedom. His specific contributions to this thesis are hard to pinpoint, but his guidance during our weekly meetings has most certainly shaped it as a whole. More importantly, he was always available for questions and discussions, whether those stayed on-topic or not.

Similarly I want to thank my promotor Braham Ferreira. Some may consider the monthly meetings 'a waste of time', but I definitely do not.

Next, I want to thank all people at Aeronamic, but especially Dennis Zeilstra and Sido Kermans, for handling the practical side of the project and asking the annoying questions I did not want to ask myself; my thesis greatly benefitted from this! The same goes for Alte de Boer of the NLR, for handling the more administrative aspects of the projects.

The 'power-electronics-people', Johan, Emile and Mark, should also be mentioned. A high performance machine needs high performance power electronics, and they made that happen and let me use it for my experiments, for which I am very grateful.

To all co-authors: thank you for your help, suggestions and corrections, or just insightful discussions! Without you, none of the papers would have materialized.

Colleagues, past and present, from the EPP and DCE&S groups: thank you for keeping the life in the office more interesting and bearing my poor jokes. Maybe you won't miss me, but I won't forget you. This applies especially to my office mates, Anoop and Sílvio.

I also want to thank the lab managers, Rob, Harry, Chris, Joris, Kasper, for supporting or enduring my sometimes strange or smelly experiments.

And finally, I want to thank my parents and sister for their continued support.

List of publications

Main papers:

- M. van der Geest, J. J. Wolmarans, H. Polinder, J. A. Ferreira, and D. Zeilstra, "Rotor losses in laminated magnets and an anisotropic carbon fiber sleeve," in *6th IET Int. Conf. Power Electron. Machines Drives (PEMD)*, 2012.
- M. van der Geest, H. Polinder, J. A. Ferreira, and D. Zeilstra, "Optimization and comparison of electrical machines using particle swarm optimization," in *20th Int. Conf. Elec. Machines (ICEM)*, 2012, pp. 1380–1386.
- M. van der Geest, H. Polinder, J. A. Ferreira, and D. Zeilstra, "Machine selection and initial design of an aerospace starter/generator," in *IEEE Int. Electric Machines Drives Conf. (IEMDC)*, 2013, pp. 196–203.
- M. van der Geest, H. Polinder, J. A. Ferreira, and D. Zeilstra, "Stator winding proximity loss reduction techniques in high speed electrical machines," in *IEEE Int. Electric Machines Drives Conf. (IEMDC)*, 2013, pp. 340–346.
- M. van der Geest, H. Polinder, J. Ferreira, and D. Zeilstra, "Current sharing analysis of parallel strands in low voltage high speed machines," *IEEE Trans. Ind. Electron.*, vol. 61, no. 6, pp. 3064–3070, Jun. 2014.
- M. van der Geest, H. Polinder, and J. A. Ferreira, "Efficient finite element based rotor loss calculation for permanent magnet synchronous machines," in *Int. Conf. Electrical Machines (ICEM)*, 2014, pp. 1133–1138.
- M. van der Geest, H. Polinder, and J. A. Ferreira, "Short-circuit faults in high-speed PM machines with parallel strands and coils," in *7th Int. Conf. Power Electron. Machines Drives (PEMD)*, 2014.
- M. van der Geest, H. Polinder, and J. A. Ferreira, "Influence of PWM switching frequency on the losses in PM machines," in *Int. Conf. Electrical Machines (ICEM)*, 2014, pp. 1243–1247.
- M. van der Geest, H. Polinder, and J. A. Ferreira, "Experimental determination of stator winding failure behavior," in *16th European Conf. Power Electron. Appl. (EPE-ECCE Europe)*, 2014.
- M. van der Geest, H. Polinder, J. A. Ferreira, and M. Christmann, "Quantitative power density limits of aerospace permanent magnet synchronous machines," in *More Electric Aircraft Conference (MEA)*, Toulouse, 2015.
- M. van der Geest, H. Polinder, J. A. Ferreira, and D. Zeilstra, "Design and testing of a high-speed aerospace permanent magnet starter/generator," in *3rd Int. Conf. Electrical Systems Aircraft, Railway, Ship propulsion and Road Vehicles (ESARS)*, 2015.
- M. van der Geest, H. Polinder, J. A. Ferreira, A. Veltman, J. J. Wolmarans, and N. Tsiara, "Analysis and Neutral Voltage Based Detection of Inter-Turn Faults in High-Speed Permanent Magnet Machines with Parallel Strands," *IEEE Trans. Ind. Electron.*, vol. 62, no. 6, pp. 3862–3873, Jun. 2015.
- M. van der Geest, H. Polinder, J. A. Ferreira, and M. Christmann, "Power density limits and design trends of high-speed permanent magnet synchronous machines," *IEEE Trans. Transportation Electrification*, vol. 1, no. 3, pp. 266–276, Oct. 2015.

- M. van der Geest, H. Polinder, and J. A. Ferreira, "Computationally efficient 3D FEM rotor eddy-current loss calculation for permanent magnet synchronous machines," in *IEEE Int. Electric Machines Drives Conf. (IEMDC)*, 2015.

Co-authored:

- J. J. Wolmarans, M. van der Geest, H. Polinder, J. A. Ferreira, and D. Zeilstra, "Composite materials for low loss rotor construction," in *IEEE Int. Elec. Mach. Drives Conf.*, 2011, pp. 295–299.
- J. J. Wolmarans, M. van der Geest, H. Polinder, J. A. Ferreira, and D. Zeilstra, "A low conductivity composite rotor for fractional pitch concentrated winding machines," in *IEEE Energy Conversion Congr. Expo. (ECCE)*, 2011, pp. 2536–2542.
- D. Papaoikonomou, M. van der Geest, and H. Polinder, "Comparison between induction and pm machine for high speed starter-generator applications," in 7^{th} *IET Int. Conf. Power Electronics, Machines Drives (PEMD)*, 2014.

Biography

Martin van der Geest was born in Rijpwetering, Netherlands, in 1987. He received the BSc and MSc (cum laude) degrees in Electrical Engineering and Electrical Power Engineering in 2009 and 2011, respectively, from the Delft University of Technology, Delft, The Netherlands. From June 2011 he pursued the PhD degree with the Electrical Power Processing group at the Delft University of Technology.
His main research interests are the accurate and efficient modeling of electrical machines and the automated optimization of those machines, as well as any related topics.